Metamaterial-Inspired Structures for Microwave and Terahertz Applications

by

Amir Ebrahimi

B. Eng. (Electrical and Electronic Engineering, First Class Honours),
University of Mazandaran, Iran, 2008

M. Eng. (Electronic Engineering, First Class Honours),
Babol Noshirvani University of Technology, Iran, 2011

Thesis submitted for the degree of

Doctor of Philosophy

in

Electrical and Electronic Engineering,
Faculty of Engineering, Computer and Mathematical Sciences
The University of Adelaide, Australia

2016

Supervisors:

Dr Said Al-Sarawi, School of Electrical & Electronic Engineering

Dr Withawat Withayachumnankul, School of Electrical & Electronic Engineering

Prof Derek Abbott, School of Electrical & Electronic Engineering

THE UNIVERSITY of ADELAIDE

To my dearest wife, Aida
and to my Mum, Dad, and Sister
with all my love.

Contents

Statement of Originality

I certify that this work contains no material, which has been accepted for the award of any other degree or diploma in my name, in any university or other tertiary institution and, to the best of my knowledge and belief, contains no material previously published or written by another person, except where due reference has been made in the text.

I give consent to this copy of my thesis, when deposited in the University Library, being available for loan, photocopying, and dissemination through the library digital thesis collection subject to the provisions of the Copyright Act 1968.

I also give permission for the digital version of my thesis to be made available on the web, via the University's digital research repository, the Library Search, the Australian Digital Thesis Program (ADTP), and also through web search engines, unless permission has been granted by the University to restrict access for a period of time.

06/01/2016

Signed Date

Acknowledgments

First and foremost, I would like to convey my deepest gratitude to my supervisors **Dr Said Al-Sarawi**, **Dr Withawat Withayachumnankul** and **Prof. Derek Abbott** for their guidance and support throughout my candidature. My principal supervisor, Dr Al-Sarawi advised me with his open view and broad knowledge in the field of electronic engineering and circuit design. His critical, and thoughtful comments were always constructive and fruitful to improve the quality of my research. I had also the pleasure to work with Dr Withawat Withayachumnankul. His deep knowledge in the field of electromagnetics, microwave and terahertz engineering have been of great importance toward my research. He always welcomed scientific discussion and has given me critical feedback. I have endured many hard times in throughly revising the drafts to satisfy his strict requirements. But eventually in turned out it was worth doing so. He defined the word 'quality' for the research. I would like to gratefully acknowledge his enthusiastic supervision, encouraging attitude, and genereously sharing his knowledge. Dear Withawat, you become more of a mentor and freind, than a supervisor. I would also like to thank my other co-supervisor, Prof. Derek Abbott, who has been of great help, support and advice, when it counted most. His enthusiastic supervision, unwavering optimism, constructive suggestions, linguistic finesse, and genereous travel financial assistance have been helpful in propelling my research forward.

Another key person whom I am strongly indebted to is **Prof. Christophe Fumeaux**. As a leader of Adelaide Applied Electromagnetic Group, he provided me the opportunity of attending the group meetings. The experiences, discussions and comments in the group meeting were really insightful in my research direction. Christoph never hesitated in giving constructive feedback and discussing electromagnetic issues, whenever I asked.

I wish to express my warm thanks to Prof. Zhongxiang Shen for inviting me to visit his research group at the Nanyang Technological University, Singapore. Prof. Shen's broad theoretical and experimental knowledge in the field of electromagnetic theory and FSS design were of great importance towards my PhD research. I would like to thank my

good friends Jiang Wang, Ali Al-Sheikh, Alex Hu, Zhuozhu Chen, Changzhou Hua, and Yue Cen for making a freindly research environment during my stay in Singapore.

I would like to express my gratitude to Dr Sarath Sriram, Dr Madhu Bhaskaran and Ms Shruti Nirantar at the Functional Materials and Microsystems Research Group, RMIT University, Melbourne for their support and fabrication of the terahertz FSS prototype.

I wish to thank Mr Simon Doe, and Mr Dipankar Chugh at the Ian Wark Research Institute, University of South Australia for their technical assistance in microfabrication of the microfluidic sensors.

There are many people who helped me throughout my PhD candidature. Within the school of Electrical & Electronic Engineering, I am indebted to Dr Thomas Kaufmann and Dr Ali Karami for their kindness, passion in discussing around different research issues and critical suggestions. I would also express my appreciation to my freinds and colleagues in the Applied Electromagnetics Group at the University of Adelaide, Dr Longfang Zou, Dr Zahra Shaterian, Tiaoming (Echo) Niu, Shengjian (Jammy) Chen, Chengjun (Charles) Zou, Nghia Nguyen Trong, Cheng Zhao, Sree Pinapati, Wendy Lee, Andrew Udina, Deshan Govender, and Fengxue Liu, and to the people at the Adelaide T-ray Group, Mr Henry Ho, Dr Gretel M. Png, Dr Alex Dinovitser, Dr Benjamin Ung, Mr Shaoming Zhu, Mr Jining Li, Mr Daniel Headland, and Dr Azhar Iqbal.

My first days in the school were great and happy because of the support and friendliness of Dr Pouria Yaghmaee, Dr Sam Darvishi and Mr Mehdi Kasaei. Indeed, one of the most respected freinds I had in the school, has been Dr Mostafa Rahimi, who was always there for me and I could count on his help and advice. Thank you very much Mostafa.

I also like to thank the office & support staff of the school including Danny Di Giacomo for the logistical supply of required tools and items, IT officers, David Bowler, Mark Innes, and Ryan King, and the administrative staff, Stephen Guest, Greg Pullman, Ivana Rebellato, Rose-Marie Descalzi, Deborah Koch, Lenka Hill, and Jodie Schluter for their kindness and assistance. I would also like to thank the head of school, Associate Prof. Cheng-Chew Lim, for his support regarding my research travels and software required for my PhD research. I am also thankful to my other friends and colleagues within the school. In addition, I sincerely thank my other friends and colleagues Mariam Ebrahimpour, Solmaz Kahourzadeh, Arash Mehdizadeh, Neda Shabi, Muhammad Asraful Hasan, Nicholas P. Lawrence, Mostafa Numan, Vichet Duk, Sarah Immanuel, Robert Moric, Tran Nguyen, and Yansong (Garrison) Gao, for making such

a friendly research environment. Also my wife and I appreciate support of our family friends in Adelaide, Meisam Valizadeh, Reza Salari, Hassan Amirparast, Amin Mahmoudi, Sara Chek, Ryan Darvishi, Hedy Minoofar, Saeid Sedghi, Masoumeh Eyvazi, Ali Gholampour, and Hadis Afshar for their help to make our life in Adelaide so good.

I am also indebted to all my good teachers for planting love of knowledge in my heart, Mr Akbarzadeh, Mr Mashafi, Mr Mohammadpour, Mr Mehdipour, Mr Kheyri, Mr Barari, Mr Hedayat-Zadeh among others. I have learned analog circuit design and microwave engineering from two masters: Prof. Hossein Miar-Naimi (Babol University of Technology) and Dr Withawat Withayachumnankul (The University of Adelaide), and it is appropriate to express my gratitude to them here.

I recognise that this research would not have been possible without the financial support of Australian Government via a generous International Postgraduate Research Scholarship (IPRS) and Australian Postgraduate Award (APA). During my candidature, I was awarded several travel grants, scholarships and awards by other organisations. Here, I would like to deeply appreciate these organisations support including annual travel grants from the School of Electrical & Electronic Engineering (2013-2015), the Australia's Defence Science and Technology Organisation (DSTO) Simon Rockliff Supplementary Scholarship (2015), the University of Adelaide D. R. Stranks Postgraduate Fellowship (2014), and the Australian Nano-Fabrication Facility Start Up Award (2012).

Back to my home country, my endless gratitude goes to my father and mother who always endow me with infinite support, wishes, continuous love, encouragement, and patience. I also thank my best and kindest sister for her love and support. I also wish to express my warm and sincere thanks to my father- and mother-in-law for their kindness, guidance, and earnest wishes. Also, I would like to thank my brothers-in-law for their support, inspiration, and kindness.

Last but not least, my most heartfelt thanks are due to my dearest stunning wife, *Aida*. Words are unable to express my deepest appreciation and love to her. She stood by me in all ups and downs of my PhD and always endowed me with her endless love, and support. Darling, I love you from the bottom of my heart.

Amir Ebrahimi,
January 2016,
Adelaide

Thesis Conventions

The following conventions have been adopted in this Thesis:

Typesetting

This document was compiled using LaTeX2e. Texmaker and TeXstudio were used as text editor interfaced to LaTeX2e. Inkscape and Xcircuit were used to produce schematic diagrams and other drawings.

Referencing

The Harvard style has been adopted for referencing.

System of units

The units comply with the international system of units recommended in an Australian Standard: AS ISO 1000–1998 (Standards Australia Committee ME/71, Quantities, Units and Conversions 1998).

Spelling

Australian English spelling conventions have been used, as defined in the Macquarie English Dictionary (A. Delbridge (Ed.), Macquarie Library, North Ryde, NSW, Australia, 2001).

Awards and Scholarships

2015

- Yarman-Carlin Best Paper Award, Mediterranean Microwave Symposium
- Simon Rockliff Scholarship, DSTO

2014

- D. R. Stranks Fellowship, The University of Adelaide

2013

- Australian National Fabrication Facility (ANFF) Start Up Award

2012

- International Postgraduate Research Scholarships, The Australian Government
- Australian Postgraduate Award (APA), The Australian Government

Abstract

Electromagnetic metamaterials are engineered materials that exhibit controllable electromagnetic properties within a desired frequency range. They are usually made of periodic metallic resonant inclusions with dimensions much smaller than the operational wavelength. Since their introduction, they have found many applications from the microwave frequency range up to the terahertz and optical ranges. One key advantage of metamaterial lies in their sub-wavelength resonators making them suitable for miniaturisation of RF circuits and components.

This thesis investigates applications of metamaterial-inspired resonators and structures to design improved devices and components operating at either the microwave or terahertz frequency range. The first part of the dissertation is on the design of miniaturised microwave filters for integrated portable RF systems. Dual-mode metamaterial resonators are proposed as alternatives to conventional resonators for size reduction of the RF filters. In the second part, the focus is on the design of compact metamaterial sensors with improved functionalities. Complementary metamaterial resonators are proposed for designing microfluidic sensors with improved sensitivity and linearity. The designed microfluidic sensors have been tested and verified for dielectric characterisation of chemical and biological solutions. A wide dynamic-range displacement sensor has been designed based on a microstrip-line-coupled complementary electric-LC (ELC) resonator. Furthermore, a rotation sensor is designed with coupled U-shaped resonator with a dynamic range of 180°, where the sensor linearity is improved by asymmetrically tapering the resonators shape. The third part focuses on the design of microwave and terahertz frequency selective surfaces (FSS) based on metamaterial miniaturised elements. Tunable and dual-band FSSs are proposed for reconfigurable and multi-standard microwave communications. Eventually, miniaturised-elements are used to design second-order FSSs at the terahertz frequency range. The simulation and measurement results confirm a harmonic-free and stable frequency response of the designed FSSs under oblique incidence angles.

Overall, the research outcomes in this thesis suggest the efficiency of metamaterial resonators for the design of sensing and communications devices with improved performance over a wide frequency range from the microwave up to terahertz.

Publications

Journal Articles

Ebrahimi-A., Nirantar-S., Withayachumnankul-W., Bhaskaran-M., Sriram-S., Al-Sarawi-S., and Abbott-D. (2015a). Second-order terahertz bandpass frequency selective surface with miniaturized elements, *IEEE Transactions on Terahertz Science and Technology*, **5**(5), pp. 761–769. *

Ebrahimi-A., Withayachumnankul-W., Al-Sarawi-S., and Abbott-D. (2014f). Dual-mode behavior of the complementary electric-LC resonators loaded on transmission line: Analysis and applications, *Journal of Applied Physics*, **116**, art. no. 083705. *

Ebrahimi-A., Withayachumnankul-W., Al-Sarawi-S., and Abbott-D. (2014d). Metamaterial-inspired rotation sensor with wide dynamic range, *IEEE Sensors Journal*, **14**(8), pp. 2609–2614. *

Ebrahimi-A., Withayachumnankul-W., Al-Sarawi-S., and Abbott-D. (2014c). High-sensitivity metamaterial-inspired sensor for microfluidic dielectric characterization, *IEEE Sensors Journal*, **14**(5), pp. 1345–1351. *

Ebrahimi-A., Withayachumnankul-W., Al-Sarawi-S., and Abbott-D. (2014b). Compact dual-mode wideband filter based on complementary split-ring resonator, *IEEE Microwave and Wireless Components Letters*, **24**(3), pp. 152–154. *

Ebrahimi-A., Shen-Z., Withayachumnankul-W., Al-Sarawi-S., and Abbott-D. (2015b). Varactor-tunable second-order bandpass frequency selective surface with embedded bias network, *IEEE Transactions on Antennas and Propagation*. Submitted. *

Ebrahimi-A., Withayachumnankul-W., Al-Sarawi-S., and Abbott-D. (2015b). Compact second-order bandstop filter based on dual-mode complementary split-ring resonator, *IEEE Microwave and Wireless Components Letters*. Submitted. *

EBRAHIMI-A., AND YAGHMAEE-P. (2014). A new enhanced differential CMOS Colpitts oscillator, *Journal of Circuits, Systems, and Computers*, **23**(1). DOI: 10.1142/S0218126614500030.

EBRAHIMI-A., NAIMI-H. M., AND ADRANG-H. (2011). Remarks on transient amplitude analysis of MOS cross-coupled oscillators, *IEICE Transactions on Electronics*, **94**(2), pp. 231–239.

EBRAHIMI-A., AND NAIMI-H. M. (2011). Analytical equations for oscillation amplitude of MOS colpitts oscillator, *International Journal of Electronics*, **98**(7), pp. 883–900.

EBRAHIMI-A., AND NAIMI-H. M. (2010). A 1.2 V high band-width analog multiplier in 0.18 μm CMOS technology, *International Review of Electrical Engineering*, **5**(2), pp. 803–811.

Conference Articles

EBRAHIMI-A., WITHAYACHUMNANKUL-W., AL-SARAWI-S., AND ABBOTT-D. (2015d). Microwave microfluidic sensor for determination of glucose concentration in water, *IEEE 15th Mediterranean Microwave Symposium(MMS)*, pp. 100–102. *

EBRAHIMI-A., WITHAYACHUMNANKUL-W., AL-SARAWI-S., AND ABBOTT-D. (2015c). Higher-order tunable frequency selective surface with miniaturized elements, *IEEE 15th Mediterranean Microwave Symposium(MMS)*, pp. 140–143. *

EBRAHIMI-A., NIRANTAR-S., WITHAYACHUMNANKUL-W., BHASKARAN-M., SRIRAM-S., AL-SARAWI-S., AND ABBOTT-D. (2015b). Terahertz bandpass frequency selective surface with improved out-of-band response, *IEEE 40th Int. Conf. on Infrared, Millimeter, and Terahertz Waves (IRMMW-THz)*. DOI:10.1109/IRMMW-THz.2015.7327920. *

EBRAHIMI-A., WITHAYACHUMNANKUL-W., AL-SARAWI-S., AND ABBOTT-D. (2014d). Second-order bandpass frequency selective surface for terahertz applications, *IEEE 39th Int. Conf. on Infrared, Millimeter, and Terahertz Waves (IRMMW THz)*. DOI:10.1109/IRMMW-THz.2014.6956237. *

Ebrahimi-A., Withayachumnankul-W., Al-Sarawi-S., and Abbott-D. (2014b). Design of dual-band frequency selective surface with miniaturized elements, *International Workshop on Antenna Technology: "Small Antennas, Novel EM Structures and Materials, and Applications" (iWAT)*, pp. 201–204. *

Ebrahimi-A., Yaghmaee-P., Withayachumnankul-W., Fumeaux-C., Al-Sarawi-S., and Abbott-D. (2013). Interlayer tuning of X-band frequency-selective surface using liquid crystal, *Proceedings of Asia Pacific Microwave Conference (APMC2013)*, pp. 1118–1120. *

Yaghmaee-P., Withayachumnankul-W., Horestani-A. K., **Ebrahimi-A.**, Bates-B., and Fumeaux-C. (2013). Tunable electric-LC resonators using liquid crystal, *IEEE Antennas and Propagation Society International Symposium (APSURSI)*, pp. 382–383.

Ebrahimi-A., and Naimi-H. M. (2010). An improvement on the analytical methods for amplitude analysis of the MOS Colpitts oscillator, *IEEE XIth International Workshop on Symbolic and Numerical Methods, Modeling and Applications to Circuit Design (SM2ACD)*. DOI:10.1109/SM2ACD.2010.5672336.

Ebrahimi-A., Naimi-H. M., and Gholami-M. (2010). Compact, low-voltage, low-power and high-bandwidth CMOS four-quadrant analog multiplier, *IEEE XIth International Workshop on Symbolic and Numerical Methods, Modeling and Applications to Circuit Design (SM2ACD)*. DOI: 10.1109/SM2ACD.2010.5672341.

Ebrahimi-A., and Naimi-H. M. (2010). A 1.2 V single supply and low power, CMOS four-quadrant analog multiplier, *IEEE XIth International Workshop on Symbolic and Numerical Methods, Modeling and Applications to Circuit Design (SM2ACD)*. DOI: 10.1109/SM2ACD.2010.5672334.

Gholami-M., Sharifkhani-M., **Ebrahimi-A.**, Saeedi-S., and Atarodi-M. (2010). Systematic modeling and simulation of DLL-based frequency multiplier, *IEEE XIth International Workshop on Symbolic and Numerical Methods, Modeling and Applications to Circuit Design (SM2ACD)*. DOI: 10.1109/SM2ACD.2010.5672340.

Note: Articles with an asterisk (*) are directly relevant to this thesis.

List of Figures

List of Tables

Chapter 1

Introduction

THIS chapter provides an introductory background to the area of metamaterials and discusses the characteristics that make them attractive choices in designing new or improved electromagnetic devices for microwave and terahertz applications. It also explains the objectives and motivations behind the presented research. Furthermore, the original contributions in this thesis are highlighted followed by the structural organisation of the thesis.

1.1 Introduction

1.1.1 Metamaterials definition and background

By definition, metamaterials are engineered materials that exhibit controllable electromagnetic characteristics including those not found in natural materials. They derive their exotic electromagnetic properties from the periodic arrangement of the subwavelength metallic inclusions rather than from their atomic constitution (Zheludev 2010, Withayachumnankul and Abbott 2009). Attempts to engineer materials with exotic properties for manipulation of electromagnetic radiation have their roots back to late 19^{th} century when Jagadish Chandra Bose studied the properties of electromagnetic chiral materials. After that, an artificial chiral media has been developed by Karl Ferdinand Lindman in 1914 that was made of a collection of randomly-oriented small wire helices (Engheta and Ziolkowski 2006). Since then, several other other realisations have been made to design artificial media such as artificial dielectrics or artificial chiral materials for electromagnetic beam manipulation (Ziolkowski and Engheta 2003). Although none of these studies used the metamaterials as the title for their work, they still can be categorised as metamaterials (Ziolkowski and Engheta 2003, Engheta and Ziolkowski 2006).

The electromagnetic wave propagation in an artificial material with simultaneously negative permittivity and permeability was theoretically studied by Veselago (1968). Recent advances in fabrication and realisation techniques has led to practical implementation of double negative (DNG) metamaterials with the first realisation by Smith and Schultz (Smith *et al.* 2000, Shelby *et al.* 2001). Afterwards, the subject of metamaterials attracted great attention for research from the microwave frequency regime up to high terahertz and optical frequencies and many devices with new or improved functionalities have been designed based on the artificial material concept up to now. Several different names have been suggested for the artificial electromagnetic materials including negative referactive index media (Pendry 2000, Shelby *et al.* 2001, Iyer and Eleftheriades 2002), left-handed media (Marqués *et al.* 2002, Caloz and Itoh 2004), backward wave media (Tretyakov *et al.* 2005, Grbic and Eleftheriades 2002a), double negative media (Vendik *et al.* 2006, Vendik and Gashinova 2004). According to the definition presented, all the above mentioned materials are categorised as metamaterials.

1.1.2 Research motivations and thesis objectives

As mentioned earlier, metamaterials cover a broad range of engineered media or materials to manipulate electromagnetic waves. Realisation of such media or substances requires a periodic arrangement of small metallic inclusions. These periodic structures might be in one dimensional form such as in composite right/left handed transmission lines (Lai *et al.* 2004, Gil *et al.* 2007b), two dimensional such as high-impedance ground planes (Sievenpiper *et al.* 1999) or three dimensional configurations such as in nanolenses (Casse *et al.* 2010).

Recently, many devices and components with improved characteristics have been designed based on an arrangement of one or more metamaterials constituting resonators such as split-ring resonators (SRRs) and complementary resonators (CSRRs). These new components are specified as metamaterial-inspired devices. The advantages of these metamaterial-based resonators or elements lie in their very small sub-wavelength size that provides the possibility of designing compact circuit and components such as filters (García-García *et al.* 2005, Falcone *et al.* 2004b, Sans *et al.* 2014, Vélez *et al.* 2014), couplers (Islam *et al.* 2004, Jarauta *et al.* 2004, Nguyen and Caloz 2007), antennas (Zhu and Eleftheriades 2009, Zhang *et al.* 2008, Alici and Ozbay 2007, Kärkkäinen and Ikonen 2005, Kim and Breinbjerg 2009) and so on. The compactness is a key factor in weight reduction of many portable devices such as cell phones, laptops, tablets. The sub-wavelength dimensions offer the precise modelling of their electromagnetic response through lumped-element circuits. This feature is very useful in design, modelling, and analysis of complex electromagnetic structures (Marqués *et al.* 2011). Moreover, the metamaterial-based resonators can be easily engineered to show multiband or wide-band responses (Fan *et al.* 2007, Garcia-Lamperez and Salazar-Palma 2006, Basaran and Erdemli 2009).

Furthermore, metamaterial-based resonators exhibit very high quality factor resonances with intensive concentration of electric and magnetic fields. These concentrated electromagnetic fields are very sensitive to the environmental and geometrical parameters. Any change in the environment or geometrical alignment of the resonators will be directly translated to their resonance characteristics such as resonance frequency, quality factor, and phase. This feature makes the ideal candidates for applications in sensing, which becomes a potential area for development of new metamaterial devices (Zheludev 2010). Thus, several metamaterial-based resonators have been explored for

new or improved sensor structures (Naqui *et al.* 2011, Naqui *et al.* 2012, Withayachumnankul *et al.* 2012, Withayachumnankul *et al.* 2013, Melik *et al.* 2009b, Melik *et al.* 2009a).

Another promising application of metamaterial-inspired elements is in designing metasurfaces and frequency selective surfaces (FSSs) based on miniaturised elements. The FSSs implemented with miniaturised elements exhibit stable frequency responses with respect to a change in the polarisation and incidence angle of the electromagnetic waves (Sarabandi and Behdad 2007). On the other hand, lumped-element circuit-based synthesis methods can be derived for them because of the extremely sub-wavelength size of their constituting elements (Bayatpur 2009). This feature significantly facilitates the design procedure of the FSSs for achieving the desired frequency response (Bayatpur and Sarabandi 2008b, Behdad 2008, Al-Joumayly and Behdad 2009, Li and Shen 2013, Chiu and Chang 2009).

In light of the above background, this dissertation investigates the applications of metamaterial-inspired resonators and elements in miniaturised microwave planar filters, sensors and miniaturised-element frequency selective surfaces (MEFSSs) for microwave and terahertz applications. The first part of this thesis studies the application of dual-mode metamaterial resonators in miniaturisation of microwave planar filters in Chapter 3. The second part in Chapters 4 & 5 presents improved microwave devices based on metamaterial resonators for microfluidic and rotation sensors. The metamaterial concept of miniaturised element FSS is presented in Chapters 6 & 7.

1.2 Statement of original contributions

This dissertation involves several contributions in the area of metamaterials-based devices in the microwave and terahertz frequency ranges. These contributions can be generally categorised in three self-contained topics within the metamaterial framework. The first part of the thesis is on the design of compact filters using metamaterial-based dual-mode resonators. The second part is focused on the design of improved microwave sensors based on the metamaterials concept. Eventually, the third phase is on the design of frequency selective surfaces using metamaterial miniaturised elements.

1.2.1 Metamaterial-inspired compact filters

This section outlines the contributions in the first part of this thesis that is about the compact metamaterial-based filters.

- Dual-mode resonators are well-known for their role in miniaturisation of microwave filters. So, a dual-mode complementary resonator has been developed by modifying the geometrical structure of the complementary split-ring resonator (CSRR). This dual-mode resonator has been used for designing a second-order bandpass filter with wideband response and highly compact structure. This design has been published in *IEEE Microwave and Wireless Components Letters* under the title of "Compact dual-mode wideband filter based on complementary split-ring resonator"(Ebrahimi *et al.* 2014a).
- The developed dual-mode complementary resonator has also been used to design a compact second-order bandstop filter with wide harmonic free out-of-band response. The design idea was inspired from a first-order notch filter with a realisation of mutual coupling between the resonators for obtaining a second-order response.
- The microstrip transmission lines loaded with complementary electric-LC elements have been studied and it has been demonstrated that the special configuration of this type of resonators exhibits a dual-mode resonance when they are excited with the electromagnetic fields generated by the microstrip line. Both of the bandstop and bandpass configurations have been studied and compact dual-mode filters have been designed and implemented. The outcomes of this research are published in the *Journal of Applied Physics* under the title of "Dual-mode behavior of the complementary electric-LC resonators loaded on transmission line: Analysis and applications"(Ebrahimi *et al.* 2014f).

1.2.2 Metamaterial-inspired sensors

This section summarises the contributions made in the design of metamaterial-inspired sensors.

- A high-sensitivity microwave microfluidic sensor has been designed based on complementary split-ring resonator (CSRR) loaded on a microstrip line. By using complementary split-ring resonator instead of the split-ring resonator, the

effective sensitive area of the sensor has been increased resulting in a sensor with four time higher sensitivity with respect to the conventional SRR-based sensor. A prototype of the designed sensor has been implemented and verified by measurements for determining the ethanol volume fractions in water solutions. This improved design has been appeared in *IEEE Sensors Journal* under the title of "High-sensitivity metamaterial-inspired sensor for microfluidic dielectric characterization"(Ebrahimi *et al.* 2014c).

- A microwave microfluidic sensor for determination of glucose concentrations in water has been designed based on the complementary electric-LC resonator loaded microstrip line. It is shown that the complementary electric-LC resonator produces a highly concentrated electric field at its odd mode resonance. So, this property is used to sense the glucose contents of water solutions based on dielectric loading effect of the glucose solutions on the sensing area. The results of this research have been presented in *IEEE Mediterranean Microwave Symposium (MMS)*, 2015 under the title of "Microwave microfluidic sensor for determination of glucose concentration in water".

- A wide dynamic range rotation sensor has been designed based on a pair coupled meandered U-shaped resonators. By rotating the resonators with respect to each other, the overlapping area of the resonators is increased resulting in a stronger coupling between them. This is translated into a resonance frequency shift in the transmission response of the sensor that can be used for detection of angular rotation. The dynamic range of the proposed sensor is 180° and its linearity is improved by asymmetrically tapering the resonators. This work has been published in *IEEE Sensors Journal* under the title of "Metamaterial-inspired rotation sensor with wide dynamic range"(Ebrahimi *et al.* 2014d).

1.2.3 Frequency selective surfaces (FSSs)

The contributions in designing metamaterial-based frequency selective-surfaces (FSSs) with low profiles and stable frequency responses are presented in this section.

- A challenge in FSSs is designing structures with tunable or reconfigurable frequency responses. One major difficulty in these designs is biasing the individual active tuning elements such as varactors. In this context, we proposed a single-pole varactor-based tunable FSS structure in which all the varactors are biased in

parallel and there is no need to bias every individual varactor with a RF choke. The application of this structure in designing FSSs with higher-order responses has also been investigated. The outcomes of this work have been presented in *IEEE Mediterranean Microwave Symposium (MMS)*, 2015 under the title of "Higher-order tunable frequency selective surface with miniaturised elements."

- The spurious response associated with the metallic bias network drastically deteriorates the performance of the tunable frequency selective surfaces. In this regard, we have developed a new design based on miniaturised-elements that removes the need for any bias network. The bias network has been embedded in the FSS structure by considering wire grids in all FSS layers. The proposed FSS comprises three metallic layers and exhibits a second-order bandpass frequency response. The structure has been realised by using multilayer PCB fabrication process and tested with a parallel plate waveguide setup for validation.

- The implementation of tunable FSSs for higher microwave frequencies beyond the X-band is more challenging since the available flip-chip tuning elements such as varactor or PIN diodes fail to operate properly at these ranges. We have proposed a new X-band tunable FSS based on liquid crystals instead of varactors. Tunability is achieved by integrating liquid crystal cells in overlapping areas between different metallic layers of the FSS, where there are inter-layer capacitances. By applying bias voltage between the different layers the effective permittivity of liquid crystals will be tuned resulting in a tunable frequency response. The tuning concept has been shown through full-wave electromagnetic and circuit model simulations. This design has been presented in *IEEE Asia and Pacific Microwave Conference (APMC)*, 2013 under the title of "Interlayer tuning of X-band frequency-selective surface with liquid crystal"(Ebrahimi *et al.* 2013).

- Frequency selective surfaces with multiple independent transmission bands are highly desirable in nowadays multi-standard and multi-functional communication and imaging systems. The sensitivity of the frequency response in multiband FSS structures to the incidence angle is very critical especially at the upper passband. We proposed a dual-band frequency selective surface with miniaturised elements unit cell, where the unit cell size is smaller than $\lambda_0/10$ at the lower passband frequency. The designed FSS offers an independent setting of the passband frequencies simply by varying the unit cell dimensions. This work has been presented in *International Workshop on Antenna and Propagation (iWAT)*, 2014 with

the title of "Design of dual-band frequency selective surface with miniaturised elements"(Ebrahimi *et al.* 2014a).

- Highly-selective FSSs with higher-order frequency responses and wide harmonic-free out-of-band are essential in terahertz spectrometry and imaging systems. In most of the conventional THz-FSS designs, the unit cell size is comparable with half of the wavelength at the operational frequency. This renders their frequency response sensitive to the angle of incidence and non-planar phase front of the electromagnetic radiation. In order to address these challenges, we designed terahertz second-order bandpass frequency selective surfaces based on miniaturised-element unit cells. Our proposed FSS structures offer very stable frequency responses around the operational frequency for both of the TE and TM polarisations of the obliquely incident waves. They also provide extended harmonic-free out-of-band responses. Our designs have been published in *IEEE Transactions on Terahertz Science and Technology* under the title of "Second-order terahertz bandpass frequency selective surface with miniaturised elements"(Ebrahimi *et al.* 2015a) and *IEEE International Conference on Infrared, Millimeter, and Terahertz Waves (IRMMW-THz)* with the title of "Second-order bandpass frequency selective surface for terahertz applications"(Ebrahimi *et al.* 2014e).

1.3 Overview of the thesis

As outlined in Fig. 1.1, this thesis encompasses five parts including the background, three parts of the original contributions and the conclusion. The detailed description for each part of the thesis is presented as follows.

Background (Chapters 1 & 2) includes the current introductory chapter and Chapter 2 that provides the introductory information and background required for the rest of the thesis chapters. The fundamental theory of metamaterials is introduced and discussed in this chapter. Then their application in designing composite left/right handed wave propagation media is explained. The application of metamaterial-based resonators in designing compact filters and microwave sensors is discussed. Moreover, a brief discussion regarding the frequency selective surfaces (FSSs), miniaturised elements and their role in designing high-performance and low profile FSSs is presented in this chapter.

Figure 1.1. Thesis outline and original contributions. This dissertation is composed of 8 chapters in total, divided in five major parts. The original contributions are distributed in 3 parts: filters, sensors and frequency selective surfaces (FSSs). All the chapters are virtually self-contained.

Filters (Chapter 3) involves the design of metamaterial-inspired compact microwave filters based on dual-mode resonators. First, a dual-mode complementary resonator has been developed by modifying the shape of conventional complementary split-ring resonator (CSRR) and then the application of this resonator in designing compact filters is verified by designing second-order bandpass and bandstop filter prototypes. Second, it has been demonstrated that by loading a microstrip line with a special configuration of electric-LC resonators, a dual-mode frequency behaviour will be observed. This configuration has been employed in designing dual-mode microwave filters with compact size.

Sensors (Chapters 4 & 5) present our designs of improved microwave sensors based on metamaterial concepts. In Chapter 4, a microfluidic sensor for determination of ethanol volume fractions in water has been designed and verified. It is demonstrated that the new sensor achieves four timed higher sensitivity with respect to the conventional metamaterial microfluidic sensors by using CSRR instead of the SRR for sensing. In addition, a microfluidic sensor for measuring the glucose contents in water solutions has been proposed and verified in this chapter. Chapter 5 explains new designs of microwave rotation and displacement sensors. Improved designs of rotation and displacement sensors with high linearity and wide dynamic ranges are presented in this chapter.

Frequency Selective Surfaces (Chapters 6 & 7) focus on the design of miniaturised-element frequency selective surfaces (FSSs) for microwave and terahertz applications. The FSS designs for reconfigurable and multi-standard microwave systems are discussed in Chapter 6 by introducing tunable FSS configurations and also a design of dual-band FSS with miniaturised elements. Chapter 7 presents the incorporation of miniaturised-elements in designing FSSs with higher-order responses and improved selectivity for terahertz purposes.

Conclusion (Chapters 8) summarises the results and contribution in this dissertation and outlines the possible future research works and improvements.

Chapter 2

Fundamentals of metamaterials

METAMATERIALS are artificially engineered materials with exotic electromagnetic properties that do not commonly exist in natural materials. This chapter introduces the basic concept of metamaterials and their implementation in planar circuits. Their operation principle is explained from the circuit model prospective. The applications of the resonance-based metamaterial components in designing microwave filters and sensors are discussed. In addition, the miniaturised elements inspired by metamaterials are presented as alternative components in designing frequency selective surfaces.

2.1 Introduction

Metamaterials are commonly considered as the homogeneous structures with exotic electromagnetic properties. A metamaterial is composed of resonant inclusions with sizes much smaller than the wave length λ_g. The average unit cell size of $d \leq \lambda_g/4$ is required for homogeneity. In this condition, the structure shows a uniform electromagnetic behaviour that is dependent on the unit cell properties and their near-field coupling behaviours. The electromagnetic properties refer to the relative permittivity ϵ_r, relative permeability μ_r, and the refractive index that is defined as $n = \pm\sqrt{\mu_r \epsilon_r}$, where the $\pm$ sign is considered for generality (Caloz and Itoh 2005). Therefore, according to the permittivity and permeability values, electromagnetic materials can be categorised in four domains demonstrated in Fig. 2.1. Dielectric materials are all categorised as double positive (DPS) materials. Materials with negative permittivity can be found in nature including plasmas with low losses and metals at optical and infrared frequencies (Marqués *et al.* 2011). Materials with negative permeability are less common in nature since the magnetic interactions in most materials are too weak. Magnetised ferrites in saturation can show negative magnetic permeability (Marqués *et al.* 2011). Materials with simultaneously negative permittivity and permeability usually known as '*double negative materials*' do not naturally exist. Despite that, the propagation of electromagnetic waves in a medium with simultaneously negative permittivity and permeability was theoretically studied in Veselago (1968). The first realisation of this kind of medium was conducted in the early 2000s (Smith *et al.* 2000, Smith *et al.* 2004). Media with simultaneously negative permittivity and permeability are implemented using metallic inclusions with dimensions much smaller than the wavelength. Double negative materials exhibit interesting electromagnetic phenomena and add a new degrees of freedom for designing new devices with improved performances. Although initially, the term 'metametarial' was used mostly for DNG structures, nowadays metamatrials refer to any artificially engineered materials with subwavelength inclusions for manipulating electromagnetic waves.

In this chapter, first the wave propagation in double negative materials is explained through electromagnetic theory. Then the realisation of metamaterials in planar transmission lines and circuits is explained with a focus on resonant structures. The application of the metamaterial-based resonant unit cells in the design of microwave filters and sensors are briefly discussed. Eventually, metamaterial-based miniaturised-elements are introduced as an effective approach to designing frequency selective surfaces (FSSs).

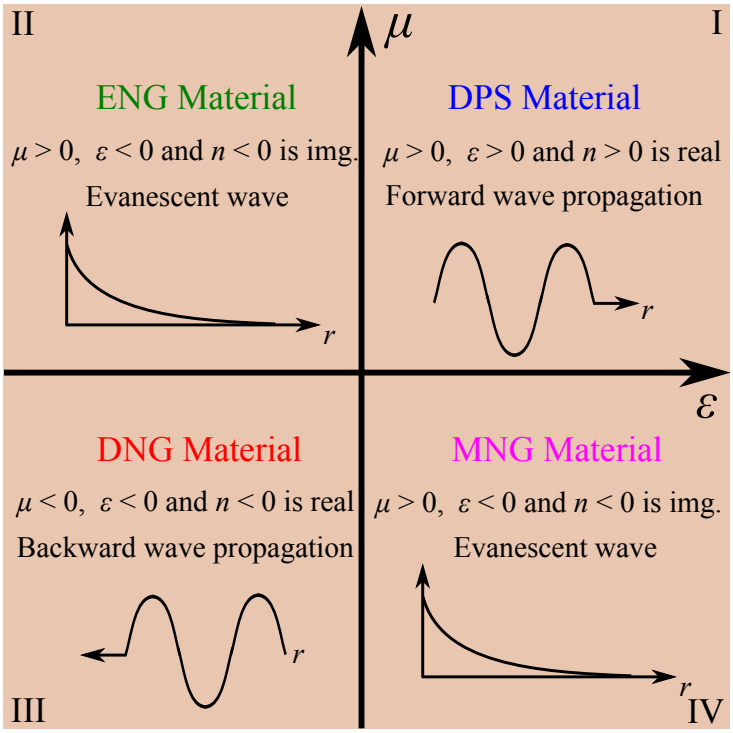

Figure 2.1. Material categories based on the permittivity and permeability. Based on the permittivity and permeability, materials can be categorised in four major groups: double positive materials (DPS), epsilon negative materials (ENG), mu negative materials (MNG), and double negative materials (DNG).

2.2 Wave propagation in double negative materials

To understand the electromagnetic wave propagation in a double negative medium, we should start with Maxwell's equations. By assuming a linear and isotropic medium, the Maxwell's equations in a source-free region can be written as

$$\nabla \times \mathbf{E} = -\frac{\partial \mathbf{B}}{\partial t}, \tag{2.1}$$

$$\nabla \times \mathbf{H} = \frac{\partial \mathbf{D}}{\partial t}, \tag{2.2}$$

for which the constitutive relations are

$$\mathbf{B} = \mu \mathbf{H}, \tag{2.3}$$

$$\mathbf{D} = \epsilon \mathbf{E}. \tag{2.4}$$

By assuming time-dependent harmonic fields, the electric or magnetic fields can be defined as

$$\mathbf{F}(\mathbf{r},t) = \mathrm{Re}[\mathbf{F}(\mathbf{r})e^{j\omega t}]. \tag{2.5}$$

From the above assumption, (2.1) and (2.2) can be rewritten as

$$\nabla \times \mathbf{E} = -j\omega\mu\mathbf{H}, \tag{2.6}$$

$$\nabla \times \mathbf{H} = j\omega\epsilon\mathbf{E}. \tag{2.7}$$

By considering the plane wave propagation with a wavevector of $\mathbf{k}$, we have

$$\mathbf{E} = E_0 e^{-j\mathbf{k}\cdot\mathbf{r}}, \tag{2.8}$$

$$\mathbf{H} = \frac{E_0}{\eta} e^{-j\mathbf{k}\cdot\mathbf{r}}. \tag{2.9}$$

where, $\eta = \sqrt{\frac{\mu}{\epsilon}}$ is the wave impedance. Based on the above relations, the Maxwell's equations can be reduced to

$$\mathbf{k} \times \mathbf{E} = \omega\mu\mathbf{H}, \tag{2.10}$$

$$\mathbf{k} \times \mathbf{H} = -\omega\epsilon\mathbf{E}. \tag{2.11}$$

It can be inferred from (2.10) and (2.11) that if both ϵ and μ are positive, the electric field vector $\mathbf{E}$, the magnetic field vector $\mathbf{H}$, and the wave vector $\mathbf{k}$ constitute a right-handed triplet. Conversely, if both ϵ and μ are negative, the three vectors $\mathbf{E}$, $\mathbf{H}$, and $\mathbf{k}$ make a left-handed triplet. In addition, the power flow through the electromagnetic waves is related to the Poynting vector, which is defined as

$$\mathbf{S} = \mathbf{E} \times \mathbf{H}^*. \tag{2.12}$$

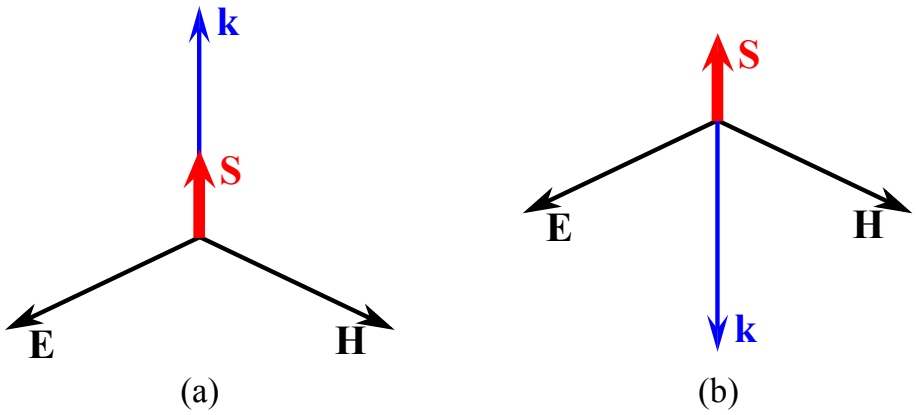

Figure 2.2. Wavevector and Poynting vector. Description of the electric field, magnetic field and wavevector triad obtained from Maxwells equations together with the Poynting vector obtained from the Poynting theorem. (a) Double positive medium and (b) Double negative medium.

This relation clearly demonstrates that the **S**, **E**, and **H** vectors will always make a right-handed triplet. So, in a double negative medium, the **S** and **k** vectors are in the opposite directions, whereas they are pointing to the same direction in a double positive medium. This phenomenon is clearly described through Fig. 2.2, where Fig. 2.2(a) demonstrates the double positive medium and Fig. 2.2(b) describes the double negative medium.

The Poynting vector shows the direction of the energy propagation over the time, and so is parallel to the group velocity v_g. On the other hand, the wavevector **k** is in a same direction as the phase velocity. Therefore, in a double negative medium, the phase and group velocities are in the opposite directions. This type of wave propagation is known as *backward wave propagation* (Veselago 1968).

Despite of the theoretical investigation by Veselago, the first practical realisation of the double negative medium was achieved by Smith *et al*. They implemented a homogeneous double negative medium by incorporating periodic arrangement of subwavelength split-ring resonators (SRRs) and wires (Smith *et al.* 2000). This structure is demonstrated in Fig. 2.3(a). In order to achieve simultaneously negative permittivity and permeability, it should be excited with the electric field along the wire axis and the magnetic field perpendicular to the SRR plane. The transmitted power is demonstrated in Fig. 2.3(b), where the solid line shows the transmitted power through the SRR array whereas the dashed line represents the power transmitted through the array of combined SRRs and wires. As seen, there is a bandstop region for the SRR array,

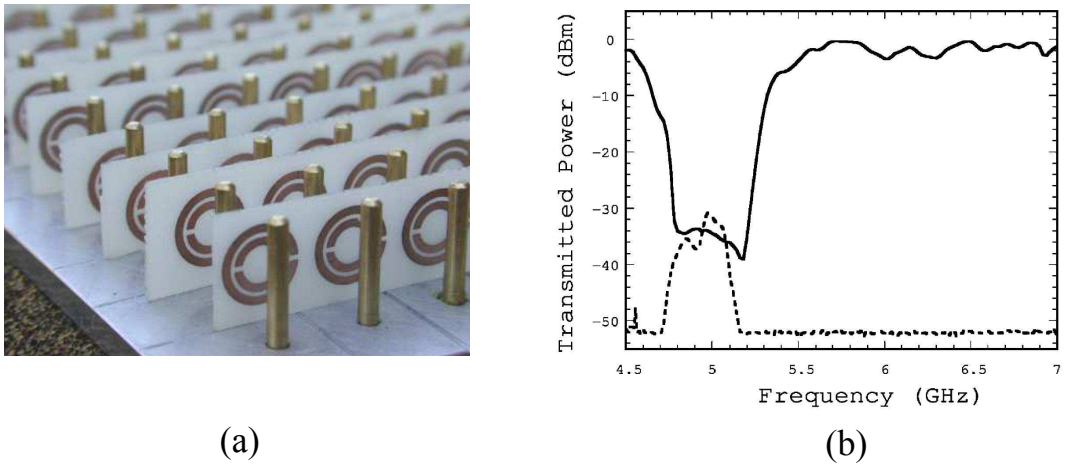

Figure 2.3. First implementation of double negative medium. (a) First realisation of left-handed media by combination of SRRs. (b) Power transmission response of the structure, where solid line shows the response of SRR array and the dashed line for the composite array of SRRs and wires. After Smith *et al.* (2000).

arising from a negative permittivity at these frequencies (Smith *et al.* 2000). However, the dashed curve indicates a passband that is due to the double negative behaviour around these frequencies (Smith *et al.* 2000).

Soon after the first experimental demonstration of the double negative media, several new electromagnetic structures have been developed based on the same concept. In what follows, we will discuss the implementation of artificial transmission lines and then introduce some of their applications.

2.3 Metamaterial transmission lines

Soon after implementing a three dimensional double negative medium by Smith *et al.*, it has been realised that the transmission line implementation of left-handed media (LHM) is also possible (Eleftheriades *et al.* 2003, Caloz and Itoh 2004). Here, we will discusse the theory of left-handed transmission line and their applications.

2.3.1 Purely left-handed transmission lines

The purely left-handed transmission line can be obtained by cascading the unit cell sections in Fig. 2.4(b), which is obtained by interchanging the inductance and capacitance in the unit cell of the conventional right-handed transmission line unit cell in

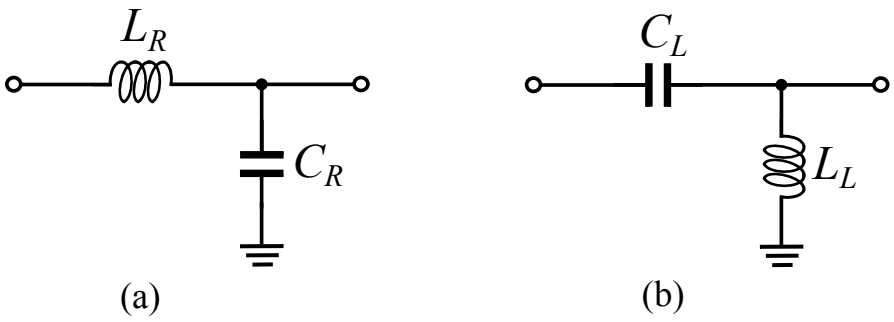

Figure 2.4. Unit cells of the purely right-handed and purely left-handed transmission lines. Lumped-element unit cell models of the (a) purely right-handed and (b) purely left-handed transmission lines.

Fig. 2.4(a). In this figure, the subscription "R" stands for the right-handedness whereas "L" stands for the left-handedness. Based on Fig. 2.4, the propagation constant and the Bloch impedance of the right-handed transmission lines can be calculated as

$$\cos(\beta_R d) = 1 - \frac{L_R C_R}{2}\omega^2, \tag{2.13}$$

$$Z_{BR} = \sqrt{\frac{L_R}{C_R}\left(1 - \frac{\omega^2}{\omega_{cR}^2}\right)}, \tag{2.14}$$

where d is the unit cell length, and $\omega_{cR} = 2/\sqrt{L_R C_R}$ is the angular cutoff frequency of the right-handed transmission line. In addition, the propagation constant and the Bloch impedance of the left-handed transmission line can be calculated as

$$\cos(\beta_L d) = 1 - \frac{1}{2L_L C_L \omega^2}, \tag{2.15}$$

$$Z_{BL} = \sqrt{\frac{L_L}{C_L}\left(1 - \frac{\omega_{cL}^2}{\omega^2}\right)}, \tag{2.16}$$

where $\omega_{cL} = 2/\sqrt{L_L C_L}$ is the cutoff angular frequency of the left-handed transmission line (Marqués *et al.* 2011). In order to have a better insight, the propagation constant and the blotch impedances have been simulated and plotted against the frequency for a right-handed transmission line with $L_R = 2$ nH and $C_R = 0.5$ pF and a left-handed transmission line with $L_L = 0.5$ nH and $C_L = 0.5$ pF. Fig. 2.5 presents the plots for right-handed transmission lines, whreas the propagation constant and Bloch impedance for the left-handed transmission lines are demonstrated in Fig. 2.6.

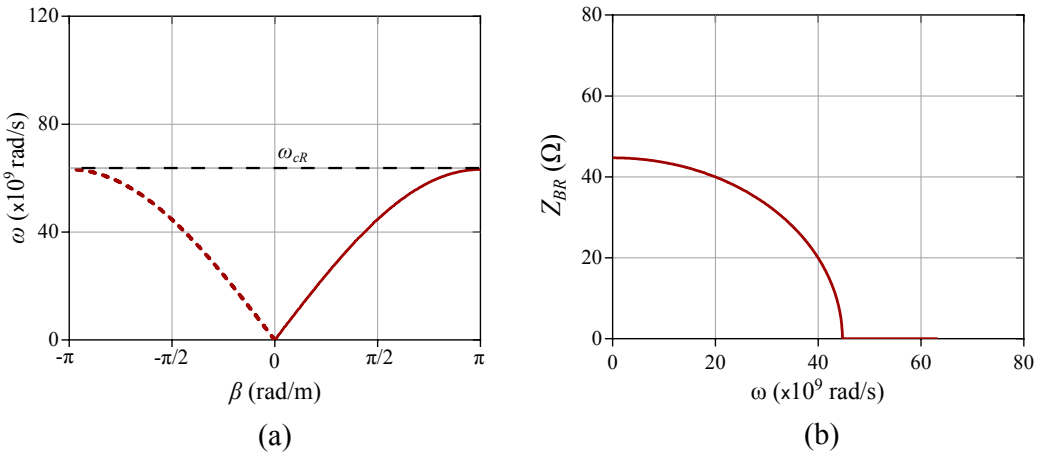

Figure 2.5. Propagation constant and Bloch impedance of a right-handed transmission line. (a) Propagation constant of a right-handed transmission line. (b) Bloch impedance of a right-handed transmission line.

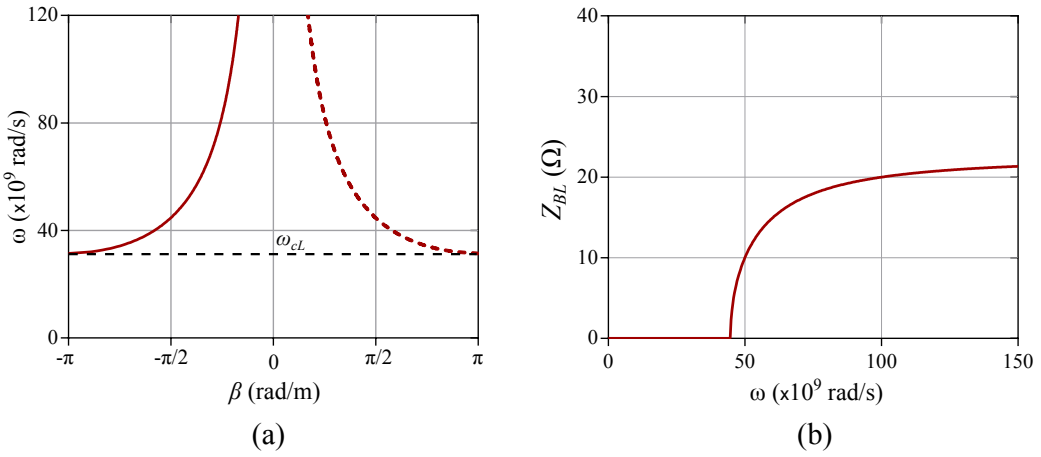

Figure 2.6. Propagation constant and Bloch impedance of a left-handed transmission line. (a) Propagation constant of a left-handed transmission line. (b) Bloch impedance of a left-handed transmission line.

Now, under long wavelength assumption of $d \ll \lambda_g$, the above relations converge to homogeneous transmission line models. In this condition, the propagation constant and Bloch impedance of the right handed transmission line can be expressed as

$$\beta_R = \omega\sqrt{L_R C_R}, \tag{2.17}$$

$$Z_{BR} = \sqrt{\frac{L_R}{C_R}}. \tag{2.18}$$

This results in parallel phase and group velocities for the right-handed transmission lines as

$$v_{pR} = v_{gR} = \frac{1}{\sqrt{L_R C_R}}. \tag{2.19}$$

Under homogeneous assumption, the propagation constant and Bloch impedance of the left-handed transmission lines can be expressed as

$$\beta_L = \frac{1}{\omega\sqrt{L_L C_L}}, \tag{2.20}$$

$$Z_{BL} = \sqrt{\frac{L_L}{C_L}}, \tag{2.21}$$

that result is anti-parallel phase and group velocities as follows

$$-v_{pL} = v_{gL} = \omega^2\sqrt{L_L C_L}. \tag{2.22}$$

This can be also inferred from the dispersion diagrams of the right and left-handed transmission lines in Fig. 2.5(a) and Fig. 2.6(a). In these figures, the solid line represents the waves propagating in positive direction and the dashed line represents the wave propagating in negative direction. However, by considering just one of them and choosing appropriate coordinates, only the positive group velocity (solid line) is acceptable according to causality (Marqués *et al.* 2011). So, based on these figures, both β and v_p are positive for the right-handed transmission, while they are negative in the left-handed case.

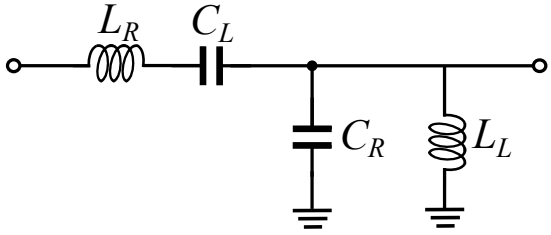

Figure 2.7. Composite left/right-handed transmission line. Lumped-element model of composite left/right-handed transmission line unit cell.

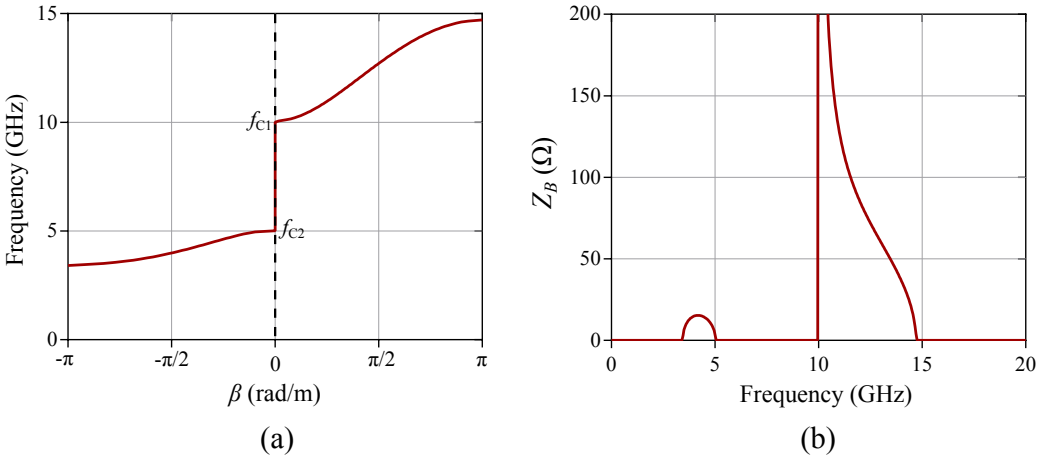

Figure 2.8. Propagation constant and Bloch impedance of a typical composite right/left-handed transmission line. (a) Propagation constant of a right/left-handed transmission line. (b) Bloch impedance of a right/left-handed transmission line.

2.3.2 Composite right/left-handed transmission lines

Purely left-handed transmission lines are not practically implementable because of the inherent parasitic series inductance and parallel capacitances (Caloz and Itoh 2005, Dong 2012). These parasitic elements cause a composite left/right-handed behaviour in practical implementations. Thus, the practical artificially implemented metamaterial transmission lines are called *composite left/right-handed transmission lines* (Caloz and Itoh 2005). The lumped-element unit cell model of a Composite right/left hand transmission line (CRLH TL) is depicted in Fig. 2.7, where the L_R and C_R represent the parasitic inductance and capacitance of the host line respectively. In order to have a better insight about the operation principle of the CRLH TLs, the propagation constant and the Bloch impedance of a typical CRLH TL with the element values of $L_R = 2$ nH, $C_R = 0.5$ pF, $L_L = 0.5$ nH, and $C_L = 0.5$ pF are simulated and plotted in Fig. 2.8. As seen, the transmission line shows two passbands with a stopband in between. In the lower passband the effects of L_L and C_L are dominant so, the transmission line shows a left-handness behaviour. Conversely, in the higher passband, L_R and C_R are dominant and the transmission line shows a right-handness behaviour (Eleftheriades *et al.* 2002). In the stopband between the two passband regions, the transmission line acts as a single negative media, so it inhibits the wave propagation

(Caloz and Itoh 2005, Marqués *et al.* 2011). The edge frequencies of the stopband are obtained as (Marqués *et al.* 2011):

$$f_{C1} = \max\left(\frac{1}{2\pi\sqrt{L_R C_L}}, \frac{1}{2\pi\sqrt{L_L C_R}}\right), \tag{2.23}$$

$$f_{C2} = \min\left(\frac{1}{2\pi\sqrt{L_R C_L}}, \frac{1}{2\pi\sqrt{L_L C_R}}\right). \tag{2.24}$$

The dual-passband characteristic of this kind transmission lines can be incorporated in designing dual-band circuits and components. In special case, the stopband region will be vanished when

$$L_R C_L = L_L C_R. \tag{2.25}$$

This kind of transmission line is known as balanced CRLH TL that exhibits a continuous transition between the left-handed and right-handed regions. The dispersion diagram and the Bloch impedance of a typical balanced CRLH TL with the unit cell parameters of $L_R = 2$ nH, $C_R = 2$ nH, $L_L = 0.5$ nH, and $C_L = 0.5$ pF are simulated and plotted in Fig. 2.9. As demonstrated in Fig. 2.9(a), there is continuous transition from left-hand to right-hand propagation. This property makes these transmission lines suitable for designing wide-band components.

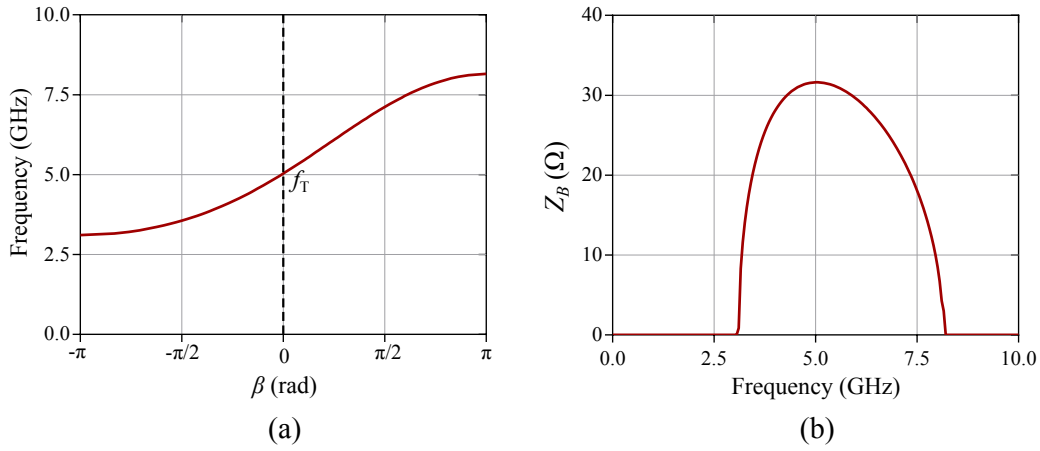

Figure 2.9. Propagation constant and Bloch impedance of a balanced composite right/left-handed transmission line. (a) Propagation constant of a balanced transmission line. (b) Bloch impedance of balanced transmission line.

2.4 Implementation of the CRLH TLs

The CRLH TLs discussed in Section 2.3 can be implemented in different ways in various transmission line technologies. However, generally we can divide them into two major categories as: (i) *LC*-loaded lines. (ii) resonator loaded lines. In the following, we will briefly discuss both of the methods.

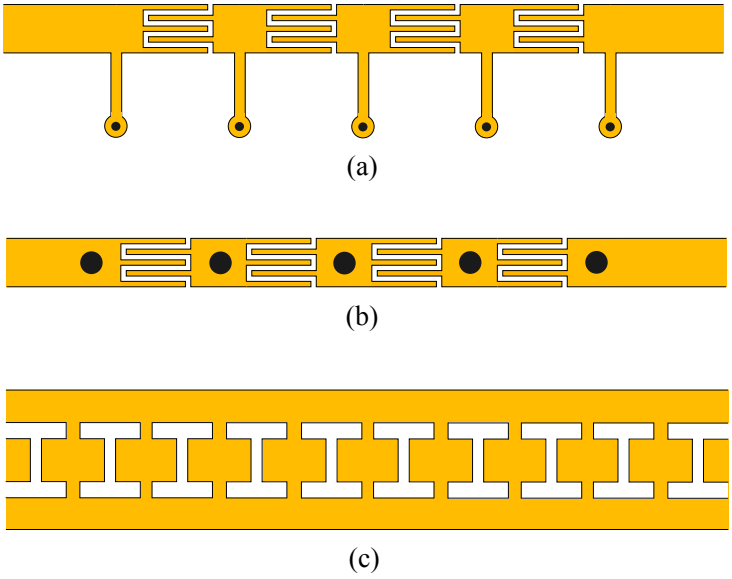

Figure 2.10. Implementation of *LC*-loaded CRLH TLs. (a) Implementation in microstrip line technology with series capacitive gaps and parallel short ended inductive stubs. (b) Implementation in microstrip line with via holes as parallel inductive paths to the ground. (c) Realisation in coplanar waveguide technology with series capacitive gaps and inductive paths to the ground. The metallisation is shown with yellow and via holes are indicated as black dots. After Aznar *et al.* (2008a).

2.4.1 *LC*-loaded lines

In this method, a conventional transmission line is periodically loaded with series capacitors and parallel inductors. These elements can be added by using discrete lumped components (Eleftheriades *et al.* 2002) or they can be embedded in the host transmission lines by using series capacitive gaps and parallel inductive stubs. Fig. 2.10 shows three examples from this configuration. In Fig. 2.10(a), a CRLH TL is implemented in microstrip technology by adding inter-digital series capacitive gaps for providing series capacitance and short-ended parallel stubs for realising parallel inductances (Caloz

and Itoh 2004, Caloz and Itoh 2005). Fig. 2.10(b) indicates another possible implementation in microstrip technology, where the parallel inductance in implemented by making via holes to the ground plane (Aznar *et al.* 2008a). This approach can be used in coplanar technology as well by introducing series capacitive gapes to the signal strip line and parallel inductive paths connecting the signal strip to the ground metallisation on the two sides (Grbic and Eleftheriades 2002b). This structure is demonstrated in Fig. 2.10(c).

2.4.2 Resonator loaded lines

The resonant type metamaterial transmission lines can be designed by periodically loading a host transmission lines with sub-wavelength resonators. Different kinds of resonators can be used as the loading elements on the transmission lines. Among all, the split-ring resonators SRR and its complementary structure known complementary split-ring resonator CSRR are very common due to their compact size. A basic structure of a SRR together with its equivalent circuit model is demonstrated in Fig. 2.11. In this figure, $C_0 = 2\pi r_0 C_{\text{pul}}$ represents the total capacitance between the rings, where C_{pul} is the per unit length capacitance between the rings (Baena *et al.* 2005). The inductance L_S can be approximated by a single ring with the average radius of r_0 and the ring width of t (Marqués *et al.* 2003). Therefore, the resonance frequency of a SRR can be calculated as $f_0 = 1/\left(2\pi\sqrt{L_S C_0/4}\right)$. The SRR can be excited through an axial magnetic field in the z direction. It can also be driven through an electric field along the x axis. If the effects of metal and substrate thicknesses and also the losses are neglected, an exact dual complementary behaviour can be expected from the CSRR in Fig. 2.12. The circuit model of the CSRR can be deducted from the SRR circuit model, where the L_S in SRR is replaced by the capacitance C_C of a circular disc with an average radius of $r_0 - t/2$ that is surrounded by the ground plane at a distance of t from its edge. On the other hand, the two $C_0/2$ capacitances are replaced with two parallel $L_0/2$ inductances each representing the inductive behaviour of the metallic traces that connect the inner disc to the ground plane. The resonance frequency of a CSRR can be obtained as $1/\left(2\pi\sqrt{C_C L_0/4}\right)$. The resonance frequency of a CSRR can be obtained as $1/\left(2\pi\sqrt{C_C L_0/4}\right)$ and the CSRR can be excited through an axial electric field in the z direction or through a magnetic field in the y direction (Baena *et al.* 2005). These resonators have been widely used for designing artificial transmission lines in planar technologies. In the following, we will review some of these artificial structures.

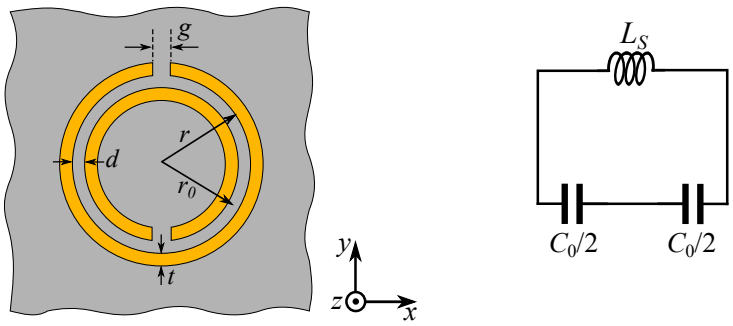

Figure 2.11. Split-ring resonator (SRR). A typical topology of split-ring resonator (SRR) and its equivalent circuit model. Metallisation is shown in yellow.

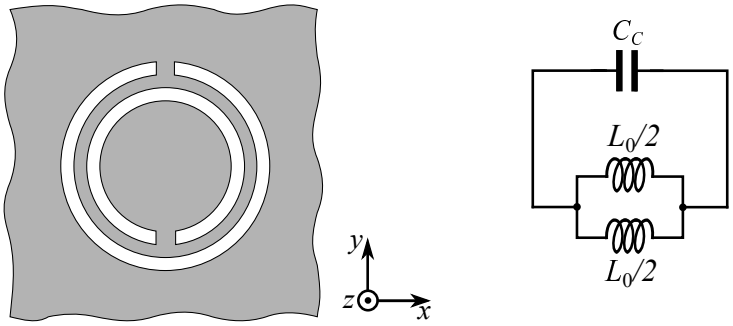

Figure 2.12. Complementary split-ring resonator (SRR). A typical topology of complementary split-ring resonator (CSRR) and its equivalent circuit model. Metallisation is shown in grey.

First, we consider the structures in coplanar waveguide technology. Fig. 2.13 shows a coplanar waveguide with split-ring resonators (SRRs) aligned with the slots and patterned on the back side of the substrate. In this condition, the SRRs will be excited by the magnetic fields generated by the signal strip and produce a bandstop in the transmission response in the vicinity of their resonance frequency. The bandstop is mainly associated with the negative permeability of the structure around the resonance of SRRs that make a single negative medium. Now, by adding parallel strips connecting the coplanar waveguide to the ground metallisation on the sides, a double negative propagation medium will be obtained that shows a bandpass behaviour in vicinity of the SRRs resonance frequency. This coplanar CLRH TLs in demonstrated in Fig. 2.14.

The SRR-based artificial transmission lines can also be implemented in microstrip technology. Fig. 2.15 shows a single negative transmission line with negative permeability around the SRRs resonance frequency. This provides a bandgap in the spectral response of the transmission line. This bandgap is depicted in the transmission response

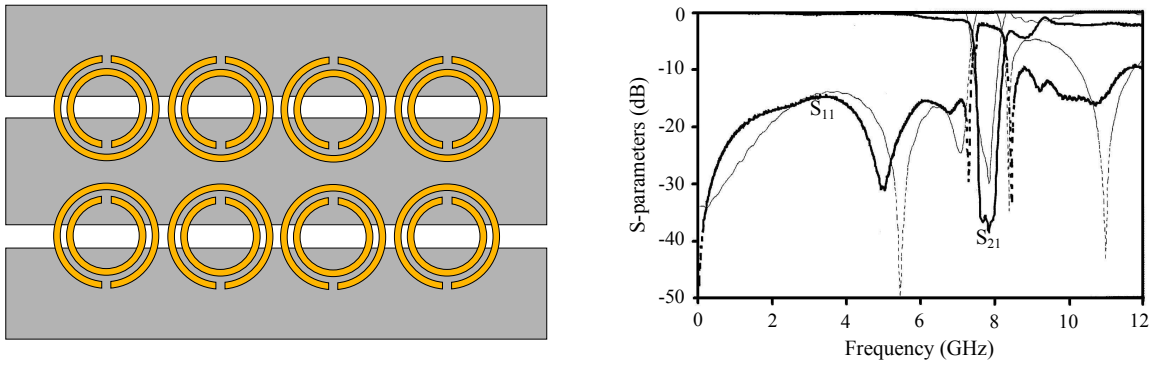

Figure 2.13. SRR-based transmission line in colpanar technology. (a) Layout of a typical metamaterial transmission line in coplanar waveguide technology. (b) Measured and simulated S-parameters of the structure. The split-ring metallisation is shown in yellow and the waveguide metallisation is grey. After Martín *et al.* (2003b).

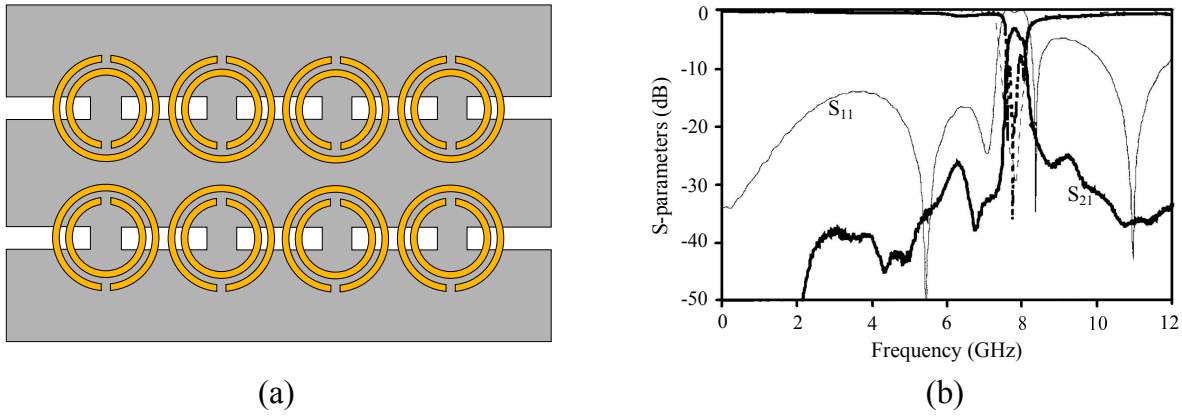

Figure 2.14. CRLH TLs in coplanar waveguide technology. (a) Layout of a typical CRLH TL in coplanar waveguide technology. (b) Measured and simulated S-parameters of the structure. The split-ring metallisation is shown in yellow and the waveguide metallisation is grey. After Martín *et al.* (2003a).

of the device in Fig. 2.15(b). Again the banstop frequency behaviour can be switched to bandpass by adding parallel inductive paths to the ground that produce negative permittivity. An implementation of this idea is presented in Fig. 2.16, where the metallic via holes connecting the microstrip to the ground plane provide the parallel inductive paths. A typical S-parameters of the SRR-based CRLH microstrip line is demonstrated in Fig. 2.16. As seen, the transmission line shows a passband in which it acts a left-handed wave propagation media (Marqués *et al.* 2011).

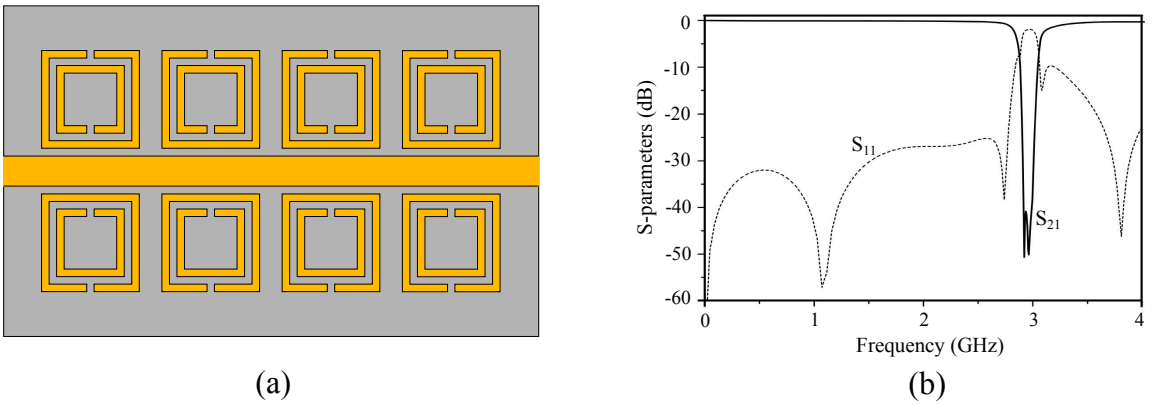

Figure 2.15. Artificial transmission line in microstrip technology. (a) Layout of a microstrip line loaded with SRRs on the sides. (b) Simulated S-parameters of the structure. The microstrip metallisation is shown in yellow. After Marqués *et al.* (2011).

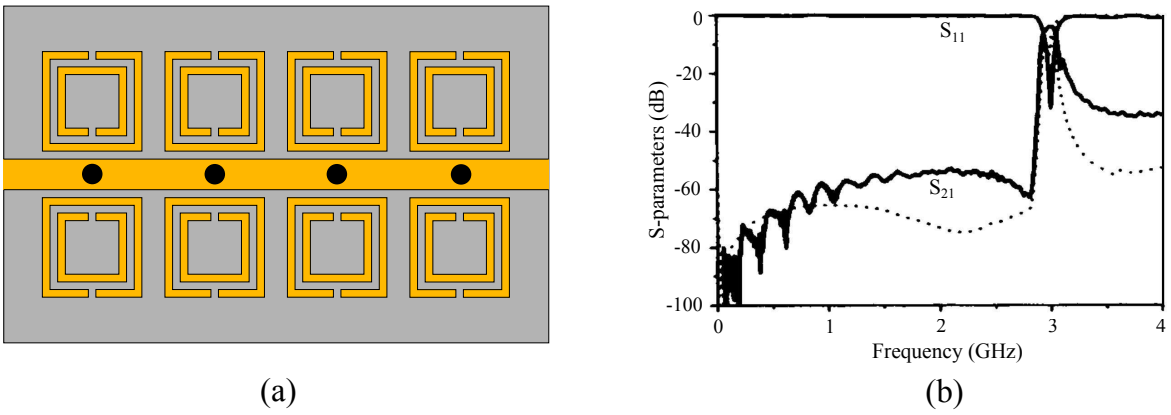

Figure 2.16. CRLH TL in microstrip technology. (a) Layout of a microstrip CRLH TL. (b) Simulated and measured S-parameters of the structure. The microstrip metallisation is shown in yellow and the via holes are shown as black circles. After Marqués *et al.* (2011).

The complementary split-ring resonators (CSRRs) can also be incorporated in designing metamaterial transmission lines. The CSRRs should be etched out of the ground plane metallisation and can be excited by axial electric fields.

One possibility for designing CSRR-based artificial transmission line is by using the microstrip. A microstrip line loaded with CSRRs etched in the ground plane is demonstrated in Fig. 2.17. This transmission line acts as a one dimensional effective propagation medium with negative permittivity. So, as shown in Fig. 2.17(b) it precludes the wave propagation in vicinity of the CSRRs resonance frequency (Baena *et al.* 2005). In

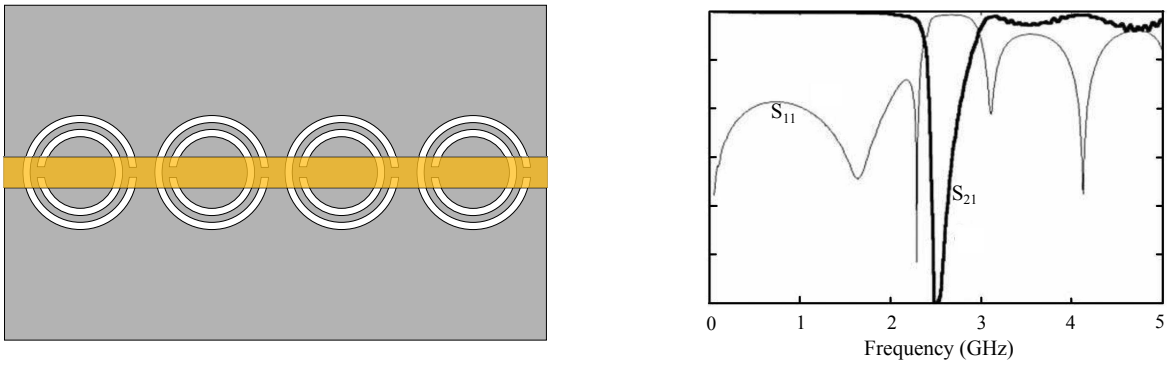

Figure 2.17. Artificial transmission line based on CSRRs. (a) Layout of a microstrip line loaded with CSRRs. (b) Measured S-parameters of the structure. The microstrip metallisation is shown with yellow and the ground plane metallisation is grey. After Baena *et al.* (2005).

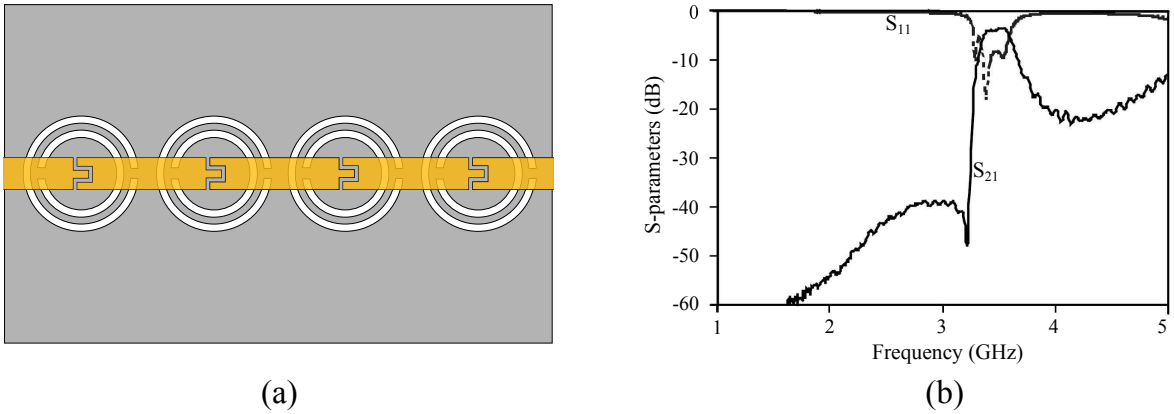

Figure 2.18. CSRR-based CRLH TL in microstrip technology. (a) Layout of a CSRR-based microstrip CRLH TL. (b) Measured S-parameters of the structure. The microstrip metallisation is shown with yellow and ground plane metallisation is grey. After Baena *et al.* (2005).

order to obtain a left-handed CSRR-based transmission line, we should introduce effective negative permeability to the structure. This can be implemented by adding periodic capacitive gaps to the conductive strip of the transmission line (Baena *et al.* 2005). These capacitive gaps will provide effective negative permeability in a specific frequency band. If this frequency band overlaps with the resonance frequency of CSRRs, a narrow left-handed transmission passband will be produced as demonstrated in Fig. 2.18(b) (Baena *et al.* 2005).

2.5 Applications of resonant-type metamaterials in filter and sensor designs

In the design of resonator-loaded artificial transmission lines, the main goal was firstly to achieve a left-handed behaviour in a desired frequency band (Gil *et al.* 2007b). However, soon the sub-wavelength structure of the SRRs and CSRRs and their high quality factor resonances attracted RF designers to use them as building blocks in developing new circuits and devices. Two of these interesting applications are microwave filters and sensors that are the focus of this dissertation.

2.5.1 Application in microwave filters

Compact and high performance filters compatible with integrated circuit technologies are of great interest in RF communication systems and portable devices. Key factors in the design planar microwave filters are high quality factor, and compact size. The SRRs and CSRRs opened the doors for developing new strategies of designing compact filters. In contrast to the conventional resonators used in filter designs such as parallel coupled lines, closed or open loop resonators, the SRRs provide much smaller sizes by the virtue of distributed capacitance between the two rings and the overall ring inductance (Bonache *et al.* 2006a). In addition, the negative image of SRR known as the CSRR offers much compacter size in comparison with conventional complementary resonators (Gil *et al.* 2007b). Many novel compact filter structures have been designed and implemented by different groups. To name just a few examples, the composite right/left-handed behaviour of unbalanced CSRR-loaded microstrip line has been used to design dual-band bandpass filter (Wu *et al.* 2007, Bonache *et al.* 2008). The balanced CSRR-based CRLH TLs have been used for deign of ultra-wide-band bandpass filters (Gil *et al.* 2007b). Compact differential filters with common-mode suppression are developed by combining SRRs and CSRRs (Vélez *et al.* 2013). The effective size of the filters have been even decreased further by considering S-shaped SRRs and CSRRs (Horestani *et al.* 2014b, Horestani *et al.* 2014a). In this thesis, we have designed very compact bandpass and bandstop filters by introducing metamaterial-based resonators with dual-mode resonance behaviour. The dual-mode resonator acts as a doubly tuned resonant circuit element and the number of the resonator needed for a specific filter response is reduced by half resulting in more compact structure (Hong *et al.* 2007). A full

explanation and analysis of these resonators with their application in bandpass and bandstop filter designs will be presented in Chapter 3.

2.5.2 Application in microwave sensors

In addition to their potential applications in compact filters and circuit elements, the metametrial-inspired resonators such as SRRs and CSRR can be used in the design of compact and high-resolution microwave sensors (Albishi *et al.* 2012, Boybay and Ramahi 2012, Yang *et al.* 2010). In principle this is because of their high quality factor resonance, their compact size, and the high-sensitivity of their resonance with respect to the geometrical parameters and surrounding constituting materials. Furthermore, it is demonstrated that the sensitivity of the conventional sensors can be improved by incorporating metamaterial-based resonators (Niu *et al.* 2010, Taya and Shabat 2011). Thus, the sensing applications of metamaterials have been a very active research area in recent years. Some of the latest examples of the metamaterial-based sensors are: symmetry and displacement sensors (Naqui *et al.* 2011, Naqui *et al.* 2012, Horestani *et al.* 2013b), rotation sensors (Horestani *et al.* 2013a, Naqui and Martín 2013), biological sensors (Lee *et al.* 2012), strain sensors (Melik *et al.* 2009b, Melik *et al.* 2009a), and gas sensors (Kim *et al.* 2014).

In this regard, Chapter 4 and Chapter 5 of this thesis focus on the sensing applications of metamaterials. The metametrial-inspired resonators are applied in the design of microwave microfluidic sensors in Chapter 4, and Chapter 5 explains a design of wide dynamic range metamaterial rotation sensor based on a pair of coupled meandered resonators.

2.6 Metamaterial-inspired frequency selective surfaces

Frequency selective surfaces (FSSs) are usually formed by two-dimensional periodic arrangement of metallic elements on a dielectric substrate (Munk 2005). Based on the geometry and arrangement of the metallic unit cell, the array might show different functionalities such as bandpass or bandstop spatial filter, absorber, reflectarray, and etc. (Bayatpur 2009). Important factors in evaluating the performance of FSSs are their overall size, the sensitivity of their frequency response to the angle of the incident electromagnetic wave, the harmonic content of their frequency response, and their ability

to operate in close proximity to the radiation source (Munk 2005). The FSS functionality is mainly determined by its unit cell geometry and dimension. In terms of the unit cell properties, the FSSs can be divided into two major subclasses as: (i) Traditional FSSs based on resonant element unit cells, (ii) miniaturised elements FSSs based on non-resonant unit cells. In the following, we will briefly discuss the operation principles and the performance of each category.

2.6.1 Traditional FSSs with resonant unit cells

The operation of this type FSS is based on resonant elements. The elements are excited through the electric or magnetic field of the radiated wave. The incident electromagnetic wave will induce electric current in metallic traces and electric field across the capacitive gaps in the array. The magnitude of the induced current and electric field depend on the level of coupling between the electromagnetic field and the unit cells. The maximum coupling occurs at the fundamental frequency, where the length of the unit cell is equal to $\lambda/2$. So, the unit cells should be designed in a way that they resonate at the desired frequency of operation. Because of the fundamental dependence of the traditional FSSs on the unit cell length, the excitation of higher-order modes is unavoidable. As a result, the frequency response of these type of FSS usually includes several higher-order harmonic responses. This will not only degrade the out-of-band performance of the FSS, but affects the scan angle performance as well since some of the harmonic modes might be excited under oblique incidences.

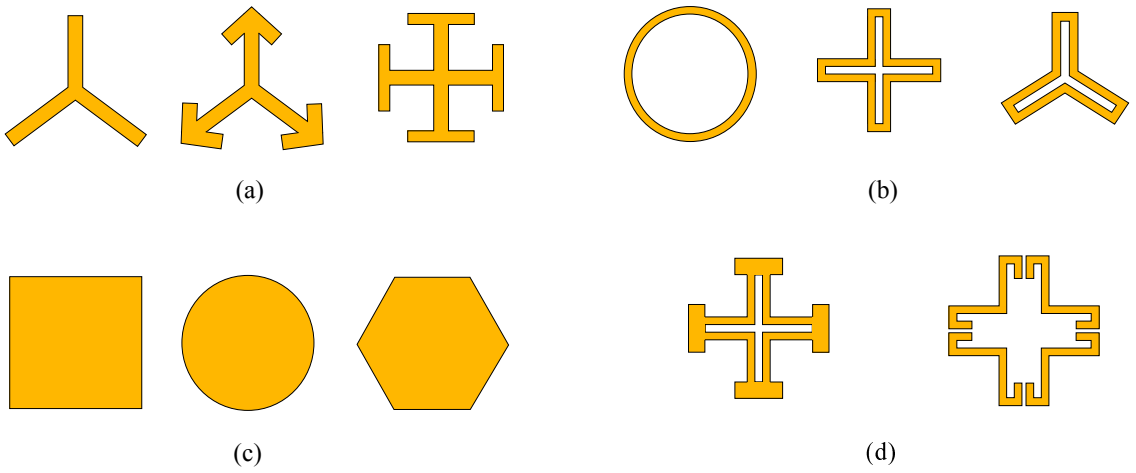

Figure 2.19. Typical FSS unit cells. Typical FSS unit cells are categorized in four groups. (a) Center connected N-poles. (b) Loop type elements. (c) Patch or plate type. (d) Combinations. Adapted from Munk (2005).

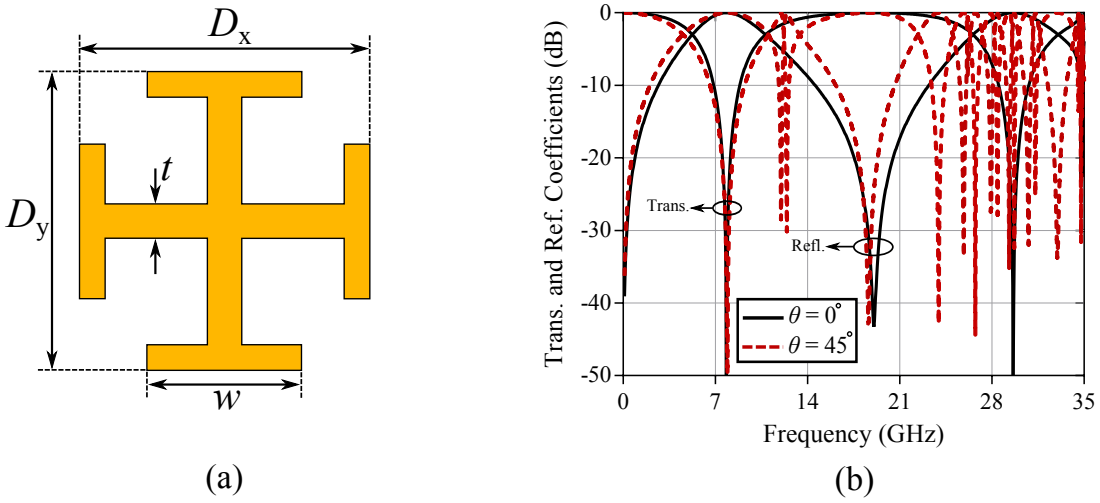

Figure 2.20. Frequency selective surfaces made of Jerusalem cross elements. (a) Jerusalem cross unit cell. (b) Simulated reflection and transmission coefficients under normal and oblique incidence angle of 45°. The dielectric substrate has a relative permittivity of $\epsilon_r = 2.2$ with a thickness of 0.254 mm. The unit cell dimensions are $D_x = D_y = 4.2$ mm, $t = 0.4$ mm, and $w = 4$ mm. The spacing between adjacent elements in the array is 0.2 mm.

Some of the typical unit cell geometries that are commonly used in the design of conventional FSSs are demonstrated in Fig. 2.19. As an example of the resonant type FSSs, a structure made of Jerusalem cross unit cell has been simulated in CST microwave studio. Fig. 2.20(a) shows the considered Jerusalem cross unit cell together with its geometrical dimensions whereas the simulated transmission and reflection coefficients of the FSS are plotted in Fig. 2.20(b). As seen, the FSS shows a transmission null at the fundamental frequency of around 8 GHz with a harmonic response at 30 GHz under normal incidence. However, by changing the incidence angle to 45°, several higher order harmonics are excited that deteriorate the frequency response. Another important issue in traditional FSSs is designing the FSSs with higher-order filtering responses. To this end, different layers of first-order FSS layer should be arranged with $\lambda/4$ spacing (Munk 2005). This results in bulky profiles that might not be desirable in many applications. To overcome these drawbacks the miniaturised-element FSSs have been proposed that will be discussed in Section 2.6.2.

2.6.2 Miniaturised elements frequency selective surfaces (FSSs)

In order to decrease the sensitivity of the FSS response to the oblique angles of the incident wave, the unit cell size should be miniaturised (Munk 2005). This is especially important when the FSS is used in close proximity to the radiation source. In order to address this issue, a new class of FSSs have been developed based on miniaturised elements. These types of FSSs operate based on a different principle that allows superior performance over the traditional structures. In this approach, instead of using fully resonant elements as the unit cell of the FSS, non-resonant unit cells with small dimensions are used. These miniaturised elements act as lumped capacitors or inductors and are arranged in a way that they couple to the incident electromagnetic wave. In this way, the electrical size of the unit cells is decreased to less than $\lambda/4$ and even in some cases smaller than $\lambda/10$ (Bayatpur and Sarabandi 2008b). They are also called metamaterial-inspired FSSs because of their extremely miniaturised unit cells (Bayatpur and Sarabandi 2008a).

The first miniaturised elements FSS was introduced in Sarabandi and Behdad (2007). As demonstrated in Fig. 2.21, this FSS is composed of metallic arrays printed on both sides of a thin dielectric spacer. The front layer is made of a large capacitive patch array whereas the back layer is an inductive wire grid. Since the FSS is made of miniaturised elements, its frequency response can be accurately modelled through a lumped element circuit model.

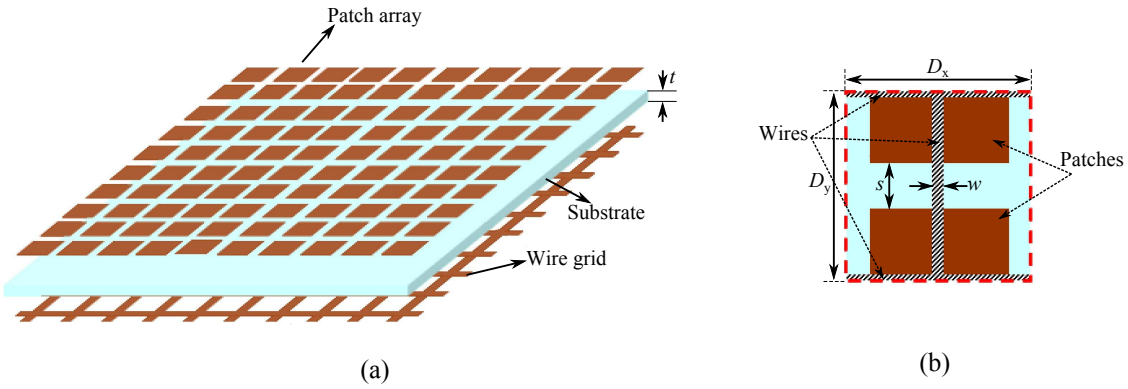

Figure 2.21. The first miniaturised elements FSS. (a) Three dimensional view of the miniaturised elements FSS. (b) The unit cell of the structure. The dimensions are: $D_x = D_y = 5$ mm, $s = 0.2$ mm, $w = 0.5$ mm, $t = 0.254$ mm. After Sarabandi and Behdad (2007).

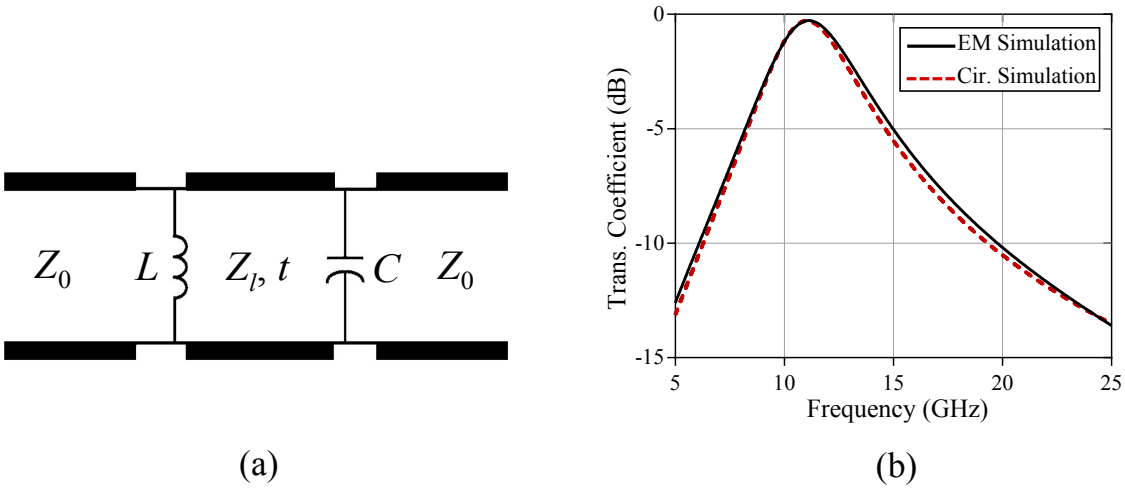

Figure 2.22. Lumped elements modelling of the miniaturised elements FSS. (a) Circuit model of the miniaturised elements FSS. (b) Comparison between the simulated transmission responses obtained from the EM and circuit model simulations. The circuit model paraemetrs are: $L = 1.08$ nH, $C = 0.15$ pF, $Z_t = 254\ \Omega$, $t = 0.254$ mm.

The circuit model of this FSS is given in Fig. 2.22(a), where the parallel capacitor models the capacitive patch array in the front layer and the L inductance stands for the wire grid in the back layer. The thin dielectric spacer is modelled with a short transmission line section with the characteristic impedance of $Z_l = Z_0/\sqrt{\epsilon_r}$, where $Z_0 = 377\ \Omega$ is the wave impedance in free space and ϵ_r is the relative permittivity of the dielectric spacer. A comparison between the simulated transmission coefficient of the FSS obtained from the circuit model simulations and the one from the full-wave EM simulations is presented in Fig. 2.22(b). The FSS dimensions and the circuit model parameters are given in the captions of Fig. 2.21 and Fig. 2.22 respectively. Fig. 2.22(b) shows a good agreement between the circuit model and full-wave EM simulation results over a wide frequency range. Fig. 2.23 shows the scan angle performance of the FSS over wide range of 0°–60° for both of the TE and TM polarisations. As demonstrated, the FSS shows a reasonable stability of the transmission response for oblique incidence angles up to 45°.

As mentioned before, an advantage of this type of FSS is that its frequency behaviour can be accurately modelled using lumped elements circuit model. So, FSSs with specified functionalities can be designed by the aid of standard circuit-based filter theory. This is a notable feature since the design and optimisation procedures can be significantly simplified by using circuit theory (Li and Behdad 2012).

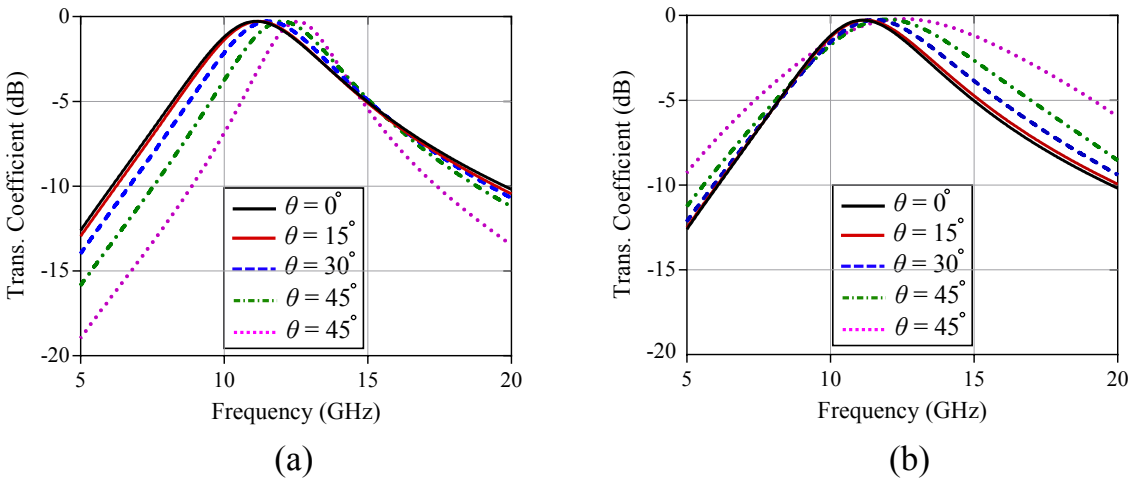

Figure 2.23. Scan angle performance of the miniaturised elements FSS. (a) Transmission responses for oblique incidences in the TE polarisation. (b) Transmission responses for oblique incidences in the TM polarisation.

After this first demonstration of the miniaturised elements FSS, several other FSSs with different improved functionalities have been designed and implemented. Some examples are: low profile second-order bandpass FSS (Behdad 2008, Al-Joumayly and Behdad 2009), dual-band FSSs with close band spacing (Al-Joumayly and Behdad 2010), FSS with quasi-elliptical frequency response (Li and Shen 2013), FSSs for high power microwave applications (Li and Behdad 2013).

In this thesis, the miniaturised element FSSs are considered for tunable microwave and also terahertz applications. The improved designs of the FSSs for tunable and multi-standard microwave purposes are investigated in Chapter 6 and the improved miniaturised element FSSs for terahertz applications are discussed in Chapter 7.

2.7 Chapter summary

This chapter has presented the definition of the metamaterials and their implementations. The fundamental theory of metamaterials have been presented through their electromagnetic analysis with Maxwell's equations. Their implementation in planar transmission line technologies has been discussed by considering both of the *LC*-loaded and resonator-loaded transmission line approaches. Since the focus of this dissertation is on filter and sensory application of the metamaterial resonators, their applications in miniaturised microwave filters and sensors have been briefly explained.

On the second part, the metamaterial-inspired frequency selective surfaces (FSSs) are discussed by giving a background regarding the traditional FSS structures. The miniaturised element FSSs have been introduced as metamaterial-based two-dimensional periodic structures. The advantages of the miniaturised element FSSs over the traditional FSSs have been discussed. These advantages enable straightforward designs of higher-order FSSs with prescribed performance.

Overall, this chapter presents the substantial background information that the rest of this dissertation is built upon.

Chapter 3

Metamaterial-inspired dual-mode filters

DUAL-mode complementary resonators are introduced for designing compact dual-mode filters in this chapter. It is demonstrated that by introducing a defected section to the centre part of the conventional complementary split-ring resonator (CSRR), a resonator with dual-mode behaviour will be obtained. In addition, it is shown that the Complementary electric-LC (CELC) resonators can also provide a dual-mode response with a strong electric-field concentration in the odd mode when they are excited via a microstrip transmission line. This dual-mode characteristic is used for designing second-order bandpass filter. Furthermore, the symmetrical property of the microstrip-line-coupled (CELCs) is used in designing a displacement sensor.

3.1 Introduction

As discussed in previous chapters, the split-ring resonators and their complementary counterparts so called complementary split-ring resonators (CSRRs) have been widely used in designing compact planar circuits with improved performance such as: filters (Martín *et al.* 2003b, Aznar *et al.* 2009, Bonache *et al.* 2006a), antennas (Dong *et al.* 2012, Alici and Ozbay 2007) and sensors (Naqui *et al.* 2011, Naqui *et al.* 2012, Horestani *et al.* 2013b, Horestani *et al.* 2014c). Key advantage of these type resonators that make them preferable choices in designing such devices lies in their highly compact size, which is much smaller than the operational wavelength. As a consequence, they can reduce the effective size of the filters and other circuits drastically. In addition, their frequency response can be approximated by a quasi-lumped elements equivalent circuit. So, an equivalent circuit-based synthesis procedure can be developed for the devices made of SRRs and CSRRs to provide an insightful and straightforward design approach.

The compactness becomes highly relevant in high-order filters that require a number of coupled resonators or a series combination of the filter sections with $\lambda/4$ spacing, where λ is the operational wavelength. Therefore, further miniaturisation of the resonators is compulsory in ultra-compact devices. The miniaturisation for metamaterial resonators is commonly performed by increasing the resonator´s equivalent capacitance or inductance through tapering the rings width or loading them with lumped or semi-lumped capacitors (Withayachumnankul *et al.* 2010, Horestani *et al.* 2012, Lin and Cui 2008). But, these approaches might induce an increase in the ohmic losses of the resonators (Horestani *et al.* 2012) that in turn cause reduced quality factors. Furthermore, there may be some fabrication limitations in implementing very narrow metallic paths. Another efficient way of increasing the equivalent inductance or capacitance of the resonators is to modify their structure (Baena *et al.* 2005). For instance, broadside coupled SRRs can be used for increasing the inter-ring capacitance (Marqués *et al.* 2003), spiral resonators can be used to achieve a higher inductance, and multiple concentric split-rings or S-shaped SRRs and CSRRs can be used to increase both of the equivalent inductance and capacitance (Baena *et al.* 2004, Bilotti *et al.* 2007, Chen *et al.* 2004, Chen *et al.* 2005).

An alternative way of miniaturisation is to use dual-mode resonators (Görür *et al.* 2003). A dual-mode resonator can be considered as a doubly tuned resonant circuit and thus, the number of resonators needed in designing specific order filters will be reduced to half resulting in much more compact size (Fok *et al.* 2006, Athukorala and

Budimir 2009, Athukorala and Budimir 2011). In this chapter, two defected ground resonators are introduced that can provide dual-mode resonances. In the first part, a dual-mode complementary split-ring resonator (DMCSRR) is developed by introducing a defected section in a conventional CSRR structure. It is shown that the microstrip line loaded with this type of resonator will constitute a double resonance module. This configuration is then used in designing very compact dual-mode bandpass filter and also a dual-mode bandstop filter. In the second part, the microstrip-line-loaded complementary electric-LC resonator is investigated and it is demonstrated that this configuration will also provide a dual-resonance structure for the special alignments of the transmission line and the resonator with respect to each other. The application of this configuration in planar structures is demonstrated by designing sample filter and sensor structures.

The chapter is organised as follows, the configuration and operation principles of the dual-mode CSRR is explained in Section 3.2 with an equivalent circuit model. Dual-mode bandpass and bandstop filters are designed based on DMCSRR and verified through simulations and measurement results in Section 3.2.2 and Section 3.2.3 respectively. Section 3.3 is dedicated to the analysing the microstrip lines loaded with complementary electric-LC resonators where different alignments are considered and analysed by using equivalent circuit model. Section 3.3.3 presents the potential applications of the microstrip-line-coupled CELC resonators in designing filters and their validation through electromagnetic simulations and measurement results. Finally, the conclusion are provided in Section 3.4.

3.2 Dual-mode complementary split-ring resonator

The first part of this section is dedicated to the analysis and working principle of the dual-mode complementary split-ring resonator (DMCSRR) through a lumped-element circuit model. The application of this type resonator in compact microwave filters will be introduced in Sections 3.2.2 and 3.2.3 through designing dual-mode bandpass and bandstop filter prototypes respectively.

3.2.1 Operation principle of the DMCSRR

A single loop conventional CSRR is shown in Fig. 3.1(a) with its equivalent lumped element circuit model in Fig. 3.1(b) (Baena *et al.* 2005). In this resonator, C_C models

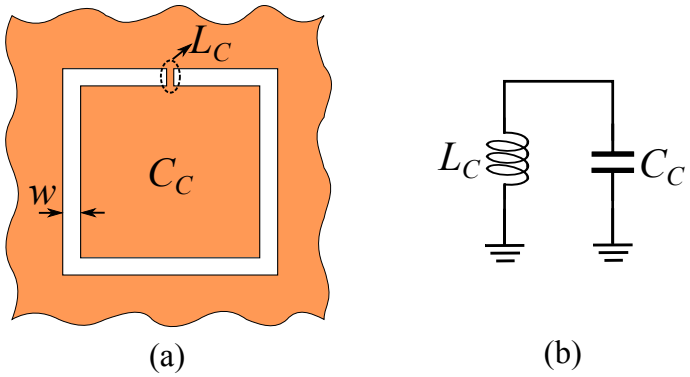

Figure 3.1. Conventional complementary split-ring resonator (CSRR). (a) A CSRR etched out of the ground plane. (b) Its equivalent circuit model. The metallisation is indicated in orange.

the capacitance between the central square plate and the surrounding ground plane separated with a distance w, and L_C stands for the inductance of the metallic strip connecting the plate to the ground plane. The value of C_C depends on the plate circumference and w and L_C is a function of w and the strip width. Based on the CSRR in Fig. 3.1, a dual-mode CSRR can be developed as shown in Fig. 3.2(a) by introducing a defected part to the middle part of the resonator to create two symmetrical sections. The equivalent circuit model of this new resonator is demonstrated in Fig. 3.2(b). In the circuit model, C_C models the capacitances of the two rectangular plates in the middle surrounded by the ground plane at a distance w from their edges. The inductor L_S models the inductances connecting the two capacitive plates to the central parallel inductive path, L_P, running to the ground plane. Finally, C_M represents the mutual capacitance between the two capacitive plates, separated by a width d.

By looking at the DMCSRR and its symmetric equivalent circuit model, it can be inferred that this resonator can resonate in both even and odd modes. Illustrated in Fig. 3.2(c) and Fig. 3.2(d) are the corresponding even and odd mode equivalent circuits respectively. The inductance L_P has no effect on the odd mode operation, whereas the mutual capacitance C_M has no affect on the even mode counterpart. From the physical point of view, this is because there is no current flowing between the capacitive plates and ground plane through L_P in the odd mode, and there is no voltage difference between the two plates in the even mode. Thus, the even and odd mode resonance frequencies can be calculated as:

$$f_{\text{even}} = \frac{1}{2\pi\sqrt{(2L_P + L_S)C_C}}, \tag{3.1}$$

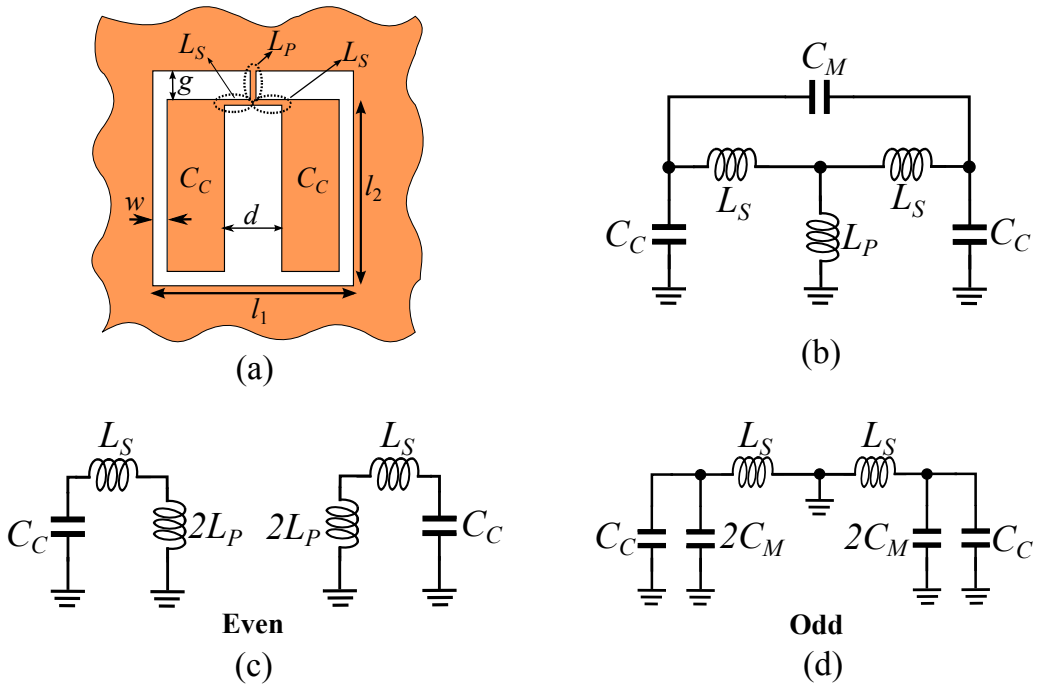

Figure 3.2. Dual-mode complementary split-ring resonator (DMCSRR). (a) Configuration of the resonator. (b) Its equivalent circuit model. (a) The equivalent circuit model in even mode resonance. (b) The equivalent circuit model in odd mode resonance. The metallisation is shown in orange colour.

$$f_{\text{odd}} = \frac{1}{2\pi\sqrt{L_S(C_C + 2C_M)}}. \tag{3.2}$$

As an illustration of the dual-mode behavior, a microstrip excited dual-mode CSRR as the one shown in Fig. 3.3(a) is considered and simulated by using a substrate with a relative dielectric constant of 10.7 and a thickness of 1.27 mm. The width of the microstrip line is $w_m = 1$ mm and the resonator geometrical dimensions are: $w = 0.3$ mm, $d = 1.4$ mm, $l_1 = 8$ mm, $l_2 = 7.7$ mm, $l_3 = 6.9$ mm, $g_c = 0.2$ mm and $g_f = 1.6$ mm. The length of the parallel inductive path (g) is varied to demonstrate its effect on the even mode resonance. As shown in Fig. 3.3(b), the even mode resonance is directly dependent on g whereas the odd mode is nearly unchanged. The small variation in the odd mode resonance is due to a small change in the capacitance C_C as a result of the varied g. The current distributions for the two modes are shown in the insets of Fig. 3.3(b). For the even mode, the current flows through both L_P and L_S from the capacitive plates directly to the ground plane, whereas for the odd mode the current flows between the two capacitive plates through L_S inductors.

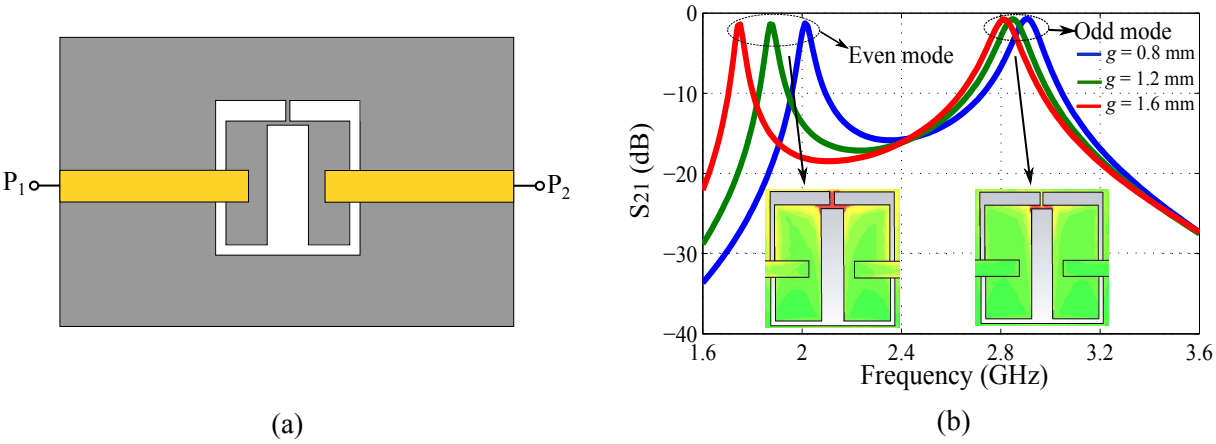

Figure 3.3. Dual-mode complementary split-ring resonator (DMCSRR) loaded on a microstrip line with a series capacitive gap. (a) The layout of the DMCSRR loaded on microstrip line with series capacitive gap. (b) The transmission responses obtained from full-wave EM simulations for different values of g. The microstrip line is shown in yellow whereas the ground plane is indicated in grey.

3.2.2 Dual-mode bandpass filter based on microstrip-line-coupled DMCSRR

As demonstrated in Fig. 3.3(b), the microstrip-line-coupled DMCSRR with a series capacitive gap shows a dual bandpass transmission response. So, this configuration can be used to design dual-mode bandpass filters. Here, a wide-band dual-mode bandpass filter is designed based on this configuration. In order to improve the transmission response in the passband, the *C*-shaped couplings have been chosen for the input/output feeds as shown in Fig. 3.4(a) (Liu *et al.* 2008). The equivalent *LC* model is available for the *C*-shaped coupling as shown in Fig. 3.4(b). In this model, the values of L_1 and L_2 inductors can be controlled by the lengths d_1, d_2 and widths w_1, w_2. Also, the ratio L_1/L_2 is related to the location of the input/output microstrip lines d_1/d_2. The gap between the two *C*-shaped couplings is represented by the capacitive π-model constructed from the series capacitors C_S and the parallel capacitors C_P. By applying this coupling scheme, the layout of the final designed filter takes the form that is demonstrated in Fig. 3.5.

The three-dimensional structure of the filter and its circuit model are shown in Fig. 3.6. The circuit model incorporates the coupling effect between the *C*-shaped feeding microstrip lines and the DMCSRR embedded in the ground plane. The lumped element values of the circuit model are initially estimated by using the method presented in

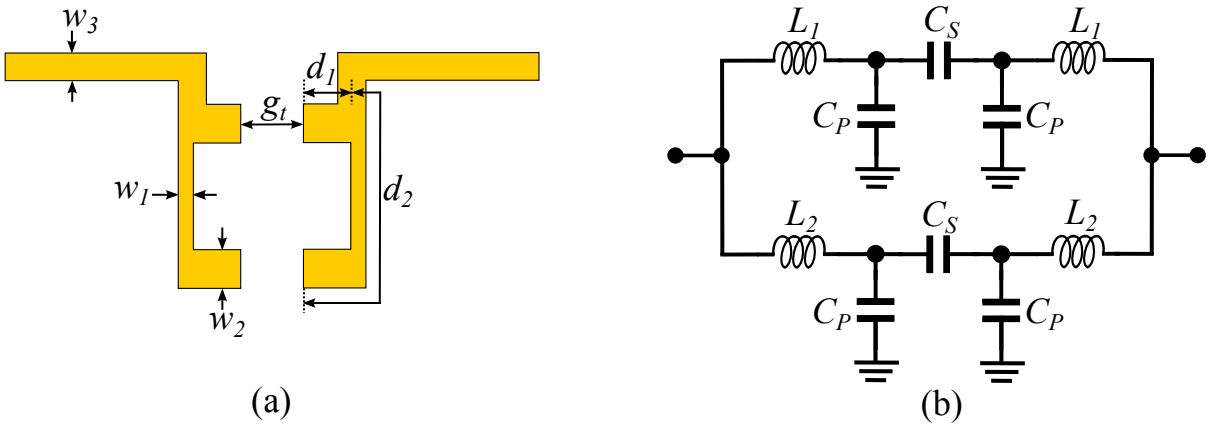

Figure 3.4. C-shaped in/output coupling. (a) The layout of the C-shaped feed structure. (b) Its equivalent circuit model.

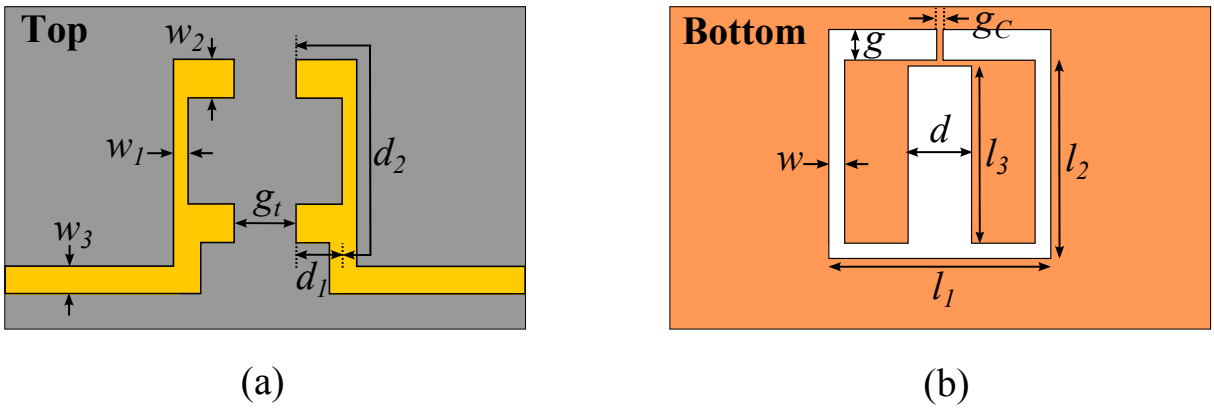

Figure 3.5. Layout of the Designed Dual-mode Filter. (a) The top layer view. (b) The bottom layer view. The microstrip metallisation is shown in yellow, the ground layer metallisation is orange and the dielectric substrate is grey. The geometrical dimension of the filter are: $l_1 = 8$ mm, $l_2 = 7.4$ mm, $l_3 = 6.9$ mm, $w = 0.3$ mm, $d = 1.4$ mm, $g = 0.8$ mm, $g_c = 0.2$ mm, $w_1 = 0.5$ mm, $w_2 = 1.5$ mm, $w_3 = 1$ mm, $d_1 = 3$ mm, $d_2 = 7.1$ mm and $g_t = 1.4$ mm.

(Bonache *et al.* 2006b), and then, more accurate values are obtained by fitting circuit simulation results to the full-wave electromagnetic simulation results. The final circuit elements values are: $L_1 = 0.61$ nH, $L_2 = 1.15$ nH, $L_S = 1.1$ nH, $L_P = 1.2$ nH, $C_M = 20$ fF, $C_S = 17$ fF, $C_P = 0.7$ pF and $C_C = 1.65$ pF.

Since the filter performance is dependent on its dimensions and geometry, the proposed filter and its circuit model are simulated in Advanced Design System (ADS) to observe the effect of different parameters. The substrate used for design and simulations is RT/duroid 6010 with a relative dielectric constant of ϵ_r= 10.7 and a thickness

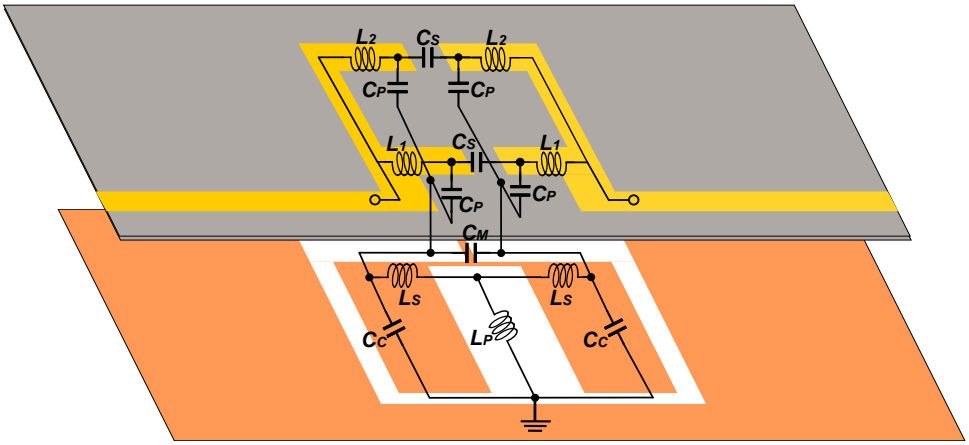

Figure 3.6. Three dimension (3-D) view of the designed dual-mode filter. 3-D view of the designed filter together with its equivalent circuit model. The microstrip metallisation is shown in yellow, the ground layer metallisation is orange and the dielectric substrate is grey.

of 1.27 mm. The filter bandwidth is mainly determined by the difference between the even and odd mode resonance frequencies of the DMCSRR. From (3.1) and (3.2), the even and odd mode resonance frequencies of the filter can be tuned separately by using C_M and L_P or equivalently by changing d and g respectively. Increasing d results in a smaller C_M and a larger L_S, but C_M is negligible for large enough d. Therefore, in this case, L_S is dominant and the odd mode resonance frequency will move downward decreasing the fractional bandwidth. A larger g shifts down the even mode resonance, which in turn causes a larger fractional bandwidth. The simulation results of varying d and g are shown in Fig. 3.7(a,b), confirming the above explanation.

From the circuit model shown in Fig. 3.6, the transmission zeros of S_{21} can be controlled through C_S. This capacitance value is dependent on the gap between the two C-shaped feeds (Bonache *et al.* 2006b). As a demonstration, the frequencies of the upper and lower transmission zeros are determined by using electromagnetic simulation of the whole structure for different C-shaped coupling gaps. As shown in Fig. 3.7(c), by decreasing the g_t, the upper transmission zero frequency moves downward and the lower transmission zero moves upward.

A prototype of the proposed filter has been fabricated with the dimensions given in Fig. 3.5. The fabricated filter is depicted in Fig. 3.8. The simulated, measured and circuit model responses of the filter are shown in Fig. 3.9 over the 0.2 to 6 GHz band. To avoid unexpected coupling of DMCSRR to the surroundings, the measurement is

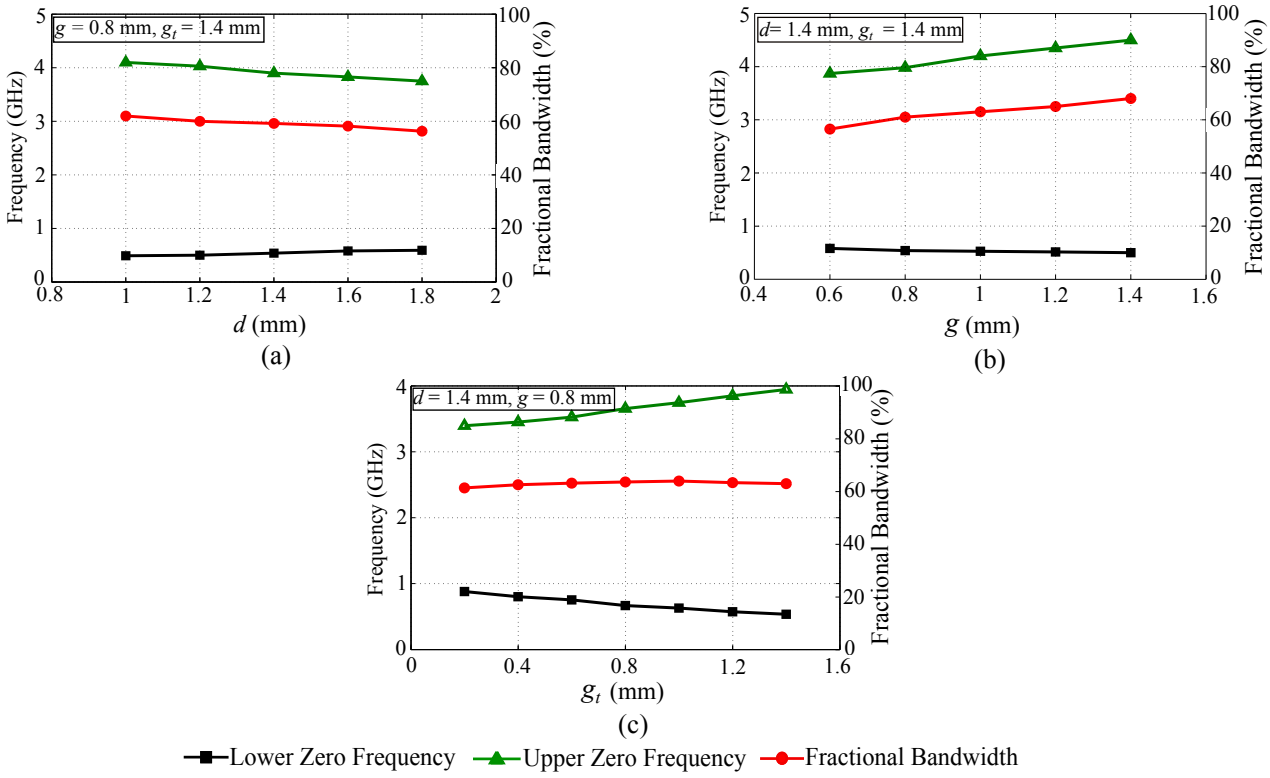

Figure 3.7. Effects of parameter variations on the filter performance. (a) Filter performance versus d. (b) Performance versus g. (c) Performance versus g_t.

Figure 3.8. Fabricated prototype of the dual-mode filter. Top view (a) and bottom view (b) of the fabricated filter prototype.

carried out on a non-metallic surface. As seen, the measurements agree with simulations. The measured centre frequency of the filter is 2.23 GHz and the -3 dB bandwidth is 1.38 GHz, which corresponds to a wide fractional bandwidth of 62%. The maximum passband IL is 0.27 dB and the stopband is extended to $2.6f_0$ below -26 dB; the maximum rejection is around 57 dB, implying a good performance in suppressing unwanted out-of-band signals. The fabricated filter occupies a very compact area of $0.0625\lambda_g \times 0.18\lambda_g$ where λ_g is the guided wavelength at the midband frequency.

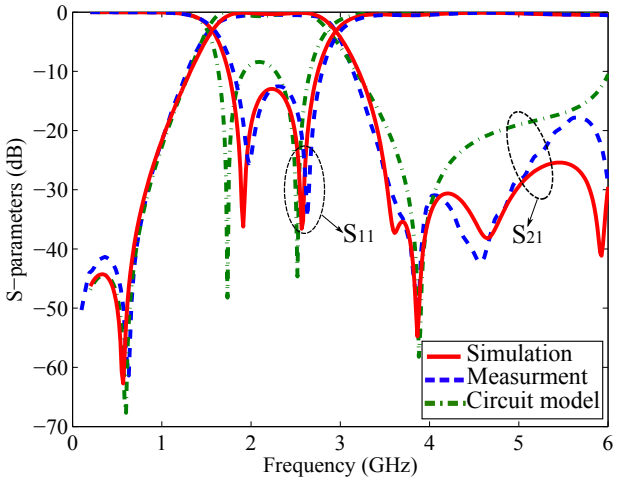

Figure 3.9. Simulated and measured S-parameters of the dual-mode bandpass filter. Comparison between the EM and circuit model simulation results and the measured S-parameters of the dual-mode bandpass filter.

3.2.3 Dual-mode bandstop filter based on microstrip-line-coupled DMCSRR

Bandstop filters are essential parts of the RF and microwave systems for suppressing the unwanted frequency components (Mandal *et al.* 2008, Shaman and Hong 2007). A critical specification in bandstop filters is to have an extended upper passband profile with harmonic-free response. Several designs of bandstop filters have been developed up to now that can extend the upper passband up to 6–7 times of the stopband central frequency (Levy *et al.* 2006, Fathelbab 2011, Naglich *et al.* 2012). However, the large footprint of these configurations makes them unsuitable to use in integrated compact systems. Here, we will develop bandstop filter with extended upper passband based on the microstrip-line-couple DMCSRR with a very compact size for integrated systems. The proposed bandstop filter is designed by incorporating the circuit model of a two-pole notch filter in Fig. 3.10(a) (Ou and Rebeiz 2011). In this model, J_{12} and J_S are impedance inverters converting the parallel resonators to their series alternatives. By introducing a capacitive or inductive coupling between the parallel resonators L_1C_1 as shown in Fig. 3.10(b), the two poles of the filter will be spectrally separated to form a dual-mode filter (Naqui *et al.* 2012, Su *et al.* 2015). The J_{12} inverter can be implemented with L_LC_L combination and the J_S inverter can be realised with the π capacitive configuration comprising C_S and $-C_S$ as indicated in Fig. 3.11(a). The lumped element values in the circuit of Fig. 3.11(a) can be synthesised by using standard filter theory.

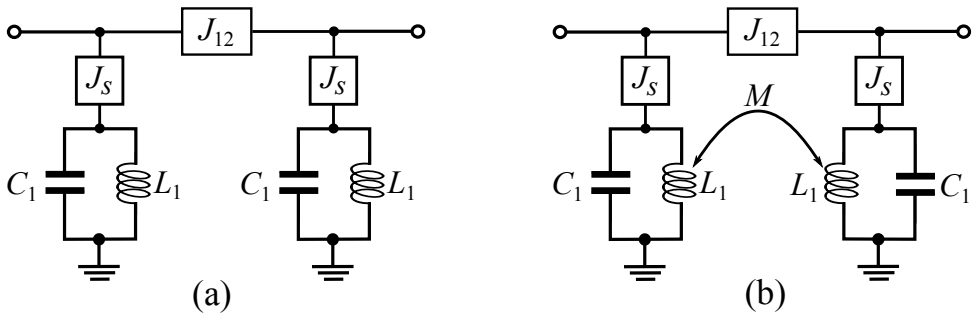

Figure 3.10. Circuit model of a notch filter. (a) Equivalent circuit model of the notch filter. (b) Second-order filter obtained by introducing an inductive coupling to the resonators in notch filter.

By choosing a practically realisable value for L_1, the closed-form equations for calculating the element values are (Ou and Rebeiz 2011):

$$C_S = \sqrt{\frac{\Delta g_1}{L_1 Z_0 \omega_0^3}}, \tag{3.3}$$

$$C_1 = \frac{1}{\omega_0^2 L_1}, \tag{3.4}$$

$$C_L = \frac{\sqrt{g_0 g_3}}{Z_0 \omega_0}, \tag{3.5}$$

$$L_L = \frac{1}{\omega_0^2 C_L}, \tag{3.6}$$

$$M = \Delta \sqrt{g_1 g_2} L_1, \tag{3.7}$$

where ω_0 is the center frequency of the filter, Δ is the fractional bandwidth, Z_0 is the characteristic impedance of the transmission line, and $g_{0,\ldots,3}$ are the element values of the lowpass filter prototype. In a special case for simplification, if C_L is forced to be equal to C_S, the equivalent circuit will take the form of Fig. 3.11(b), where $C_P = C_1 - C_S$, and the C_L capacitor is canceled by $-C_S$. The L_{12} in Fig. 3.11(b) is a larger inductor with respect to L_L in Fig. 3.11(a) to compensate for the forced value of C_L.

As an example, we design a second-order Butterworth bandstop filter with a center frequency of $f_0 = 2$ GHz and a fractional bandwidth of $\Delta = 30\%$. By considering $L_1 = 3.1$ nH, the calculated element values from (3.3)–(3.7) are: $C_S = 1.1$ pF,

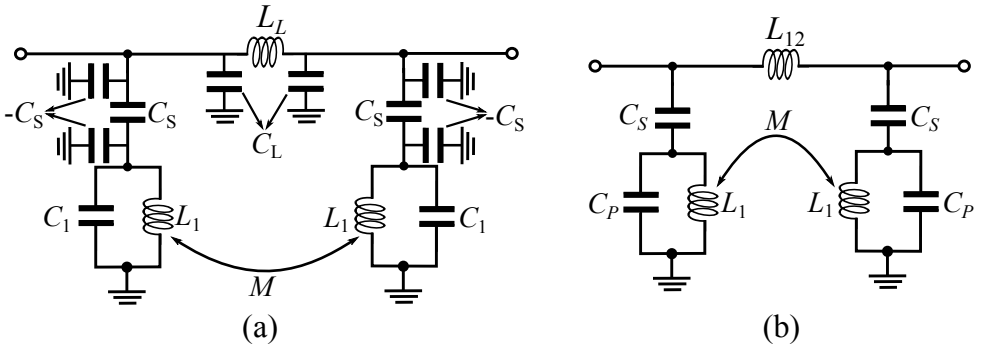

Figure 3.11. Circuit models of the proposed dual-mode bandstop filter. (a) The equivalent circuit of the proposed filter, where the impedance inverters are realized by lumped elements. (b) Simplified equivalent circuit model when $C_L = C_S$.

$C_1 = 2.05$ pF, $M = 1.3$ nH, $C_L = 1.5$ pF, and $L_L = 4.35$ nH. Now, by forcing C_L to be the same as $C_S = 1.1$ pF, the filter prototype in Fig. 3.11(b) will be obtained in which $L_L = 4.4$ nH to compensate for the new value of C_L. A comparison between the transmission responses of the filters in Fig. 3.11(a) and Fig. 3.11(b) is presented in Fig. 3.12(a). In addition, Fig. 3.12(b) compares the transmission magnitude and phase of the $L_L C_L$ impedance inverters in Fig. 3.11(a) and Fig. 3.11(b). By changing the C_L and L_L values, the transmission magnitude of the impedance inverter stays on 1 with a small phase deviation from 90°. With this simplification, the response of the filter in Fig. 3.11(b) still agrees with the Fig. 3.11(a) prototype as seen in Fig. 3.12(a).

The filter in Fig. 3.10(a) was implemented with lumped components in (Ou and Rebeiz 2011) for campactness. However, it is desirable to use planar structures for lower losses and improved quality factors. Furthermore, a planar design is fully compatible with high-frequency circuits, where lumped elements are not available. A suitable option for implementing the proposed dual-mode second-order filter is to use the dual-mode CSRR introduced in this chapter. A dual-mode CSRR loaded microstrip line and its equivalent circuit model are shown in Fig. 3.13. In this figure, C_P capacitors model the capacitances between the two rectangular halves of the resonator and the surrounding ground plane, whereas the L_S inductors model the two metallic paths that connect the two capacitive halves to each other. The L_C represents the inductance of the center metallic path running to the ground plane, L_L models the equivalent inductance of the microstrip line section, and C_S represents the coupling capacitance between the microstrip line and the resonator. The circuit in Fig. 3.13(b) is fully equivalent to the circuit in Fig. 3.11(b), where the inductances and mutual inductance are presented with

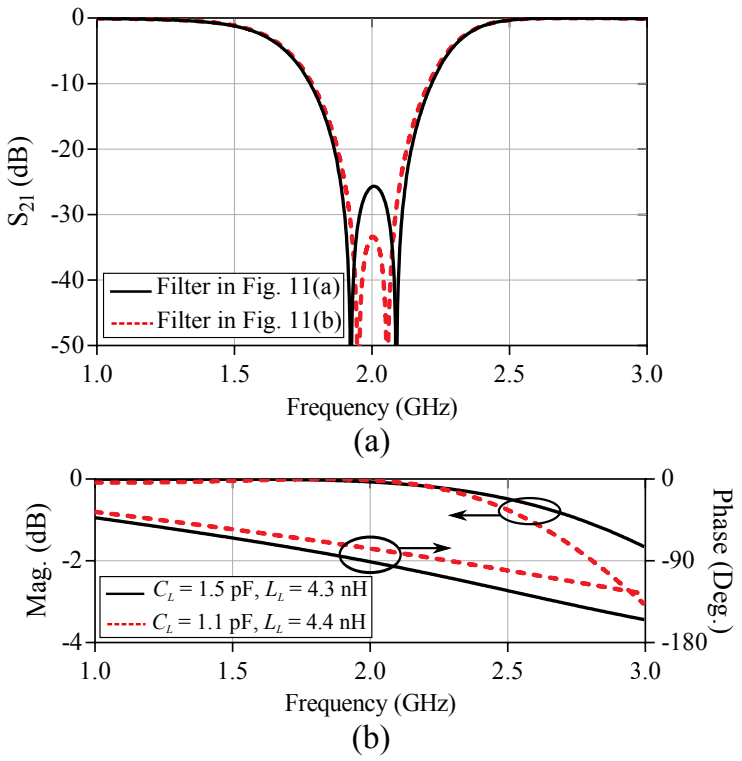

Figure 3.12. Effect of the impedance inverter on the filter response. Comparison between (a) the transmission responses and (b) amplitude and phase of the $L_L C_L$ inverters of the filters in Fig. 3.11(a) and Fig. 3.11(b).

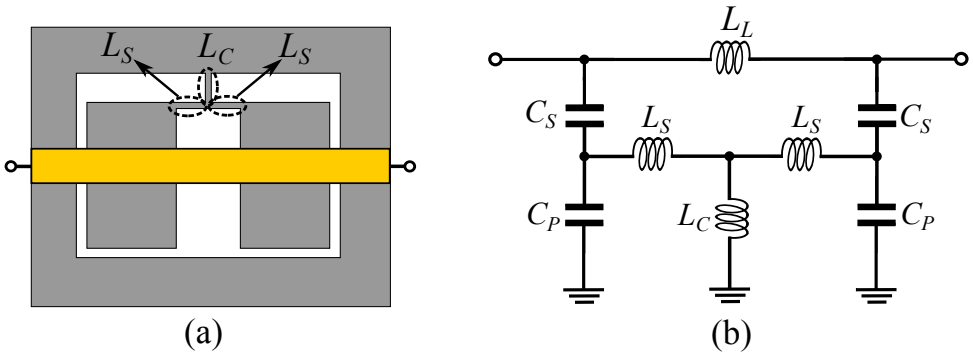

Figure 3.13. Microstrip-line-coupled DMCSRR. (a) A microstrip line loaded dual-mode complementary split-ring resonator (DMCSRR). (b) Its lumped-element equivalent circuit model. The ground plane is shown in grey and the microstrip line is drawn with yellow.

the equivalent T-model. The two circuits show the same response if $L_C = M$, and $L_S = L_1 - M$. The other parameter values are exactly the same in the two circuits.

The designed second-order bandstop filter is experimentally validated. The front and back layouts of the designed filter are depicted in Fig. 3.14. The dielectric substrate

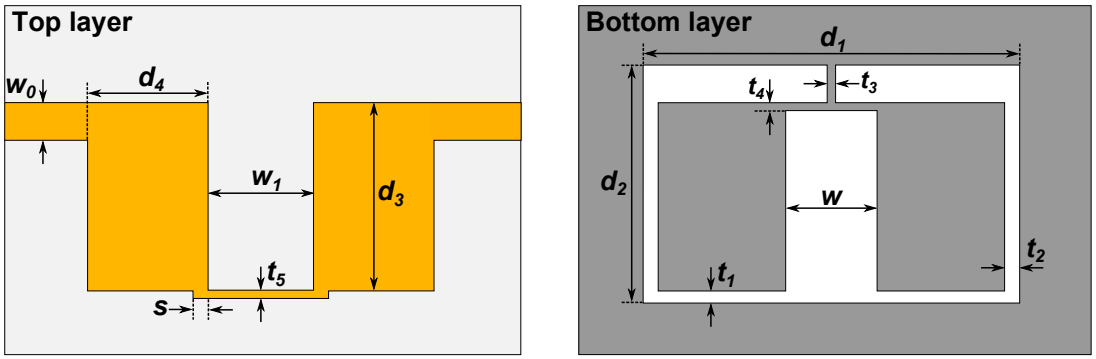

Figure 3.14. Filter layout. Layout of the designed bandstop filter. The gray layer shows the ground plane, whereas the microstrip metallization is shown with yellow. The filter dimensions are: $d_1 = 10$ mm, $d_2 = 6.3$ mm, $d_3 = 5$ mm, $d_4 = 3.2$ mm, $t_1 = 0.3$ mm, $t_2 = 0.4$ mm, $t_3 = t_4 = 0.2$ mm, $t_5 = 0.2$ mm, $w_0 = 1.3$ mm, $w_1 = 2.8$ mm, $w = 2.4$ mm, and $s = 0.4$ mm.

(a) (b)

Figure 3.15. The fabricated dual-mode bandstop filter. The fabricated filter prototype. (a) Top view. (b) Bottom view.

is a 1.27 mm thick Rogers RO3010 with a relative permittivity of 10.2 and a loss tangent of 0.0022. The filter geometrical dimensions are optimised by curve fitting of the electromagnetic and circuit model simulations in Agilent ADS software (Su *et al.* 2015, Naqui *et al.* 2012). In the filter layout, the microstrip metallisation is meandered with two widened parts for increasing the coupling capacitance between the dual-mode CSRR and microstrip to match the required C_S. The thin metallic path with a width t_5 determines the value of L_L.

A photograph of the fabricated filter prototype is illustrated in Fig. 3.15 with the top and bottom views. The measured S-parameters of the filter are plotted together with the results from the equivalent circuit model and full-wave electromagnetic simulations in Fig. 3.16(a). Good agreement is achieved between the measured and simulated results within the stopband. The desired 30% fractional bandwidth and 2 GHz center frequency are well satisfied. The measured rejection level within the stopband is more than 28 dB. Fig. 3.16(b) demonstrates the wideband measured S-parameters of the fabricated filter. The measurement show a good upper passband level above -0.6 dB up

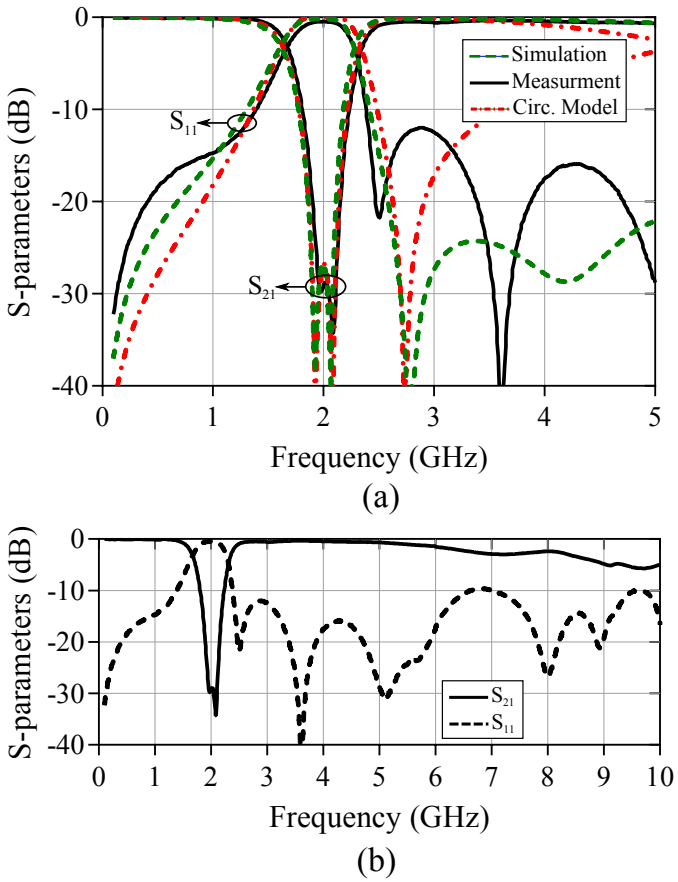

Figure 3.16. Measured and simulated results of the bandstop filter. (a) Comparison between the measured and simulated results of the filter. (b) Wideband measurement results.

to 5 GHz. The passband level decreases beyond this frequency, but it remains larger than -3 dB up to around 8.4 GHz, which corresponds to $4.2f_0$. This is achieved by tapering the resonator that increases the loading effects of L_S and L_C inductors resulting in a more compact resonator size. A comparison with other bandstop filters in terms of size and performance is presented in Table 3.1, where $f_{-3\text{dB}}$ is the frequency at which the upper passband reaches -3 dB. It is clear that the designed filter possesses the most compact size with a fairly good upper passband in comparison with the other filters.

3.3 Dual-mode complementary electric-LC resonators

The loading effect of dual-mode complementary split-ring resonators (DMCSRR) on microstrip transmission lines has been discussed in Section 3.2. This section is dedicated to the analysis of the microstrip line loaded with a special configuration of the complementary electric-LC (CELC) resonators. It will be demonstrated that by loading a microstrip line with these resonators, a dual-mode sub-wavelength element will be

Table 3.1. Comparison of various bandstop filters. A comparison between different bandstop filters in terms of performance and size.

Ref.	Order (n)	Rej. level	Frac. BW	$f_{-3\text{dB}}$	Size
(Shaman and Hong 2007)	3	-24 dB	80%	$2.5f_0$	$0.68\lambda_g \times 0.3\lambda_g$
(Naglich *et al.* 2012)	4	-20 dB	1%–4.8%	$7.8f_0$	$0.43\lambda_g \times 0.4\lambda_g$
(Levy *et al.* 2006)	12	-27 dB	34%	$6f_0$	Length$>\lambda_g$
(Fathelbab 2011)	5	-40 dB	7.5%	$4.7f_0$	Length $= 1.56\lambda_g$
This work	2	-28 dB	30%	$4.2f_0$	$0.1\lambda_g \times 0.18\lambda_g$

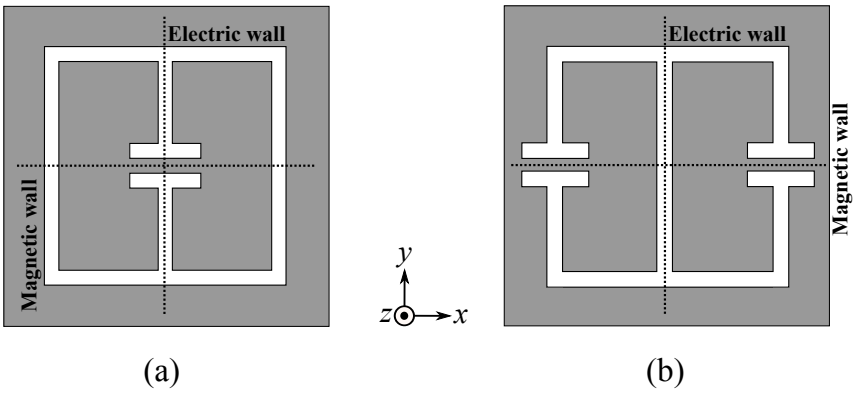

Figure 3.17. Complementary electric-LC resonators. (a) CELC1 configuration. (b) CELC2 configuration. Metallisation is shown in grey colour.

obtained and can be used to design compact microwave devices. The applications of the transmission line loaded with CELC resonators will be explained through design examples in Section 3.3.1.

3.3.1 Complementary electric-LC resonators

The complementary electric-LC resonators in Fig. 3.17 are bisymmetric resonators, where one of the symmetry lines in CELC resonators acts as an electric wall and the other is acting as a magnetic wall. The complementary resonators in Fig. 3.17 can be driven by means of a uniform in-plane (y oriented) applied magnetic field but not through a uniform out-of-plane (z oriented) electric field at the fundamental resonance mode.

The resonators in Fig. 3.17 can also be excited through the electromagnetic fields of transmission lines where the fields are no longer uniform. Furthermore, the dual symmetric property can be accessed via transmission line excitation. The behaviour of transmission line coupled CELC1 resonators has been studied in detail in Naqui *et al.* (2013b), Naqui and Martín (2013), and Naqui *et al.* (2013a). However, an analysis of transmission lines loaded with the resonator in Fig. 3.17(b) (called CELC2 here) is still lacking. A major difference between the CELC2 and CELC1 lies in existence of two symmetric *LC* resonators in its structure that provide a subwavelength dual-mode behavior making it a very attractive choice for designing new compact microwave components. Here, we will provide an in-depth study of this dual-mode resonator through a lumped element circuit model. Additionally, different configurations of the microstrip-coupled resonator as well as their potential applications in planar microwave devices will be analysed and explained.

As discussed earlier, the CELC2 can be excited by means of an in-plane (y oriented) applied magnetic field, but not through a uniform out-of-plane (z oriented) electric field. If the resonator dimensions are electrically small, it can be modelled by a lumped element equivalent circuit as in Fig. 3.18(a). The parallel resonant branches of L_gC_g model the two halves of the resonator, where C_g presents the capacitive effect between the metallic halves and the surrounding ground plane and L_g models the inductive paths running from the two capacitive regions to the ground plane. Here, C_M stands for the mutual capacitive effect between the two metallic halves of the resonator. It can be inferred from this equivalent circuit that the particle can exhibit the even and odd mode resonances with the equivalent circuits demonstrated in Fig. 3.18(b) and Fig. 3.18(c) respectively. In the even mode, the two halves of the resonator have the same voltage distribution, and thus, no current will pass through C_M and it will be open-circuited. Conversely, in the odd mode, there will be a virtual ground across the electric wall and C_M is broken into two equal parts of $2C_M$ as demonstrated in Fig. 3.18(c). Based on Fig. 3.18 and the above discussion, the even and odd mode resonance frequencies of the resonator can be defined as

$$f_{\text{even}} = \frac{1}{2\pi\sqrt{L_gC_g}}, \tag{3.8}$$

$$f_{\text{odd}} = \frac{1}{2\pi\sqrt{L_g(C_g+2C_M)}}. \tag{3.9}$$

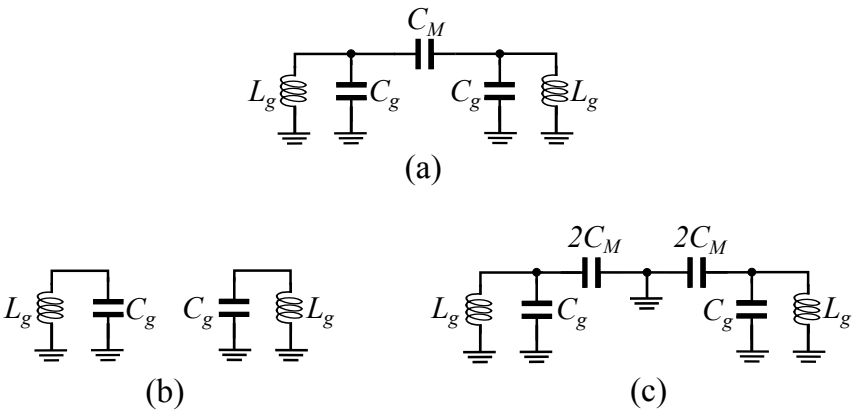

Figure 3.18. Lumped element modeling of the CELC2. (a) Equivalent circuit model. (b) Even-mode circuit model. (c) Odd-mode circuit model.

As seen, in the odd mode resonance, the C_M capacitor adds to the C_g causing a smaller resonance frequency with respect to the even mode resonance.

3.3.2 Microstrip line loaded with CELC2 resonator

As mentioned before, the CELC2 resonator can be excited through the fields generated by the planar transmission lines. This section is dedicated to the analysis of microstrip lines loaded with the CELC2 resonator. Both of the bandstop and bandpass configurations will be introduced and their electromagnetic behavior will be analysed using equivalent circuit models.

First, the bandstop behavior of microstrip transmission line loaded with the CELC2 is explained using the circuit analysis. It must be emphasised that the equivalent circuit analysis is valid as long as the unit cell dimension is electrically small (Gil *et al.* 2006b, Naqui *et al.* 2014). In order to satisfy this condition, the resonator shown in Fig. 3.19(a) is considered instead of the one in Fig. 3.17(b). In Fig. 3.19(a), the magnetic wall no longer exists, but it still shows the behavior of the CELC2 resonator for the considered case. Fig. 3.19(b) shows a CELC2 resonator that is loaded onto a microstrip line with the electric wall of the resonator aligned with the symmetry plane of the transmission line. In this structure, since the two halves of the ELC2 are equally excited by the transmission line, they will share the same voltage distribution. Therefore, only the even mode resonance will be excited and there will be just a single notch in the transmission response as shown in Fig. 3.19(c). This behavior can be also explained through the circuit model of the structure that is shown in Fig. 3.20(a). Here, the inductors L model

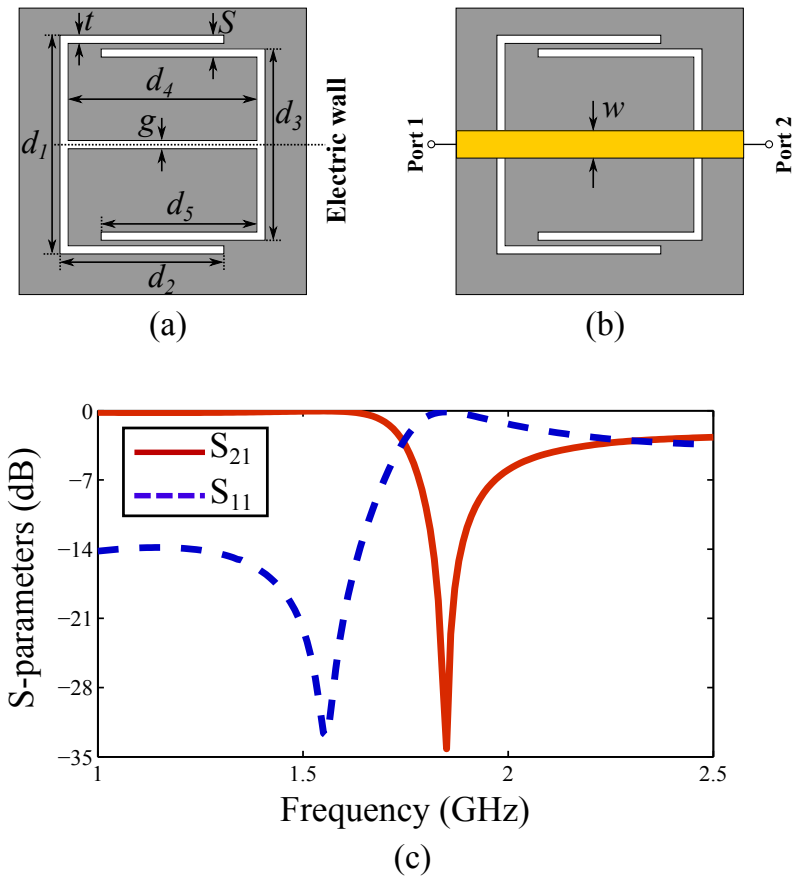

Figure 3.19. Microstrip line loaded with CELC2 resonator. (a) Modified CELC2 resonator. (b) Modified CELC2 resonator coupled with the microstrip transmission line. (c) Transmission response when the resonator electric wall is aligned with the symmetry plane of the transmission line. The resonator and transmission line dimensions are: $d_1 = 10$ mm, $d_2 = 7.2$ mm, $d_3 = 9.4$ mm, $d_4 = 9.6$ mm, $d_5 = 7$ mm, $t = g = 0.2$ mm and $S = 0.5$ mm. The considered substrate is Rogers RO6010 with $\epsilon_r = 10.2$ and $\tan\delta = 0.0023$ and a thickness of 1.27 mm.

the inductance associated with the microstrip, C_1 and C_2 present the coupling capacitances between the transmission line and the resonator and R represents the losses. If the electric wall is aligned with the microstrip symmetry plane, the C_1 and C_2 coupling capacitors will be equal ($C_1 = C_2 = C$) and no current will pass through C_M. Hence, the equivalent circuit will be simplified to that shown in Fig. 3.20(b). Based on this model, the transmission notch occurs at a frequency that nulls the shunt impedance. Hence,

$$f_{\text{notch}} = \frac{1}{2\pi\sqrt{L_g(C_g + C)}}. \tag{3.10}$$

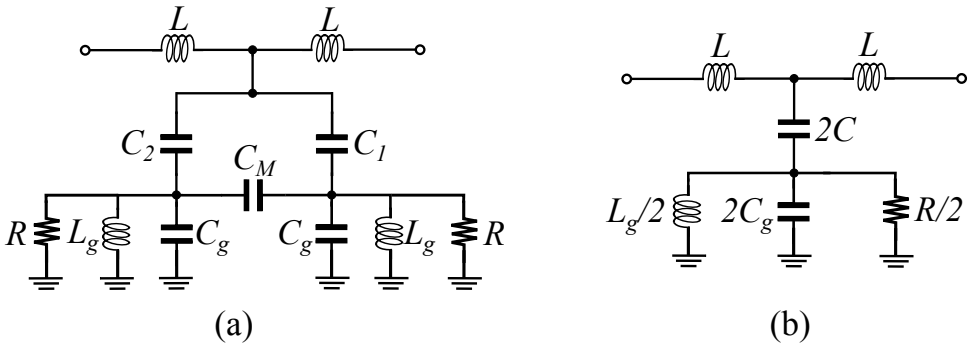

Figure 3.20. Lumped element modeling of the CELC2. (a) Equivalent circuit model. (b) Even-mode circuit model. (c) Odd-mode circuit model.

The values of circuit elements in Fig. 3.20(b) can be obtained by using the procedure reported by Bonache *et al.* (2006b) and Aznar *et al.* (2008b) that is based on characteristics of the transmission and reflection coefficients provided by electromagnetic simulations. There are four unknown parameters (L, C, L_g and C_g) that can be calculated using the following four conditions: (i) The transmission notch frequency is the frequency in which the shunt impedance nulls as described by (3.10), (ii) the frequency for which the shunt impedance is open circuited corresponds to the intersection between the reflection coefficient (S_{11}) and the normalised unit resistance circle in the Smith chart, (iii) the phase of transmission coefficient reaches (90°) when the series impedance is the complex conjugate of the shunt impedance, and (iv) the frequency at which the parallel admittance vanishes is the resonance frequency of the LC tank associated with the resonator. The resistance R can be determined by curve fitting of EM and circuit simulations. Fig. 3.21 shows a comparison between the electromagnetic and circuit-model simulations for a typical configuration in Fig. 3.19(b). The circuit parameters have been extracted through the procedure above. The plots demonstrate agreement between the EM and circuit simulations.

Now, if the symmetry planes of the transmission line and resonator are no longer aligned, C_1 and C_2 in Fig. 3.20(a) will take different values and this asymmetry allows current flowing through C_M. Hence, the odd mode resonance will be excited causing another notch in the transmission response of the structure. The structure of Fig. 3.19(b) is simulated for three laterally displaced positions of the resonator with respect to the microstrip line (0.6 mm, 1 mm and 2 mm). To extract the unknown elements of the equivalent circuit model of the displaced structure in Fig. 3.20(a), firstly, we consider the circuit elements for the aligned structure in Fig. 3.20(b) by using the four conditions described before. Then, the value of C_M will be calculated by using

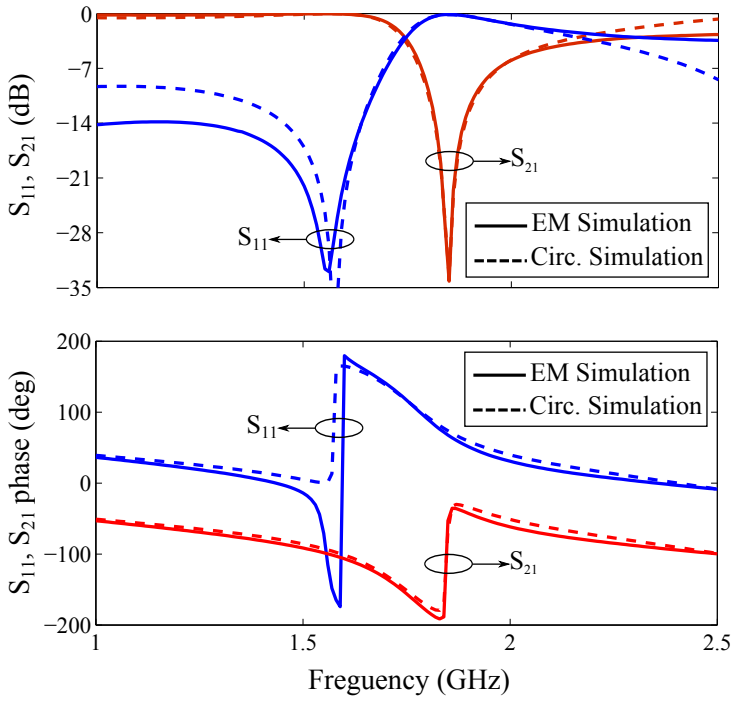

Figure 3.21. Simulation response of a CELC2 coupled microstrip line. Frequency response of the structure in Fig. 3.19(b) and its equivalent circuit model of Fig. 3.20(b). (a) Magnitude and (b) phase of the transmission and reflection coefficients. The resonator and microstrip line dimensions are listed in Fig. 3.19. The circuit parameters are: $L = 5.4$ nH, $C = 0.685$ pF, $C_g = 3.2$ pF, $L_g = 1.91$ nH and $R = 3.75$ kΩ.

(3.9) since the odd mode resonance frequency is known from the electromagnetic simulations of the displaced structure. At this point, the reflection coefficient (S_{11}) will cross the unit impedance circle on the Smith chart again because (S_{11}) has two intersections with the unit impedance circle due to the dual-mode nature of the resonator. Afterwards, the values of C_1 and C_2 capacitances can be tuned by curve fitting of the electromagnetic and the equivalent circuit simulation results. The equivalent inductance of the transmission line L may be slightly modified from the aligned structure since the line inductance is affected by the resonator positioned beneath. The other element values are nearly unchanged. Here, we use the element values of the symmetric structure given in Fig. 3.21 as the initial values since the dimensions and the considered substrate are the same. The extracted circuit model parameters are listed in Table 3.2 for these three lateral displacements. The electromagnetic simulations results are shown together with the circuit model results in Fig. 3.22. As seen, there is a reasonable agreement between the EM and circuit simulations. The agreement validates the above analysis and the proposed circuit model in Fig. 3.20.

Table 3.2. Equivalent circuit parameters. Extracted values of the equivalent circuit elements in Fig. 3.19(b) for three different displacements of the resonator.

Δx (mm)	L (nH)	C_1 (pF)	C_2 (pF)	C_M (pF)	C_g (pF)	L_g (nH)	R (kΩ)
0.6	4.15	1.05	0.34	1.73	3.2	1.9	7.5
1	4.15	1.14	0.25	1.85	3.2	1.9	7.5
2	4.15	1.18	0.09	2.05	3.2	1.9	7.5

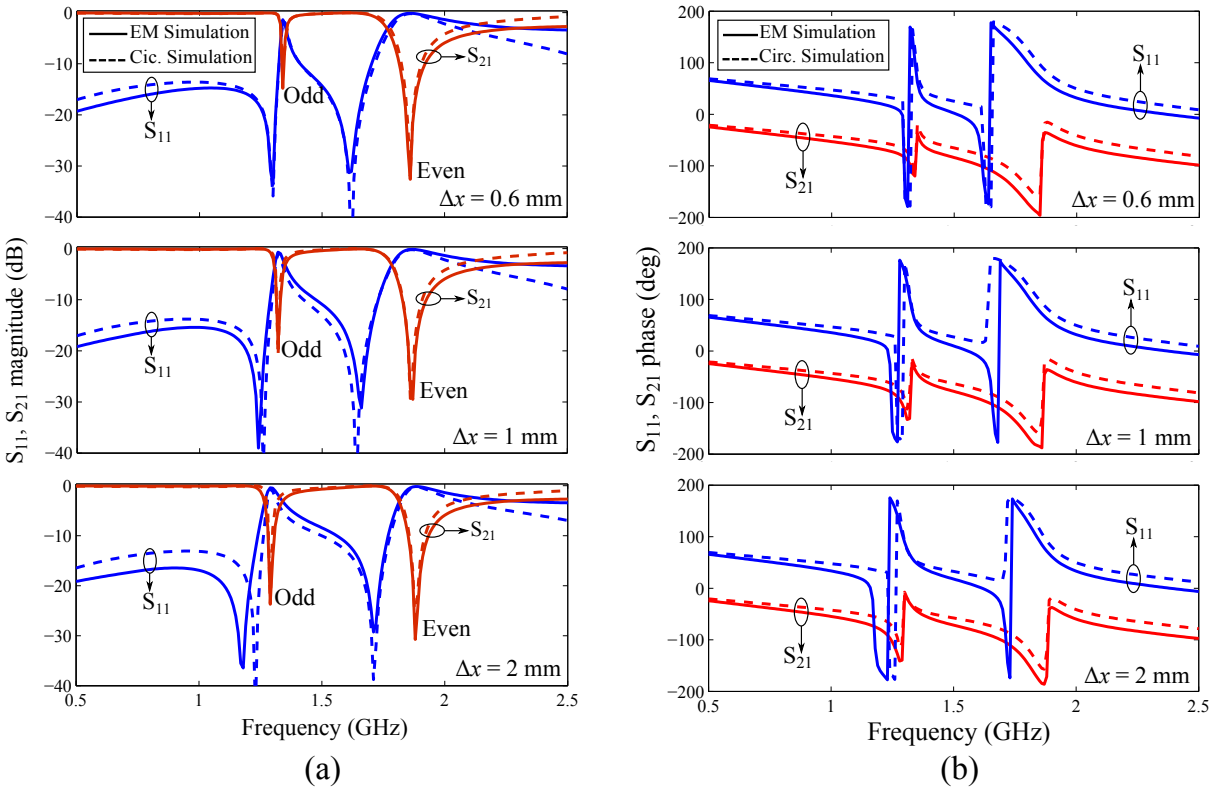

Figure 3.22. Simulation response of a CELC2-coupled microstrip line with lateral displacement. Results from the electromagnetic and circuit simulations of the structure in Fig. 3.19(b) for three different displacements (0.6 mm, 1 mm and 2 mm) of the resonator with respect to the microstrip line. (a) Magnitude and (b) phase of the transmission and reflection coefficients. The equivalent circuit parameters of the three cases are listed in Table 3.2.

By looking at the plots in Fig. 3.21 and Fig. 3.22, it can be found that there are small discrepancies between the EM and circuit model simulations around the even mode

resonance, which takes place at higher frequencies. At these frequencies, the wavelengths are shorter and closer to the resonator dimensions. As a result, the assumption of lumped elements becomes less accurate, and leads to the observable discrepancies.

The bandstop response of the microstrip line loaded with the CELC2 resonator is associated with the negative permitivity of the structure around the resonance frequencies. This behavior can be easily changed to a bandpass response by introducing series capacitive gaps to the microstrip line (Gil *et al.* 2006b, Ebrahimi *et al.* 2014a, Horestani *et al.* 2014b). The bandpass counterpart is demostrated in Fig. 3.23 with its equivalent circuit model. The circuit model is very similar to the bandstop configuration excepting for C_S, which is added to the model to represent the capacitive gap of the microstrip line. Both of the C_1 and C_2 capacitors are considered to have the same value of C due to the symmetric alignment of the resonator and the transmission line. To extract the lumped element values in the circuit of Fig. 3.23(b), firstly, the bandstop version of Fig. 3.19 should be considered and simulated for obtaining L_g, C_g and C_M values by using the procedure described in the previous section. The line inductance (L) can be estimated using a transmission line calculator or from the value obtained from the bandstop version in Fig. 3.19(b). To obtain the values of C_S and C capacitors, the input impedance seen from the ports at the even mode resonance frequency of the resonator should be considered. At the even mode resonance frequency, the parallel branch of L_gC_g is open circuited and the equivalent circuit in Fig. 3.23(b) takes the form of Fig. 3.24 in which the input impedance seen from the ports can be calculated as

$$Z_{\text{in(even)}} = 50 + j2\omega_e L + \frac{1}{j\omega_e(C_S + C_{\text{eq}})}, \tag{3.11}$$

$$C_{\text{eq}} = \frac{CC_M}{C + 2C_M}, \tag{3.12}$$

where $\omega_e = 2\pi f_{\text{even}}$ that is known from the intersection of S_{11} with the normalised unit resistance circle in the Smith chart. On the other hand, by introducing the capacitive gap to the microstrip line, the odd mode resonance frequency of the structure will be defined as

$$f_{\text{odd}} = \frac{1}{2\pi\sqrt{L_g(C_g + 2C_M + 2C_p)}}, \tag{3.13}$$

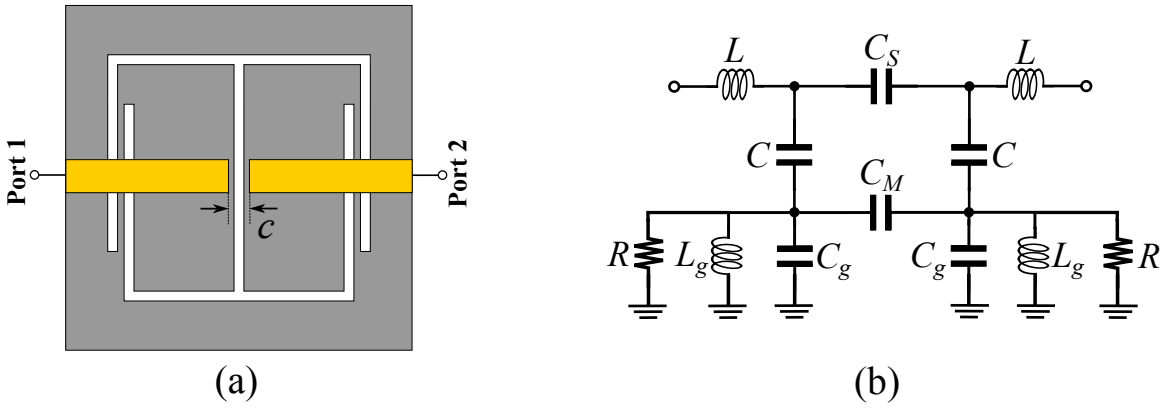

Figure 3.23. Bandpass configuration of the CELC2-loaded microstrip line. (a) Layout of the structure. (b) Its equivalent circuit model.

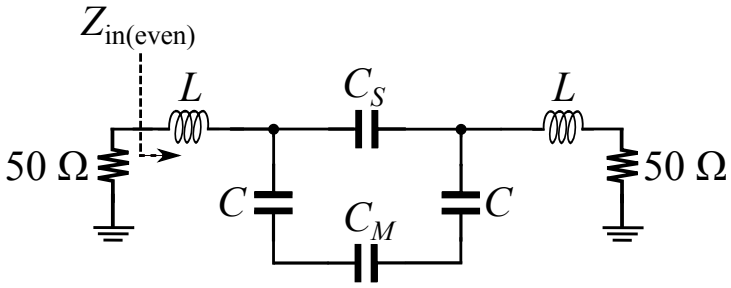

Figure 3.24. Even-mode equivalent circuit model. Equivalent circuit of the bandpass configuration of microstrip line loaded with the CELC2 at the even mode resonance frequency. The 50 Ω resistors indicate the input/output port impedance.

$$C_p = \frac{CC_S}{C + 2C_S}, \tag{3.14}$$

where f_{odd} is known from the intersection of the S_{11} with the unit resistance circle of the Smith chart. Thus, the values of C and C_S are calculated by using (3.13) and (3.14). Note that because of the dual-mode nature of the resonator, the S_{11} has two intersections with the unit resistance circle of the Smith chart and the odd mode intersection takes place at a lower frequency in comparison with the even mode based on (3.9) and (3.14). The bandpass structure in Fig. 3.23 has been simulated. A comparison between the electromagnetic and the equivalent circuit simulation results is presented in Fig. 3.25. The lumped element values of the equivalent circuit are extracted based on the procedure described above. The circuit simulations presented in Fig. 3.25 are in good agreement with the electromagnetic simulations. The results validate the proposed circuit model.

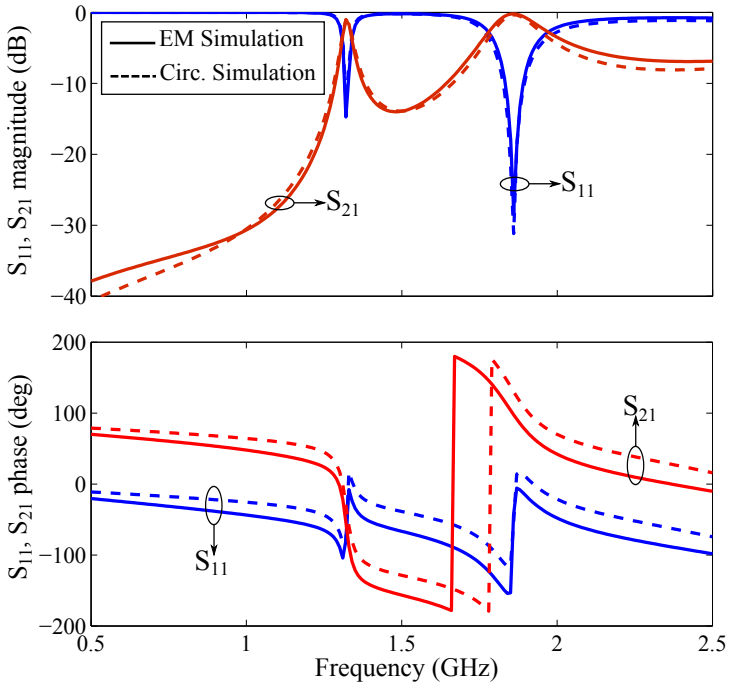

Figure 3.25. Simulation results of a bandpass configuration of CELC2-coupled microstrip line. Comparison between the electromagnetic and the equivalent circuit simulations of the bandpass configuration in Fig. 3.23. The resonator dimensions and the microstrip line width are the same as those given in Fig. 3.19. The considered capacitive gap width is $c = 0.2$ mm and the extracted equivalent circuit parameters are: $L = 4.4$ nH, $C_S = 28$ fF, $C_M = 1.91$ pF, $L_g = 1.91$ nH, $C_g = 3.13$ pF and $R = 6$ kΩ.

3.3.3 Potential applications of CELC2-coupled microstrip line

The proposed configurations of CELC2 resonators loaded with microstrip lines can be used in designing new microwave devices in different ways. For example, the bandstop configuration in Fig. 3.19 can be used for implementing bandstop filters, where the rejection bandwidth can be improved by etching several resonators with slightly different sizes in the ground plane or by having identical resonators arranged with a small distance from each other to improve the inter-resonator coupling (Martín *et al.* 2003b). It has been shown that by displacing the resonator with respect to the microstrip line, the odd mode resonance will also appear in the transmission response. This property can be used in designing dual bandstop filters (Safwat *et al.* 2007, Zhou *et al.* 2010), where again the bandwidth can be widened by using multiple resonators that are accurately displaced with respect to the transmission line.

It is known from (3.9) that the odd mode resonance frequency is dependent on the value of the mutual capacitance between the two halves of the resonator (C_M). Thus,

any change in the value of this capacitor can be detected from the frequency shift in the odd mode notch in the transmission response (S_{21}) of the device. We can make use of this charactersitic to design material characterisation sensors by loading a dielectric sample onto this capacitive gap (Ebrahimi *et al.* 2014c, Withayachumnankul *et al.* 2013, Puentes *et al.* 2012). The sensitivity of the odd mode resonance to the symmetry property of the structure in the bandstop configuration can be utilised to design displacement sensors. These potential application will be investigated throughout Chapter 4 and Chapter 5. Here, the performance of the presented structures is demonstrated by designing a bandpass filter. The bandpass configuration presented in Section 3.3.1 is used for designing a dual-mode bandpass filter.

3.3.4 Dual-mode bandpass filter design

The dual-mode bandpass configuration introduced in Section 3.3.2 is utilised for implementation of a dual-mode bandpass filter here. The layout of the designed filter is demostrated in Fig. 3.26 whereas the top and bottom views of the fabricated filter, is depicted in Fig. 3.27. The *C*-shaped input/output feeds are used for the filter to improve the passband response (Ebrahimi *et al.* 2014a, Liu *et al.* 2008).

The simulated and measured *S*-parameters of the designed filter from 0.5 GHz to 3.5 GHz are demonstrated in Fig. 3.28. The measurement shows a fractional bandwidth of 37% around the centre frequency of 2 GHz. It should be mentioned that the fractional bandwidth is determined from the difference between the even and odd mode resonance frequencies of the resonator. From (3.9) this difference can be controlled by C_M or equivalently by changing g, which is the distance between the two halves of the resonator. The out-of-band rejection level of the filter is more than 30 dB. The overall size of the fabricated filter is $0.11\lambda_g \times 0.08\lambda_g$ implying a compact structure.

3.4 Conclusion

This chapter presented dual-mode complementary resonators as miniaturised elements in designing microwave filters and sensors. A dual-mode complementary split-ring resonator DMCSRR has been developed by adding a defect to the middle part of a

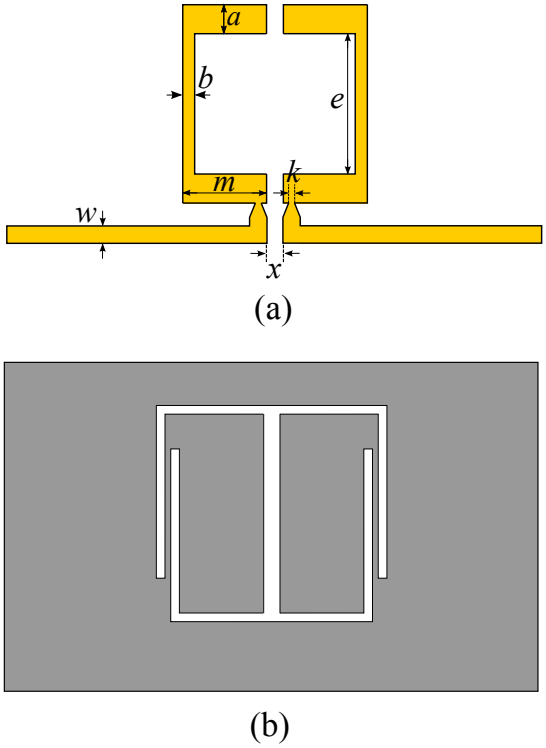

Figure 3.26. Layout of the dual-mode bandpass filter based on CELC2. (a) The top microstrip metalisation with yellow colour. (b) Bottom ground plane shown in grey. The resonator parameters are all the same as the dimenssions given in Fig. 3.19 except g, which is 1 mm here. The other dimnssions are: $a = 1.5$ mm, $b = 0.5$ mm, $e = 6.6$ mm, $m = 4$ mm, $k = 0.2$ mm, $x = 1$ mm and $w = 1$ mm.

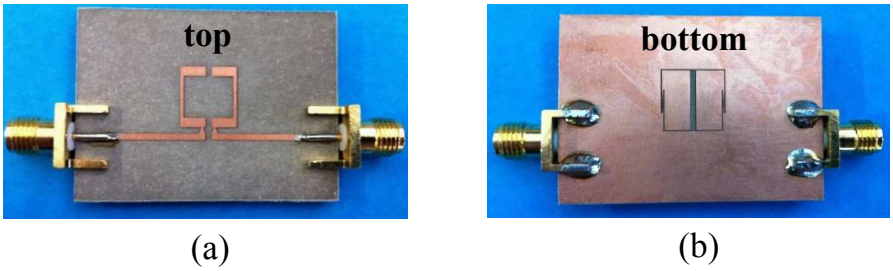

Figure 3.27. Fabricated dual-mode bandpass filter based on CELC2. Photograph of the top (a) and bottom (b) view of the fabricated filter.

CSRR. It has been demonstrated through the electromagnetic and circuit model simulations that this resonator shows a dual-mode resonance when it is excited by a microstrip line section. This configuration has been incorporated in designing both bandstop and bandpass filters. A high level of miniaturisation is achieved showing a compact size of $0.0625\lambda_g \times 0.18\lambda_g$ for the bandpass and $0.1\lambda_g \times 0.18\lambda_g$ for the bandstop configuration.

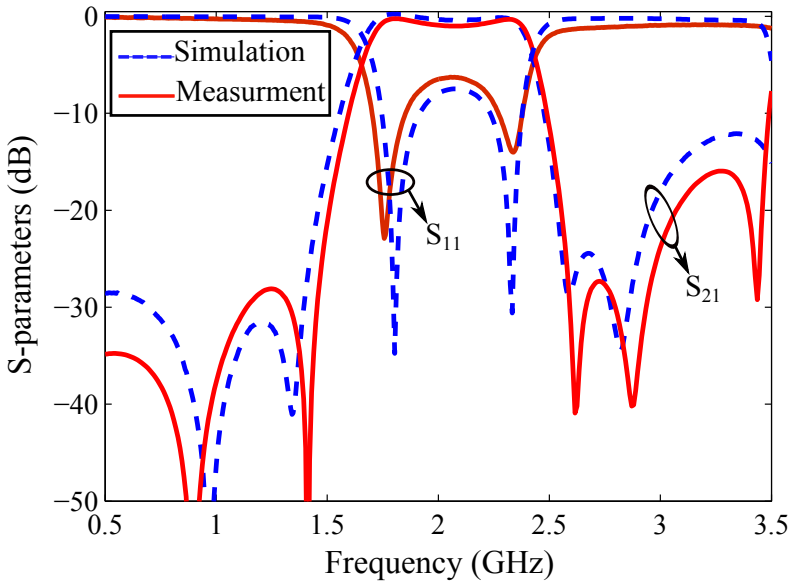

Figure 3.28. Comparison between the simulated and measures results of the CELC2-based dual-mode bandpass filter. Simulated and measured *S*-parameters of the designed dual-mode filter based on the presented bandpass configuration of CELC2 resonator loaded with microstrip line.

In the second part, the dual-mode behaviour of a special type of complementary electric-LC (CELC) has be discussed. The dual-mode response of the microstrip-line-coupled CELC2 has been analysed and verified through electromagnetic and circuit model analysis. The equivalent circuit model parameters have been extracted through an analytical procedure. The developed circuit models have been validated through good agreement between the circuit model and electromagnetic simulations. Potential application of the CELC2-coupled microstrip line sections have been demonstrated by designing a compact dual-mode bandpass filter.

The promising results all validate the potential of these dual-mode resonators in designing highly compact microwave devices. This chapter focused on miniaturisation of microwave filters by using dual-mode resonators. In Chapter 4 the application of complementary split-ring and complementary electric-LC resonators to high sensitivity microwave microfluidic sensors will be discussed.

Chapter 4

Metamaterial-inspired microfluidic sensors

METAMATERIAL resonators have attracted great attention in designing sensors. The split-ring resonators (SRRs) and complementary split-ring resonators (CSRRs) provide concentrated electromagnetic fields at their resonance with high quality factor characteristic. These electromagnetic fields are very sensitive to the environment changes such as displacement, rotation, dielectric property. Any change in these factors affect the resonance characteristics of the SRRs and CSRRs. Therefore, they can function as sensors with a compact footprint. This chapter is dedicated to an application of metamaterial-inspired resonators to high-sensitivity microfluidic sensors. Towards this aim, two high-sensitivity microwave microfluidic sensors are introduced. Firstly, a microfluidic sensor is designed based on a microstrip-line-coupled CSRR for measuring the ethanol concentration in water solutions. Secondly, a complementary electric-LC resonator coupled with a microstrip line is investigated for determination of glucose concentration in water.

4.1 Introduction

Microwave dielectric spectrometry is appealing in many applications such as chemical sensing and biological sensing (Gregory and Clarke 2006, Catalá-Civera *et al.* 2003, Jenkins *et al.* 1990). The advantages of microwave dielectric characterisation lie in contactless, real-time, high sensitivity and label free detection (Rowe *et al.* 2013, Rowe *et al.* 2012, Grenier *et al.* 2009). Augmented by microfluidic technology, the approach is applicable to liquid samples that are highly relevant to biological and chemical studies.

Microwave characterisation of liquid samples has been performed by using different designs of microwave-based sensors including cavity resonators (Kim *et al.* 2008, Neshat *et al.* 2008, Kapilevich and Litvak 2011, Yu *et al.* 2000). These studies show a large sensitivity and precise detection with high quality factors. However, most of these devices are bulky and thus not compatible with integrated lab-on-a-chip technology. A key factor that enables on-chip integration is planar-profile sensors. A number of microwave planar sensors have been proposed for microfluidic chemical and biological sensing (Chretiennot *et al.* 2013, Grenier *et al.* 2009, Zarifi *et al.* 2015, Chahadih *et al.* 2015). In Chretiennot *et al.* (2013), coplanar waveguides and resonators have been used for microfluidic sensing. Microstrip stub resonators are incorporated in Zarifi *et al.* (2015) and Chahadih *et al.* (2015) for microwave chemical sensing. However, these planar resonators and structures usually show low quality factors and small fringing fields that need to be improved in dielectric sensing (Cui *et al.* 2013).

Recently, the concept of metamaterials has been adopted for microwave microfludic sensing to improve the sensitivity and compactness of the sensors (Horestani *et al.* 2013b, Naqui and Martín 2013). Metamaterial-inspired resonators such as split-ring and complementary split-ring resonators exhibit strong resonance in response to electromagnetic excitations. They offer strong field concentrations and high quality factors that are well suited for high-sensitivity dielectric characterisation (O´ Hara *et al.* 2012, Withayachumnankul *et al.* 2012). In addition, due their compact subwavelength structure, the metamaterial-based microwave microfluidic sensors provide a compact platform compatible with lab-on-a-chip technology.

To this end, this chapter presents two different configurations for microwave microfluidic sensors with improved sensitivity. In Section 4.2, the operation principle of the SRR-based microfluidic sensor will be explained. Section 4.3 presents a design of microfluidic sensor based on microstrip-line-coupled complementary split-ring resonator

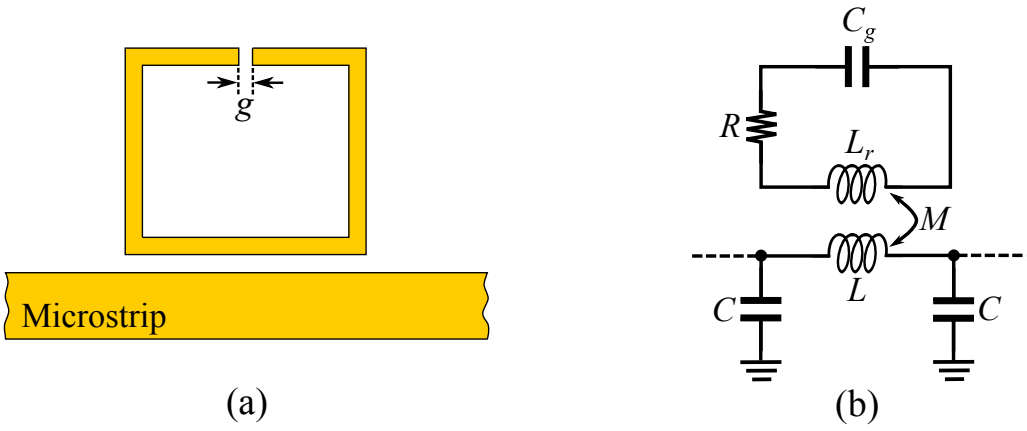

Figure 4.1. SRR-coupled microstrip line for microfluidic sensing. (a) Split-ring resonator-coupled microstrip line section. (b) Its lumped element equivalent circuit model. After Withayachumnankul *et al.* (2013).

(CSRR) with improved sensitivity. In Section 4.4, the microstrip-line-coupled complementary electric-LC resonator is proposed for compact and high-sensitivity measurement of glucose concentration in water solutions.

4.2 Operation principle of SRR-based microfluidic sensor

A basic schematic for a SRR-based microfluidic sensor is demonstrated in Fig. 4.1. As explained before, a single SRR will inhibit the wave propagation at its resonance frequency resulting in a bandstop notch in the transmission response of the structure as demonstrated in Fig. 4.2. The equivalent circuit model of the SRR-loaded microstrip line is given in Fig. 4.1(b), where the inductance L_r models the inductive effect of the SRR metallic ring, the C_g models the equivalent capacitance of the SRR in the gap area, R models the losses associated with the SRR, the L and C stand for per unit length inductance and capacitance of the microstrip transmission line respectively, and M is the mutual inductive coupling between the SRR and the microstrip line.

As shown in the inset of Fig. 4.2, at resonance there is a strong electric field along the gap area of SRR. This electric field is very sensitive to the dielectric property of the gap area. If the dielectric around the gap is changed or affected by some loading, it will cause a change in the value of the gap capacitance C_g that in turn results a change of SRR resonance frequency and the quality factor (Q) at resonance. The changes in the resonance frequency and quality factor can be detected in the transmission response (S_{21}) and used for characterising the loaded material.

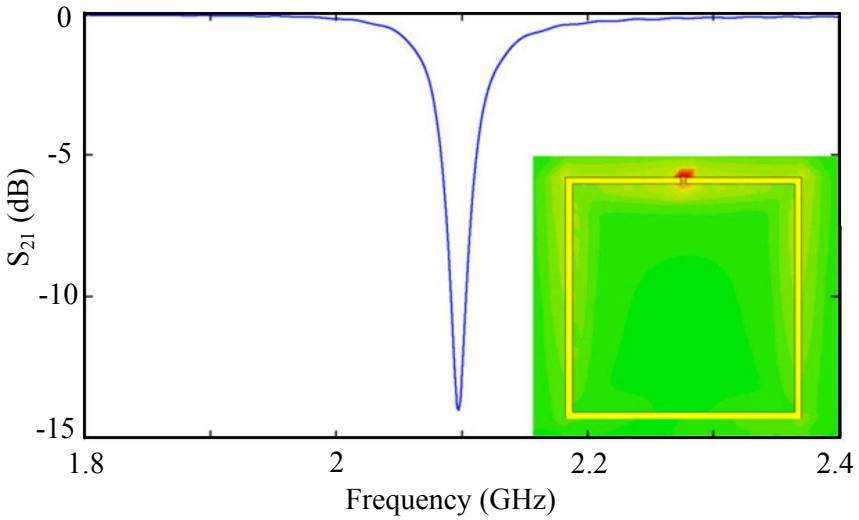

Figure 4.2. Simulated response of a SRR-coupled microstrip line section. Transmission response of a SRR-coupled microstrip section. (Inset) The field distribution of the SRR on resonance. After Withayachumnankul *et al.* (2013)

Figure 4.3. SRR-based microfluidic sensor. (a) Microfluidic channel fabricated in the gap area of the SRR. (b) The test setup for validating the SRR-based sensor concept. After Withayachumnankul *et al.* (2013)

Therefore, by including a microfluidic channel in the gap area of the SRR as in Fig. 4.3 and applying a liquid sample to the channel, the dielectric properties of the sample liquid can be measured by the sensor. The test setup for this sensor is demonstrated in Fig. 4.3(b). As seen, a change in the resonance properties is measured by a network analyser and used for characterisation.

A mixture of water-ethanol with different ethanol concentrations have been used for testing the sensor since it exhibits a broad range of dielectric constant between 10 and 80 suitable for sensor testing. The measured transmission responses for different ethanol volume fractions are shown in Fig. 4.4. As demonstrated in this figure, the

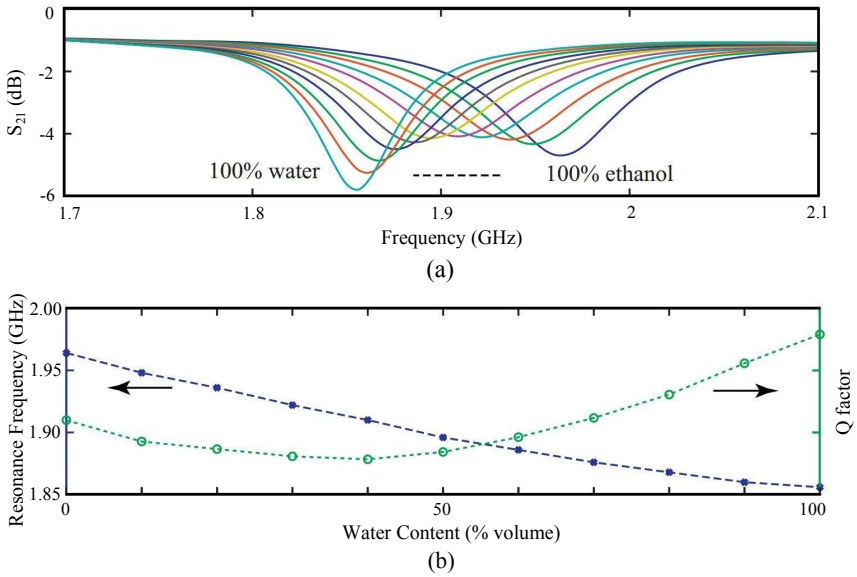

Figure 4.4. Measurement results of the SRR-based microwave microfluidic sensor. (a) Measured transmission responses of the SRR-based microfluidic sensor for different volume fractions of ethanol in water. (b) The measured resonance frequency and quality factors for different ethanol contents. After Withayachumnankul *et al.* (2013)

maximum frequency shift for the SRR-based sensor is 0.1 GHz. This frequency shift might not be sufficient to detect a small change in the ethanol volume fraction or a small change of the mixture dielectric constant. Thus, we have developed a sensor based on CSRR-coupled microstrip line than can provide a better detection resolution. The design principle and the results of the CSRR-based sensor are presented in Section 4.3.

4.3 Microfluidic sensor based on complementary split-ring resonator (CSRR)

This section is dedicated to a microfluidic sensor based on a microstrip-line-coupled complementary split-ring resonator (CSRR). The motivation is a compact structure compatible with the lab-on-a-chip technology with an improved device sensitivity in comparison with the conventional SRR-based microfluidic sensor. The new sensor is validated through experimental measurements. It is shown that the new structure shows four times better sensitivity with respect to the conventional SRR-based sensor.

4.3.1 Basics of CSRR-based microfluidic sensor

Here, a complementary split-ring resonator (CSRR) is used instead of a SRR, to provide a larger area of fringing electric field that increases the effective interaction area with the sample. The proposed sensor determines the complex permittivity of liquids based on changes in the resonance frequency and peak attenuation of the transmission response ($|S_{21}|_{\min}$) on resonance. The device is designed to operate at around 2 GHz and is compatible with lab-on-a-chip. So, it satisfies the need for low-cost and compact high sensitivity devices in microwave microfluidic applications.

The main part of the proposed sensor structure is a microstrip coupled CSRR as shown in Fig. 4.5(a). The CSRR is composed of a metallic capacitive plate that is connected through an inductive metallic path to the surrounding ground plane at a distance c from its edge. Since the CSRR is etched in the ground plane and is mainly excited by the electric field of the microstrip line, the whole coupled structure can be modelled by the lumped element circuit in Fig. 4.5(b) (Baena *et al.* 2005). In the equivalent circuit model, the parallel combination of L_C, C_C and R_C models the CSRR, where C_C stands for the capacitor between the square-shaped metallic plate and the ground plane, L_C stands for the inductance of the metallic inductive path of width g connecting the capacitive plate to the ground, and R_C models the equivalent loss associated with the CSRR (Bonache *et al.* 2006b). Here, L and C model the inductance and capacitance of the microstrip line, respectively.

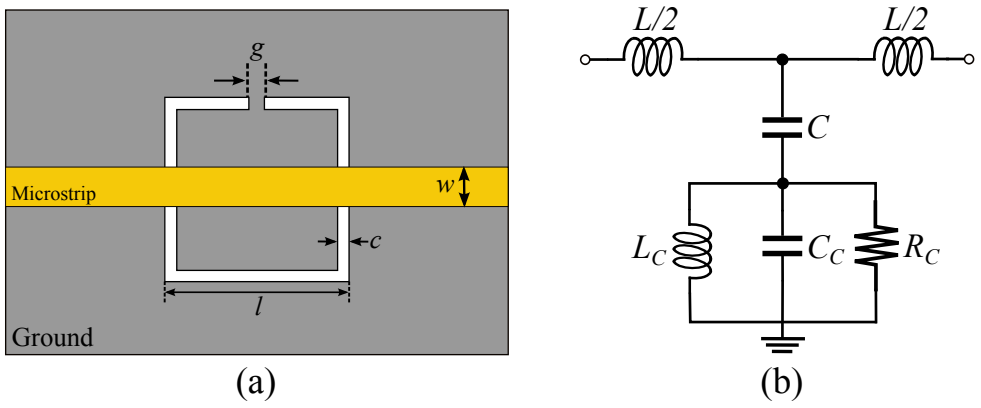

Figure 4.5. Basic schematic of the CSRR-based microfluidic sensor. (a) A microstrip coupled CSRR with the grey area showing the ground plane and yellow showing the top microstrip metalisation. (b) Its equivalent circuit model with L and C for the unit length inductance and capacitance of the microstrip respectively and $\{RLC\}_C$ for the CSRR. The CSRR and microstrip dimensions are: $w = 1.3$ mm, $l = 11$ mm, $c = 0.5$ mm and $g = 0.2$ mm.

When the microstrip is fed with a microwave signal, it develops a quasi-TEM electromagnetic wave propagation mode described by a magnetic field circulating around the microstrip and an electric field pointing towards the ground plane. This electric field excites the CSRR inducing a voltage difference between the capacitive plate and the ground plane. The resonance occurs when the electric energy stored in the C and C_C capcitors equals magnetic stored in the inductive strip of L_C. As shown in inset of Fig. 4.6, at resonance, a strong electric field will be established across the gap between the capacitive plate and ground. The electric field is stronger across the lower edge of the square-shaped CSRR making this region very sensitive to dielectric changes. Therefore, a microfliuidic channel is laid across the lower edge of the CSRR. The resonance can be observed as a notch in the transmission coefficient of the structure as illustrated in Fig. 4.6. From the circuit model of Fig. 4.5(b), the resonance frequency can be defined as (Bonache *et al.* 2006a)

$$f_0 = \frac{1}{2\pi\sqrt{L_C(C+C_C)}}, \tag{4.1}$$

and the quality factor of the resonance is

$$Q = R\sqrt{\frac{C+C_C}{L_C}}. \tag{4.2}$$

It is worth noting that the capacitor C_C is affected by the dielectric materials near the gap between the CSRR and the ground. So, it can be approximated by

$$C_C = C_0 + \epsilon_{\text{sam}} C_e, \tag{4.3}$$

where C_0 models the capacitive effects of the dielectric substrate, channel walls and surrounding space excluding the channel cavity and the term $\epsilon_{\text{sam}} C_e$ denotes the capacitive effect of the liquid sample loaded into the microfluidic channel. Here, C_e is the capacitance of the empty channel. Now, if the complex permittivity of the liquid sample is considered to be $\epsilon_{\text{sam}} = \epsilon'_{\text{sam}} + j\epsilon''_{\text{sam}}$, from (4.1)–(4.3), both of the resonance frequency and the quality factor will be a function of the liquid sample permittivity or

$$f_0 = F_1(\epsilon'_{\text{sam}}, \epsilon''_{\text{sam}}), Q = F_2(\epsilon'_{\text{sam}}, \epsilon''_{\text{sam}}). \tag{4.4}$$

The above discussion indicates that the resonance characteristics of the microstrip coupled CSRR device are dominated by the complex permittivity of a liquid sample. Therefore, by analysing this dependency, we can determine the complex permittivity of an unknown liquid sample simply by measuring the transmission resonance characteristics.

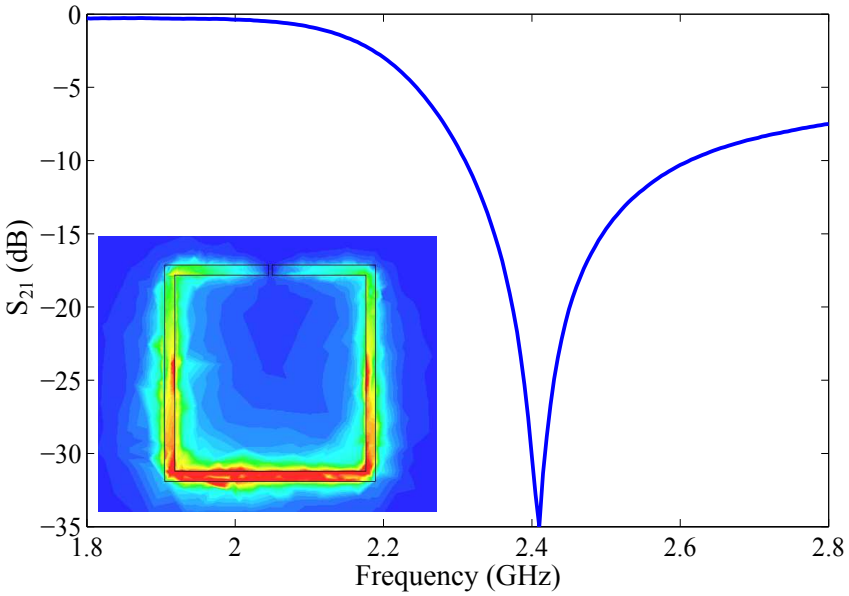

Figure 4.6. Simulated transmission response of CSRR-loaded microstrip line. Simulated resonance of the microstrip coupled CSRR of Fig. 4.5 in CST microwave studio. The resonance appears as a transmission zero in S_{21} around 2.4 GHz. (Inset) A strong electric field is established between the capacitive plate and the ground plane at resonance.

4.3.2 Fabrication process

The designed device has been fabricated on Rogers RO6002 microwave substrate with a relative permittivity of 2.94 for allowing significant fringing field in the sensing area and hence increasing the sensitivity. The substrate thickness is 0.508 mm. The copper metalisation for the ground plane and 50 Ω microstrip line is 18 μm.

As mentioned before, the microfluidic channel is positioned along the lower edge of the CSRR. The microfluidic channel is made of polydimethylsiloxane (PDMS) since it is inexpensive, widely available, biocompatible, durable, and easy to process (Grenier *et al.* 2009, Chretiennot *et al.* 2013). For channel fabrication, a mold has been prepared on a silicon substrate by using a thick photoresist mask and chemical etching. Then, a PDMS layer is deposited on the prepared mold and cured at 80°C. Finally, the PDMS channel is peeled off and attached to the microstrip coupled CSRR. The channel is manually positioned to the lower side of CSRR where the fringing electric field is strongest and therefore, the sensitivity to the dielectric property changes is maximum. The height, width and length of the channel are 0.06 mm, 0.7 mm and 14 mm, respectively. Fig. 4.7 shows the bottom view and cross-section of the structure when the channel is attached to the substrate.

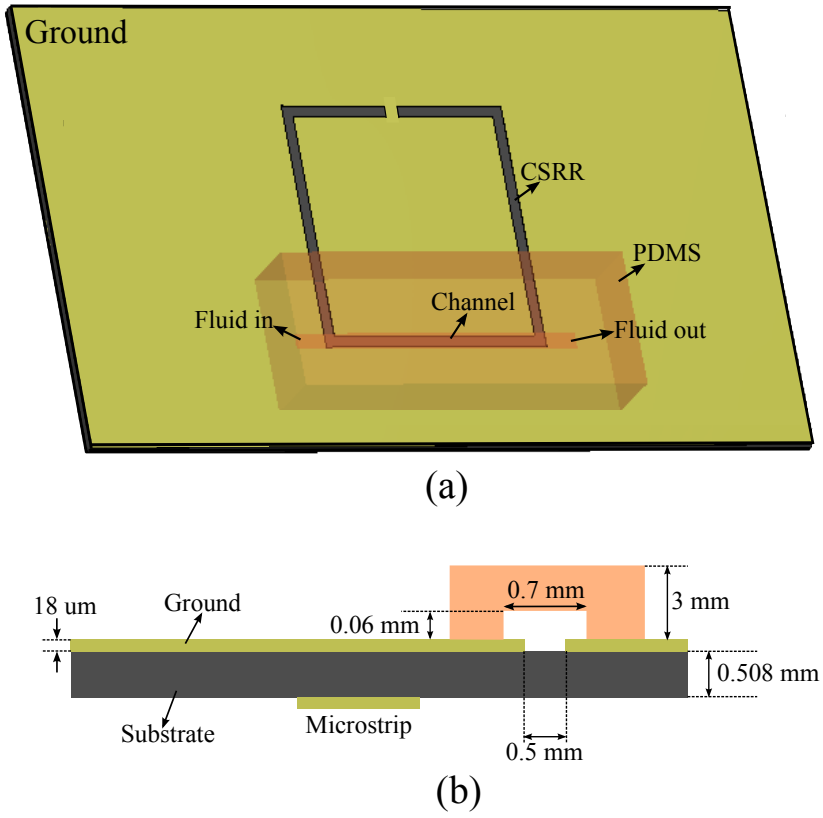

Figure 4.7. Three dimensional view of the designed sensor with microfluidic chamber. Schematic of the microstrip coupled CSRR with the PDMS microfluidic channel (a) Perspective view of the structure (b) Side view with dimensions.

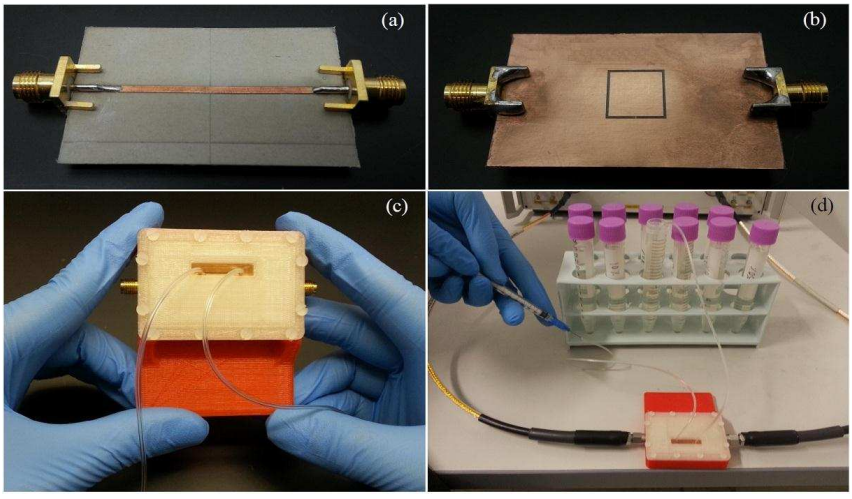

Figure 4.8. Fabricated sensor prototype. (a) Top view of bare CSRR. (b) Bottom view of bare CSRR. (c) The complete sensor module when the PDMS channel and inlet/outlet tubes are attached and the device is packaged. (d) The complete test setup when the device is connected to the network analyser for measurments.

The PDMS channel ensures a constant volume and shape of the liquid sample across the sensing area. The PDMS chamber is mechanically fixed onto the sensor by using a 3D-printed plastic package as shown in Fig. 4.8(c). It should be mentioned that the device response might be influenced by the position of the channel but it should not be an issue since the channel position is kept unchanged during all measurements. Similarly to Withayachumnankul *et al.* (2013), the measurements are carried out based on a stop-flow technique. A binary solution of distilled water and ethanol is used as a test sample since it provides a broad range of the complex permittivity at the low microwave frequency range (Bao *et al.* 1996). Teflon tubes, together with a syringe, connected to the inlet and outlet of the channel are used for filling and draining the channel. During the measurements, a very low pressure is applied to the syringe to avoid channel deformation. In each step, the channel is firstly filled with the liquid sample and then the flow is stopped for measurement. The resonance frequency and peak attenuation parameters are then recorded to characterise the liquid test samples. As seen in Fig. 4.9, the resonance frequency and peak attenuation are maximum when the channel is not attached to the sensor. By adding the PDMS channel, the resonance frequency is shifted down with a small decrease of peak attenuation since a part of the CSRR is covered with the PDMS.

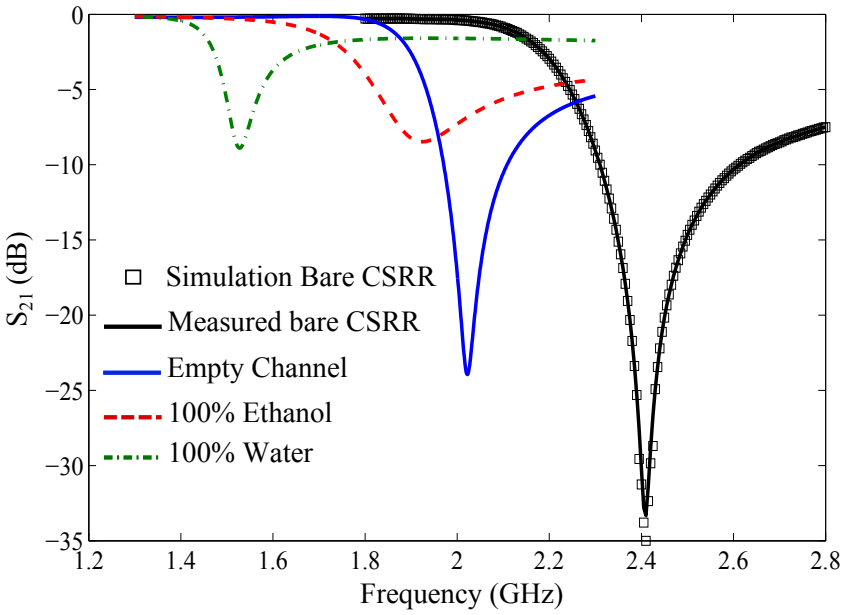

Figure 4.9. Sensor transmission responses. Simulated and measured transmission response of the sensor in different conditions.

Table 4.1. Permittivity of water-ethanol mixture. Complex permittivity of water-etahnol mixture at 1.9 GHz. The volume fraction of water is changed from 10% to 90% for device testing.

Water Fraction(%)	ϵ'	ϵ''	$\Delta\epsilon'$	$\Delta\epsilon''$
10	16.5	12.3	-30.5	-2.7
30	31.5	15.55	-15.5	0.55
50	47	15	0	0
70	61	12.8	14	-2.2
90	72	10.6	25	-4.4

4.3.3 Calibration of the sensor

For investigating the effect of the complex permittivity $(\epsilon'_{\text{sam}} + j\epsilon''_{\text{sam}})$ on the resonance frequency and peak attenuation, a set of experiments has been performed using binary mixtures of distilled water and ethanol. The dielectric properties of water-ethanol mixture was accurately studied in Bao *et al.* (1996). The accurate complex permittivity of the test fluid samples from Bao *et al.* (1996) are listed in Table 4.1. For the first set of measurements, the volume fraction of water is changed from 10% to 90% with a step size of 20% and at each step, the resonance frequency and peak attenuation of the sensor are recorded giving a data set of 5 samples. The measurement results of the resonance frequency and maximum attenuation for the 5 test samples are shown in Fig. 4.10. As seen, the resonance frequency is shifted from 1.875 GHz down to 1.57 GHz as the water volume fraction increases from 10% to 90%. The peak attenuation is minimum when the water volume fraction is 30%. It is worth noting that the observed nonlinearity in the peak attenuation with respect to the water content follows the nonlinear loss function of water mixture (Withayachumnankul *et al.* 2013, Bao *et al.* 1996).

Based on the measurement results of the five test samples, an approximated is derived for resonance frequency shift and peak attenuation variations as a function of the complex permittivity. This simplified model can be defined as

$$\begin{bmatrix} \Delta f_0 \\ \Delta|S_{21}| \end{bmatrix} = \begin{bmatrix} m_{11} & m_{12} \\ m_{21} & m_{22} \end{bmatrix} \begin{bmatrix} \Delta\epsilon'_{\text{sam}} \\ \Delta\epsilon''_{\text{sam}} \end{bmatrix}, \tag{4.5}$$

where $\Delta\epsilon'_{\text{sam}} = \epsilon'_{\text{sam}} - \epsilon'_{\text{ref}}$, $\Delta\epsilon''_{\text{sam}} = \epsilon''_{\text{sam}} - \epsilon''_{\text{ref}}$ and $\Delta f_0 = f_{0,\text{sam}} - f_{0,\text{ref}}$ with subscript 'sam' for the sample under test and 'ref' for the reference mixture. Here, the mixture with a 50% water fraction is considered as the reference. The unknown parameters

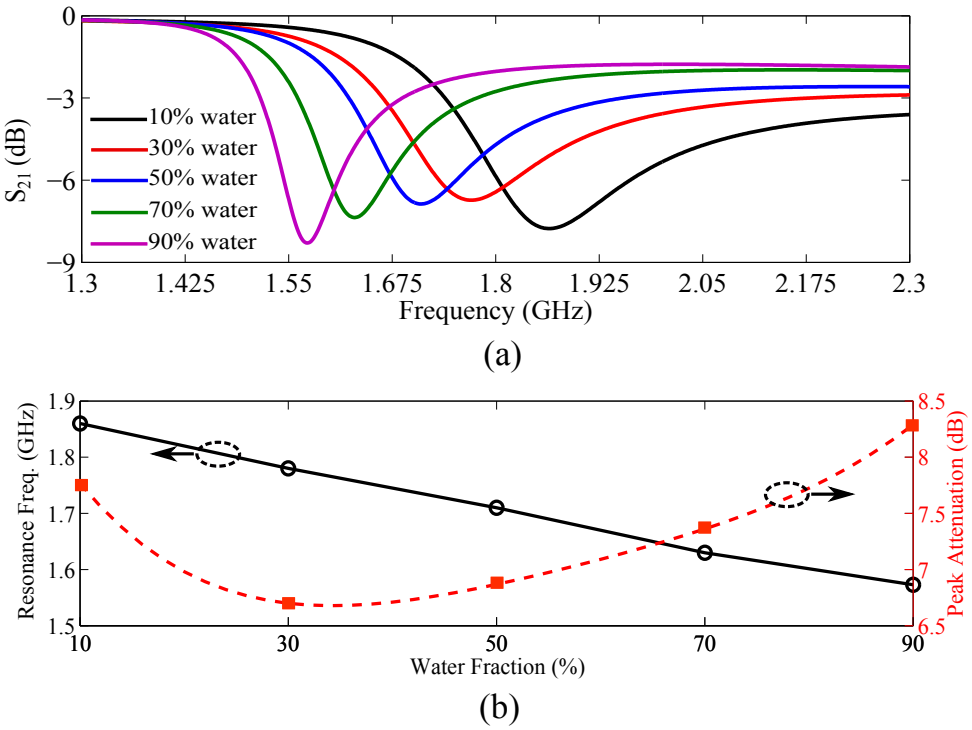

Figure 4.10. Measurement results for sensor calibration. (a) The measured transmission response of the water-ethanol test samples for calibration of the sensor. The water volume fraction is changed from 10% to 90% with the step size of 20%. (b) Corresponding resonance frequency and peak attenuation at different steps with solid and dashed line for visual guidance.

of the matrix can be determined from the data available from the measurement results of Fig. 4.10, together with the reported complex permittivity in Table 4.1. The benefit of this model is that all the fabrication tolerances of the device are fully taken into account. The coefficients of the model in (4.5) are over-determined by test datasets. So, the least-squares method explained in Withayachumnankul *et al.* (2013) can be used to approximate the coefficients. This method yields the following matrix that relates the resonance frequency and maximum attenuation changes to the complex permittivity

$$\begin{bmatrix} \Delta f_0 \\ \Delta|S_{21}| \end{bmatrix} = \begin{bmatrix} -0.00528 & 0.000256 \\ -0.00045 & -0.292 \end{bmatrix} \begin{bmatrix} \Delta\epsilon'_{\text{sam}} \\ \Delta\epsilon''_{\text{sam}} \end{bmatrix}. \tag{4.6}$$

By comparing the coefficients in (4.6), it is found that the effect of ϵ' on the resonance frequency is approximately 20 times larger than the effect of ϵ''. On the other hand,

the impact of ϵ'' on the peak attenuation is 650 times higher than the influence of ϵ'. Considering the samples of Table 4.1

$$\left|\frac{\Delta\epsilon'}{\Delta\epsilon''}\right|_{\max} \approx 28, \qquad \left|\frac{\Delta\epsilon''}{\Delta\epsilon'}\right|_{\max} \approx 0.176. \tag{4.7}$$

So, by neglecting m_{12} and m_{21} the maximum errors in Δf_0 is

$$\left|\frac{m_{12}\Delta\epsilon''}{m_{11}\Delta\epsilon'}\right|_{\max} \approx 0.9\%, \tag{4.8}$$

and the maximum error in $\Delta|S_{21}|$ can be obtained as

$$\left|\frac{m_{21}\Delta\epsilon'}{m_{22}\Delta\epsilon''}\right|_{\max} \approx 4.3\%. \tag{4.9}$$

From (4.8) and (4.9) it can be inferred that the contributions of ϵ'' on the resonance frequency shift and ϵ' on the peak attenuation changes are negligible. So, the characteristic matrix of (4.6) can be simplified as

$$\begin{bmatrix} \Delta f_0 \\ \Delta|S_{21}| \end{bmatrix} = \begin{bmatrix} -0.00528 & 0 \\ 0 & -0.292 \end{bmatrix} \begin{bmatrix} \Delta\epsilon'_{\text{sam}} \\ \Delta\epsilon''_{\text{sam}} \end{bmatrix}. \tag{4.10}$$

The complex permittivity of unknown liquid samples can be determined using matrix inversion. Inverting (4.10) leads to

$$\begin{bmatrix} \Delta\epsilon'_{\text{sam}} \\ \Delta\epsilon''_{\text{sam}} \end{bmatrix} = \begin{bmatrix} -189.39 & 0 \\ 0 & -3.424 \end{bmatrix} \begin{bmatrix} \Delta f_0 \\ \Delta|S_{21}| \end{bmatrix}, \tag{4.11}$$

which can be used for determining the complex permittivity of unknown liquid samples from the resonance characteristics.

4.3.4 Validation of the sensing concept

In order to verify the sensor performance together with the parameter retrieval model in (4.11), the water ethanol mixture is used again. This time, the volume fraction of water is changed from 0% to 100% with the step size of 20% giving a dataset of 6 measurements. The measured transmission responses of the sensor for these sets of samples are shown in Fig. 4.11 together with the extracted resonance frequency and peak attenuation. As seen, the corresponding frequency shift for 0%–100% of the water

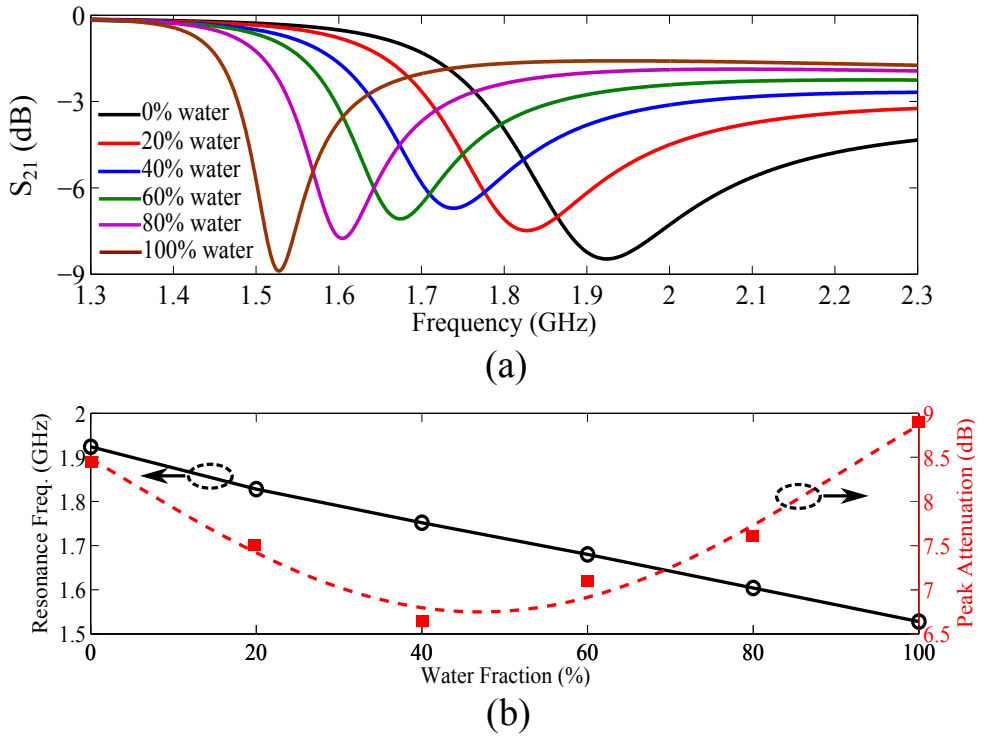

Figure 4.11. Measurements for validating the sensing concept. (a) The measured transmission response of the water-ethanol test samples for validating the (4.11) model. The water volume fraction is changed from 20% to 100% with the step size of 20%. (b) Corresponding resonance frequency and peak attenuation at different steps with solid and dashed line for visual guidance.

volume fraction is around 400 MHz, showing 4 times higher sensitivity with respect to SRR-based sensor with a 100 MHz frequency shift. The model presented in (4.11) is used to determine the $\Delta\epsilon'$ and $\Delta\epsilon''$ for each mixture from a pair of the resonance frequency and peak attenuation, where 50% water-ethanol mixture is considered as the reference. Then, the complex permittivity of each sample can be calculated as

$$\epsilon'_{\text{sam}} = \epsilon'_{\text{ref}} + \Delta\epsilon'_{\text{sam}}, \tag{4.12}$$

$$\epsilon''_{\text{sam}} = \epsilon''_{\text{ref}} + \Delta\epsilon''_{\text{sam}}, \tag{4.13}$$

with a subscript 'sam' for the values obtained from (4.11). For comparison, the obtained complex permittivity values of the samples are plotted against the exact values in Fig. 4.12. This figure shows an acceptable accuracy of the simplified model of (4.11).

Table 4.2. Permittivity of water-ethanol mixture. Complex permittivity of water-ethanol mixture at 1.9 GHz. The volume fraction of water is changed from 0% to 100%.

Water Fraction(%)	ϵ'	ϵ''	$\Delta\epsilon'$	$\Delta\epsilon''$
0	9	10	-38	-5
20	24	13.6	-23	-1.4
40	39	15.6	-8	0.6
60	53	14.6	6	-0.4
80	67	13.4	20	-1.6
100	79.5	9	32.5	-6

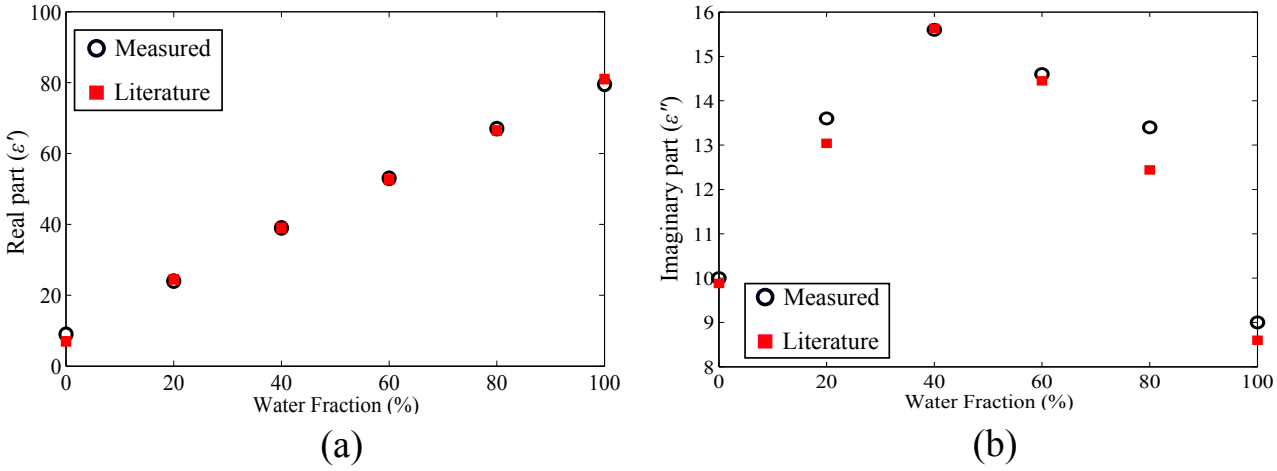

Figure 4.12. Measured and actual values of the complex permittivity. Comparison between the measured and litrature values of complex permittivity for the water-ethanol mixture at around 1.9 GHz. The volume fraction of water is changed from 0% to 100% with the step size of 20%. (a) Real part of the complex permittivity. (b) Imaginary part of the complex permittivity.

The small disagreements between the measured and literature values of complex permittivity may arise from the measurement uncertainties or the simplified linear approximation of the sensing model. The accuracy can be increased by using a higher-order approximation. The device can also be tested with other sets of liquid samples covering wider ranges of complex permittivity values to produce a more accurate sensing model.

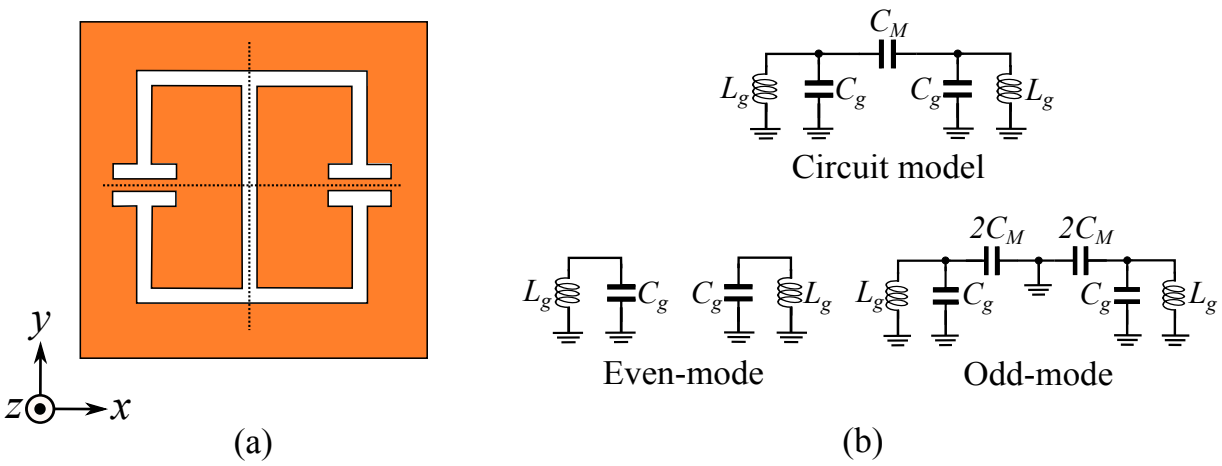

Figure 4.13. Type-2 complementary electric-LC (CELC2) resonator. (a) The resonator structure with the ground plane shown in orange. (b) The corresponding equivalent circuit model with the even and odd mode resonances.

4.4 Microfluidic sensor for determination of glucose content in water solutions

In Section 4.3, the application of complementary split-ring resonator (CSRR) in improving the sensitivity of microfluidic sensors has been discussed. This section presents a microwave microfluidic biosensor based on a complementary electric-LC (CELC) resonator excited by a microstrip line that is introduced in Chapter 3 (Ebrahimi *et al.* 2014f). The dual-mode nature of CELC resonator allows designing an even more compact structure because of a large capacitive effect in the odd mode. Here, it is demonstrated that by positioning a microfluidic channel in the middle part of the CELC resonator and filling the channel with water-glucose solution, the transmission characteristics of the device (S_{21}) are modified and can be used for quantifying the glucose concentration in the solution.

4.4.1 Structure of the sensor

A main part in this sensor is the type-2 complementary electric-LC (CELC2) resonator discussed in Chapter 3. The CELC2 resonator in Fig. 4.13(a) can be modelled by the circuit in Fig. 4.13(b), where C_g models the capacitive effect between each halve of the CELC resonator and the surrounding ground plane. The L_g inductors model the inductance of the metallic strips that connect the halves to the ground. The C_M stands for the mutual capacitive effect between the two halves of the CELC resonator. Based on

the equivalent circuit, the CELC resonator exhibits the even and odd mode resonances with the equivalent circuits shown in Fig. 4.13(b) (Ebrahimi *et al.* 2014a, Ebrahimi *et al.* 2014f).

Now, if a CELC2 resonator is loaded on a microstrip line as in Fig. 4.14(a), the equivalent circuit model of the whole structure can be given as Fig. 4.14(b). In Fig. 4.14(b), the L inductors stand for the inductance associated with the microstrip and C_1 and C_2 present the coupling capacitances between the microstrip and the CELC resonator. In Fig. 4.14(a) the sides of the CELC resonator are meandered for compactness. Here, the microstrip is widened in its middle part for a more symmetric S_{21} around the odd mode resonance.

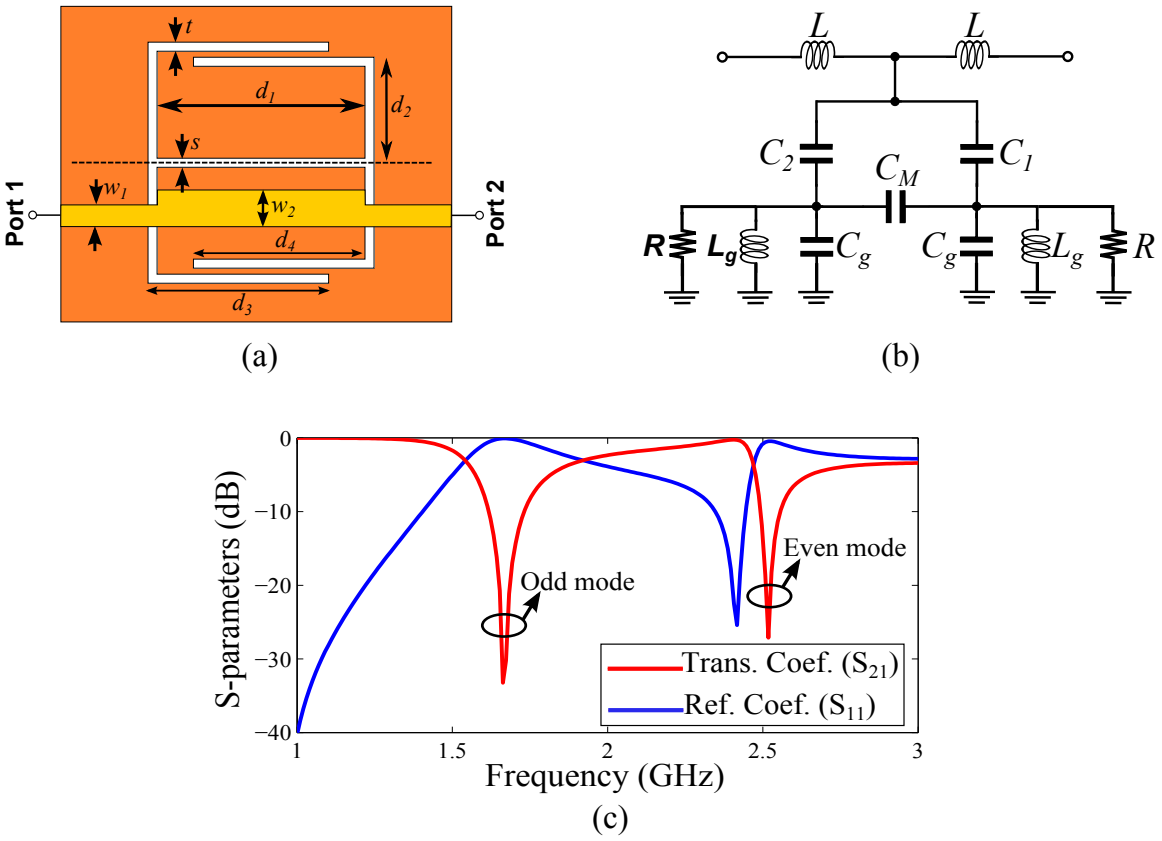

Figure 4.14. Microstrip loaded CELC2 resonator. (a) Schematic of the structure where the microstrip is shifted with respect to the symmetry line of the CELC. (b) Its equivalent circuit model. (c) S-parameters of the structure. The dimensions are: $w_1 = 1.3$ mm, $w_2 = 1.9$ mm, $t = 0.3$ mm, $s = 0.5$ mm, $d_1 = 10.4$ mm, $d_2 = 5.55$ mm and $d_3 = d_4 = 9$ mm. The microstrip metallisation is shown with yellow and the ground is indicated in orange.

As explained in Chapter 3, if the microstrip is displaced with respect to the symmetry line of the resonator, both of the even and odd mode resonances will be excited to produce two bandstop notches in the transmission response of the structure as shown in Fig. 4.14(c). From Fig. 4.13(b), the odd mode resonance frequency is strongly dependent on the C_M value and any changes in C_M would be translated to a shift in the odd mode resonance frequency (Ebrahimi *et al.* 2014f). Here, we use this property for designing a microfluidic sensor by loading a microfluidic channel between the two halves of the CELC resonator. By introducing a liquid sample into the channel, the dielectric property of the occupied area will be changed resulting in a variation of C_M that in turn affects the odd mode notch frequency and depth. This change in resonance can be measured for characterising the liquid sample inside the channel.

4.4.2 Test setup and experimental verification

A prototype of the designed sensor is fabricated on Rogers RO6002 substrate with a low relative permittivity of 2.94. The substrate thickness is 0.508 mm. The sensor dimensions are given in Fig. 4.14. The microfluidic channel is made of PDMS using micro-fabrication technology. The channel height, width and length are 0.06 mm, 0.7 mm and 15 mm respectively. The channel has been precisely aligned with the sensing area and mechanically pressed against the substrate for ensuring the consistency of the volume and shape of the solution over the sensing area. Fig. 4.15 shows the top and bottom views and the final assembled prototype of the fabricated microfluidic sensor.

Measurements have been carried out to verify the proposed biosensing concept based on a stop-flow method. Two flexible Teflon tubes with a syringe connected to the inlet/outlet of the channel are used for filling and draining liquid solutions. As mentioned before, the changes in the odd mode resonance are used here for sensing since the channel is applied to the middle part of the resonator between the two halves. For each sample measurement, the channel is firstly filled with the test liquid and the corresponding transmission coefficient is recorded for analysis. In Fig. 4.16, the transmission coefficient (S_{21}) of the sensor is plotted for three different cases: the bare resonator, the resonator with empty channel and with pure water filled channel. As seen, by adding the channel and filling it with the liquid sample, the resonance frequency is shifted down with a decrease in the peak attenuation.

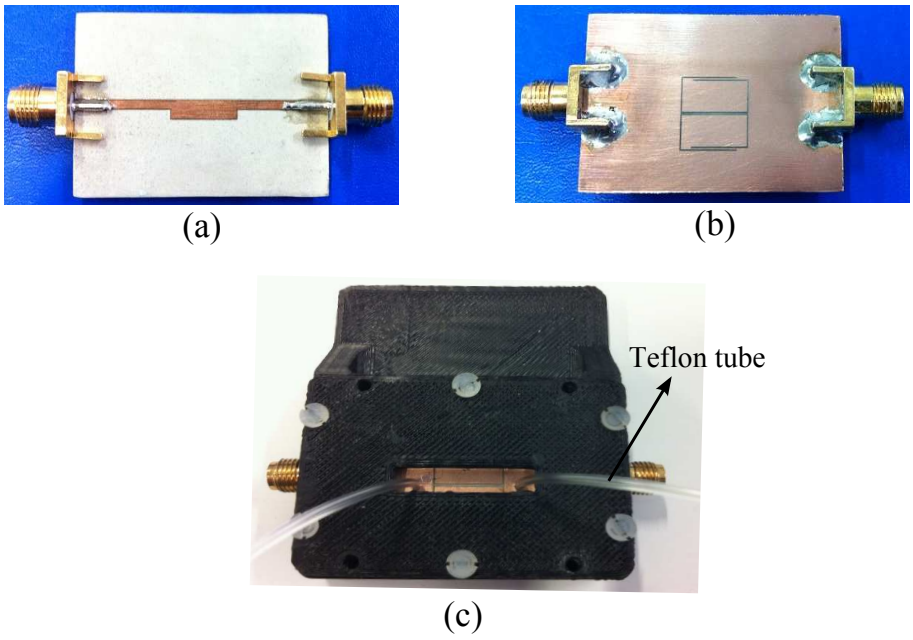

Figure 4.15. Fabricated microfluidic biosensor. (a) Top view. (b) Bottom view. (c) The final assembled sensor with the microfluidic PDMS channel and the Teflon tubes added to the inlet and outlet.

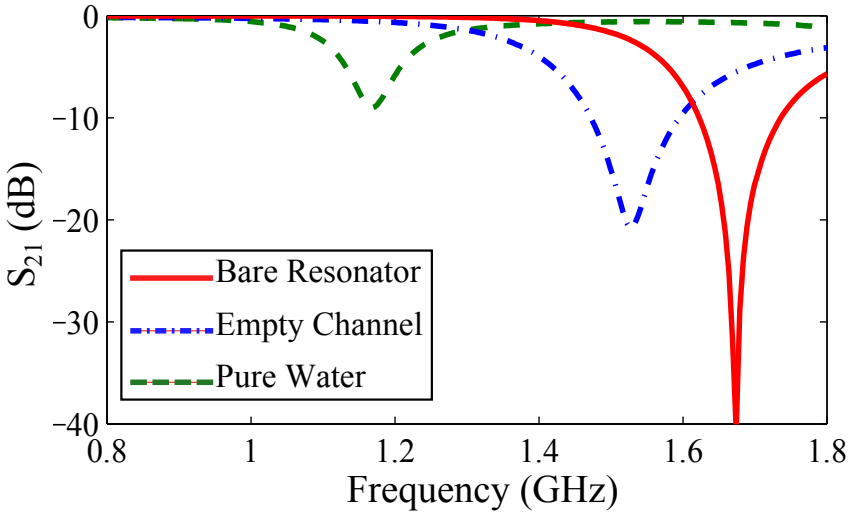

Figure 4.16. Measured transmission response of the sensor for different cases. Measured transmission response (S_{21}) of the sensor around the odd mode resonance for three different cases: the bare resonator, the resonator with empty channel and with water filled channel.

In order to test the sensor, the water-glucose solutions have been prepared with 20, 40, 60, 80 and 100 mg/mL glucose concentrations (Hofmann *et al.* 2013). The sensor transmission coefficient is recorded for each sample. The measured S_{21} profiles for these samples are demonstrated in Fig. 4.17(a). For pure water, the resonance frequency is

1.16 GHz. The resonance frequency shifts up by increasing the glucose concentration. This is mainly because of a decrease in the relative permittivity of the solution that results in smaller capacitance (C_M) around the sensing area. The resonance frequency shift as a function of the glucose concentration is shown in Fig. 4.17(b) where the resonance frequency of the pure water is considered as a reference. The regression analysis proves a good linear dependency ($r^2 = 0.995$) of the resonance frequency shift to the glucose concentration as

$$\Delta f_{\mathrm{r}} = 2.11\rho, \tag{4.14}$$

where Δf_r is the resonance frequency shift in MHz, ρ is the glucose concentration in mg/mL. Therefore, the glucose concentration can be determined based on the frequency shift using

$$\rho = 0.474\Delta f_{\mathrm{r}}. \tag{4.15}$$

For verification of the above mathematical model, the sensor is tested again with the water-glucose solutions with 10, 30, 50, 70 and 90 mg/mL glucose concentrations. The transmission responses of the senor for these samples are plotted in Fig. 4.18 versus frequency. The model in (4.15) is used for prediction of the glucose concentration based on the frequency shift. The measured glucose concentration and the actual values are plotted together in Fig. 4.19 for comparison. This result proves a good accuracy of the proposed sensor. The errors might be due to the simplified model in (4.15) or the measurement uncertainties. The measurement accuracy may be improved by considering the peak attenuation in sensor modelling in conjucntion with the resonance shift.

4.5 Conclusion

This chapter has presented two metamaterial-inspired microwave microfluidic sensors. The first sensor was made of microstrip-line-loaded CSRR resonator. By using the CSRR instead of SRR to increase the fringing electric field, the sensitivity can be improved by four times. Binary mixtures of water-ethanol have been used for testing and verification of the sensing concept, and a linear sensing model has been developed for characterisation of the liquid samples. The measurements demonstrated the

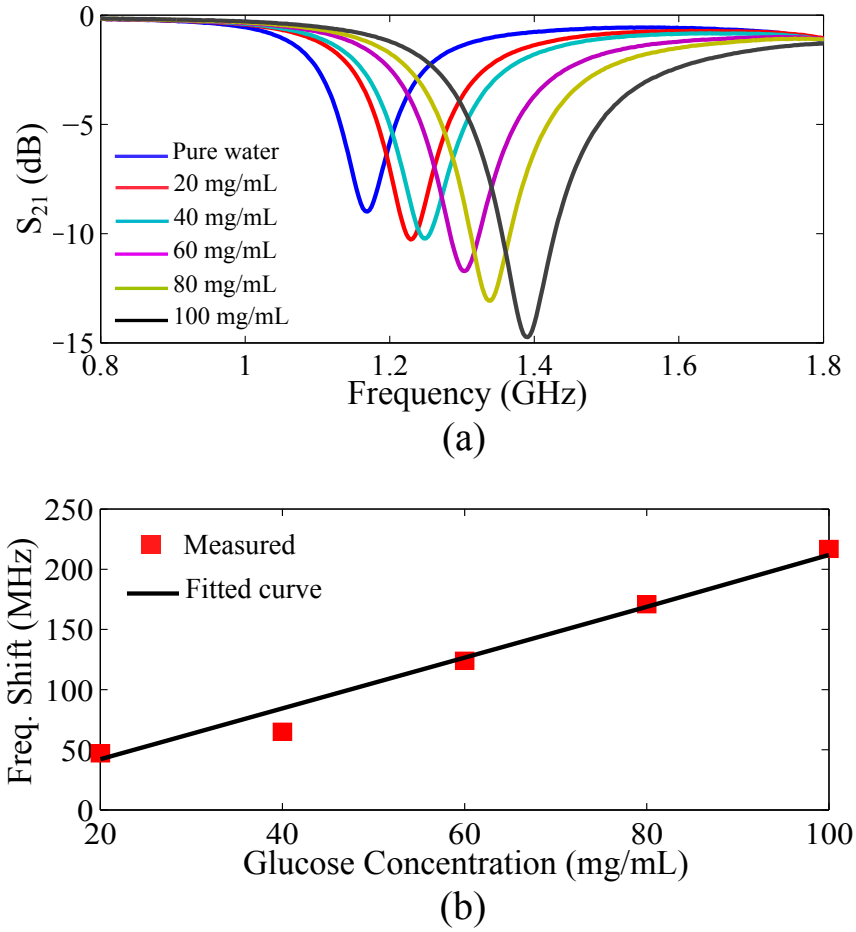

Figure 4.17. Measured resonance characteristics. (a) Measured transmission responses of the sensor for water-glucose solutions with different glucose concentrations. (b) The resonance frequency variation as a function of glucose concentration, where the pure water is considered as the reference.

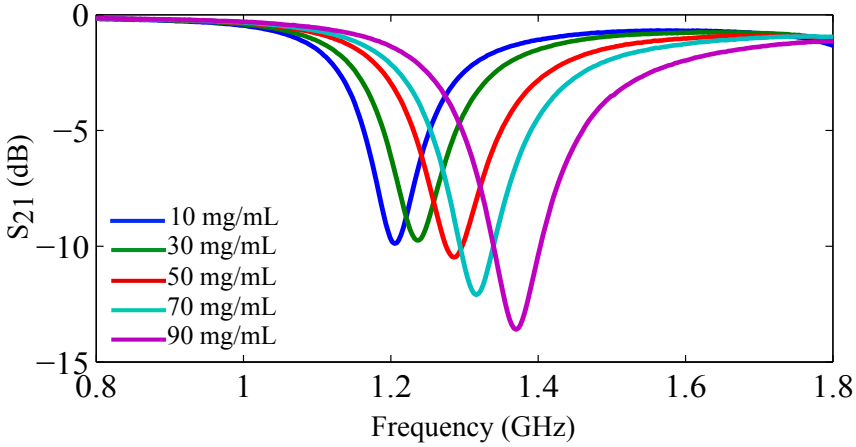

Figure 4.18. Verification of the sensing model. Measured transmission responses of the sensor for water-glucose solutions for validation of (4.15).

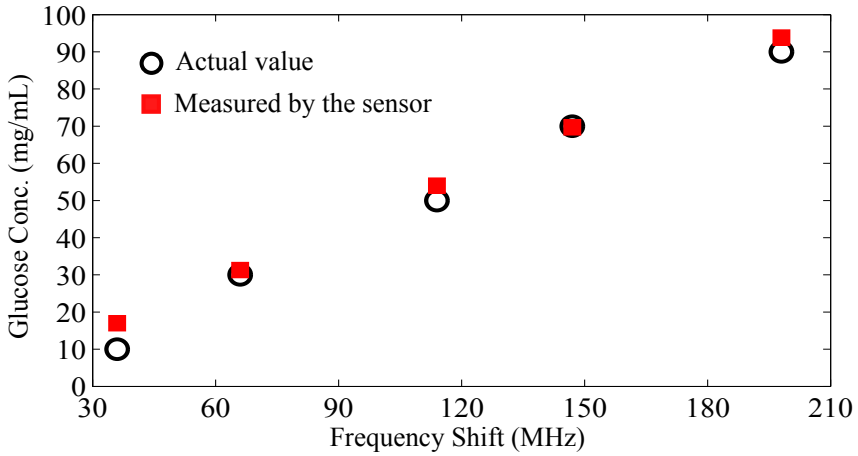

Figure 4.19. Comparison between the the retrieved and actual glucose concentrations. Comparison between the concentration values obtained by the sensor and the actual glucose concentrations.

good accuracy of the sensor in dielectric characterisation of the liquid samples at low microwave frequencies.

A CELC-based microfluidic sensor has been designed and tested. The CELC resonator result in a compacter size because of the larger capacitance in the odd mode resonance. This sensor has been tested with binary mixtures of water and glucose. Again, a simple linear model has been developed for the sensor for measurement of glucose concentration in water solutions. The measurements proved the accuracy of the device for glucose sensing.

The use of microfluidic channel in both cases enabled the microfluidic sensing with a little amount of liquid sample where the cross-section of the sensing area is smaller than $2 \times 10^{-5}\lambda_0^2$ where, λ_0 is the operational guided wavelength. The compact designs promise the potential of the designed sensors for integration in lab-on-a-chip technology.

Chapter 5

Metamaterial-inspired rotation and displacement sensors

ON resonance, metamaterial-inspired resonators will provide localised electromagnetic fields that are very sensitive to variations in dielectric properties and their geometries. The sensitivity to the geometry can be used to design displacement and rotation detectors. To this end, in this chapter, the coupling between two coupled U-shaped resonators is used to design a rotation sensor with a wide dynamic range. In addition, the odd mode resonance in the complementary electric-LC resonator coupled with a microstrip line is used to design a displacement sensor. The sensing principle of the designed structures is analysed by circuit model analysis and full-wave electromagnetic simulations, and validated through measurement of the fabricated sensor prototypes.

5.1 Introduction

Split-ring resonators (SRRs) and their complementary structures called complementary split-ring resonators (CSRR) have been used to design many new or improved electromagnetic structures such as artificial electromagnetic media (Smith *et al.* 2000, Schurig *et al.* 2006), composite left/right hand transmission lines (Falcone *et al.* 2004a, Martín *et al.* 2003a, Gil *et al.* 2006a), filters (Bonache *et al.* 2006a, Horestani *et al.* 2014b, Horestani *et al.* 2014a), antennas (Pucci *et al.* 2012, Takemura 2013, Alici and Ozbay 2007). Beyond these common applications, recently, they have attracted great attention to be used in designing new electromagnetic-based sensing structures (Zheludev 2010). This is mainly due to the exceptional sensitivity of these resonators with respect to environmental or geometrical changes in their structures. So, metamaterial-inspired sensing has become one promising application of metamaterials (Chen *et al.* 2012).

Many configuration of metamaterial-based sensors have been developed up to now for different purposes such as strain sensing (Melik *et al.* 2009b, Melik *et al.* 2009a, Li *et al.* 2011), microwave mass flow sensing (Angelovski *et al.* 2011, Penirschke *et al.* 2007), biomedical sensing (Lee *et al.* 2008, Lee *et al.* 2012), and chemical microfluidic sensing (Boybay *et al.* 2013, Abduljabar *et al.* 2014, Rowe *et al.* 2014).

In Chapter 4, we have presented two high-sensitivity microfluidic sensors for chemical and biological sensing (Ebrahimi *et al.* 2014c). The focus of this chapter is on rotation and displacement sensing based on metamaterials. To this end, a wide dynamic range rotation sensor is introduced in Section 5.3 the variation in the coupling coefficient of the two U-shaped resonators is exploited for rotation detection (Ebrahimi *et al.* 2014d). In Section 5.4, a displacement sensor is designed by using the microstrip-line-coupled CELC2 resonator introduced in Chapter 3. The operation principle and validation of the proposed rotation and displacement sensors will be presented throughout this chapter.

5.2 Fundamentals

As mentioned before, SRR arrays can be used for planar transmission lines for designing artificial transmission lines. In addition, a single SRR coupled with a planar transmission line can provide a bandpass or bandstop transmission response depending on the geometry in vicinity of the SRR resonance frequency (Bonache *et al.* 2006b).

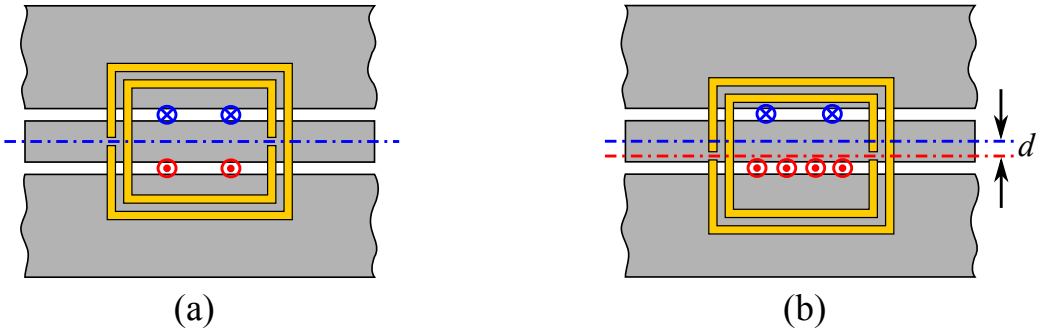

Figure 5.1. Coplanar waveguide loaded with a single SRR for displacement sensing. (a) The symmetry axis of SRR is aligned with the symmetry axis of the coplanar waveguide. (b) The symmetry line of SRR is displaced with respect to the symmetry axis of coplanar waveguide. The SRR metallisation is shown in yellow and the coplanar waveguide metallisation is indicated in grey. After Horestani *et al.* (2013b).

This characteristic has been applied to designing different bandpass or bandstop filters (Gil *et al.* 2007a, Bouyge *et al.* 2011, Vélez *et al.* 2013, Vélez *et al.* 2010). Furthermore, the symmetry property of the single SRR loaded with a transmission line is used for implementation of displacement or rotation sensors (Naqui *et al.* 2011, Naqui *et al.* 2012). The idea behind these designs is explained through Fig. 5.1.

As shown in Fig. 5.1(a), when the symmetry axis of the SRR is aligned with the symmetry axis of the CPW, the total magnetic flux passing through the SRR is zero and the SRR will not be excited. In this condition the transmission property of the CPW is not altered by the presence of the SRR. However, if the symmetry is broken by displacing the resonator with respect to the CPW as shown in Fig. 5.1(b), there will be a net magnetic flux through the surface of the SRR and the SRR will be excited causing a spectral notch in the transmission response of the structure. By increasing the displacement of the SRR with respect to the CPW, the depth of this transmission notch will increase and this phenomenon can be used to quantifying the amount of displacement. A rotation sensor can be developed by using the same principle but with a circular SRR instead of the rectangular SRR.

In spite of the high sensitivity to a very small amount of rotation and displacement, the SRR-loaded CPW has a number of limitations such as a small dynamic range and the shift in the resonance frequency as a result of displacement or rotation. The latter has been addressed in Horestani *et al.* (2013b) by using a tapered diamond shaped SRR for a displacement sensor and a horn-shaped SRR for a rotation sensor (Horestani *et al.*

2013a). The dynamic range of the rotation sensor has been increased up to 90° by using a circular ELC resonator in Naqui and Martín (2013).

In following, a rotation sensor based on coupled U-shaped resonators will be introduced that improves the dynamic range up to 180°. Additionally, a wide dynamic range displacement sensor based on a CELC2 resonator loaded with a microstrip line is proposed. The sensor configurations, analysis and measurement results of the fabricated prototypes will be presented in Section 5.3 and Section 5.4.

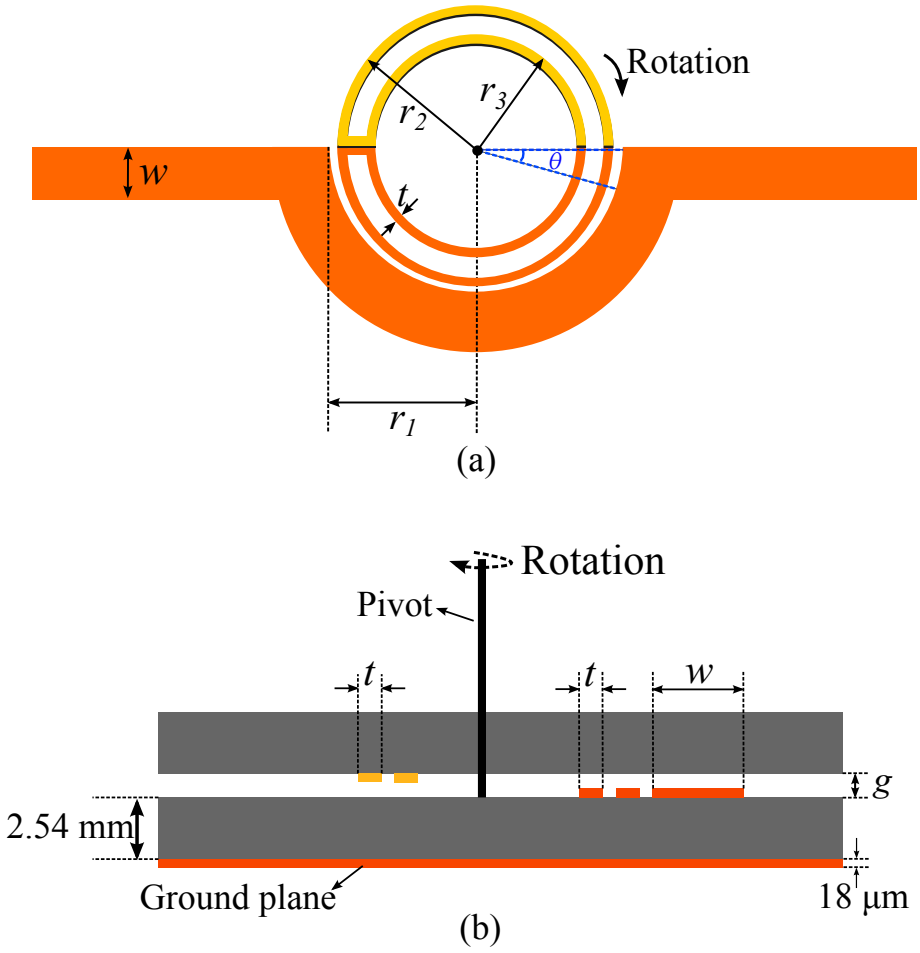

Figure 5.2. Basic schematic of the proposed rotation sensor. (a) Top view with removed dielectric substrates for clarity. (b) Cross section of the proposed sensor. The yellow part indicates the upper resonator metallisation, and the orange shows the lower resonator and the microstrip line metallisation. The top and bottom substrates are indicated in grey color. The dimensions are: $w = 8.3$ mm, $t = 0.3$ mm, $r_1 = 15$ mm, $r_2 = 14.8$ mm, $r_3 = 12.6$ mm and $g = 0.25$ mm.

5.3 Wide-dynamic range rotation sensor

Here, a new design of metamaterial-inspired rotation sensors is introduced with improvement in the dynamic range up to 180°. Advantages of the proposed design in comparison with conventional rotation sensors (e.g. rotary encoders and potentiometers) include a wider dynamic range, lower fabrication cost, and MEMS compatibility. Top and cross sectional views of the proposed rotation sensor are given in Fig. 5.2. As shown, the sensor is composed of two identical U-shaped resonators that are coupled to a single microstrip line. The first resonator is positioned on the same substrate with the microstrip line, whereas the second U-shaped resonator is positioned on another substrate located on the top of the first substrate, as shown in the cross-sectional view in Fig. 5.2(b). The middle part of the microstrip line is rounded to provide an optimum coupling area for the resonators. The two substrates are separated from each other by a very thin air gap. The upper substrate can freely rotate relative to the bottom one. If the upper substrate is rotated around the axis as shown in Fig. 5.2(a), the overlapping area between the resonators will be altered resulting in a change in the electric and magnetic coupling between the two resonators. Effectively, the resonance frequency will be shifted, from which the rotation angle can be determined. This phenomenon can be explained by using the circuit model of the structure.

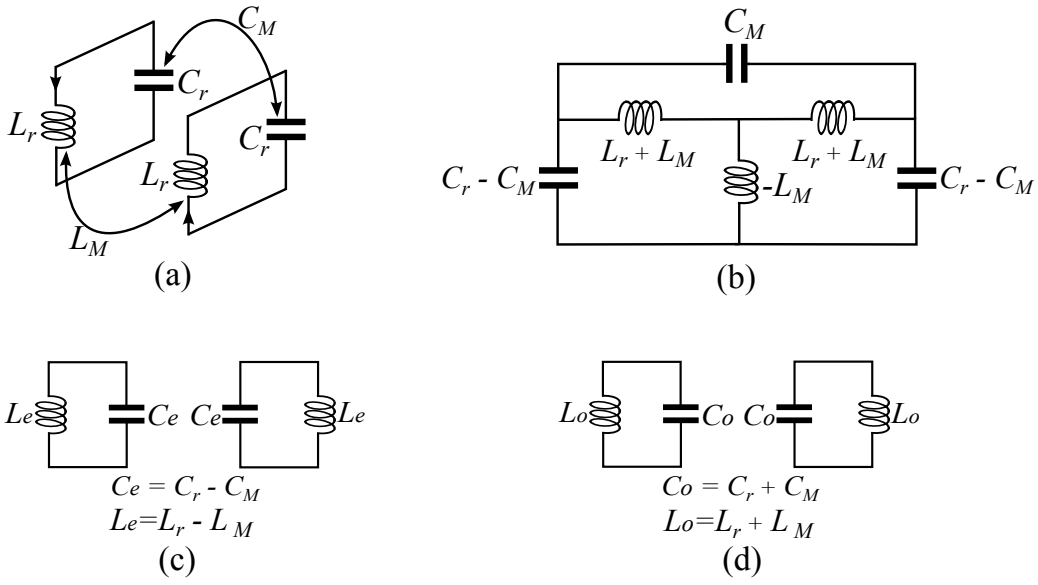

Figure 5.3. Equivalent circuit models. (a) Circuit model of the two coupled U-shaped meandered resonators. (b) Simplified model of the two coupled U-shaped resonators. (c) Equivalent circuit for even mode resonance. (d) Equivalent circuit for odd mode resonance.

The equivalent circuit model of the two coupled U-shaped resonators is presented in Fig. 5.3(a), where L_r represents the equivalent inductance of the resonators and C_r corresponds to the equivalent capacitance. Since the dimensions of the two U-shaped resonators are exactly the same, the equivalent circuit parameters are the same for them. As shown, C_M is the mutual capacitance and L_M is the mutual inductance between the two resonators. The L_M and C_M values are proportinal to the overlapping area and inversely proportional to the distance between the two resonators. By using a simple circuit analysis, the circuit in Fig. 5.3(a) can be simplified to circuit shown in Fig. 5.3(b), where the capacitive coupling is modelled by a π equivalent model and inductive coupling is replaced by its equivalent T circuit model (Hong and Lancaster 2004). By further simplification, the circuits of Fig. 5.3(c) and Fig. 5.3(d) are obtained that show the even and odd mode resonances respectively. Based on Fig. 5.3(c) and Fig. 5.3(d), the even and odd mode resonance frequencies can be found to be

$$f_{\text{even}} = \frac{1}{2\pi\sqrt{L_e C_e}} = \frac{1}{2\pi\sqrt{(L_r - L_M)(C_r - C_M)}}, \tag{5.1}$$

$$f_{\text{odd}} = \frac{1}{2\pi\sqrt{L_o C_o}} = \frac{1}{2\pi\sqrt{(L_r + L_M)(C_r + C_M)}}. \tag{5.2}$$

By increasing the overlapping area between the two resonators, the values of L_M and C_M are increased. As a result, the even mode resonance frequency will move upward, whereas the odd mode resonance frequency will be shifted downwards. Here, the odd mode resonance change is exploited to determine the rotation angle since it yields a more compact sensor with respect to the operation wavelength. This resonance frequency change can be observed in the transmission amplitude ($|S_{21}|$) of the transmission line. An equivalent circuit for the resonator-loaded microstrip line is shown in Fig. 5.4(a), where L and C are the parameters associated with the microstrip, and M is the coupling coefficient between the microstrip line and the resonator (Baena *et al.* 2005). In order to validate the circuit of Fig. 5.4(a), the equivalent circuit parameters have been calculated for a sample rotation angle of 80° by using the method presented in Aznar *et al.* (2008b). The obtained parameters are fed into the ADS circuit simulator and the result is compared with that obtained from Momentum ADS electromagnetic simulation. The dielectric substrate is Rogers 5880LZ with a low relative permittivity of $\epsilon_r = 1.96$ to increase the free-space electric fringing field and hence improving the capacitive coupling between the two resonators. The loss tangent

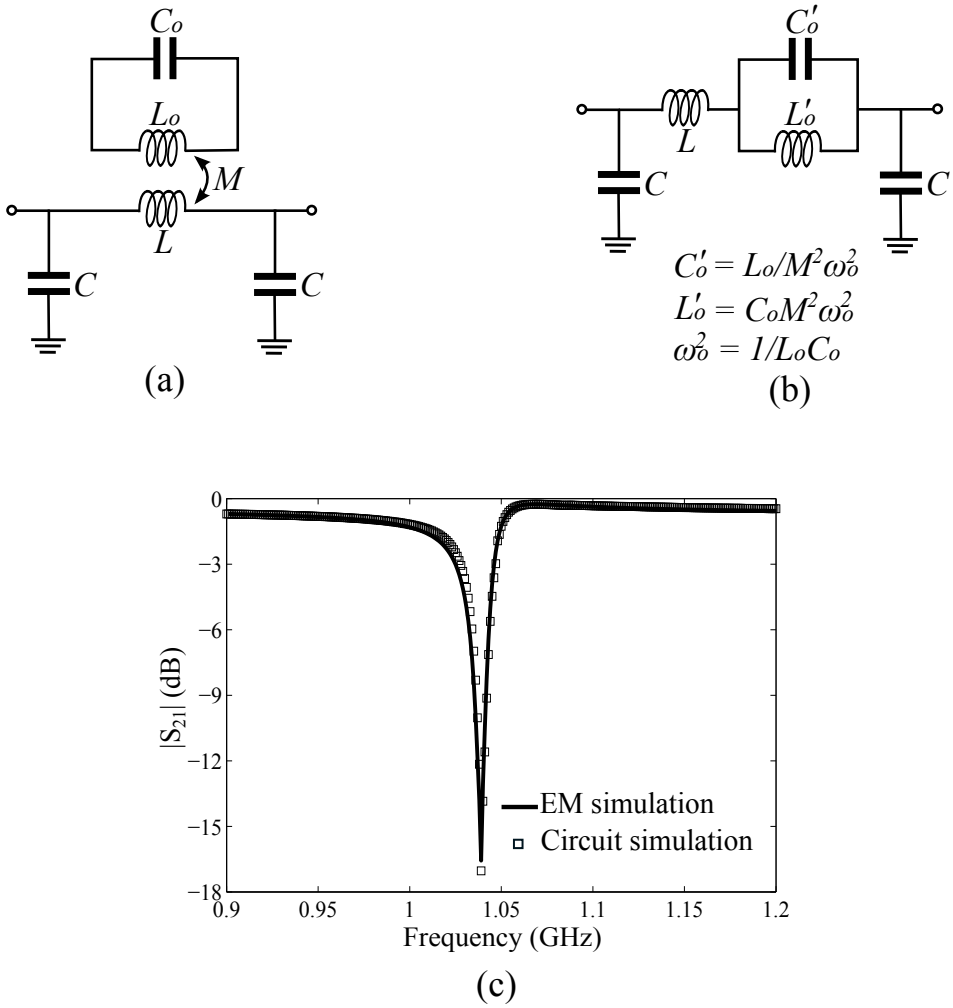

Figure 5.4. Circuit model for analysing the sensor operation. (a) Equivalent circuit model of the proposed rotation sensor in the odd mode resonance. (b) Simplified equivalent circuit after applying the inductive coupling. (c) Comparison between the the equivalent circuit and electromagnetic simulation results for the rotation angle of 80 degree. The circuit parameters are: $L_o^{'} = 0.0974$ nH, $C_o^{'} = 240.6$ pF, $L = 8.85$ nH and $C = 2.13$ pF. The quality factor of the resonance is 200 if it is defined as $f_0/\Delta f$ where Δf is the bandwidth at +3 dB with respect to the minimal transmission.

of the substrate is 0.0019. As shown in Fig. 5.4(c), the good agreement of the results confirm the validity of the proposed circuit model.

As a proof of the sensing concept, the sensor is fully simulated in Momentum ADS by using the dimensions and parameters given in Fig. 5.4. The electromagnetic simulations results of the sensor are shown in Fig. 5.5. As seen, the sensor is able to sense a rotation angle up to 180°. The resonance frequency shift is relatively large between

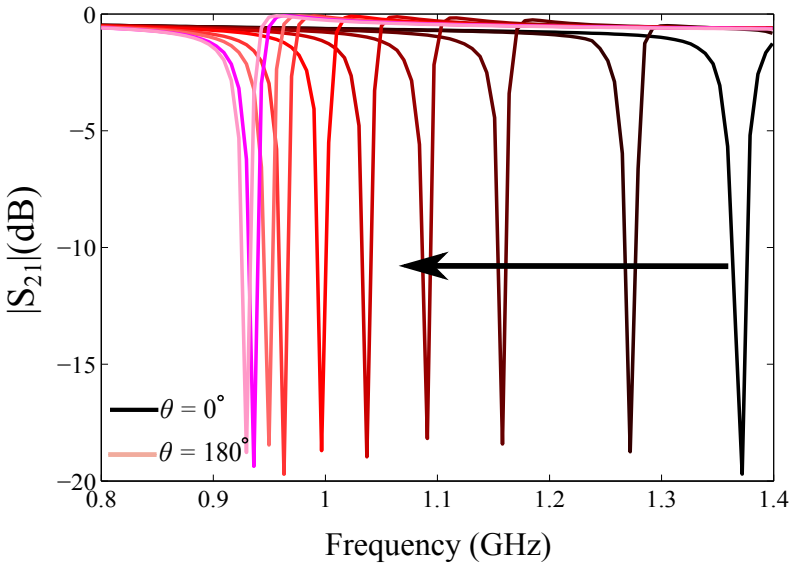

Figure 5.5. Simulated transmission coefficients for different rotation angles. Simulation results of the transmission coefficient for the designed sensor of Fig. 5.2 for different rotation angles up to 180°. The rotation step size is 20°.

0°and 80°, implying high sensitivity. However, the frequency shift and hence the sensitivity reduce significantly beyond 80°. This nonlinearity is due to the uniform shape of the two resonators. In fact, with this uniform shape the overlapping area between the two resonators varies linearly when the upper resonator is rotated with respect to the bottom one and this causes a linear change in L_oC_o. But, the linear change in the L_oC_o causes a nonlinear shift in resonance frequency as suggested by the relation in (5.2).

5.3.1 Linearising the sensor response

In order to improve the sensor linearity, the overlapping area of the two resonators should be changed nonlinearly as a function of the rotation angle. This can be carried out by modifying the resonators shape. An improved design is illustrated in Fig. 5.6. In this structure, the outer arms of the two U-shaped resonators are asymmetrically tapered. Using this approach, the overlapping area of the two resonators will be developed slowly at the beginning of rotation. As a result, the mutual inductance and capacitance changes will be small. By increasing the rotation angle, tapering causes a greater change in the overlapping area, and hence the mutual inductance and capacitance changes will be larger and the sensitivity will be increased for the large rotation angles around 180°.

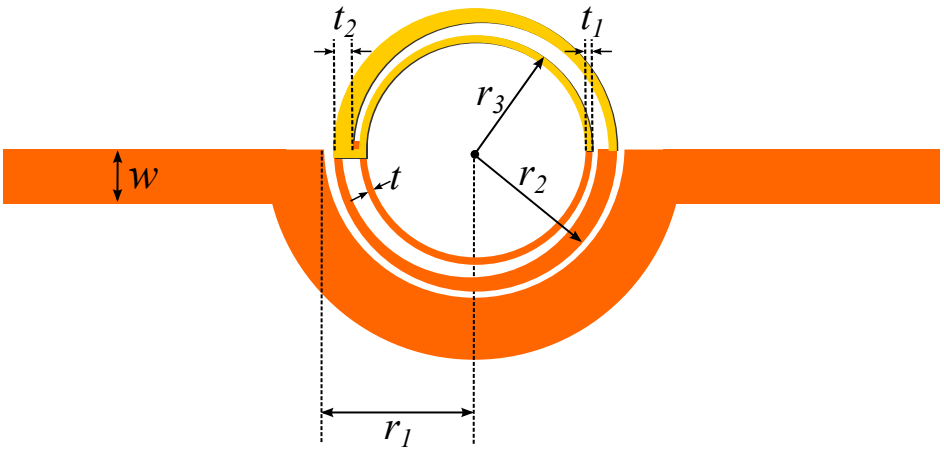

Figure 5.6. Modified rotation sensor for better linearity. The tapered-resonator design for improving the linearity of sensor response. The dimensions are: $w = 8.3$ mm, $t = t_1 = 0.3$ mm, $r_1 = 15$ mm, $r_2 = 14.8$ mm, $r_3 = 12.6$ mm and $t_2 = 1.7$ mm.

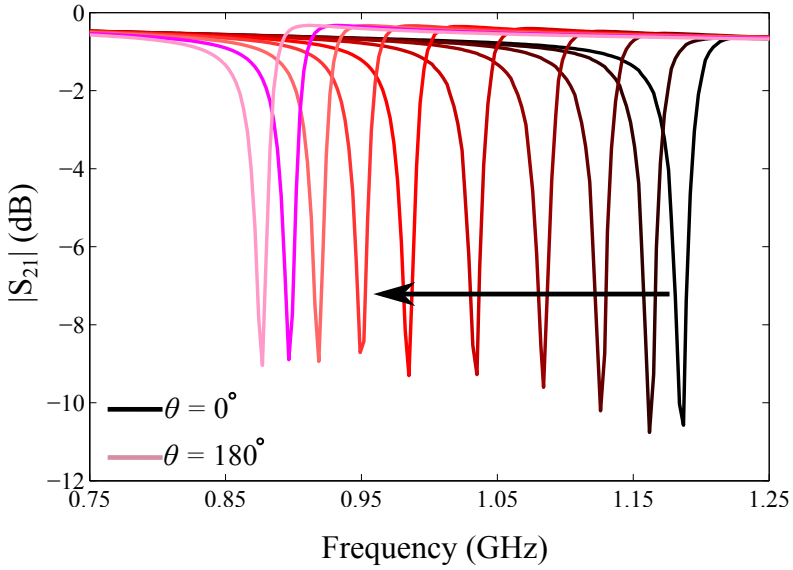

Figure 5.7. Simulated transmission responses of the improved sensor. Simulated transmission coefficient for the improved sensor in Fig. 5.6 for different rotation angles up to 180°. The rotation step size is 20°.

Fig. 5.7 depicts the simulated resonance frequency shifts for the improved design of Fig. 5.6 at different rotation angles. As seen, the modified sensor shows better sensitivity for large rotation angles close to 180°. For a better comparison in terms of linearity, the resonance frequencies for the sensor in Fig. 5.2 and the modified structure in Fig. 5.6 are plotted versus the rotation angle in Fig. 5.8. As shown, the structure in Fig. 5.6 offers an improved linearity in comparison with the initial design in Fig. 5.2.

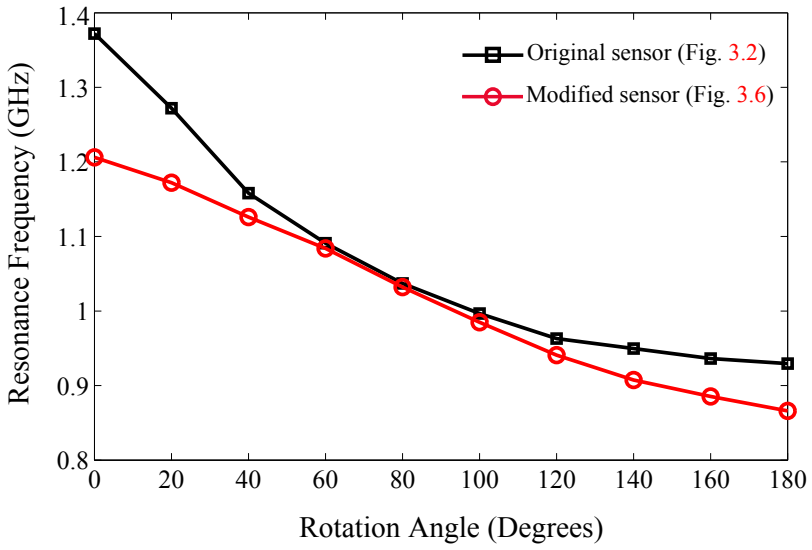

Figure 5.8. Comparison of the sensitivity curve between the two rotation sensors. Comparison between the simulated resonance frequency of the simple design in Fig. 5.2 and the improved design in Fig. 5.6 for different rotation angles.

5.3.2 Sensitivity analysis

The sensitivity of the rotation sensor can be defined as

$$S_{\theta}^{f_0} = \frac{\theta}{f_0}\frac{df_0}{d\theta} \tag{5.3}$$

where, $S_{\theta}^{f_0}$ is the sensitivity of the rotation sensor with respect to the rotation angle, f_0 is the resonance frequency of the sensor and θ is the rotation angle. From (5.3) and Fig. 5.8, the sensitivity of the simple design in Fig. 5.2 at three rotation angles of 20°, 90° and 180° are calculated as 1.1, 0.18 and 0.03 respectively. On the other hand, the sensitivity of the improved sensor in Fig. 5.6 at these three rotation angles are calculated as 0.98, 0.93 and 0.89 respectively. The above analysis clearly demonstrates that the improved design in Fig. 5.6 retains a constant sensitivity of around 0.9 over 0 to 180° rotation angle, while the sensitivity of the simple sensor of Fig. 5.2 is high at small rotation angles and very small at large rotation angles around 180° showing the sensitivity saturation. It should be mentioned that the improved linearity of the modified design in Fig. 5.6 is achieved at the expense of reduced sensitivity for small rotation angles.

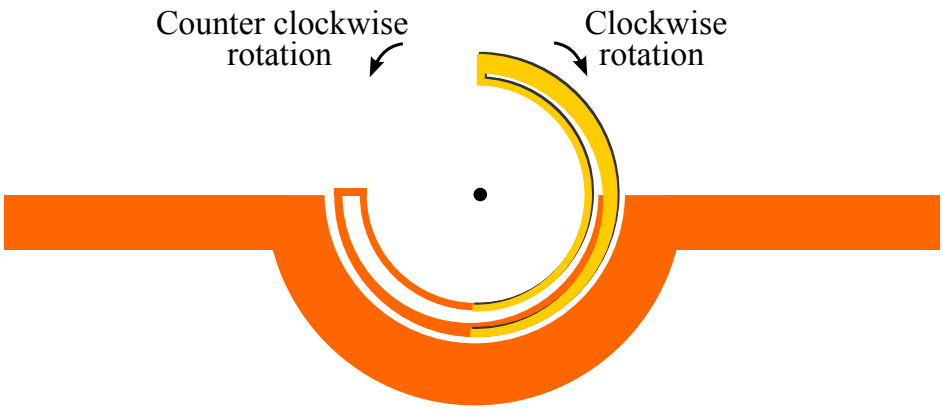

Figure 5.9. Detection of the rotating direction. Sensor arrangement for detecting the direction of rotation.

5.3.3 Detecting the rotating direction

The proposed sensor can be used to sense the rotation direction. For this application, the zero (starting) point of the rotation can be set to 90° degrees as shown in Fig. 5.9. In this arrangement, if the upper resonator is rotated clockwise, the overlapping area of the two resonators will be increased causing a stronger coupling between the two resonators, hence the resonance frequency shifts downwards. On the other hand, if the upper resonator is rotated counterclockwise, the coupling between the two resonators will be decreased and the resonance frequency moves upwards. In this way, the rotation angles within 90° degrees can be detected.

5.3.4 Experimental results

In order to verify the rotation sensing concept presented in Section 5.3.1 and validate the simulation results of the improved sensor design, a sensor prototype has been fabricated based on the dimensions given in Fig. 5.6. The device is fabricated on Rogers 5880LZ dielectric substrate. Fig. 5.10 illustrates the fabricated sensor.

Fig. 5.11 shows the measured transmission coefficient (S_{21}) of the fabricated sensor for different rotation angles. In each measurement step, the upper plate is rotated using the rotating knob and the transmission response is recorded by using the network analyser. The sensor with tapered resonators shows a linear frequency shift for large rotation angles close to 180° while maintaining a compact size with respect to the operational wavelength. Fig. 5.12 compares the measured and simulated resonance frequencies as a function of the rotation angle. The plot shows agreement between

the simulated and measured results. The differences between the measured and simulated responses can be attributed to the fabrication and assembling tolerances. Based on these results, the proposed rotation sensing concept and the improved design for linearising the sensor response are validated.

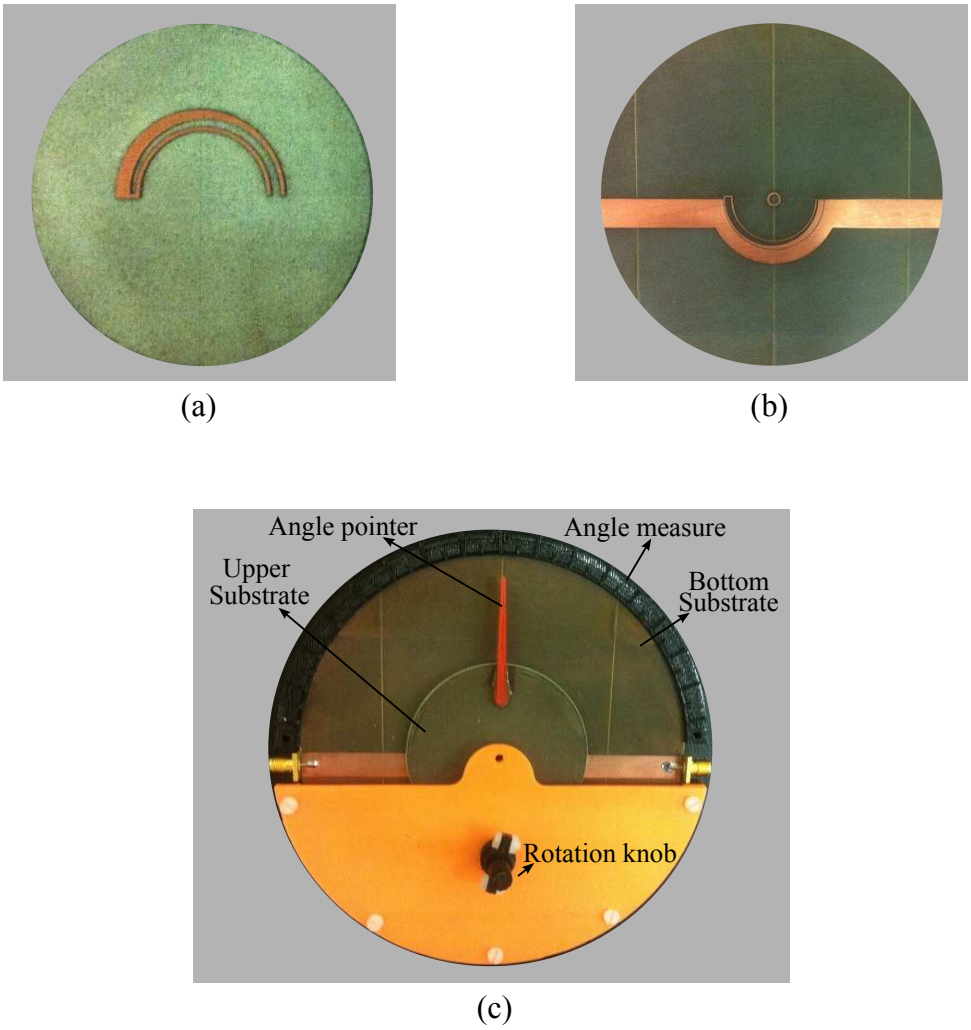

Figure 5.10. The fabricated sensor module. (a) The upper plate containing a resonator. (b) The lower plate containing a resonator coupled with a microstrip line. (c) The assembled sensor module, packaged with parts obtained from 3D printing. A rotation knob connects to the pivot through set of gears for rotating the upper resonator with respect to the bottom one. The angle scale and pointer are included for setting the rotation angle accurately.

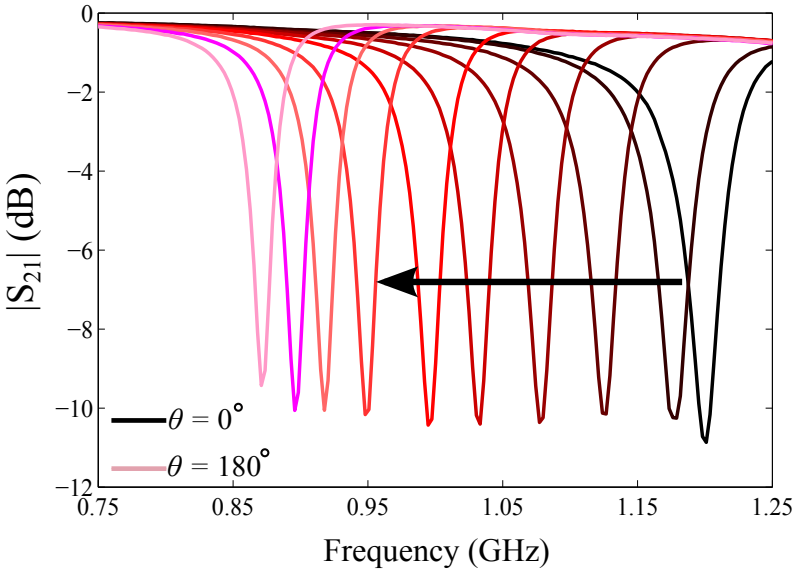

Figure 5.11. Measured transmission coefficients for different rotation angles. Measurements results of the transmission coeficient for the fabricated sensor prototype for different rotation angles up to 180°. The rotation angle step size is 20°.

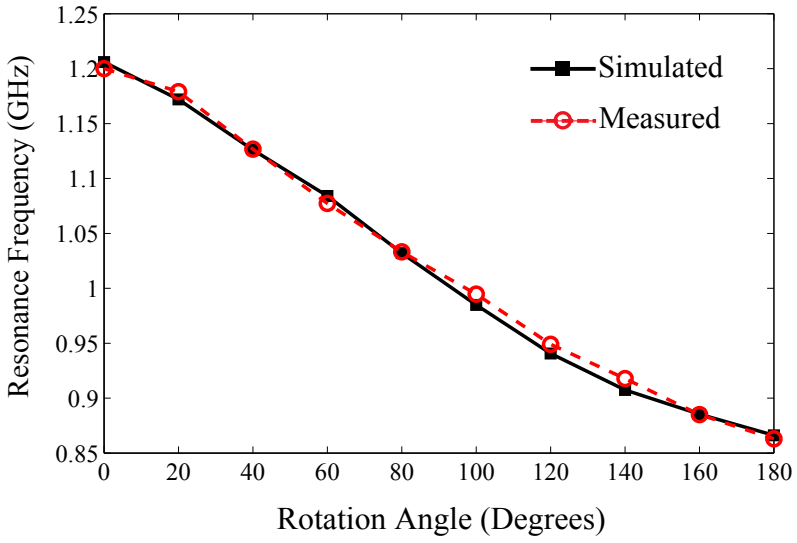

Figure 5.12. Measured and simulated resonance frequencies. Comparison between the measured and simulated resonance frequency of the improved designed sensor in Fig. 5.6.

5.4 Displacement sensor

This section represents a design of a wide-dynamic-range displacement sensor based on complementary electric-LC resonator. As mentioned before, one limitation associated with the displacement sensors based on CPW loaded with SRRs is the low dynamic range that makes them unsuitable for detection of large displacement or asymmetry. The maximum dynamic range of the CPW loaded with rectangular SRR is reported to be around 0.3 mm (Naqui *et al.* 2012). The dynamic range is improved to around 1 mm in Horestani *et al.* (2013b) by considering a diamond shaped SRR. In this section, a displacement sensor is introduced based on a CELC2 resonator loaded on a microstrip line that can extend the detection range up to 1.6 mm.

5.4.1 Operation principle of the sensor

As demonstrated in Chapter 3, the odd mode of the CELC2 resonator in Fig. 5.13 cannot be accessed if the symmetry axes of the resonator and the microstrip line are aligned. However, the structure will inhibit the propagation of the electromagnetic signal if the resonator is displaced with respect to the microstrip line. The effect is manifested as a transmission notch in the frequency response of the device. The depth of this transmission notch increases by increasing the displacement of the resonator with respect to the transmission line. We used this property for designing a displacement sensor in this Section.

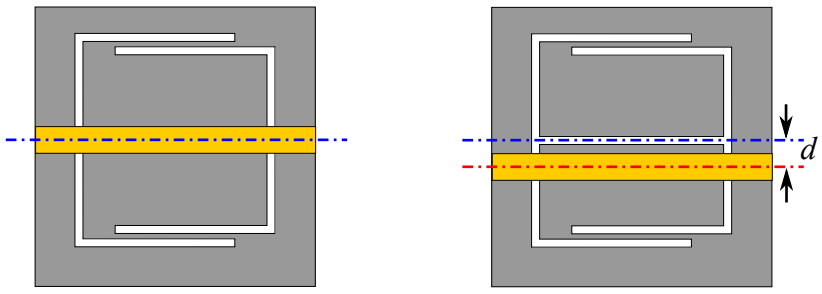

Figure 5.13. Single CELC2 resonator loaded on a microstrip line. (a) Symmetry axis of the resonator is aligned with the symmetry axis of the microstrip. (b) The resonator is displaced with respect to the microstrip line. The ground plane is indicated in grey and the microstrip metallisation is yellow.

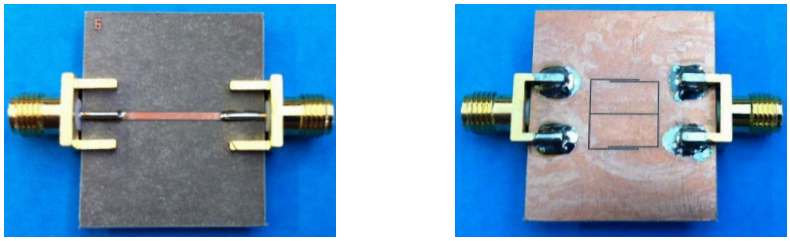

Figure 5.14. Fabricated the prototypes of the displacement sensor. (a) Top view of the microstrip line. (b) Bottom view showing the ground plane and the CELC2 resonator that is displaced by 0.6 mm with respect to the microstrip line.

5.4.2 Measurement results

We have fabricated the prototypes of the sensor on 1.27 mm thick Rogers RO6010 substrate with the relative dielectric constant of 10.2 and the loss tangent of 0.0023. Fig. 5.14 shows the top and bottom views of a prototype sample, where the CELC2 is displaced by 0.6 mm with respect to the microstrip line. Note that due to high sensitivity of the sensor to a small amount of displacement, the proposed sensor is verified through a series of fabricated samples with fixed displacement values (Naqui *et al.* 2011). The measured transmission coefficient (S_{21}) for the odd mode are shown in Fig. 5.15. As seen, the notch depth increases by increasing the resonator displacement. Furthermore, a change in the notch depth as a function of displacement is plotted in Fig. 5.16. The odd mode resonance frequency is shifted due to displacement of the resonator, which in turn prohibits the use of a continuous-wave microwave setup, this frequency variation might be compensated by optimising the resonator shape (Horestani *et al.* 2013a). Additionally, the shape optimisations may be carried out for improving other specifications of the sensor such as sensitivity, dynamic range, and linearity.

5.5 Conclusion

This chapter has presented a rotation sensor and a displacement sensor with an extended dynamic range. The rotation sensor is based on broadside coupled U-shaped resonators, where the rotation affects the coupling coefficient between them. A change in the coupling shifts the resonance frequency of the structure. This effect can be used to measure the rotation angle. The designed sensor operates in the low microwave frequency range with a compact size. A linear sensing characteristic is achieved by

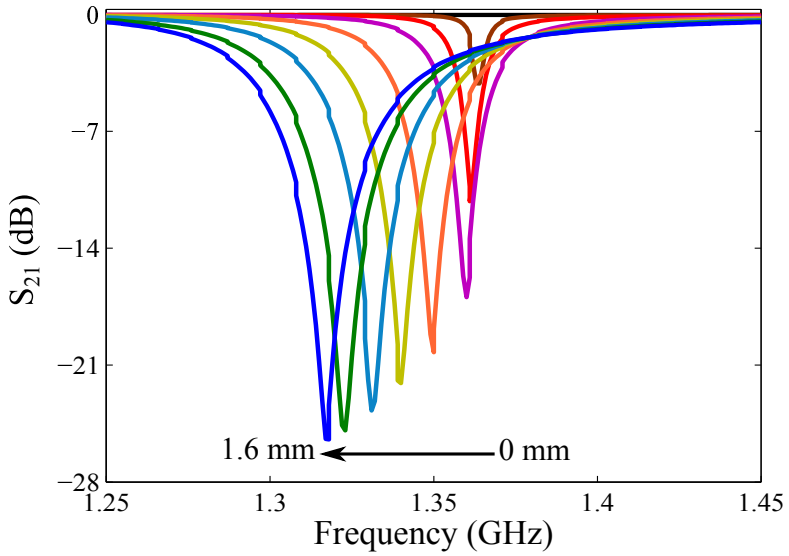

Figure 5.15. Transmission responses of the displacement sensor. The transmission responses of the displacement sensor for different amount of displacements from 0 mm up to 1.6 mm where, the displacement step is 0.2 mm.

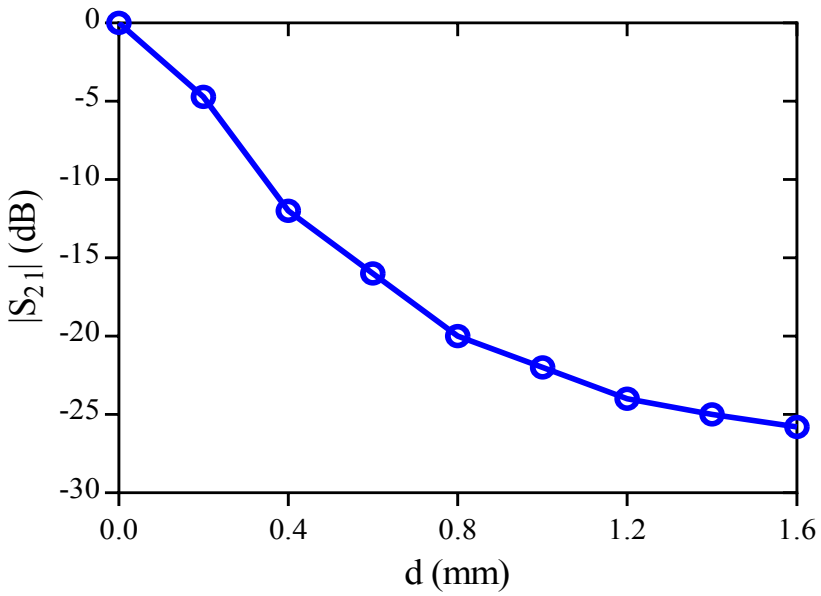

Figure 5.16. Changes in notch depth. The measured transmission notch depth for different displacements of the resonator with respect to the transmission line.

asymmetrically tapering the two resonators. It is shown that this new configuration can improve the dynamic range up to 180°. The rotation direction can also be detected.

The chapter has also presented a displacement sensor by exploiting the symmetry property of a CELC resonator loaded with a microstrip line. The designed sensor provides a sensing range up to 1.6 mm. The sensitivity, linearity, and the dynamic

range of the proposed sensor can be improved by optimisation of the resonator or the microstrip line section.

Chapter 6

Microwave tunable and dual-band frequency selective surfaces

THIS chapter focuses on microwave frequency selective surfaces (FSSs) with either tunable or dual-band functionality. FSSs are spatial filters made of two-dimensional periodic arrangement of metallic elements supported by dielectric surfaces. Depending on unit-cell design, they exhibit different filtering responses. They have seen wide spread usage in electromagnetic beam forming applications including radome for radar applications, planar lenses, reflectarrays and etc. Recent advances in multiband and multifunctional communication systems has raised the need for multiband, tunable, or reconfigurable FSS structures. In response to these requirements, FSSs with tunable or dual-band functions are proposed in this chapter. Varactor-based tunable bandpass FSS structures have been designed with improved bias network that enables tuning without dedicated bias network. Another tunable FSS is designed based on the liquid crystal for the X-band. In addition, a dual-band FSS based on miniaturised unit cell is proposed for multi-standard communication systems. The design method and the validation of the proposed FSS structures will be presented.

6.1 Introduction

Multiband and tunable microwave components are essential in reconfigurable and multi-standard communication systems. These advances rise the need for FSSs with agile frequency responses. In order to design an FSS with a dynamic frequency behaviour, the unit cell characteristics should be controlled through a tuning mechanism (Munk 2005). The literature on tunable and reconfigurable FSSs contains a variety of approaches for designing dynamic frequency response. For example, magnetically tunable ferrite or liquid substrates are used by Chang *et al.* (1994), Li *et al.* (1995), and Lima *et al.* (1994) for tuning the FSS spectral response. Mechanical deformation of the unit cells has also been incorporated for tunable FSSs (Fuchi *et al.* 2012, Azemi *et al.* 2013). The mechanical, magnetic and liquid substrate tuning methods provide tuning with low loss and without additional bias networks. However, they suffer from low tuning speeds and narrow tuning ranges. Tunability is achieved in Coutts *et al.* (2008), Schoenlinner *et al.* (2004), and Zendejas *et al.* (2006) by utilising micro-electromechanical (MEMS) switches and capacitors. However, they require complicated fabrication procedures. In Li *et al.* (2010), and Li and Behdad (2012), tunable FSS structures are developed by integrating tiny channels inside the substrate and applying liquid metal droplets to them, where, by moving the liquid metal droplets between different unit cells, their equivalent capacitance will be varied resulting in a tunable frequency response. Although fine tuning of FSSs with high-order filtering characteristics is achieved in these designs, they require costly and complicated fabrication processes.

A well developed method of tuning at the microwave frequency range is by using active semiconductor elements such as PIN diodes or varactors. The advantages of varactor-based tuning are the low fabrication costs, high tuning speed and wide tuning ranges. Varactor-based tuning concept has been applied in designing FSS structures as well (Huang *et al.* 2015, Mias 2005, Pan *et al.* 2013, Costa *et al.* 2011, Kiani *et al.* 2010). However, most of these structures require additional components and a dedicated bias network. In biasing, RF chokes are needed for each individual varactor to separate RF from DC signal to maintain the operation of the FSS. However, with a large array of unit cells, a large number of RF chokes might be needed to bias every varactor. The bias networks add additional metallic pattern to the original FSS structure and thus affect the out-of-band frequency response of the FSS by causing spurious frequency responses (Bayatpur and Sarabandi 2009a, Bayatpur and Sarabandi 2010).

Apart from tunability, there is a great interest in designing dual-band FSSs for mutli-functional or multi-standard applications. Several design techniques such as fractal metallic arrays (Romeu and Rahmat-Samii 2000, Gianvittorio *et al.* 2001), perturbation techniques (Hill and Munk 1996) and genetic algorithms (Manara *et al.* 1999) have been proposed to design multiband FSSs up to now. The most critical limitation of these structures is relatively large size of the unit cell in comparison with the operational wavelength of the filter. This degrades the FSS performance under oblique incidence angles especially at the second operational band.

In order to address the drawbacks associated with the biasing elements, Section 6.2 presents a single-pole tunable FSS in which all the varactors in unit cells are biased in parallel and therefore, just one RF choke is enough to bias all of them properly. In Section 6.3, a second-order bandpass FSS has been proposed that does not need a dedicated bias network for varactor tuning. The bias network is embedded in the FSS structure itself in the form of uniform wire grids in each layer of the FSS structure. This new design alleviates the problem associated with the bias network. Furthermore, a liquid crystal-based tunable X-band FSS is proposed as an alternative approach for designing tunable FSSs at higher frequencies. Another contribution is on a dual-band FSS with miniaturised-element unit cell as is proposed in Section 6.5 to address the unit cell size issue associated with dual-band FSSs. The modelling, design approach and experimental validation of the proposed FSS configurations will be explained.

6.2 Varactor-based tunable single-pole FSS

In this section, a unit cell is proposed for designing tunable frequency selective surfaces. The proposed unit cell provides a first-order bandpass response with an adjacent transmission zero that can be used for improving the out-of-band rejection. Tunability can be achieved by integrating four varactor diodes in each unit cell. Two wire grids together with metallic via holes are included for biasing the varactors. An equivalent circuit model is considered for modelling the FSS response to facilitate the design process. The FSS structure and its operation principle will be described in Section 6.2.1.

6.2.1 FSS structure and operation principle

The front and back views of the proposed FSS unit cell are shown in Fig. 6.1. The unit cell is composed of a square ring surrounded by an inductive wire grid in one layer.

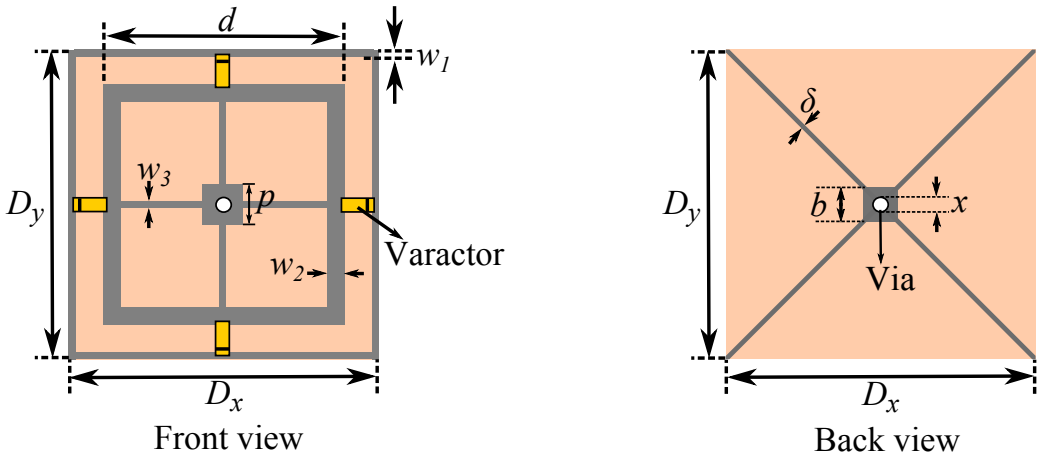

Figure 6.1. Unit cell of the designed tunable FSS. The dimensions are as follows: $D_x = D_y = 10.2$ mm, $d = 9.2$ mm, $w_1 = 0.1$ mm, $w_2 = 0.5$ mm, $w_3 = 0.2$ mm, $p = 1$ mm, $\delta = 0.14$ mm, $x = 0.3$ mm and $b = 0.5$ mm. Metalic parts are represented with grey and the via hole is shown in white. The varactors cathode is shown with the black strip.

Four varactor diodes are loaded between the square loop and wire grid for tuning the capacitance between them. The diagonal thin wire grid in the back layer together with the metallic via hole are electrically connected to the square loop in the front layer through a square patch and four thin wires. These wires are responsible for providing the negative bias voltage for the varactors and the positive bias voltage is provided by the wire grid in the front layer. The biasing wire grid in the back layer are running in the diagonal directions for improved stability of the frequency response under oblique incidence angles of the EM excitation (Kiani *et al.* 2008). The dielectric substrate is RO5880 with a relative dielectric constant of 2.2 and a loss tangent of 0.0009. The substrate thickness is 0.254 mm for a low profile.

Since the designed FSS comprises miniaturised unit cell, its frequency response can be modelled by a lumped element circuit (Ebrahimi *et al.* 2014a, Sarabandi and Behdad 2007). The equivalent circuit model of the FSS is presented in Fig. 6.2. In the circuit model, the inductance L models the inductive behaviour of the front layer wire grid, whereas the square loop is modelled by the series resonator L_1C_1 (Bayatpur and Sarabandi 2008b), where C_1 represents the summation of varactor capacitance C_{var} and the capacitive effect between the edges of the square loop and surrounding wire grid C_0.

The dielectric substrate with a thickness of h is modelled through a transmission line section with a length of h and a characteristic impedance of $Z_T = Z_0/\sqrt{\epsilon_r}$, where $Z_0 = 377\ \Omega$ is characteristic impedance of free space and ϵ_r is the relative permittivity

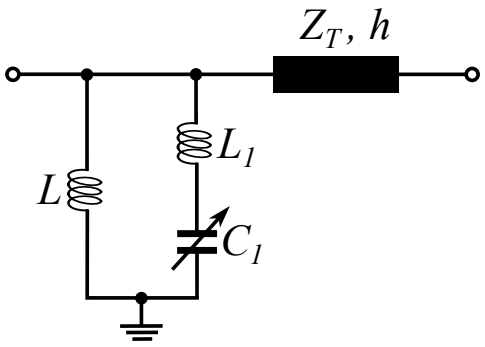

Figure 6.2. Circuit model. Equivalent circuit model of the proposed FSS.

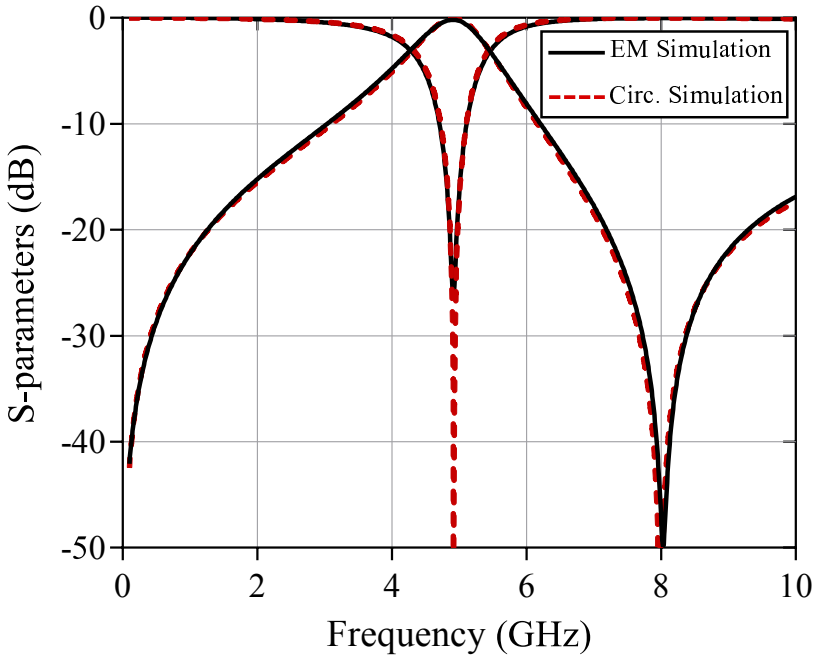

Figure 6.3. Circuit and electromagnetic simulation results of the FSS. Comparison between the equivalent circuit model and full-wave electromagnetic simulation results of the proposed FSS when the varactor capacitance is 0.2 pF. The equivalent circuit parameters are: $L = 2.27$ nH, $L_1 = 1.388$ nH, $C_1 = 0.285$ pF, $Z_T = 254\ \Omega$ and $h = 0.254$ mm.

of the dielectric substrate. A comparison between the circuit model and the full-wave electromagnetic simulation results of the proposed FSS under normal incidence angle in presented in Fig. 6.3 for varactor capacitance of 0.2 pF. As seen, there is a very good agreement between the circuit model and EM simulation results. The FSS offers a first-order bandpass response with an upper stopband zero that can be used to improve the out-of-band rejection of the transmission response.

By applying a bias voltage between the front and back layer wire grids, the capacitance of the varactors, and hence the frequency response of the FSS, can be tuned. The

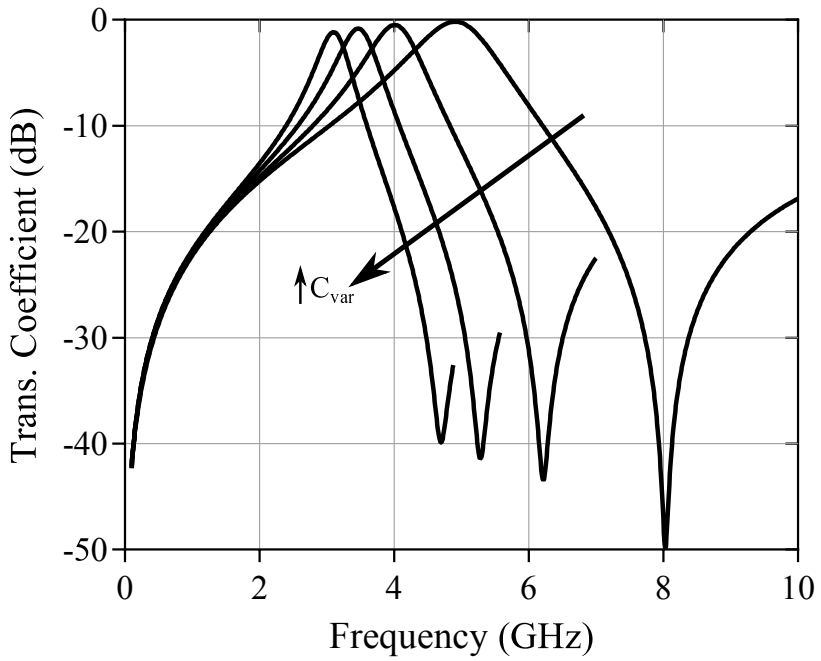

Figure 6.4. Tuning performance of the single-pole FSS. Transmission responses of the FSS when the varactor capacitance is changed from 0.2 pF to 0.8 pF with a step size of 0.2 pF.

transmission responses of the FSS when the varactor capacitance is tuned from 0.2 pF to 0.8 pF are demonstrated in Fig. 6.4. The results in Fig. 6.4 show that the passband frequency is tuned from around 4.9 GHz to 3.1 GHz for the considered capacitor range with an increase in the insertion loss. Also, the bandwidth is decreased with increasing the varactor capacitance, because the bandwidth is inversely propotional to the C_1 in the circuit in Fig. 6.2. A good candidate to provide this range of capacitance is a surface mounted MA46H120 varactor from M/A-COM. It should be mentioned that this varactor diode shows a quality factor around 100 that is also considered in simulations.

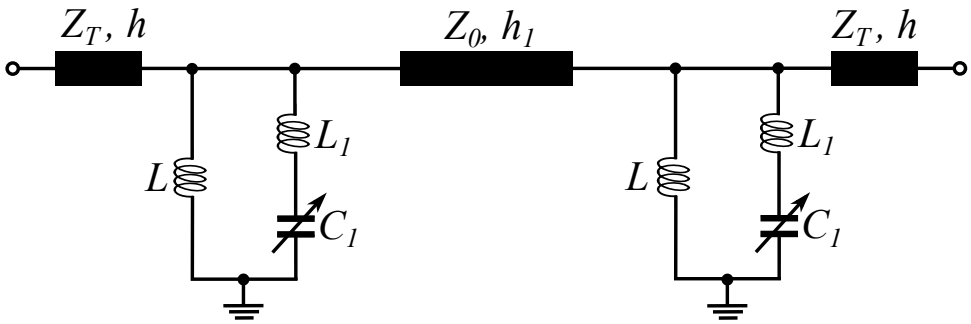

Figure 6.5. Second-order FSS design. Equivalent circuit model of a second-order tunable FSS obtained by cascading two single-pole FSS layers.

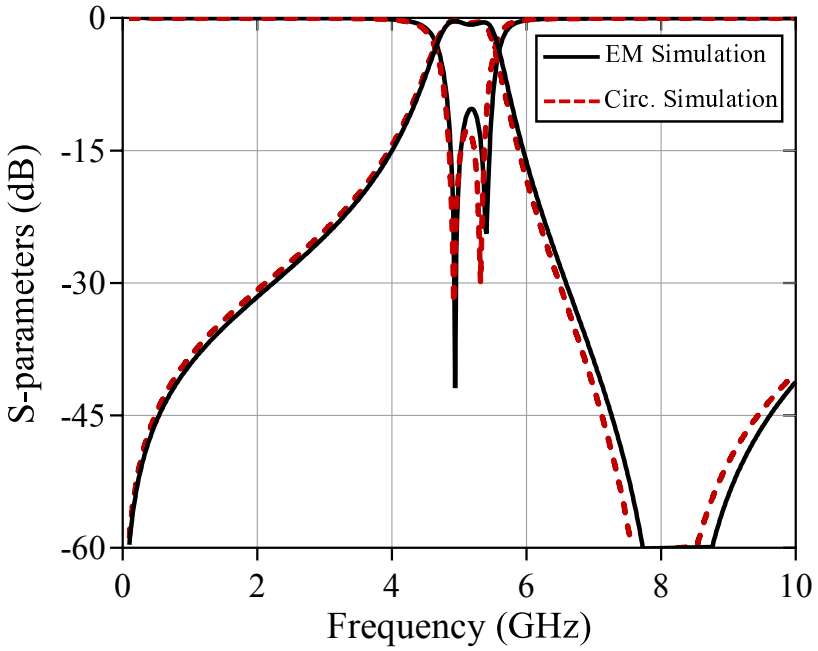

Figure 6.6. Simulation results of the second-order FSS. Comparison between the EM and circuit model simulations of the second-order FSS formed by cascading two layers of the single-pole FSSs when the varactor capacitance is 0.2 pF. The equivalent circuit parameters are the same as those given in Fig. 6.3 and $h_1 = 9$ mm.

6.2.2 Application in higher-order FSS design

The proposed FSS unit cell can be used in designing tunable filters with higher-order responses. As an example, a second-order tunable bandpass FSS is designed and verified through simulations in this Section. A second-order filtering characteristic can be attained by cascading two layers of the first-order FSS designed in Section 6.2.1 with a sub-wavelength air gap between them (Li and Shen 2013, Pan *et al.* 2013). The equivalent circuit model of the second-order FSS is formed by the cascade of two single-pole FSS are given in Fig. 6.5, where the transmission line section with a length of h_1 and characteristic impedance of $Z_0 = 377\ \Omega$ models the h_1 air gap between the two layers.

For verification, a cascade of two single-pole FSSs with same dimensions as Fig. 6.1 is simulated in CST Microwave Studio and its frequency response is presented in Fig. 6.6. The air gap between the two FSS layers is 9 mm. As seen, a second-order filter response is obtained. The results from the circuit model simulation are also plotted in Fig. 6.6. As demonstrated, the circuit model precisely predicts the frequency behavior of the multilayer FSS structure.

Table 6.1. Comparison with other structures. A comparison between the designed tunable FSS and a number of existing configurations

Ref.	Tuning Mech.	Tuning Range (%)	IL (dB)
Azemi *et al.* (2013)	Spring Resonator	17	<1
Li and Behdad (2012)	Liquid metal	32	<1
Li *et al.* (2010)	Liquid metal	25	<2.5
Pan *et al.* (2013)	Varactor	10	1.6–7.2
This Work	Varactor	40	0.7–5

The frequency response of the second-order configuration can also be tuned by tuning the varactor capacitances in each FSS layer. The simulated transmission responses of the second-order FSS when the varactor capacitances are tuned from 0.2 pF to 0.8 pF are given in Fig. 6.7. Effectively, it achieves a continuous tunability of the filter centre frequency from 5.1 GHz to 3.4 GHz. This tuning range is slightly different from the tuning range of the single-pole version, because the circuit in Fig. 6.5 is a coupled input/output resonator and the transmission line section between the front and back resonators also contributes in determining the central frequency (Ebrahimi *et al.* 2015a). In addition, the filter bandwidth decreases by increasing C_{var} because the bandwidth is inversely proportional to C_1 in the front and back layers resonators.

The results presented in Fig. 6.6 and Fig. 6.7 are all with a normal-incident excitation. However, the responses change for oblique angles of incidence in the TE and TM polarisations. The simulated transmission responses of the second-order FSS under oblique incidence angles are demonstrated in Fig. 6.8 for both of the TE and TM polarisations. Simulations show a reasonably stable passband frequency response for both polarisations over a wide ranges of oblique angles up to 45°. However, the FSS bandwidth decreases as the incidence angle increases in the TE polarisation. Conversely, the bandwidth increases for larger incidence angles in the TM polarisation. As explained in Ebrahimi *et al.* (2015a), this phenomenon is mainly attributed to a change in the impedance of the incident EM wave. A comparison between the designed tunable FSS and a number of existing tunable FSSs is provided in Table 6.1 in terms of

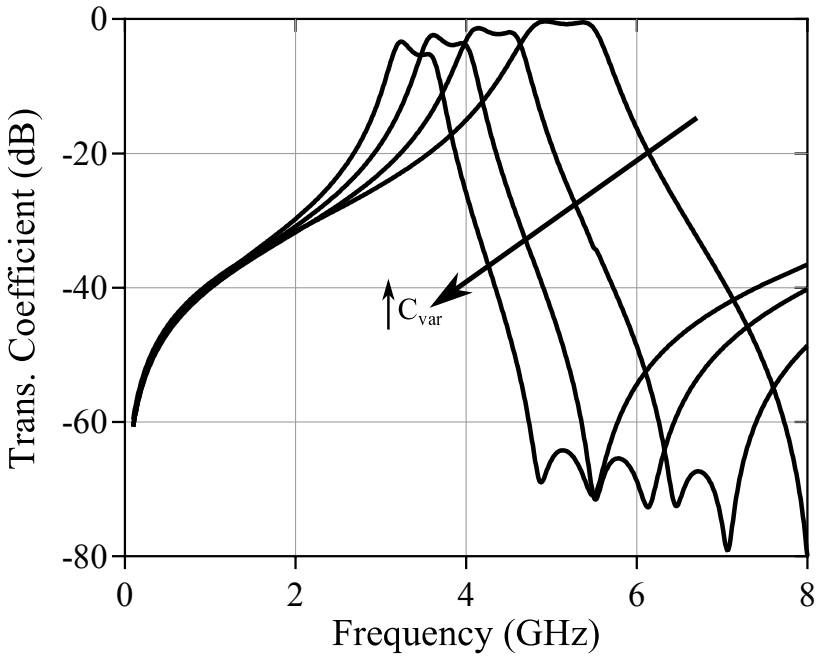

Figure 6.7. Tuning of the second-order FSS. Tuning performance of the second-order FSS when the varactor capacitance is tuned from 0.2 pF to 0.8 pF. The step size is 0.2 pF.

tuning mechanism, tuning range and insertion loss (IL). The table shows that the proposed FSS offers the widest tuning range. However, it shows a higher insertion loss since the series resistance of varactor diodes increases by decreasing the bias voltage.

6.3 Varactor-based second-order tunable FSS with embedded bias network

In this section, a second-order bandpass FSS is proposed based on miniaturised elements with varactor-based tuning capability. The designed FSS is composed of three metallic layers separated from each other by thin dielectric spacers. The bias network is embedded in the FSS structure that comprises wire grids in all layers and via holes that connect the varactors in the front and back layers to the middle layer. This configuration enables tunability without the need for any additional circuit or network for biasing the individual varactors. So, it avoids the spurious response associated with the bias grid. Since all the varactors are biased in parallel, only a single RF choke is needed for RF/DC isolation. Furthermore, miniaturised non-resonant or hybrid (combination of resonant and non-resonant) elements offer a low profile configuration

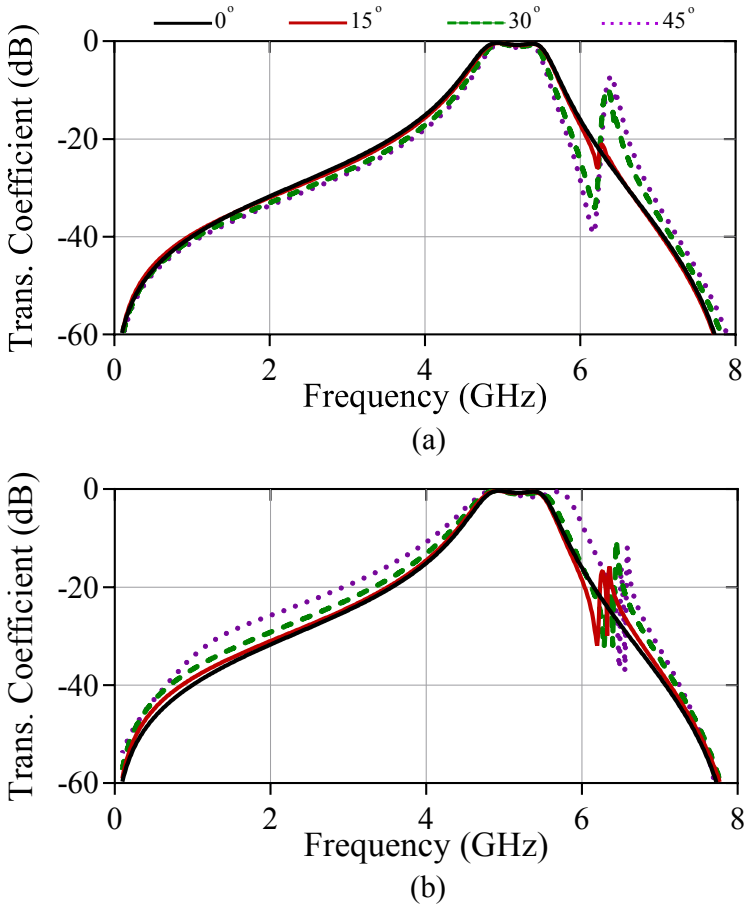

Figure 6.8. Scan angle performance of the second-order FSS. Simulated transmission responses of the second-order FSS under oblique incidence angles. (a) Responses for the TE polarisation. (b) Responses for the TM polarisation.

with stable frequency response with respect to the incidence angle of the electromagnetic wave (Ebrahimi *et al.* 2015a, Bayatpur and Sarabandi 2008b, Kashanianfard and Sarabandi 2013, Al-Joumayly and Behdad 2010). The explanation of the FSS structure, modelling and experimental validation will be presented in next sections.

6.3.1 FSS structure and equivalent circuit model

A three-dimensional view of the proposed FSS and the unit cells are demonstrated in Fig. 6.9. The structure is composed of three metallic layers that are separated from each other by two thin dielectric spacers. The top and bottom metallic layers consist of miniaturised meandered cross-shaped resonators surrounded by the inductive wire grid. The middle layer is made of another inductive wire grids. In the ideal form, the top and bottom metallic layers are exactly the same and the whole structure is

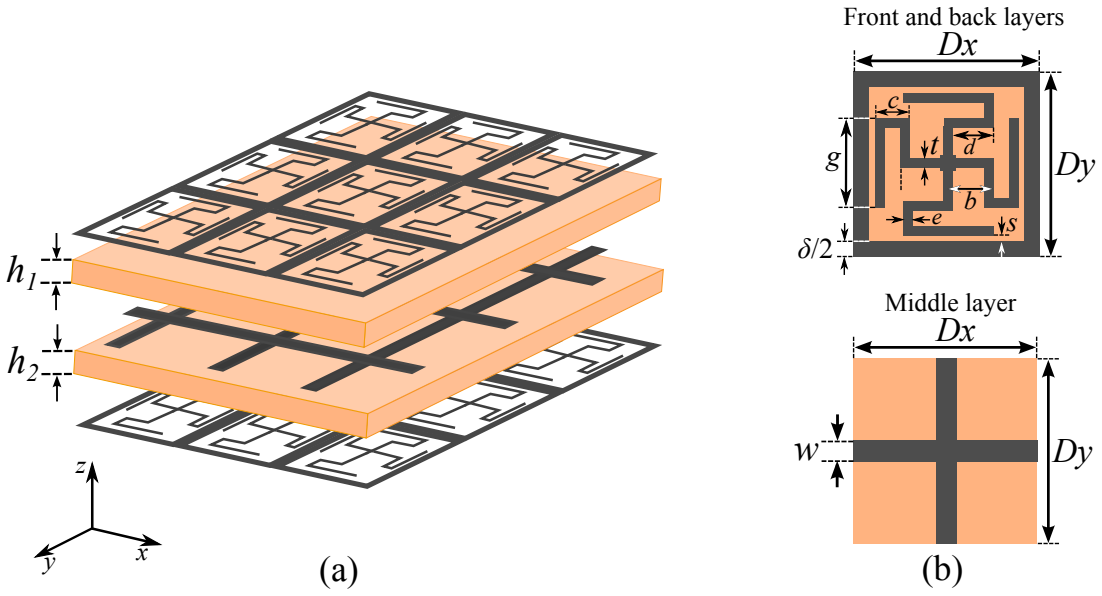

Figure 6.9. Proposed second-order tunable FSS. Structure of the proposed FSS. (a) 3-D exploded view of the FSS. (b) 2-D view of the unit cell.

symmetric with respect to the middle layer. The crossing points of the wire strips in middle layer are aligned with the centre of the resonators on the front and back layers. The overall thickness of the structure is $2h$, where h is the thickness of each dielectric spacer. The dimensions of the unit cell along the x and y directions are specified by $D_x = D_y = D$.

Since the FSS is designed based on the miniaturized elements sub-wavelength unit cells, its electromagnetic response can be modelled through an equivalent lumped-element circuit model. The circuit model provides a more insightful understanding of the FSS behaviour. In addition, it can be used to develop a synthesis procedure for designing the desired filtering response. The FSS circuit model under a normally incident plane wave is presented in Fig. 6.10(a), where the front and back layers of the FSS are modelled with the series $L_C C_C$ resonators in parallel with L inductor, where 1 and 2 denote the front and back layers, respectively. The inductor L models the inductive effect of the wire grid. The series $L_C C_C$ resonators model the cross-shaped resonators, where L_C is the equivalent inductance of the resonator arms and C_C stands for the capacitive effect between the edges of the wire grid and the resonator arms in each unit. The middle layer wire grid is modeled with the parallel inductor L_m. Furthermore, the two dielectric spacers are modelled with the transmission line sections of length h with characteristic impedance of $Z_T = Z_0/\sqrt{\epsilon_r}$, where $Z_0 = 377\ \Omega$ is the free space characteristic impedance and ϵ_r is the relative permittivity of the dielectric material.

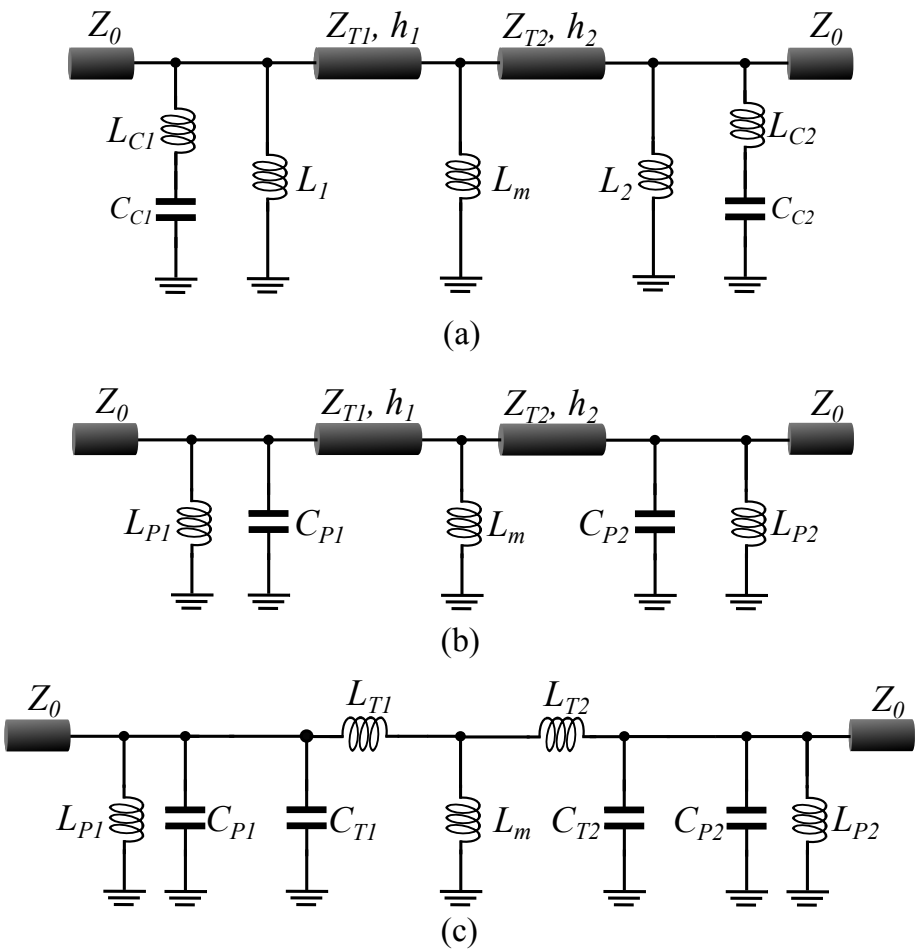

Figure 6.10. Circuit model of the proposed FSS. (a) Equivalent lumped-element circuit model of the proposed FSS. (b) Simplified circuit with the hybrid resonators replaced by their parallel LC equivalences. (c) Circuit with the transmission lines replaced with equivalent lumped elements models.

The free space on the two sides of the FSS is modelled with transmission lines having a characteristic impedance $Z_0 = 377\ \Omega$. The equivalent circuit in Fig. 6.10(a) can be simplified to the one in Fig. 6.10(b) by replacing the front and back hybrid resonators with their parallel LC equivalence. The relations between the hybrid resonator and the parallel LC resonator are as follows (Bonache *et al.* 2006a, Bonache *et al.* 2007): First, the frequency at which the equivalent admittance is nulled should be the same between the hybrid resonators in Fig. 6.10(a) and the parallel LC resonators in Fig. 6.10(b); this means

$$\frac{1}{\sqrt{(L+L_C)C_C}} = \frac{1}{\sqrt{L_P C_P}}. \tag{6.1}$$

Second, the susceptance slope of the two resonators should be equal to each other at the centre frequency of the filter. This condition leads to

$$C_C \left(\frac{L + L_C}{L} \right)^2 = C_P. \tag{6.2}$$

The third condition for determining the hybrid resonator element values is obtained by considering the transmission zero frequency provided by the series $L_C C_C$ branch in the hybrid resonator in Fig. 6.10(a). The transmission zero will improve the out-of-band rejection of the filter. The frequency of the transmission zero is given by

$$f_z = \frac{1}{2\pi\sqrt{L_C C_C}}. \tag{6.3}$$

A choice of the transmission zero is arbitrary. In this case it is positioned close to the passband to improve the sharpness of the filter response in the upper rejection band.

6.3.2 Synthesis procedure for the FSS

By using the telegrapher's equation (Pozar 2009), the sub-wavelength transmission line sections can be presented by their equivalent circuit models with series inducance $L_T = \mu_0 \mu_r h$ and shunt capacitance $C_T = \epsilon_0 \epsilon_r h/2$ where h is the spacer thickness and μ_r and ϵ_r are the permeability and permittivity of the dielectric spacer respectively. So, the circuit in Fig. 6.10(b) can be re-drawn as the one in Fig. 6.10(c) that is a second-order coupled-resonator bandpass filter. Based on the circuit in Fig. 6.10(c), a synthesis procedure can be developed for the proposed FSS by applying the concept of coupled-resonator filter with inductive coupling (Zverev 1967, Al-Joumayly and Behdad 2009). By specifying the centre frequency of the FSS f_0 and the fractional bandwidth $\delta = \mathrm{BW}/f_0$ to realise a desired filter type, e.g., Chebyshev, Butterworth, the element values can be designed for the circuit in Fig. 6.10(c). The design procedure can be summarised as follows:

1. The summation of the C_P and C_T capacitors for each of the front and back layers can be calculated by using the following equation:

$$C_i = C_{Pi} + C_{Ti} = \frac{q_i}{\omega_0 r_i Z_0 \delta}, \quad i = 1, 2 \tag{6.4}$$

where q_1 and q_2 are the normalised quality factors of the front and back layers resonators respectively, $Z_0 = 377\ \Omega$ and r_1 and r_2 are the normalised source and load impedances for the circuit in Fig. 6.10(c).

2. The input and output inductances L_{P1} and L_{P2} can be calculated as follow:

$$L_{Pi} = \frac{1}{\omega_0^2(C_i - k_{12}\delta\sqrt{C_1C_2})}, \qquad i = 1,2 \tag{6.5}$$

where k_{12} is the normalised coupling coefficient between the input and output resonators in Fig. 6.10(c).

3. The middle layer inductance L_m is determined as:

$$L_m = \frac{Z_0}{\omega_0 k_{12}} \cdot \frac{(k_{12}\delta)^2}{1-(k_{12}\delta)^2} \cdot \sqrt{\frac{r_1 r_2}{q_1 q_2}}. \tag{6.6}$$

4. The equivalent inductances of the transmission line sections can be obtained as follows:

$$L_{T1} = \frac{\sqrt{L_m^2(1+\alpha)^2 + 4\alpha L_m L_{12}} - L_m(1+\alpha)}{2\alpha}, \tag{6.7}$$

$$L_{T2} = \alpha L_{T1}, \tag{6.8}$$

$$L_{12} = \frac{1}{\omega_0^2(k_{12}\delta\sqrt{C_1C_2})}, \tag{6.9}$$

$$\alpha = \frac{q_1}{q_2} \cdot \frac{1 - k_{12}\delta\sqrt{\frac{q_2 r_1}{q_1 r_2}}}{1 - k_{12}\delta\sqrt{\frac{q_1 r_2}{q_2 r_1}}}. \tag{6.10}$$

The normalised quality factors q_1, q_2 and coupling coefficients k_{12} for the second-order filter of different types can be found in Zverev (1967) and Al-Joumayly and Behdad (2009). As mentioned before, the circuit in Fig. 6.10(c) is obtained from the one in Fig. 6.10(b) by using the telegrapher's equation. So, the lengths of the transmission

line sections representing the dielectric spacer thickness in Fig. 6.10 can be calculated as:

$$h_i = \frac{L_{Ti}}{\mu_0 \mu_{ri}}, \qquad i = 1, 2. \tag{6.11}$$

The values of the parallel capacitances C_{P1} and C_{P2} can then be obtained from

$$C_{Pi} = C_i - \frac{\epsilon_0 \epsilon_{ri} h_i}{2}, \qquad i = 1, 2. \tag{6.12}$$

Now, the element values of the front and back resonators in Fig. 6.10 can be determined by using (6.1)-(6.3). The parameters of the equivalent circuit in Fig. 6.10(a) can be mapped to the geometrical dimensions of the FSS by using the method explained in Behdad *et al.* (2009). It should be noted that the substrate thicknesses calculated from (6.11) might not be commercially available. These calculated geometrical values are treated as an initial approximation in the optimisation procedure of the FSS using the full-wave EM simulations. The effective inductance of a wire grid can be related to wire width w and the unit cell size D by using (Munk 2005, Bayatpur 2009)

$$L = \mu_0 \mu_{\text{eff}} \frac{D}{2\pi} \ln\left(\frac{1}{\sin\frac{\pi w}{2D}}\right), \tag{6.13}$$

where μ_{eff} is the effective relative permeability of the substrate. Therefore, this equation can be used to design the middle layer wire grid dimensions. To this end, the unit cell size D can be chosen arbitrarily, but it should be considered that a very small unit cell size leads to very thin wires that might not be implementable due to fabrication limits. The next step is to design the front and back hybrid resonators in a way that they satisfy the designed equivalent circuit elements (L and $L_c C_c$). Equation (6.13) provides an approximation to the dimensions of the wire grids. Since the resonators are included, the wire grids in the front and back layers require optimisation to account for parasitic effects induced by the resonators. As the initial step, the unit cell size of the hybrid resonator is the same as the size considered for the middle layer wire grid D. Then, the width of the wire grid that surrounds the cross-shaped resonator can be calculated from (6.13). Next, the cross-shaped resonator dimensions and the wire grid width should be optimised by knowing that the equivalent inductance of the cross-shaped resonator (L_C) mainly depend on the width t and the length ($b + c + g$) of the resonator arms. In addition, the values of capacitance C_C is mainly controlled by the distance between the cross-shaped resonator arms and the wire grid edges s and the g

portion of the cross-shaped resonator. A practically realisable value can be chosen for the gap S between the crossshaped resonator arms and the wire grid. The length of the cross-shaped resonator arms $2(b+c+g)$ is considered to be $\lambda_g/2$ at the transmission zero frequency f_z, where $\lambda_g/2$ is the guided wavelength with arbitrary equal values for t and e. Now, the L_C and C_C values associated with the cross-shaped resonator can be determined by a semi-analytical procedure as follow: the zero frequency of the FSS is calculated from (6.3). This frequency can be obtained from the EM simulation in CST Microwave Studio as well. By considering an arbitrary lumped capacitor of C_{ar} between the resonator arms and the wire grid the transmission zero frequency will be

$$f_{z1} = \frac{1}{2\pi\sqrt{L_C(C_C + C_{ar})}}. \tag{6.14}$$

Thus, by solving (6.3) and (6.14), the values of L_C and C_C associated with the cross-shaped resonator are calculated. If the obtained L_C and C_C are matched with the designed parameters using the circuit synthesis, the optimisation is finished for the cross-shaped resonator otherwise, the procedure should be repeated until reaching a good match between the parameters obtained from the EM simulation and the synthesised ones. After optimising the cross-shaped resonators dimensions, the width of the wire grid δ can be optimised by the curve fitting of the EM and circuit simulation around the null frequency of the hybrid resonator that is described by (6.1). After obtaining the optimised δ, the transmission zero frequency f_z might be shifted a bit. This shift can be compensated by small variations of the cross-shaped resonator arm $(b+c+g)$ and t.

6.3.3 Tuning mechanism

The proposed FSS can be simply modified to exhibit a tunable response by loading varactors in the front and back layers, as shown in Fig. 6.11(a) (with the back layer excluded for clarity). A metallic via in each unit cell is used to electrically connect the front and back cross-shaped resonator to the middle layer wire grid. This configuration is depicted in Fig. 6.11(b) through the cross-sectional view of the unit cell. The varactors are loaded in the gaps between the cross-shaped resonator arms and the front and back wire grids. By applying a DC bias voltage between the middle wire grid and the front and back wire grids, the equivalent capacitance (C_{C1} and C_{C2}) between the cross-shaped resonators the front and back wire grids can be varied resulting in a tunable

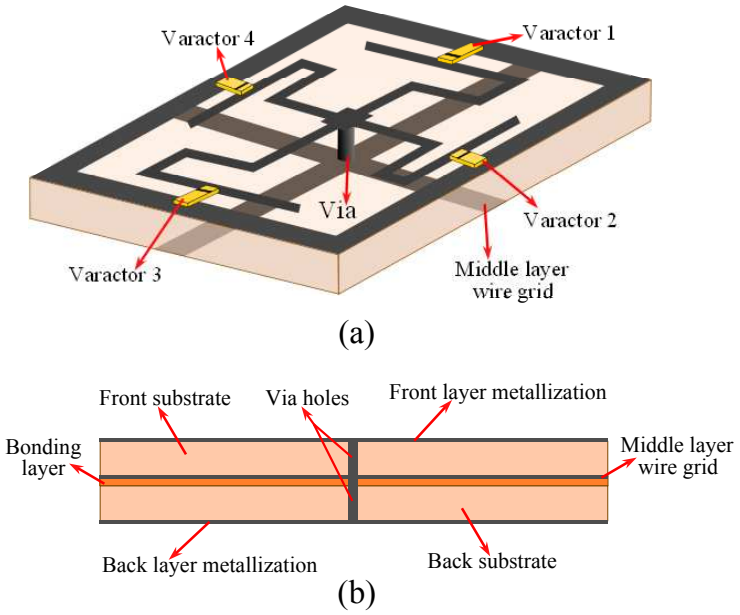

Figure 6.11. Varactor loaded unit cell with via hole. (a) 3D view of the front and middle layers of the unit cell. A metallic via and four varactor diodes are included in each unit cell for tuning. The back layer and the other dielectric spacers are not drawn for clarity. The black strips show the cathode side of the varactors. (b) Cross-section view of the unit cell indicating the three metallisations, via holes and the bonding layer.

frequency response for the FSS. In this condition, the equivalent capacitances of the hybrid resonators can be defined as a summation of the varactor capacitance C_{var} and the capacitance between the cross-shaped resonators and wire grids C_0,

$$C_{Ci} = C_{\text{var}} + C_{0i}, \qquad i = 1, 2. \tag{6.15}$$

A significant benefit of this structure compared with other varactor-tunable FSSs (Mias 2005, Huang *et al.* 2015, Pan *et al.* 2013) is in this case, all the varactors are electrically biased in parallel and no additional bias network such as thin bias wires, resistors, or lumped capacitors are needed. It requires only a single RF choke to connect in series with the DC voltage supply to isolate the DC signal from the RF signal.

6.3.4 Structure realisation

The described synthesis procedure has been used to design a varactor-loaded FSS having a centre frequency of 5.2 GHz and a fractional bandwidth of $\delta = 9\%$. The loaded varactor is with minimum capacitance of 0.12 pF. A transmission zero is positioned at

$f_z = 6$ GHz to improve the upper band selectivity of the filter. The FSS is designed to exhibit a Butterworth response, and so the extracted k_{12} and q values are 1.4142 and 0.707 respectively. The Teconic TLY-5 with a relative permittivity of 2.2 and a loss tangent of 0.0009 is chosen as the dielectric substrate. Based on this specification and from (6.1)–(6.10), the equivalent circuit parameters are calculated as: $L_m = 4.5$ nH, $C_{C1} = C_{C2} = 0.21$ pF, $L_{C1} = L_{C2} = 2.78$ nH, $L_1 = L_2 = 1.7$ nH. The calculated spacers thickness $h_1 = h_2 = 1.65$ mm is not commercially available. Therefore, we have chosen $h = 1.52$ mm that is the closest commercially available thickness. Furthermore, the front and back dielectric spacers have to be bonded to each other. The bonding layer consists of a 0.1 mm thick Rogers 4450F with a relative permittivity of $\epsilon_r = 3.58$. The presence of this thin bonding layer introduces asymmetry, which can be compensated via optimisation. The optimisation has been carried out at the circuit level in Advanced Design System (ADS). In the simulation, this bonding layer is represented by a transmission line with a length of 0.1 mm and a characteristic impedance of 207.5 Ω in series with the transmission line that represents the back spacer. The h values are kept constant, whereas the other circuit parameters are tuned to achieve the specified filter characteristics. It should be mentioned that in the optimisation the circuit parameters obtained from (6.1)–(6.10) are considered as initial values. Having these initial values significantly simplifies the optimisation process.

In the next step, the optimised circuit parameters in ADS are converted to the physical dimensions of the FSS by using a procedure explained in Section 6.3.2. In full-wave simulations, four lumped capacitors each with 0.12 pF are placed between the cross-shaped resonator arms and wire grids in each of the front and back layers of the FSS to model the varactor diodes. The varactor diode is MA46H120 from M/A-COM which is a GaAs flip-chip diode and provides a range of capacitance between 0.12–1 pF for a reverse bias voltage between 16 V and 0 V. The optimised equivalent circuit and the geometrical parameters of the designed FSS are listed in the caption of Fig. 6.12. The slight difference in the dimensions and circuit parameters between the front and back layers reflect the asymmetry that is imposed by the bonding layer. The simulated fractional bandwidth is 8.8% and the upper stopband transmission zero is achieved at 5.97 GHz, close to the desired filter specifications. A comparison in Fig. 6.12 shows a good agreement between the circuit model and 3D EM simulation results.

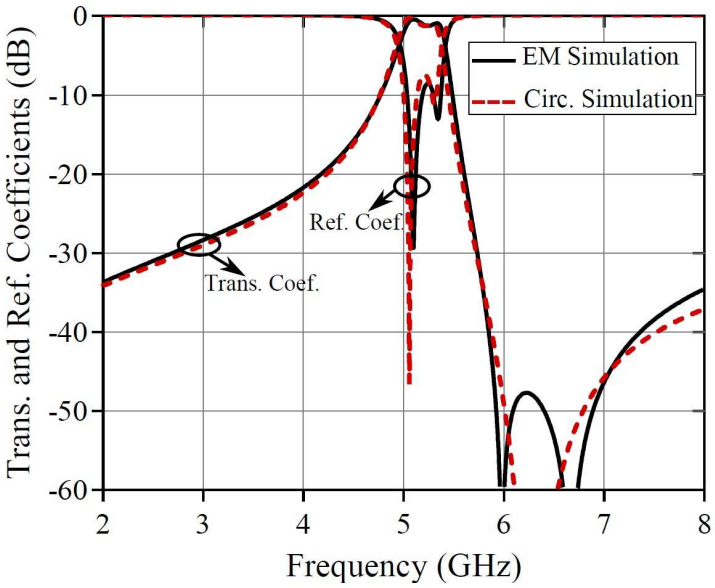

Figure 6.12. Circuit versus EM simulation results. Comparison between the circuit model and full-wave electromagnetic simulation results of the designed FSS. The optimised equivalent circuit parameters are: $h_1 = h_2 = 1.52$ mm, $C_{C1} = 0.251$ pF, $C_{C2} = 0.231$ pF $L_{C1} = 2.48$ nH, $L_{C2} = 2.65$ nH, $L_1 = 1.95$ nH, $L_2 = 2.07$ nH, $L_m = 3.1$ nH. The unit cell geometrical dimensions are: $D_x = D_y = 8$ mm, $\delta_1 = \delta_2 = 0.9$ mm, $g_1 = 3.8$ mm, $t_1 = t_2 = e_1 = 0.6$ mm, $e_2 = 0.3$ mm, $s_1 = s_2 = 0.3$ mm, $b_1 = b_2 = 2.3$ mm, $c_1 = c_1 = 1.25$ mm, $d_1 = 1.6$ mm, $d_2 = 1.5$ mm, and $w = 0.65$ mm.

6.3.5 Results and discussion

A prototype of the designed FSS has been fabricated and tested inside a parallel-plate waveguide to show the validity of the design and the effectiveness of the tuning method. An array of 3×18 unit cells is fabricated to match the dimensions of the waveguide aperture. The overall thickness of the fabricated sample is 3.14 mm, which is less than $\lambda_0/18$ at 5.2 GHz. The cross-shaped resonators in the front and back layers of the FSS are connected to the middle layer wire grid through via holes with 0.3 mm diameter. A 47 kΩ resistor is soldered to the middle layer wire grid to act as an RF choke. The fabricated prototype and its front and back unit cells are demonstrated in Fig. 6.13. Since the TEM mode can be excited inside the parallel-plate waveguide in the frequency range of interest (Shang *et al.* 2013, Li and Shen 2014, Shang *et al.* 2014), only two varactors aligned with the E-field direction are soldered in each front and back unit cell. The FSS is then placed inside the waveguide and the bias wires are connected to a variable DC power supply. In this way, all the varactors are reverse-biased and by changing the DC bias voltage (V_b), the varactors capacitance will be tuned.

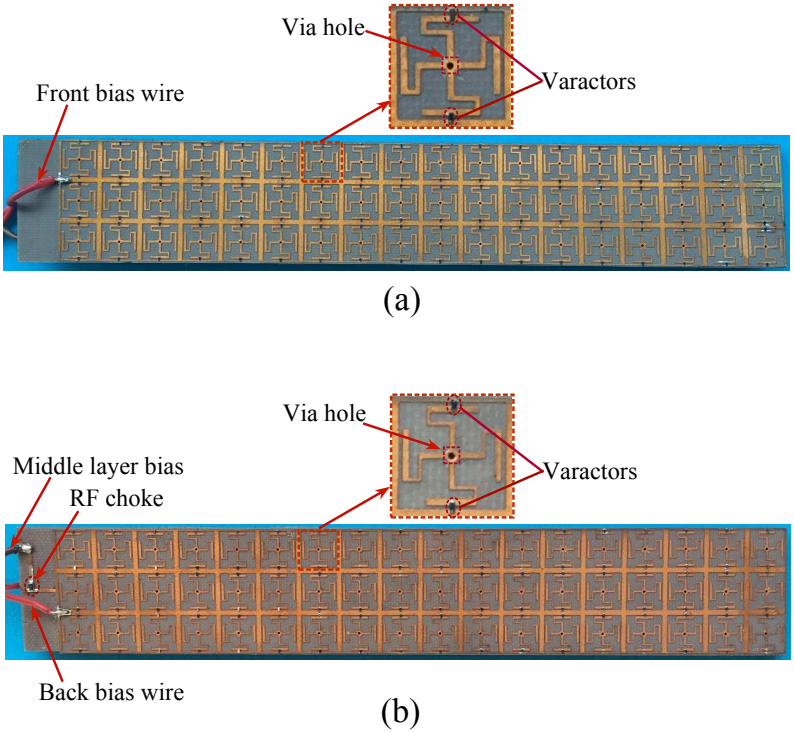

Figure 6.13. Realised FSS sample. Fabricated FSS prototype. (a) Front layer with an inset showing a unit cell. (b) Back layer with an inset showing a unit cell. Two red wires are soldered to the front and back wire grids to apply the negative bias voltage. A black wire in series with the RF choke is soldered to the middle wire grid to provide the grounding.

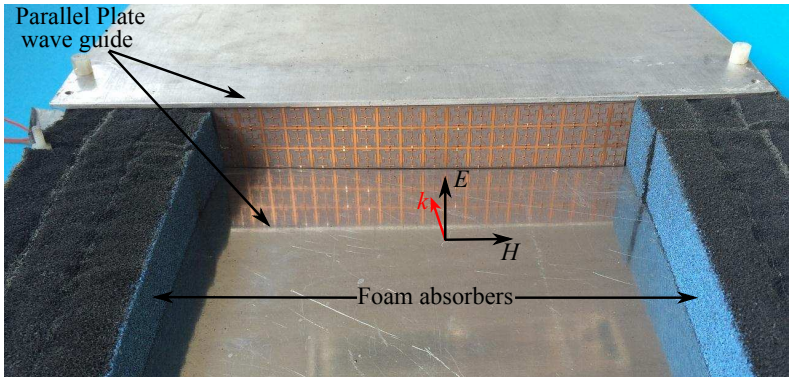

Figure 6.14. FSS test setup. FSS inside the parallel-plate waveguide testing platform.

In the measurements, first the bias voltage is set to 16 V to yield the lowest capacitor value of 0.12 pF for each varactor, which corresponds to a center frequency of 5.2 GHz for the filter response. Then, the bias voltage is decreased step by step and the corresponding transmission response has been recorded for each step. The normalised measured transmission responses of the FSS for different bias voltages are plotted in

Fig. 6.15 together with the results from EM simulations for normal incidence. The EM simulations in CST Microwave studio are carried out with Floquet boundary condition to replicate an infinite planar array of the unit cells.

There is a good agreement between the simulated and measured results. The discrepancies between them are mostly attributed to the small air gap between the top and bottom plates of the waveguide and the FSS edges that would be improved if free-space measurement setup is used. The passband is defined at -3 dB from the peak of the transmission response. The maximum measured insertion loss within the FSS passband varies from 3 dB to around 6 dB when the reverse bias voltage changes from 16 V to 4 V. This is mostly caused by the ohmic loss in the varactor diodes. The insertion loss increases by decreasing the bias voltage. This is because the varactor possesses a higher series resistance in lower bias voltages. Fig. 6.16(a) plots the series parasitic resistance of the varactor obtained from the spice model. The FSS center frequency and the varactor capacitance versus the bias voltage are pltted in Fig. 6.16(b). As seen, the simulated and measured center frequencies are very close to each other. The variation of the center frequency is smoother for the voltages above 10 V, but it gets sharper for the smaller voltages. This is due to the nonlinear relationship between the varactor capacitance and the bias voltage, where below 10 V the slope of the capacitance is larger than the slope for higher bias voltages.

The sensitivity of the FSS transmission response to the oblique incidences is examined by using 3D EM simulations for both of the TE and TM polarisations of the incident wave. The results are demonstrated in Fig. 6.17 for both of the upper and lower limits of the tunning band. It is observed that the designed FSS shows a stable passband frequency response over a wide range of the incident angles up to 60° for both polarisations. This stability is a result of the very thin profile and the miniaturised dimensions of the unit cells (Bayatpur 2009). However, weak resonances appear in the out-of-band response for oblique incidences, and sharp harmonics appear in the upper stopband for the TM responses. The weak resonances are mainly attributed to the field imbalance across the FSS unit cells that excites higher-order resonance modes. The out-of-band sharp harmonics in the TM responses are because of the conductive via holes. For the TM-polarised excitations, the longitudinal component of the electric field exists and couples to the metallic via holes. This effect can be modelled by adding an inductance between the middle layer and series $L_C C_C$ resonators. These out-of-band week resonances can be suppressed by fabricating via holes with a thinner diameter.

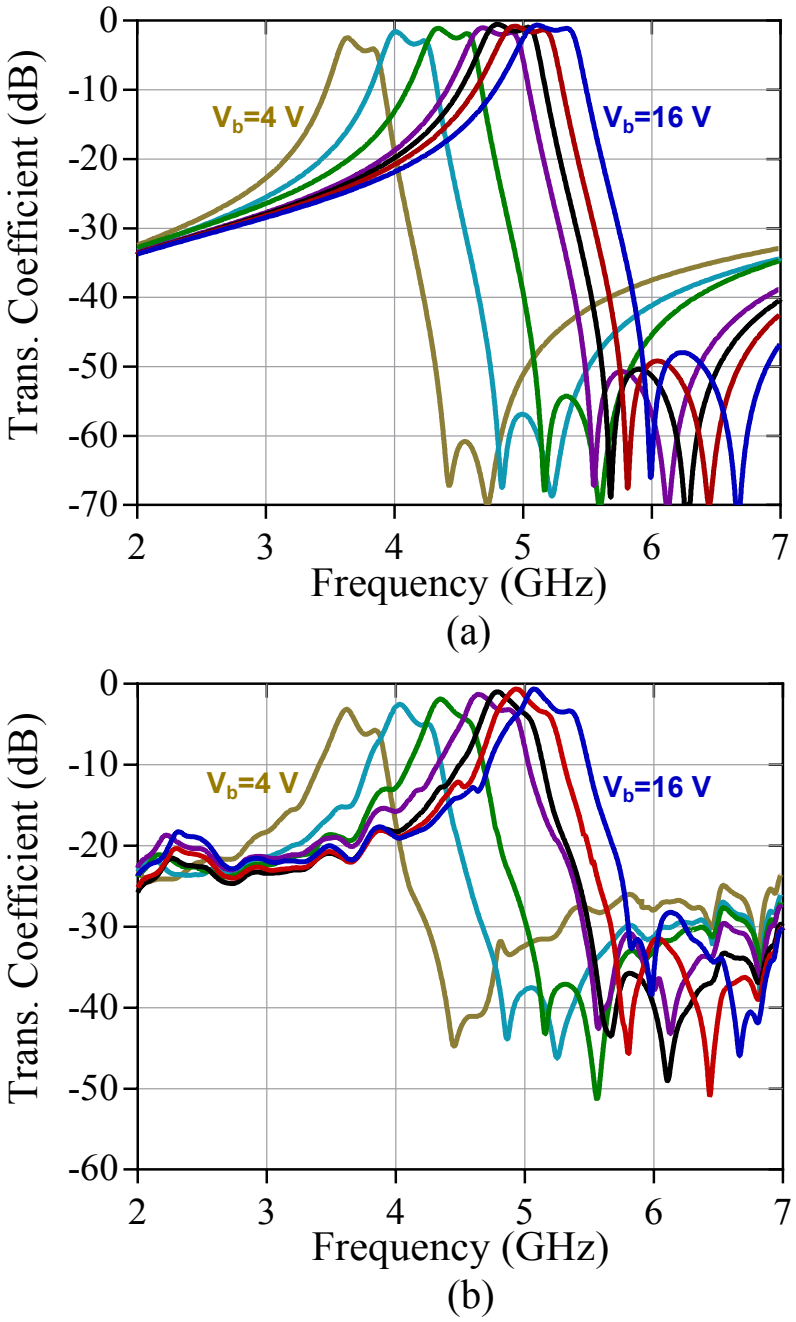

Figure 6.15. Measured versus simulated transmission coefficients of the FSS. Transmission responses of the designed tunable FSS under normal incidence for different values of varactor bias voltage. The reverse bias voltage (V_b) is varied from 16 V to 4 V with a step size of 2 V. (a) The results obtained from EM simulations. (b) Measured transmission responses.

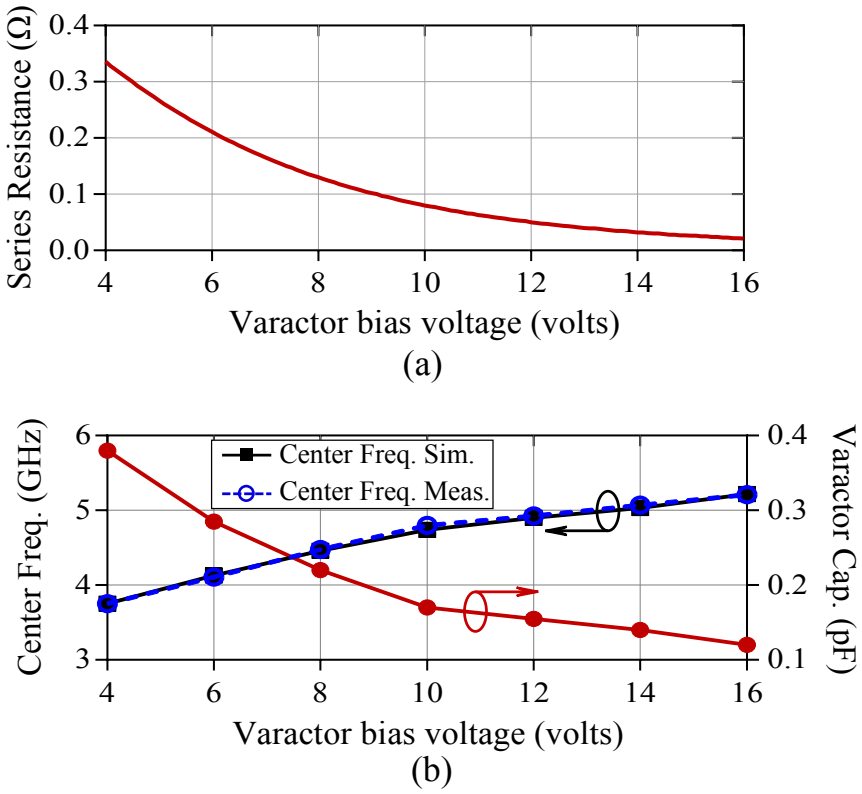

Figure 6.16. Varactor characteristics and centre frequency variation. (a) Series resistance of the varactor as function of the bias voltage. (b) Variation of the varactor diode capacitance and the center frequency of the FSS as a function of the reverse bias voltage.

6.4 Ka-band tunable FSS based on liquid crystals

Despite their easy tuning, low fabrication cost and wide tuning range, the varactor diodes demonstrate low quality factors at higher microwave frequencies. This drawback urges the designers to look for alternative tuning mechanisms at frequencies beyond the C-band. Several tuning techniques such as MEMS technology, Barium Strontium Titanate (BST) varactors, and ferrite substrates have been utilised in designing tunable or reconfigurable devices (Zendejas *et al.* 2006, Chang *et al.* 1994, Sazegar *et al.* 2011, Sazegar *et al.* 2012). Among all these methods, recently the liquid crystals have shown promising advantages such as lower losses at higher frequencies, low bias voltage and continuous tuning (Yaghmaee *et al.* 2013a, Yaghmaee *et al.* 2012b). Several liquid crystals-based tunable devices for high frequency applications from the microwave up to the infrared and terahertz are reported in the literature (Hu *et al.* 2006, Yaghmaee *et al.* 2012a, Goelden *et al.* 2009, Kuki *et al.* 2002).

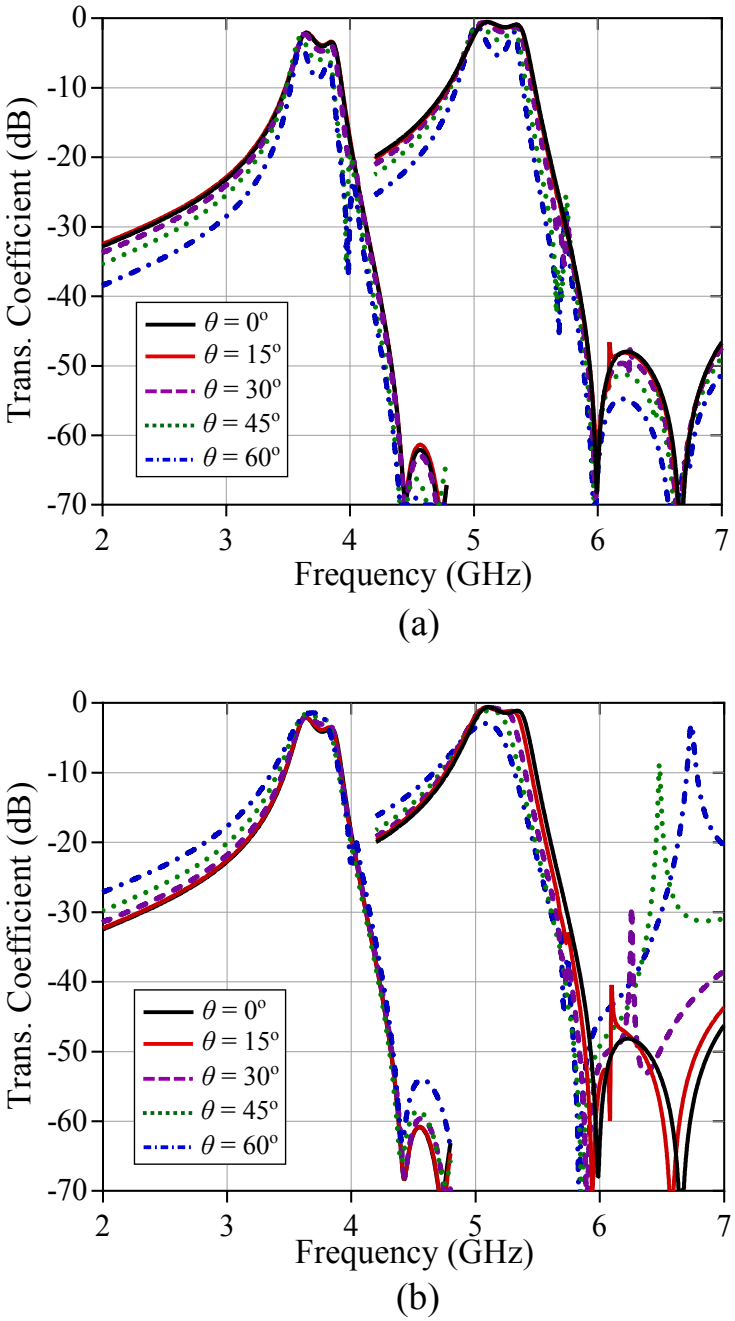

Figure 6.17. Scanning angle performance of the proposed FSS. Simulated transmission responses of the tunable FSS for oblique incidece angles (a) TE polarisation, and (b) TM polarisation.

This section presents a single-pole tunable X-band FSS based on liquid crystals. Tunability is obtained by integrating the liquid crystal cells inside the dielectric substrate that separates the front and back metallic arrays. A brief explanation of the liquid crystal tuning mechanism is given in Section 6.4.1. The FSS design procedure and electromagnetic simulation results are presented afterwards.

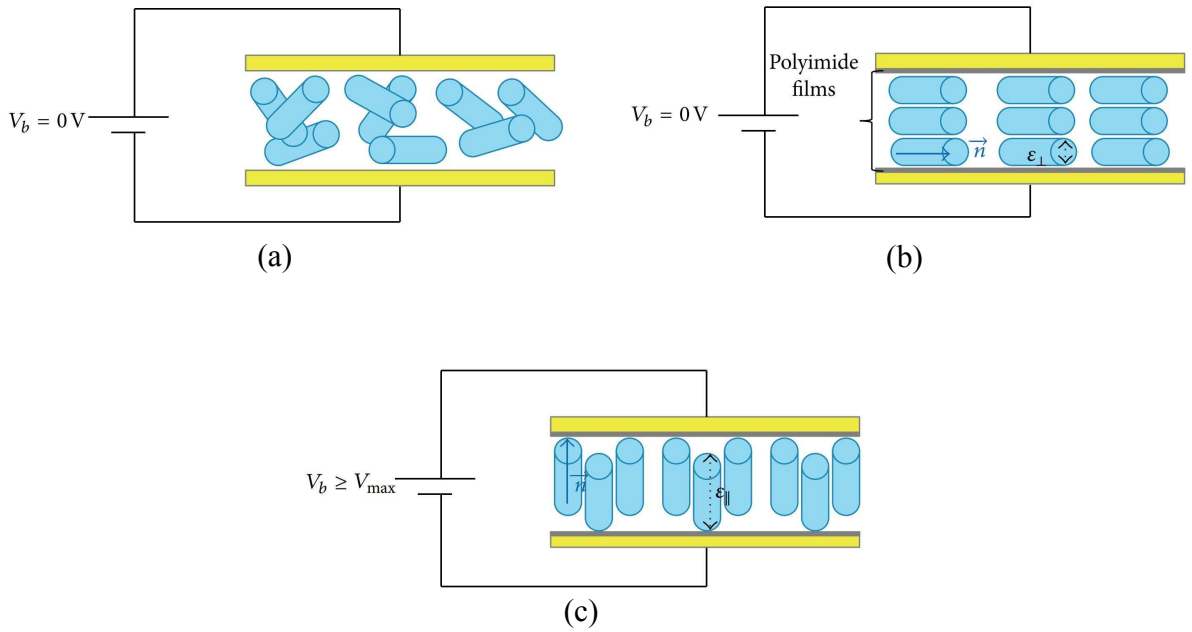

Figure 6.18. Liquid crystal tuning mechanism. The molecule orientation of liquid crystals results in variable dielectric property. (a) Random orientation in absence of polyimide film. (b) Perpendicular orientation by introducing polyimide film. (c) Parallel orientation by applying bias voltage to the capacitive plates. After Yaghmaee *et al.* (2013a).

6.4.1 Liquid crystal-based tuning mechanism

Liquid crystals are dielectric materials, with anisotropic characteristics that exhibit three different mesophases, between solid (crystalline) and liquid (isotropic) states, known as nematic, smetic, and cholesteric phases (Mueller *et al.* 2005). The nematic phase with thread- or rod-like molecules is of interest, existing in both the solid and the liquid states. Compared to other commercially available electrically tunable materials e.g. Barium Strontium Titanate (BST) (Sazegar *et al.* 2012), they typically require a very low bias voltage for tuning ($V_b \leqslant 30$ V), are widely commercially available and can be integrated with flexible printing technologies (Yaghmaee *et al.* 2012a). The macroscopic anisotropy unit vector that points in the main average direction of the liquid crystal molecules is known as the director $\vec{n}$. The anisotropy tensor exhibits a relative permittivity $\epsilon_{||}$ in the director direction, and $\epsilon_\perp$ in the orthogonal directions as demostrated in Fig. 6.18. In a typical capacitive arrangement, where a liquid crystal cell is sandwiched between two metal electrodes, a thin layer of polyimide film (≈ 0.4 μm) with fine grooves is placed on top and bottom to align the liquid crystal molecules in the unbiased state (Garbovskiy *et al.* 2011). Because of the grooves, the director will be aligned in parallel with the metallic layers in the unbiased state and the effective

relative permittivity for the inter-layer capacitance is $\epsilon_{\perp}$ (perpendicular state). Alternatively, when a bias voltage is applied ($V_b \gg V_{th}$, where V_{th} is the threshold voltage), the molecules will re-orientate so that the relevant effective permittivity will gradually become the relative permittivity along the director. The final state ($\epsilon_{eff} = \epsilon_{||}$), corresponds to a full alignment of the liquid crystal directors along the static electric field lines associated with the applied voltage (parallel state). The bias-dependent transition from the perpendicular to parallel state provides a continuous variation of the effective permittivity between these two states. The difference between these two extreme permittivity states can be described as $\Delta = \epsilon_{||} - \epsilon_{\perp}$ which is commonly known as the dielectric anisotropy or anisotropy of the liquid crystal (Mueller *et al.* 2008).

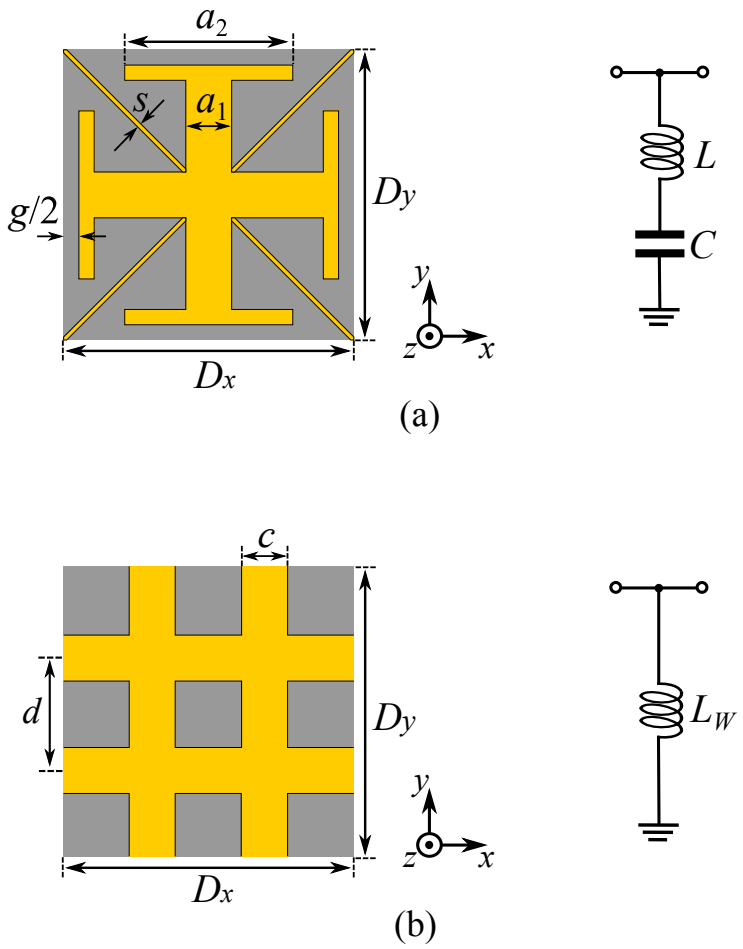

Figure 6.19. Unit cells of the designed FSS. (a) The front layer unit cell and its equivalent circuit model. (b) The back layer unit cell and its equivalent circuit model. The dimensions are: $a_1 = 1.6$ mm, $a_2 = 1$ mm, $b = 0.3$ mm, $d = 6.2$ mm, $s = 0.3$ mm, $c = 1$, $D_x = D_y = 7$ mm. The dielectric substrate is shown in grey colour and the metallisation is indicated in yellow.

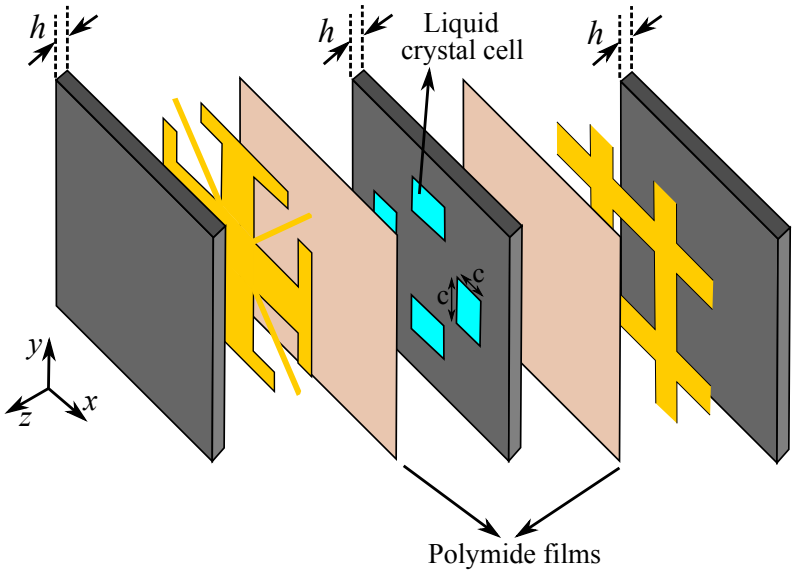

Figure 6.20. Structure of the designed FSS. Single unit cell of the multi-layered FSS structure, illustrating each individual layer and the liquid crystal sample placed in the middle layer, in the overlapping areas between the front pattern and the back copper grid. The dimensions are as follows: $c = 1$ mm and $h = 0.127$ mm.

6.4.2 Design and modelling of the FSS

In order to demonstrate the tuning performance of the liquid crystal-based FSS, a two-layer FSS is designed to act as a simple single-pole filter with an adjacent transmission zero. The front layer is composed of cross-shaped metallic elements printed on one side of a thin dielectric substrate, as shown in Fig. 6.19(a). In this structure, for an x-polarised wave incident normally onto the FSS, the array acts as a series LC resonant circuit of Fig. 6.19(a), where the inductance L is mainly determined by the length d and width c of the cross wires and the capacitance C is mainly determined by the gap between the two adjacent caps g and their dimension a_2. Due to symmetry of the design, the array also shows the same behaviour for a y-polarized incident wave.

The back layer of the FSS, shown in Fig. 6.19(b), is composed of a wire grid printed on a thin dielectric substrate. It is well-known that these thin metallic strips will generate an inductive response if excited by an incident electromagnetic wave (Bayatpur and Sarabandi 2009b). Therefore, this layer can be modelled through a lumped inductor L_W as shown in Fig. 6.19(b). These two metallic arrays are separated by an intermediate dielectric layer. The middle dielectric layer should be thin enough (≥ 0.2 mm) to allow strong electromagnetic interaction between the front and the back arrays. This very thin intermediate dielectric layer will create an interlayer capacitor where the front

cross shape resonators and the back wire grid overlap in the overall configuration as shown in Fig. 6.20. The tuning characteristic of this FSS is achieved by controlling this interlayer capacitance value C_{int}. In this work, in order to tune the FSS, the liquid crystal is introduced in cells created in the substrate at the location of the capacitors. As in Withayachumnankul *et al.* (2011), thin conductor strips with a width s are added in the design to electrically connect every unit cell for facilitating application of an external bias voltage (see Fig. 6.18). Due to the very narrow width of the conductor strips, they show a very large inductance, which is negligible at high frequencies compared with L and L_W and hence their effect on the transmission response is minimal. Varying the bias voltage changes the effective permittivity of the liquid crystal, and hence causes a change in the interlayer capacitor value. The change in the capacitance leads to a frequency shift in the transmission response of the FSS. The final schematic of the FSS unit cell is shown in Fig. 6.20, where the location of the liquid crystal cells are visible in the overlap areas of the front and back metallic arrays.

To gain better insight into the qualitative FSS behavior, a lumped element equivalent circuit is developed to describe the expected frequency response of the entire structure. As shown in Fig. 6.21, the equivalent model is composed of two parallel branches representing the two array layers. The left branch of the circuit models the cross-shaped metallic array that shows a bandstop behaviour. The capacitor in this branch is a function of the gap between two adjacent cross elements g. The L_1 is a portion of inductor L before the centre of the overlap capacitor and L_2 models the portion which is located after the centre of the overlap capacitor. Their values are a function of a_1 and d (Fig.6.18). The right branch, on the other hand, models the back side of the FSS, which shows a purely inductive behaviour and has a low-pass response. Finally, the interlayer capacitor is modelled by a lumped voltage dependent capacitor C_{int}, which can be tuned by applying a voltage between the metallic elements of the two array layers. Furthermore, in the circuit model, the substrates are modelled by three short pieces of transmission lines having the characteristic impedance of $Z_0/\sqrt{\epsilon_r}$, where ϵ_r is the relative permittivity of the thin substrate layers. The free space on the either sides of the FSS is modelled with a characteristic impedance of Z_0. In this circuit, all metallic and dielectric losses are ignored for simplicity.

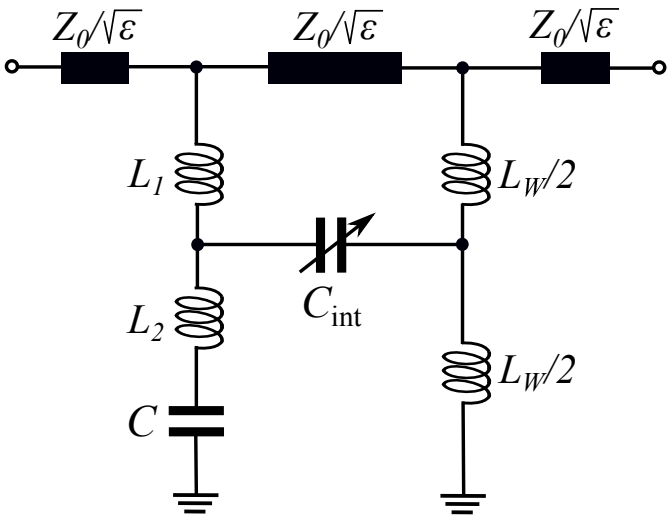

Figure 6.21. Circuit level modelling of the designed FSS. Lumped element circuit model of the designed tunable FSS. Elements values are: $L_1 = 0.76$ nH, $L_2 = 0.38$ nH, $C = 0.094$ pF, $L_W = 0.58$ nH, and $C_{\text{int}} = 0.1$ pF.

Table 6.2. Tuning performance of different liquid crystals samples. Comparison of full-wave simulation results for K15, BL037 and GT3-23001 liquid crystals.

Models	$\epsilon_\perp$	$\epsilon_{\|\|}$	$\tan\delta_\perp$	$\tan\delta_{\|\|}$	Δ	freq. (GHz)
K15	2.72	2.9	0.03	0.03	0.18	1-10
BL037	2.35	2.61	0.06	0.06	0.26	1-10
GT3-23001	2.50	3.30	0.0143	0.0038	0.8	19

6.4.3 Results and discussions

The unit cell of the frequency selective surface is simulated in CST Microwave Studio, using the frequency-domain solver over a frequency range of 6–15 GHz. For this full-wave electromagnetic simulation the front, middle and back dielectric layers are simulated as a RT/duroid 5880 substrate ($\epsilon_r = 2.2$, $\tan\delta = 0.0009$, thickness $h = 0.127$ mm). Also, the lumped element circuit model is developed in Advanced Design System (ADS) software using the first-order element values approximation presented in Yaghmaee *et al.* (2013b) and with the values selected to best fit the full-wave simulations. The continuous frequency tuning of the FSS is studied using three different liquid crystal samples, known as K15 (5CB), BL037 and the new GT3-23001 mixture, with corresponding dielectric anisotropy of 0.18, 0.26 and 0.80 respectively. The anisotropy of

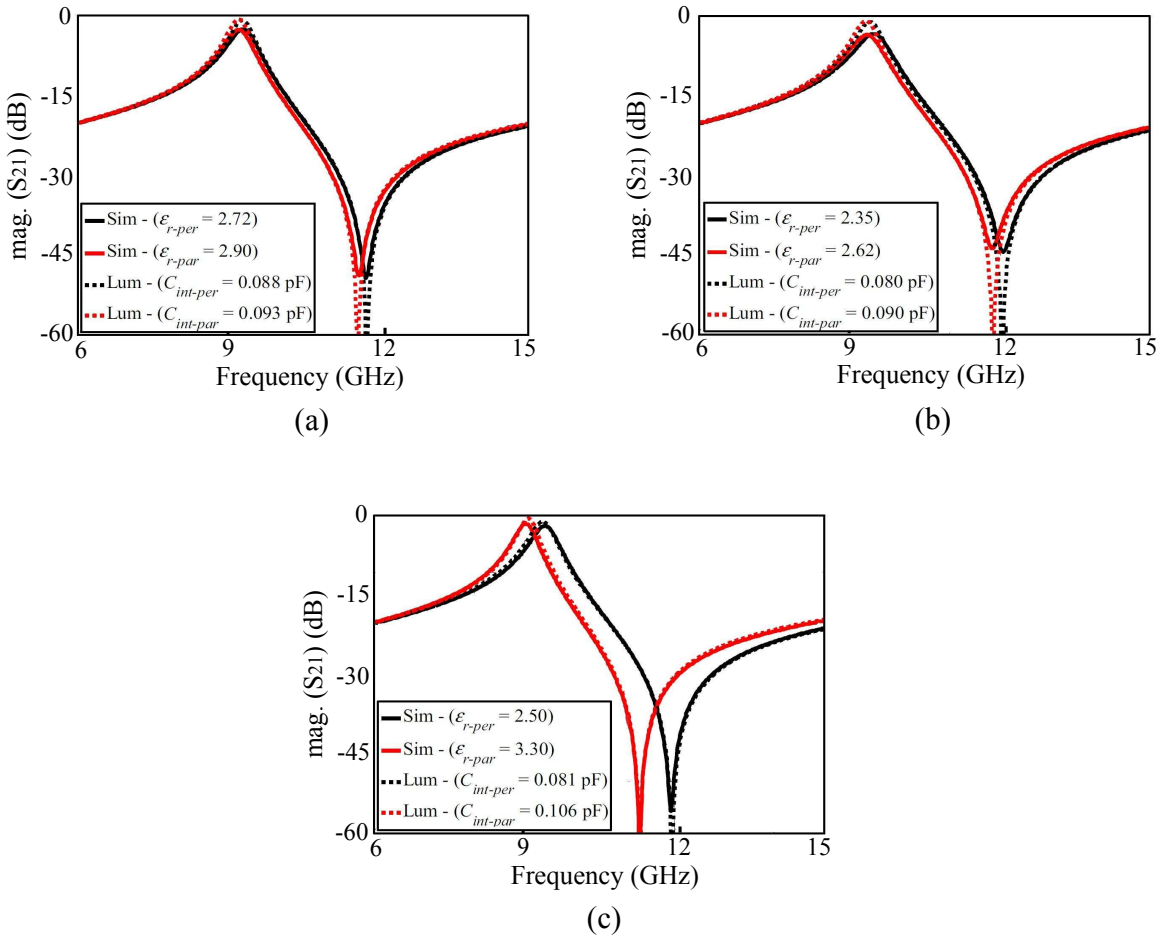

Figure 6.22. Full-wave electromagnetic and circuit model simulation results. Frequency tuning range and insertion loss comparison for, (a) K15 (5CB) (c) BL037 and (b) GT3-23001.

the liquid crystal is taken into account by considering the two permittivity tensor values in the extreme states ($\epsilon_{||}$ and $\epsilon_{\perp}$), with their corresponding loss tangent ($\tan\delta_{||}$ and $\tan\delta_{\perp}$), given in Table 6.2 (Yaghmaee *et al.* 2012a, Yaghmaee *et al.* 2013b). The full-wave electromagnetic simulations indicate that by varying the effective relative permittivity of the liquid crystal for the K15 sample from $\epsilon_{\text{eff}} = 2.72$ to 2.90, the pass-band centre frequency of the designed FSS shifts from 9.32 to 9.20 GHz (120 MHz) as shown in Fig. 6.22(a). This is equivalent to a frequency shift of 1.3% relative to the lower frequency. However, when the BL037 liquid crystal sample is used, the frequency shifts from 9.50 to 9.29 GHz, indicating a frequency shift of around 2.2% i.e. approximately twice the frequency tuning obtained with the K15 liquid crystal (Fig. 6.22(b)). Finally, as plotted in Fig. 6.22(c), when the cells are filled with the GT3-23001 liquid crystal mixture from Merck, the pass-band centre frequency of the structure shifts from 9.49 to 8.98 GHz (510 MHz), which corresponds to the larger frequency shift of 5.6%. In the

Table 6.3. Tuning performance of different liquid crystals samples. Comparison of full-wave simulation results for K15, BL037 and GT3-23001 liquid crystals.

Models	$f_{\perp,\text{zero}}$ (GHz)	$f_{\|\|,\text{zero}}$ (GHz)	$f_{\perp,\text{pole}}$ (GHz)	$f_{\|\|,\text{pole}}$ (GHz)	Tun. (%)
K15	11.76	11.61	9.32	9.20	1.3
BL037	12.06	11.85	9.50	9.29	2.2
GT3-23001	11.94	11.31	9.49	8.98	5.6

ADS circuit simulations corresponding to the three cases above, the value of C_{int} was modified based on variation of ϵ_{eff}. These results illustrate that C_{int} changes from 0.088 to 0.093 pF for K15, 0.080 to 0.090 pF for BL037 and from 0.081 to 0.106 pF for GT3-2300, for the both perpendicular and parallel states respectively as shown in Table 6.3.

The obtained information suggests the feasibility of using liquid crystals to tune the frequency response of this single-pole FSSs, and the principle can be scaled for operation at higher frequencies, e.g. in the Ka-band, where the dissipation of liquid crystal is low and lumped varactors become too bulky for integration into the FSS.

6.5 Dual-band FSS based on miniaturised elements

In advanced microwave systems, multiband FSSs are needed to cover different operational frequency bands (Al-Joumayly and Behdad 2010). Different schemes are proposed for designing multiband FSSs such as: fractal metallic arrays (Gianvittorio *et al.* 2001, Romeu and Rahmat-Samii 2000), perturbation techniques (Hill and Munk 1996) and genetic algorithms (Manara *et al.* 1999, Bossard *et al.* 2005). In most of the presented structures, the unit cell size or element spacing is comparable to the resonance wavelength and this makes them highly sensitive to the incidence angle of the electromagnetic wave and causes undesirable low-order harmonics in the frequency response. Recently, new types of dual-band frequency selective surfaces have been introduced (Al-Joumayly and Behdad 2010, Bayatpur and Sarabandi 2008a, Salehi and Behdad 2008) that make use of non-resonant elements in their structures. These recent designs show a lower dependency to oblique angles of the incident wave. However, the element sizes are not small enough (around $\lambda_0/6$) for the applications where the FSS should be used in very close proximity to the radiation source.

In this section, a dual-band FSS is designed with the unit cell size as small as $\lambda_0/10$. The proposed FSS is composed of an inductive wire grid and an array of square-loop cells that are printed onto the two sides of a thin dielectric substrate. The new design provides an advantage of controlling the two passband frequencies independently by varying the different physical parameters of the unit cells. The synthesis method and design procedure of the proposed FSS will be presented in the Section 6.5.1.

6.5.1 The FSS design principle

Fig. 6.23(a) shows the basic circuit model of the dual-band microwave filters that forms the basis of the proposed FSS. The filter is composed of a hybrid resonator separated from an inductor through a short piece of transmission line. The hybrid resonator is composed of a parallel LC resonance circuit of L_2, C_2 that is in series with the capacitor C_1. The transmission line has the length l and the characteristic impedance of Z_l. The frequency of the first passband is mainly determined by L_1, C_1 and the length of the transmission line l. On the other hand, the second passband frequency is dominated by L_2, C_2. Fig. 6.23(b) shows the equivalent circuit model of the filter for the first passband. In this model, it is assumed that the two passbands frequencies are sufficiently seperated, so that L_2C_2 possesses a low impedance and can be ignored. The transmission line ($l \ll \lambda$) is replaced with L_l inductor. Therefore, by using a simple circuit analysis, the frequency of the first passband can be found as

$$f_1 \approx \frac{1}{2\pi\sqrt{C_1(L_1 + L_l)}}. \tag{6.16}$$

If the relative permeability of the transmission line is considered to be μ_r, L_l can be calculated as (Bayatpur and Sarabandi 2008b)

$$L_l = \mu_0\mu_r l. \tag{6.17}$$

So,

$$f_1 \approx \frac{1}{2\pi\sqrt{C_1(L_1 + \mu_0\mu_r l)}}. \tag{6.18}$$

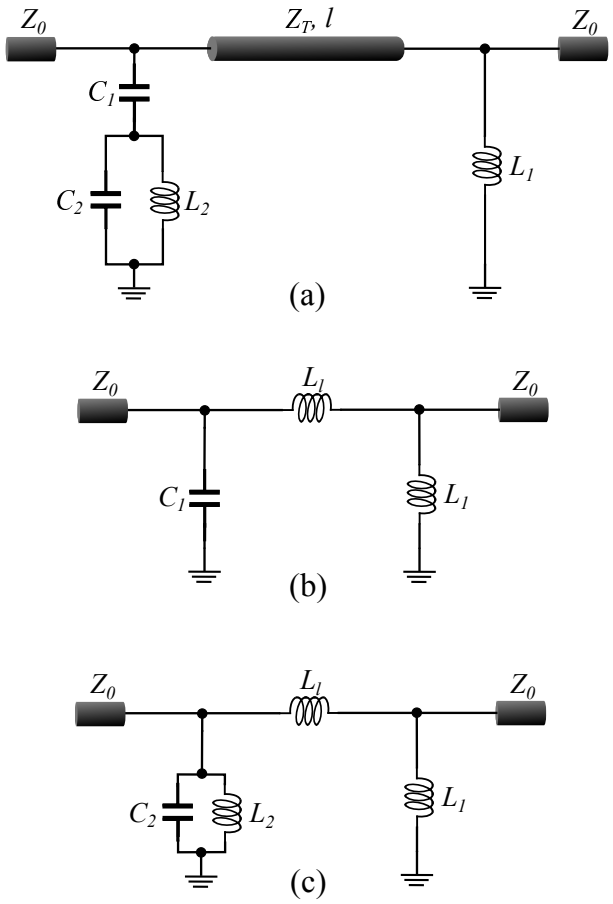

Figure 6.23. Lumped-element model of the dual-band FSS. (a) Equivalent circuit model of the dual-band filter. (b) Simplified circuit model for the first operational passband. (c) Simplified circuit model for the second operational passband.

At the second passband, the parallel L_2C_2 is dominant and the filter can be modelled by the circuit of Fig. 6.23(c). For this passband, the effect of C_1 is ignored and the second passband frequency is approximated as

$$f_2 \approx \frac{1}{2\pi}\sqrt{\frac{1}{C_2}\left(\frac{1}{L_2}+\frac{1}{L_1+L_T}\right)}. \tag{6.19}$$

The circuit shows a transmission zero arising from the hybrid resonator of C_1, L_2 and C_2. This zero notch separates the two passbands and improves the out-of-band rejection of the filter. From Fig. 6.23(a), this zero frequency can be obtained as

$$f_z = \frac{1}{2\pi\sqrt{L_1(C_1+C_2)}}. \tag{6.20}$$

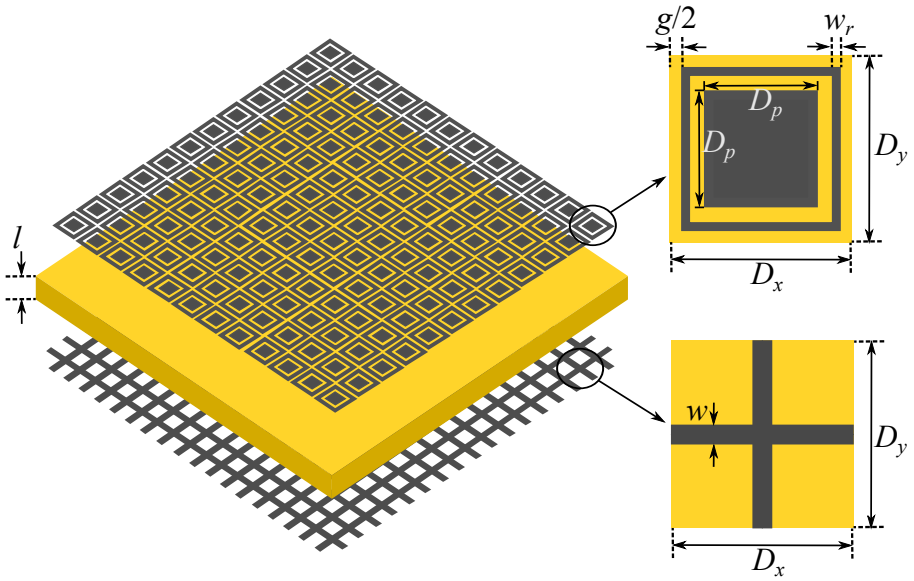

Figure 6.24. Three dimensional view of the designed FSS. Topology of the synthesised dual-band FSS. The unit cells of the top and bottom metallic arrays are shown on the right hand side of the figure. The black shading denotes denots the metal.

From (6.16) it is found that the first passband frequency (f_1) is independent of C_2. Also, (6.19) shows that f_2 is not dependent on C_1. This allows to control the two passband frequencies independently. This characteristic will be studied in detail in simulations.

6.5.2 FSS synthesis based on the circuit model

A dual-band frequency selective surface can be synthesised by using the filter model described in the previous Section 6.5.1. A 3-D view of the synthesised FSS is shown in Fig. 6.24. The structure is composed of two metallic arrays that are separated from each other by a dielectric substrate with a thickness of l. The back layer is composed of a metallic wire grid, which presents the inductor L_1 of the equivalent circuit. By interacting with the normal incident electromagnetic wave, this wire grid shows an inductive behaviour, where increasing w or decreasing D will decrease the inductance of L_1. The top layer on the other side comprises a square-loop array that presents the hybrid resonator (C_1, L_2, C_2) of the equivalent circuit in Fig. 6.23. In this pattern, each square-loop cell has a side length of $D - g$ and the adjacent cells are separated from each other by a distance of g. The gap between the unit cells show a capacitive effect to the incident wave. This capacitive effect is denoted by C_1 of the hybrid resonator, where increasing g causes a smaller C_1. In addition, the loop and square patch in each unit cell provide the parallel L_1C_1 resonance behaviour where L_1 is provided by the

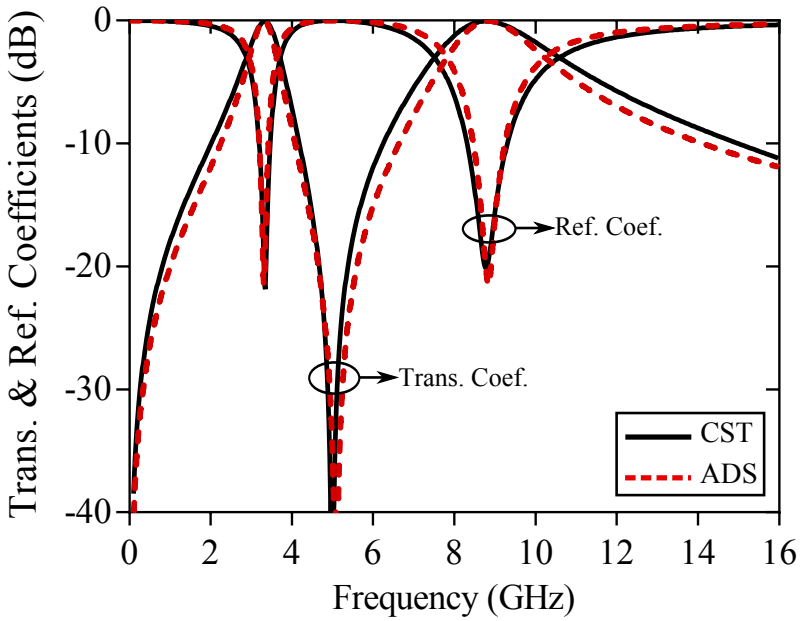

Figure 6.25. Simulated transmission and reflection coefficients of the designed FSS. Free space full-wave simulation result of the designed dual-band FSS using periodic boundary condition in CST in comparison with the ADS circuit model simulation results for normal incidence. The FSS unit cell dimensions and the equivalent circuit parameters are: $D_x = D_y = 8.8$ mm, $g = 0.1$ mm, $w = 0.2$ mm, $w_r = 0.15$ mm, $D_p = 8$ mm, $L_1 = 2.8$ nH, $L_2 = 0.98$ nH, $C_1 = 0.54$ pF, $C_2 = 0.46$ pF and $Z_T = 254\ \Omega$.

inductive effect of the loop sides and C_1 is provided by the capacitive effect between the square patch and the loop sides. In the top pattern, increasing w_r causes a smaller L_2 and decreasing D_P causes a smaller C_2.

6.5.3 Simulation results and discussions

Based on the circuit model and the procedure discussed in Section 6.5.1, a dual-band FSS with passbands at the S and X bands with central frequencies of 3.3 and 9.5 GHz has been designed and simulated in CST Microwave Studio full-wave simulator. The physical parameters of the designed FSS are listed in the caption of Fig. 6.25 together with its equivalent circuit parameters values. The top and bottom metallic layers are patterned on the both sides of 0.254 mm thick Rogers RO5880 dielectric substrate with the relative permittivity of $\epsilon_r = 2.2$ and loss tangent of $\tan\delta = 0.0009$. The full-wave simulations are carried out using unit cell boundary condition that simulates an infinite array of FSS cells that are exposed to an electromagnetic wave with an arbitrary incidence angle. In addition, the equivalent circuit of the FSS (Fig. 6.23) is simulated in

ADS using the parameters listed in the caption of Fig. 6.25. These circuit parameters are optimised by curve fitting of the circuit and EM simulation results. The full-wave simulation results of the FSS are plotted in Fig. 6.25 together with the results obtained by using ADS. As seen, there is a good agreement between the full-wave and circuit model simulations. The passband frequencies of the filter are 3.3 and 8.6 GHz with a transmission zero at around 5 GHz that improves the out-of-band rejection of the FSS.

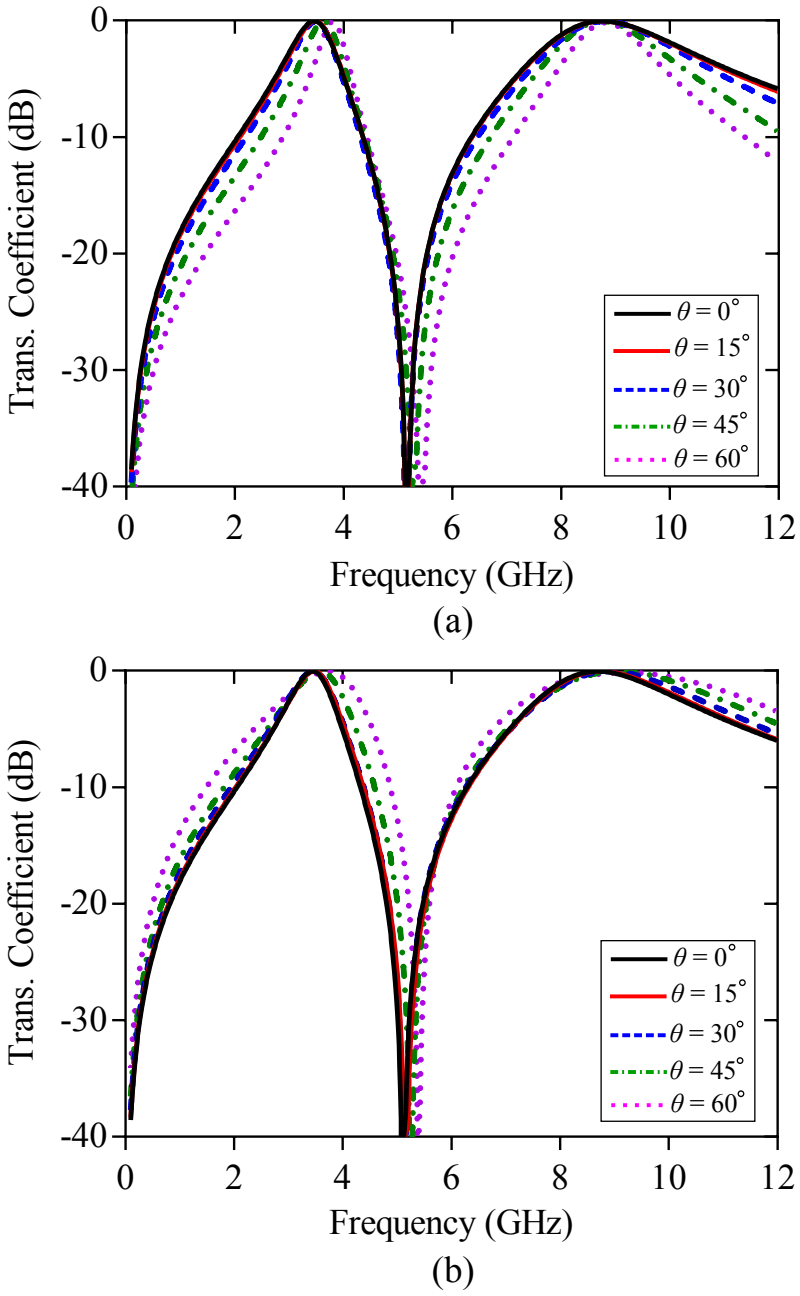

Figure 6.26. Scan angle performance of the designed FSS. Full-wave simulation results of the transmission coeficient of the designed FSS as function of the electromagnetic wave incidence angle for (a) TE polarisation (b) TM polarisation.

The scan angle performance of the designed FSS is shown in Fig. 6.26 showing a low sensitivity to oblique angles of the incident electromagnetic wave. This low sensitivity arises from the miniaturised unit cell size since the unit cell dimension is as small as $\lambda_0/10$, where λ_0 is the wavelength at the first operational passband. This feature provides a freedom to use the designed FSS in the applications with non-planar incident phase fronts (Bayatpur and Sarabandi 2008a).

As discussed in Section 6.5.1, the two passband frequencies of the proposed FSS can be controlled independently by controlling C_1 and C_2 element values. The value of the C_1 capacitor can be tuned by varying the gap (g) between adjacent square-loop unit cells where decreasing g increases C_1 and shifts the first passband frequency downward without affecting f_2. This phenomenon is investigated using the full simulations in CST by changing g and the results are shown in Fig. 6.27. As demonstrated in Fig. 6.27, the smaller value of g causes a lower f_1 without a significant effect on the second passband frequency.

On the other hand, the C_2 capacitor can be tuned by changing the square patch size D_P. A larger D_P causes a larger C_2 which shifts the upper passband frequency downward without a sensible change in f_1. Fig. 6.28 demostrates the full-wave simulation results of D_P variations effect on the FSS transmission response. As seen, a larger D_P leads to

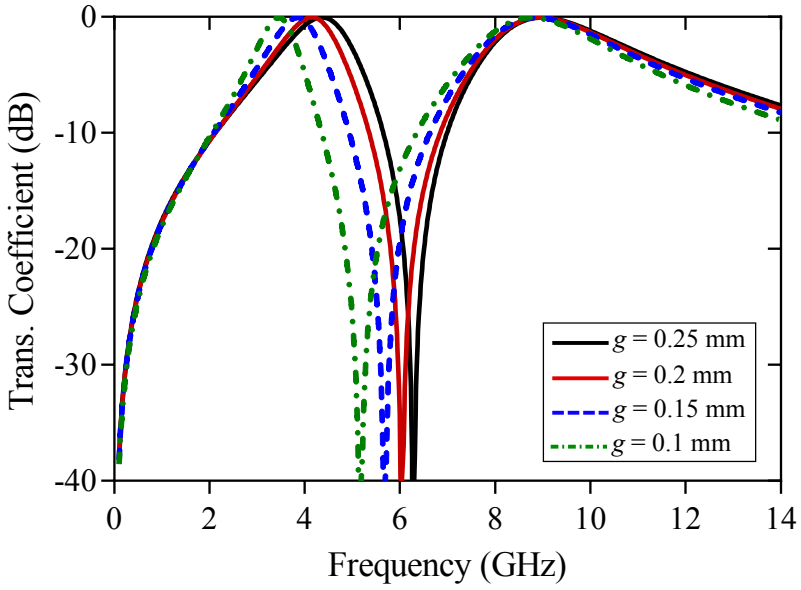

Figure 6.27. Effect of g on transmission coefficient. Full wave simulation of the transmission coeficient of the dual-band FSS as a function of the g. In simulations g is varied from 0.1 mm to 0.25 mm with a step size of 0.05 mm.

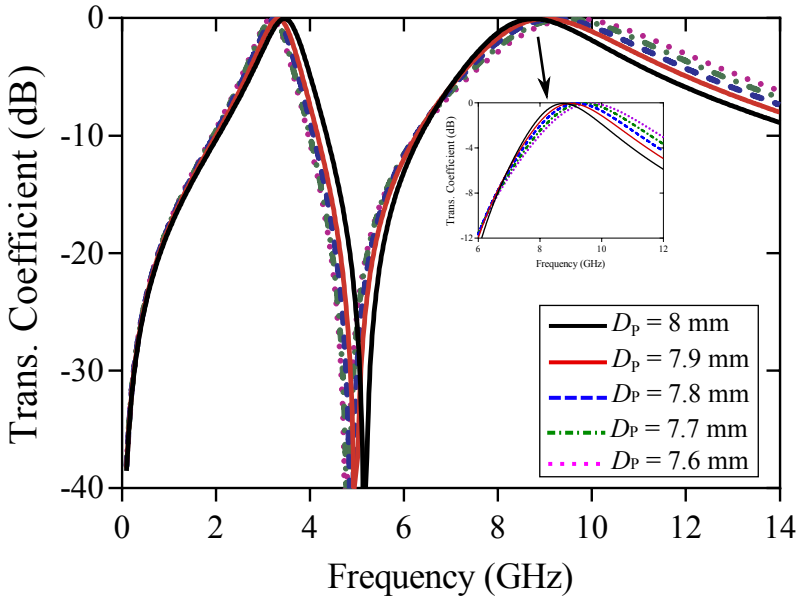

Figure 6.28. Effect of D_P on transmission coefficient. Full wave simulation of the transmission coeficient of the dual-band FSS as a function of the D_P. In simulations D_P is varied from 8 mm to 7.6 mm with a step size of 0.1 mm.

a lower f_2 without a significant variation in the lower passband frequency, confirming the analysis presented in Section 6.5.1.

6.6 Conclusion

In summary, this chapter has proposed new structures and approaches for designing FSSs for tunable and multiband applications. The first FSS was a single-pole tunable prototype in which all the varactor diodes were biased in parallel. An application of the proposed FSS in designing higher-order FSSs has been studied by developing a second-order FSS made of two cascaded single-pole sections. The proposed FSS showed a stable response under oblique incidences for both TE and TM polarisations.

The second design was a low-profile second-order varactor-tuned FSS with embedded bias network. A superiority of this design over the other designs is that it avoids the need of any additional metallic network for biasing the varactor diodes. A circuit-based synthesis method has been developed for designing the desired filtering response. The proposed synthesis procedure and tuning mechanism have been verified by fabricating an FSS prototype and testing it inside a parallel plate waveguide. The good agreement between the simulation and measurement results validated the proposed second-order tunable FSS concept.

A liquid crystal-based tunable FSS has been proposed for higher frequencies around the X-band. The FSS is made of metallic patterns printed on both sides of very thin dielectric spacer. Tunability has been achieved by integrating liquid crystal cells into the overlapping areas between the front and back layers metallic patterns that form interlayer capacitors. By applying bias voltage between the front and back layers the overlap capacitors are tuned resulting in a tunable frequency response. The frequency behaviour has been modelled by a lumped element circuit and the tunability has been verified using both electromagnetic and circuit model simulations.

Finally, a dual-band FSS has been designed based on miniaturised elements with stable scanning angle performance for multi-band and multi-standard applications. The designed FSS incorporates the unit cells with dimensions as small as $\lambda_0/10$ at the first operational passband providing desired independency of the transmission response with respect to the angle of the incident wave. In addition, the proposed design approach gives the benefit of independent controllability of the two passband frequencies simply by adjusting the different unit cell physical parameters.

This chapter focuses on FSS designs for microwave frequencies. The FSS designs for millimetre-wave and terahertz applications will be presented in Chapter 7.

Chapter 7

Terahertz frequency selective surfaces

THIS chapter is dedicated to designing high performance frequency selective surfaces (FSSs) for terahertz applications. Here, miniaturised-element concept is used to design FSSs with a second-order filtering responses that are highly desirable in terahertz systems. The miniaturised elements enable accurate modelling of the FSS frequency response through a lumped element circuit model. So, a circuit-based synthesis approach can be developed for the desired response type that facilitates the FSS design and optimisation procedure. Additionally, the miniature unit cell provides a good stability of the frequency response over oblique excitations and non-planar electromagnetic phase fronts. A full description of the design approaches and results validating the proposed concepts are presented throughout the chapter.

7.1 Introduction

The terahertz radiation covers a frequency range between 0.1 THz and 10 THz. Technically, it fills the gap between the electronics and photonics as demonstrated in Fig. 7.1. In the last decade, there has been a great interest in using this frequency spectrum for communication applications since it promises a wider bandwidth and higher communication speed. In addition, a number of materials show spectral fingerprints at this frequency range making this frequency band attractive for sensing and screening applications. A major challenge in designing devices for this frequency range is the relatively low signal-to-noise ratio and low radiation power of compact terahertz systems (Yardimci *et al.* 2015). Therefore, there is a great interest nowadays for developing new designs and methodologies to bridge the gap between the microwave and optical frequency ranges.

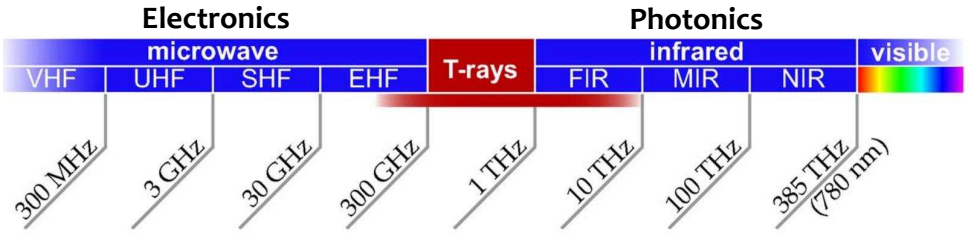

Figure 7.1. Electromagnetic spectrum. The terahertz band is loosely defined between 0.1 THz to 10 THz. After Withayachumnankul *et al.* (2007)

One of the key components in terahertz systems is the frequency selective surface (FSS). Several FSS structures have been proposed for bandpass filtering at terahertz and millimeter-wave frequencies (Zhu *et al.* 2012, Lan *et al.* 2014, Chiang *et al.* 2011, Lu *et al.* 2011, Paul *et al.* 2009). A common specification among these conventional FSS structures is that their unit cell dimensions are comparable to half of the operational wavelength. As a result, their frequency response is highly sensitive to the angle of incidence (Bayatpur 2009). In order to circumvent this problem, a new class of FSS structures called miniaturised-element FSSs (MEFSSs) has been introduced in Sarabandi and Behdad (2007) at microwave frequencies. These structures are composed of multilayer arrays of non-resonant metallic elements with dimensions much smaller than the operation wavelength. The sub-wavelength unit cells provide a more consistent response of the whole structure with respect to non-planar and oblique phase fronts. Since then, a large number of MEFSS structures for higher-order spatial filtering have been designed and proposed at microwave frequencies (Chiu and Chang 2009, Ebrahimi *et al.* 2014b,

Li and Behdad 2013, Li and Shen 2013, Momeni Hasan Abadi *et al.* 2014). However, they have not been demonstrated for sub-millimeter-wave and terahertz applications yet. Recently, a MEFSS has been proposed by Moallem and Sarabandi for suppressing an image component provided by a harmonic mixer in MMW radars (Moallem and Sarabandi 2012). The structure in Moallem and Sarabandi (2012) is composed of metallic patches and I-shaped wires that provide a first-order bandpass response with an adjacent transmission zero. Higher-order filters with wide out-of-band rejection are required in certain applications to enhance the spectral selectivity. This chapter introduces THz miniaturised-elements FSSs (MEFSSs) with second-order filter response for sub-millimeter-wave and terahertz applications with wide rejection band and large angular tolerance.

7.2 Second-order terahertz FSS on quartz substrate

This section presents the design of a terahertz spatial filter with a second-order transmission response. The FSS is composed of miniaturised-element metallic arrays printed on both sides of a quartz substrate. The deeply sub-wavelength unit cell enables a high stability of the frequency response over a wide range of incidence angles.

7.2.1 FSS topology

Fig. 7.2 shows the unit cell of the designed THz FSS. The front layer of the unit cell is composed of a capacitive metallic patch enclosed by a metallic loop. The back layer of the unit cell is made of a Jerusalem cross resonator surrounded by a metallic loop. These metallic arrays are to be patterned on the two sides of a 135 μm thick quartz substrate. The front and back metallisation is 0.2 μm thick gold, well above the skin depth at terahertz frequencies.

The proposed FSS can be modelled by an equivalent circuit model shown in Fig. 7.3. In this model, the front layer of the FSS is modelled with a parallel L_1C_1 resonator where, L_1 models the inductive behavior of the front layer wire grid and C_1 models the capacitive effect between the wire grid and the square patches. The back layer is modelled as a hybrid resonator consisting of L_2 inductor in parallel with L_3C_3 series resonator. The L_2 inductor represents the wire grid of the back layer and the L_3C_3 series resonator describes the Jerusalem cross resonator. In addition, the quartz substrate that

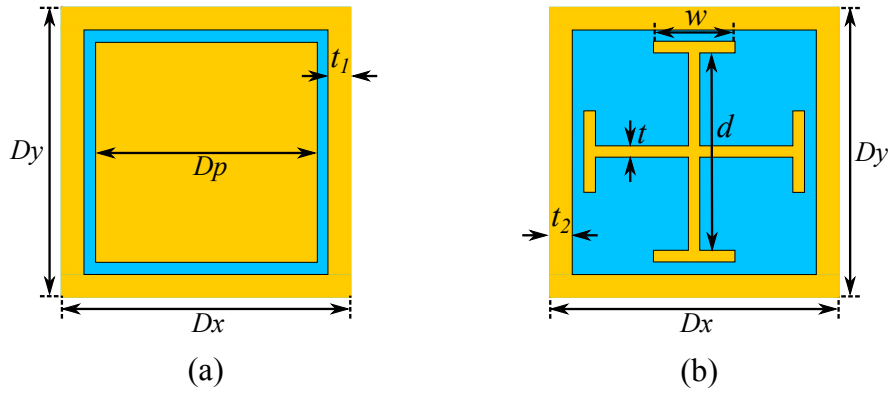

Figure 7.2. Unit cell views of the FSS. (a) Front layer. (b) Back layer. The dimensions are as follows: $D_x = D_y = 175$ µm, $D_P = 120$ µm, $t_1 = 22.5$ µm, $t_2 = 22.5$ µm, $d = 110$ µm, $t = 5$ µm, $w = 25$ µm. The yellow areas represent metal, and the blue areas for the substrate.

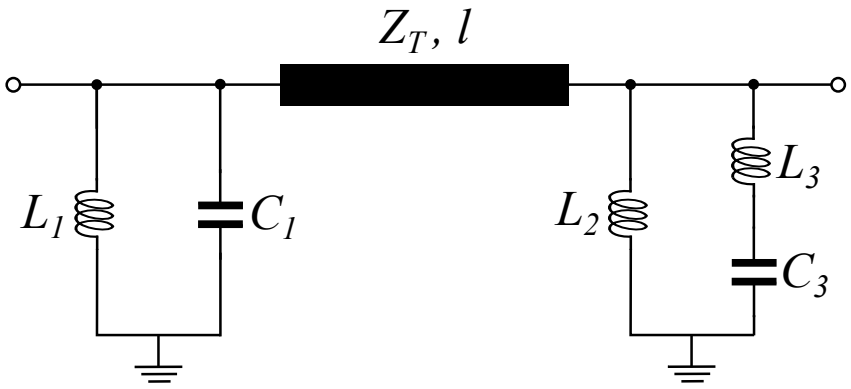

Figure 7.3. Lumped-element circuit model of the FSS. The element values are: $L_1 = 9.3$ pH, $C_1 = 25$ fF, $L_2 = 70$ pH, $L_3 = 25$ pH, $C_2 = 2.5$ fF, $Z_T = 169\ \Omega$ and $l = 135$ µm.

separates the two metallic layers is modelled as a section of a transmission line with the length of 135 µm and a characteristic impedance of $Z_T = Z_0/\sqrt{\epsilon_r}$, where $Z_0 = 377\ \Omega$ is the free space impedance and ϵ_r is the relative permittivity of the quartz substrate. The equivalent circuit parameters obtained from the closed-form equations and the curve fitting of EM and circuit simulations are listed in the caption of Fig. 7.3.

7.2.2 Simulation results and discussion

The designed FSS and its equivalent circuit model are simulated by using the parameters given in Fig. 7.3 and Fig. 7.2. Fig. 7.4 shows the transmission response (S_{21}) of the FSS obtained from the full-wave electromagnetic simulation together with its circuit model simulation. As seen, there is a good agreement between the EM and circuit

model simulations confirming the validity of the circuit model. The bandpass characteristic is achieved with a center frequency around 0.4 THz. As seen, the filter has no harmonic response up to 0.8 THz. There is a zero in the transmission response of the FSS at around 0.6 THz, which improves the out-of-band rejection of the filter. From the circuit model in Fig. 7.3, this transmission zero takes place at the resonance frequency of the back layer series resonator, which can be described as

$$f_z = \frac{1}{2\pi\sqrt{L_3 C_3}}. \tag{7.1}$$

Based on (7.1), the transmission zero frequency can be tuned by changing the value of L_3 and C_3. From the back layer unit cell in Fig. 7.2(b), the value of L_3 can be tuned by changing d and t. Increasing d or decreasing t result in a larger L_3 and vice versa. Additionally, increasing w or d will increase the value of C_3. The slope of the upper and lower sides of the passband is around 70 dB/octave, showing a good selectivity of the proposed filter.

One important feature in designing of FSSs is the immunity of the frequency response respect to the oblique incidence angles. Fig. 7.5 shows the transmission response of the designed FSS for the transverse electric (TE) polarisation of the incident wave at different incidence angles.

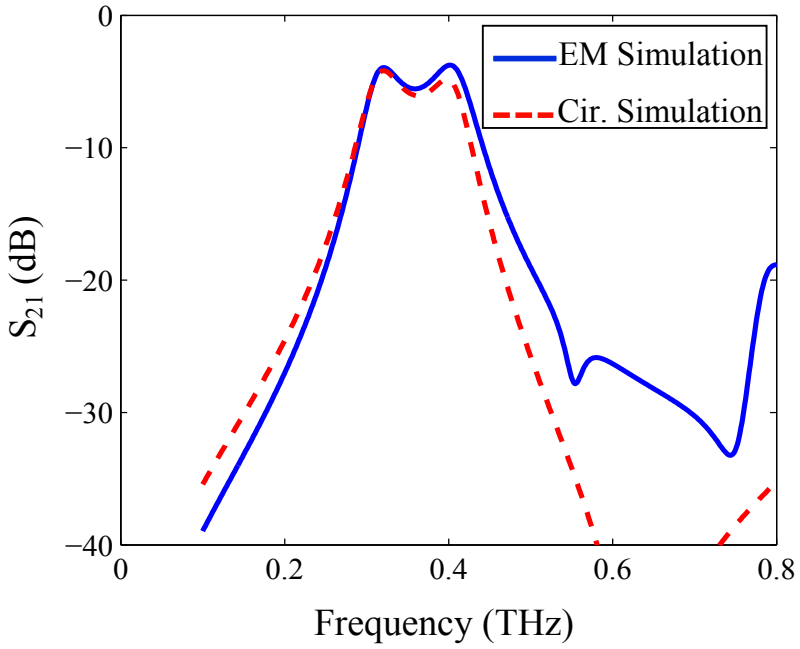

Figure 7.4. Circuit versus electromagnetic simulation results. Comparison between the full-wave electromagnetic and circuit model simulation of the proposed FSS.

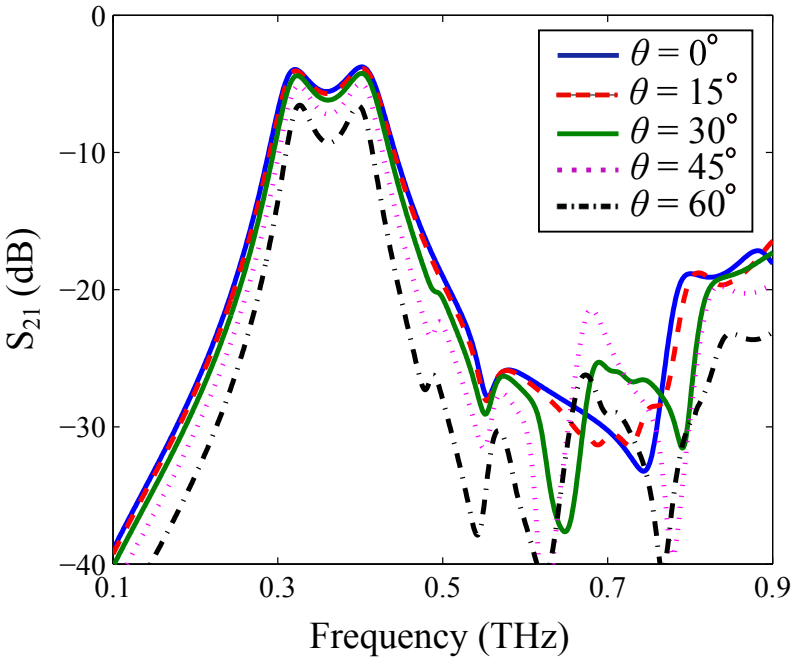

Figure 7.5. Scan angle performance for TE polarisation. Transmission response of the designed FSS for TE polarisation of the incident wave at different incidence angles ($\theta = 0^\circ$ represents the normal incidence).

The frequency response of the FSS for the transverse magnetic (TM) polarisation is demonstrated in Fig. 7.6 at different incidence angles. The structure shows the same frequency response for both of the TE and TM polarisations at normal incidence angle due to the fourfold symmetric structures of the front and back layers. However, by increasing the incidence angle, the responses for the TE and TM polarisations will change. This feature is mainly caused by the change of wave impedances for the TE and TM polarisations ($Z_{0,\mathrm{TE}} = Z_0/\cos\theta$, $Z_{0,\mathrm{TM}} = Z_0\cos\theta$). So, the wave impedance for the TE polarisation increases with increasing the incidence angle resulting in a smaller bandwidth for the TE response. On the other hand, the wave impedance of the TM polarisation will be decreased by increasing the incidence angle, which results in a larger bandwidth for the TM transmission response (Behdad 2008).

7.3 Second-order terahertz FSS on PDMS substrate

Section 7.2 presented a design of second-order bandpass FSS on a quartz substrate. However, in many designs, it is needed to have a more flexible substrate and a design that is compatible with standard fabrication techniques. In this section, a second-order

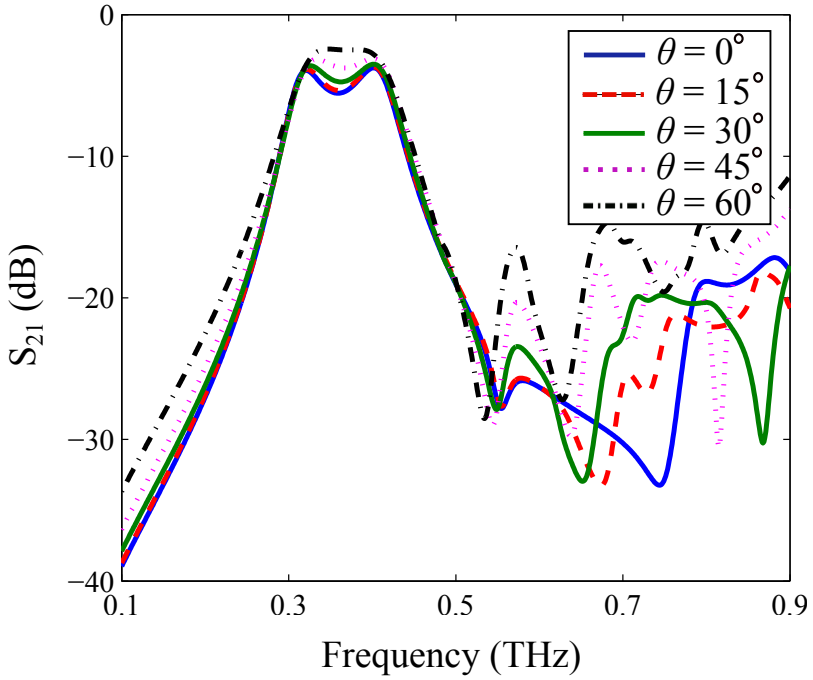

Figure 7.6. Scan angle performance for TM polarisation. Transmission response of the designed FSS for TM polarisation of the incident wave at different incidence angles ($\theta = 0^\circ$ represents the normal incidence).

FSS is designed by using Polydimethylsiloxane (PDMS) substrate. The PDMS is an easy to process polymer material with a moderate loss at terahertz frequency range. Fabricated via spin-coating, PDMS offers a broad range of thicknesses. The designed FSS has been fabricated by using microfabrication technology and measured with THz time-domain spectrometry for verification of the proposed concept.

7.3.1 FSS strucure and equivalent circuit model

A three-dimensional view of the proposed terahertz FSS is shown in Fig. 7.7(a). The structure is composed of two periodic metallic arrays that are separated from each other by a dielectric spacer having a subwavelength thickness of h. Fig. 7.7(b) shows the unit cells for the front and back layers. The dimensions of each unit cell are D_x and D_y (D_x=D_y=D) along the x and y directions, respectively. The front layer unit cell is made of a wire loop surrounding a non-resonant capacitive square patch. The back layer unit cell is very similar to the front layer excepting a complementary cross-shaped resonator (CCSR) that is embedded into the capacitive patch. Both of the front and back 2-D metallic arrays are covered by a very thin protective layer (thickness = t)

made of the same dielectric material as the spacer. Since the structure is composed of miniaturised unit cells, it can be modelled by a lumped-element equivalent circuit. The equivalent circuit model of this FSS is depicted in Fig. 7.8(a), which is valid for a normally incident plane wave.

In the circuit model, L_1 and L_2 account for the inductive behavior of the front and back layers wire grids. The capacitors C_{L1} and C_{L2} model the capacitive effect between the square patch and the inductive wire grid in the front and back layers, respectively. The CCSR in the back layer is modelled by a L_3C_3 resonator. The dielectric spacer that separates the two layers is modelled through a section of transmission line with a characteristic impedance of Z_T and length of h. It should be mentioned that $Z_T = Z_0/\sqrt{\epsilon_r}$, where $Z_0 = 377\ \Omega$ is the free space impedance and ϵ_r is the relative permittivity of the spacer. And finally, the Ohmic losses associated with the front and back wire grids and CCSR are modeled by resistors R_1, R_2 and R_3 respectively. These losses are related to the surface resistivity of the metallisation and the current distribution therein (Moallem and Sarabandi 2012). The combination of the complementary cross-shaped resonator (L_3C_3) and C_{L2} adds a transmission zero to the filter response and improves its out-of-band behavior. In fact, this transmission zero appears at the frequency where the combination of C_{L2} and L_3C_3 is short-circuited. Thus, this frequency is given by:

$$f_z = \frac{1}{2\pi\sqrt{L_3(C_3 + C_{L2})}}. \tag{7.2}$$

This transmission zero can be tuned by varying the dimensions of the complementary cross-shaped resonator (d_c, w_c), which in turn translates to the variation of L_3 and C_3 values.

Since the values of L_3 and C_3 are designed to be much smaller than L_2 and C_{L2}, the parallel combination of L_3C_3 has a very small impedance around the passband frequencies of the FSS. So, L_3C_3 can be considered as a short circuit at these frequencies. In addition, the transmission line section can be replaced with its equivalent lumped-element circuit model by using the telegrapher's equation (Pozar 2009). Fig. 7.8(b) illustrates the FSS equivalent circuit around the passband by considering L_3C_3 as a short circuit and replacing the transmission line with its circuit model ($L_{1,2}$ and C_s). The losses are not considered in Fig. 7.8(b) for simplicity. The values of $L_{1,2}$ inductor and C_s capacitors can be obtained by using the following relations (Bayatpur 2009)

$$L_{1,2} = \mu_0\mu_r h, \tag{7.3}$$

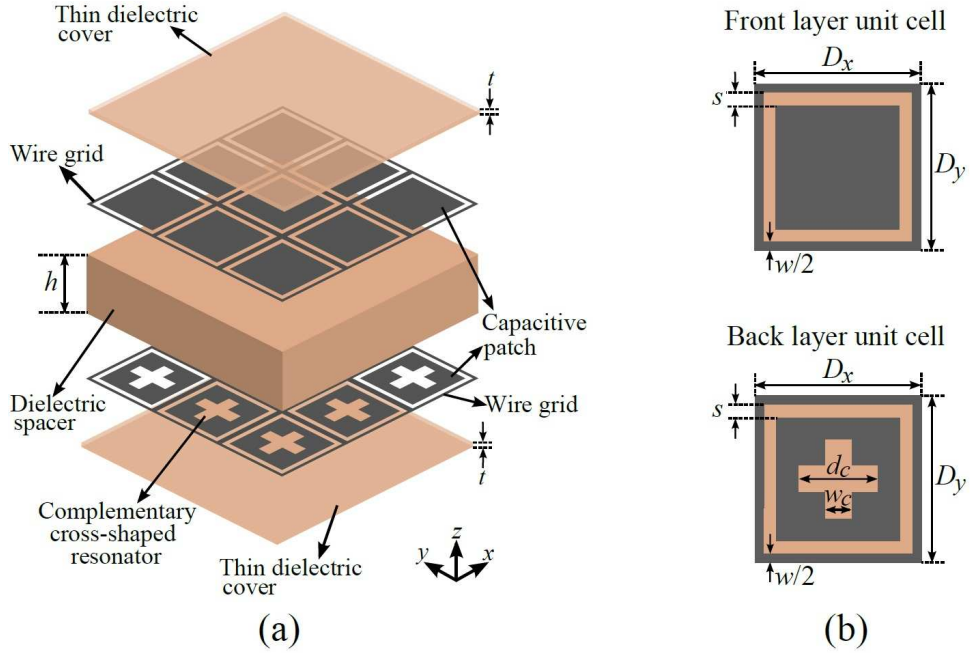

Figure 7.7. Three dimensional view of the FSS. Topology of the proposed second-order terahertz FSS. (a) 3-D view of the FSS with the grey regions showing the metallisation and the light brown regions showing the dielectric spacer. (b) Unit cells on the front and back layers along with their geometric parameters.

$$C_s = \epsilon_0 \epsilon_r h/2, \tag{7.4}$$

where μ_0 and μ_r are the permeability of the free space and the relative permeability of the spacer, respectively. Likewise, ϵ_0 and ϵ_r are the permittivity of the free space and the relative permittivity of the spacer, respectively. The circuit of Fig. 7.8(b) can be converted into the one in Fig. 7.8(c) that shows a standard basic circuit model of a second-order bandpass filter (Zverev 1967). In this form, $C_1 = C_{L1} + C_s$ and $C_2 = C_{L2} + C_s$, and the circuit can be considered as coupled input and output resonators of L_1C_1 and L_2C_2, respectively.

7.3.2 Synthesis procedure of the proposed FSS

As discussed above, the frequency response of the considered FSS around its pass-band can be described by the circuit model in Fig. 7.8(c). By using this circuit model, a desired second-order filtering response can be synthesised and then, the equivalent circuit parameters can be converted into the corresponding geometrical parameters of the proposed FSS. The lumped-element values of the equivalent circuit in Fig. 7.8(c)

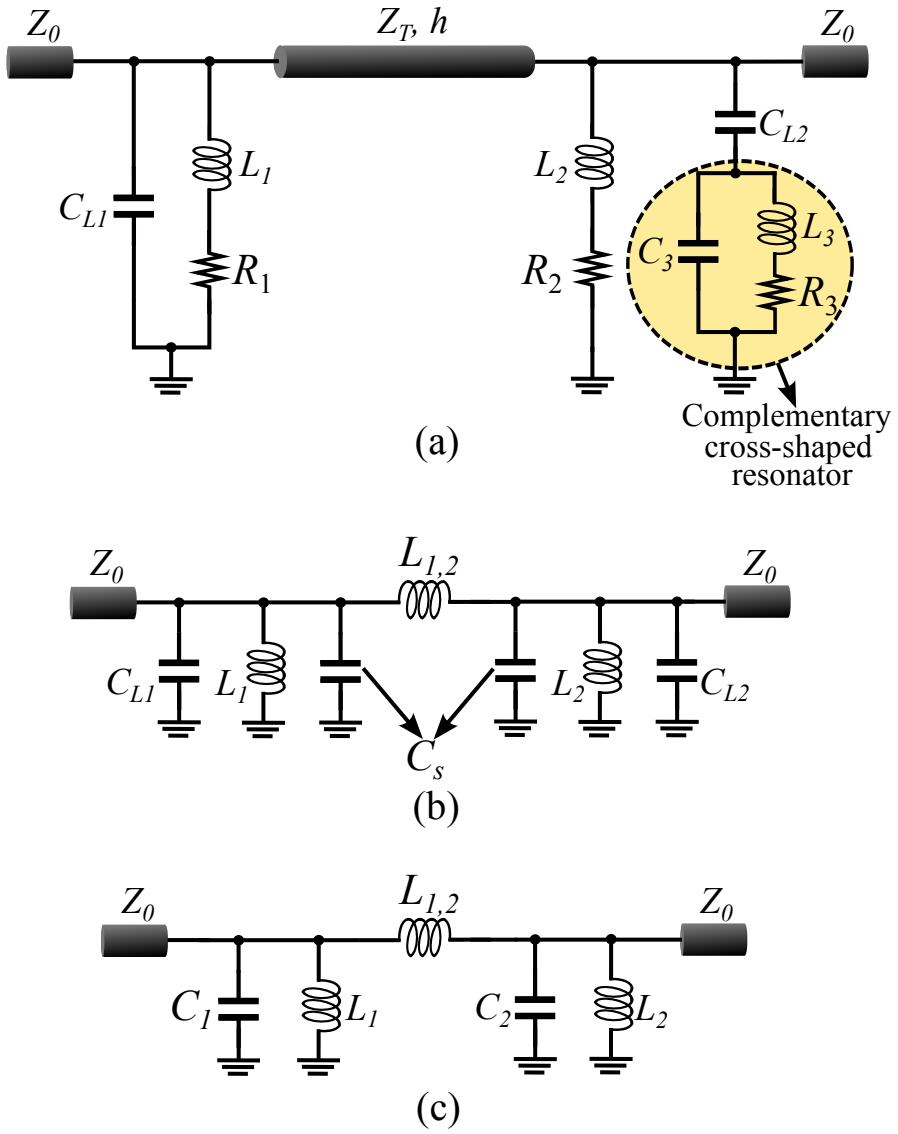

Figure 7.8. Equivalent circuit model of the THz-FSS. Circuit model of the proposed FSS for the normaly incident EM wave. (a) A full circuit model for normal incidence. (b) A simplified model with the transmission line section replaced with equivalent lump elements and the loss R neglected. (c) Standard circuit model of a second-order bandpass coupled resonator filter. This circuit is equivalent to the circuit in Fig. 7.8(b) with $C_1 = C_{L1} + C_s$ and $C_2 = C_{L2} + C_s$.

can be determined by applying the concept of coupled-resonator filter with inductive coupling (Al-Joumayly and Behdad 2010, Zverev 1967). Supposing that f_0 is the center frequency of the filter and $\delta = \mathrm{BW}/f_0$ is the fractional bandwidth, the values of the circuit elements in Fig. 7.8(c) can be obtained based on the following steps:

Table 7.1. Normalised second-order filter parameters. Normalised quality factor and coupling coefficients for different filter types. Extracted from Zverev (1967).

Filter Type	q_1	q_2	k_{12}	r_1	r_2
Gaussian	0.4738	2.185	0.9828	1	1
Butterworth	1.4142	1.4142	0.70711	1	1
Chebyshev (0.01 dB ripple)	1.4829	1.4829	0.7075	1	1.1007
Chebyshev (0.1 dB ripple)	1.6382	1.6382	0.7106	1	1.3554
Chebyshev (0.5 dB ripple)	1.9497	1.9497	0.7225	1	1.9841

1. The values of the C_1 and C_2 capacitors can be determined from the following relation:

$$C_i = \frac{q_i}{\omega_0 r_i Z_0 \delta}, \qquad i = 1, 2. \tag{7.5}$$

In (7.5), $Z_0 = 377\ \Omega$, q_1 and q_2 are the normalised quality factors of the input and output resonators, and r_1 and r_2 are the normalised source and load impedances of the filter in Fig. 7.8(c) (Zverev 1967).

2. The values of L_1 and L_2 inductors can be obtained by

$$L_i = \frac{1}{\omega_0^2 (C_i - k_{1,2}\delta\sqrt{C_1 C_2})}, \qquad i = 1, 2 \tag{7.6}$$

where, $k_{1,2}$ is the normalised coupling coefficient between the input and output resonators.

3. The coupling inductance $L_{1,2}$ can be calculated from

$$L_{1,2} = \frac{1}{\omega_0^2 k_{1,2}\delta\sqrt{C_1 C_2}}. \tag{7.7}$$

The normalised quality factors and coupling coefficient for some different filter types are extracted from (Zverev 1967) and presented in Table 7.1.

After calculating the values of the circuit elements in Fig. 7.8(c), the thickness of the dielectric spacer that separates the front and back metallic arrays can be obtained from

(7.3). Then the spacer capacitance C_s can be derived from (7.4), and the values of C_{L1} and C_{L2} capacitors can be found from (7.8).

$$C_{Li} = C_i - \frac{\epsilon_0 \epsilon_r h}{2} \qquad i = 1, 2. \tag{7.8}$$

In order to convert the calculated lumped element values into the geometrical parameters, the method presented in Al-Joumayly and Behdad (2010) can be used. The effective inductance of an infinite wire grid shown in Fig. 7.9(a) with a period of l and a wire width of w is given by (Bayatpur 2009)

$$L = \mu_0 \mu_{\text{eff}} \frac{l}{2\pi} \ln\left(\frac{1}{\sin\frac{\pi w}{2l}}\right), \tag{7.9}$$

where μ_0 is the permeability of the free space and μ_{eff} is the effective permeability of the substrate. Equation (7.9) can be used for calculating the wires width in the front and back layer metallisation of the proposed FSS. The period of the wire grid is considered to be equal to the unit cell size in Fig. 7.7 ($l = D$) and the unit cell size can be chosen arbitrarily. However, choosing very small unit cell size leads to a very thin wire that might not be practical due to fabrication limits. It is worth mentioning that (7.9) is valid when the wire grid is away from any metallic objects such as capacitive patches in Fig. 7.8 or scatterers (Al-Joumayly and Behdad 2010, Al-Joumayly and Behdad 2009). So, the value of w calculated from (7.9) can only be used as an approximation. A more accurate value of w can be obtained by fitting the full-wave simulation result to the analytical circuit calculation.

The effective capacitance of an infinite array of sub-wavelength capacitive square patches shown in Fig. 7.9(b) can be obtained by using (Bayatpur 2009)

$$C = \epsilon_0 \epsilon_{\text{eff}} \frac{2p}{\pi} \ln\left(\frac{1}{\sin\frac{\pi d}{2p}}\right). \tag{7.10}$$

In (7.10), ϵ_0 is the permittivity of free space and ϵ_{eff} is the effective permittivity of the dielectric spacer, p is the period of the array and $2d$ is the gap spacing between the adjacent patches. Although for the proposed structure the capacitive patches are surrounded by the wire grid, (7.10) can still be used as an approximation if the capacitive effect between the edges of the metallic square patches and the wire grid is approximated by a corresponding patch array in Fig. 7.9(b). To this end, the gap spacing between the adjacent metallic patches in Fig. 7.9(b) is assumed to be equal to the space

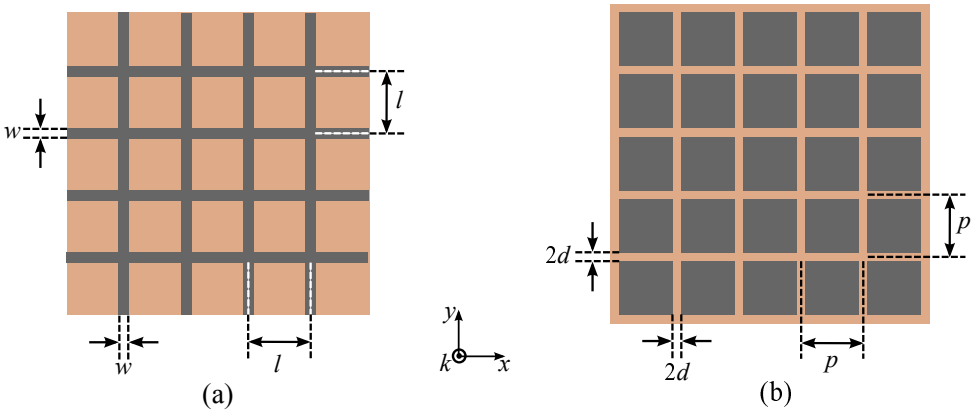

Figure 7.9. Inductive and capacitive FSS arrays. (a) Infinite metallic wire grid. (b) Infinite metallic square patch array. The wire grid shows an inductive behavior whereas the patch array shows a capacitive effect with respect to the incident electromagnetic wave. Metallisation is indicated by the grey regions.

between a capacitive patch and the wire grid in Fig. 7.7(b) ($2d = s$). By this assumption, the period of the corresponding patch array of Fig. 7.9(b) will be

$$p = D - w - s, \tag{7.11}$$

where, $D = D_x = D_y$ is the unit cell size in Fig. 7.8(b) and w is the width of the wire grid surrounding each capacitive patch. Based on (7.10) and (7.11), the spacing between the patches in Fig. 7.9(b) that corresponds to the spacing between the patches and the wire grid in Fig. 7.8 can be determined.

7.3.3 Design of terahertz FSS

Based on the synthesis procedure Section 7.3.2, this section demonstrates a design of a second-order bandpass FSS at terahertz frequencies. The design starts by considering a center frequency of $f_0 = 0.42$ THz and a -3 dB fractional bandwidth of $\delta = 35\%$ for the circuit model in Fig. 7.8(c). This frequency band is chosen to match the capabilities of most terahertz time-domain spectroscopy (THz-TDS) systems. Polydimethylsiloxane (PDMS) is considered for the dielectric spacer since it has a low dielectric constant of $\epsilon_r = 2.35$ causing a low impedance mismatch with free space (Moallem and Sarabandi 2012). The front and back metallic layers are made of 200 nm thick gold (Au) with the DC conductivity of 4.1×10^7 S/m and the sheet resistance of around $0.2 + j0.22\ \Omega$/square at the passband of the FSS. In order to improve the mechanical strength of the filter, two encapsulating PDMS layers with a thickness of 10 μm are

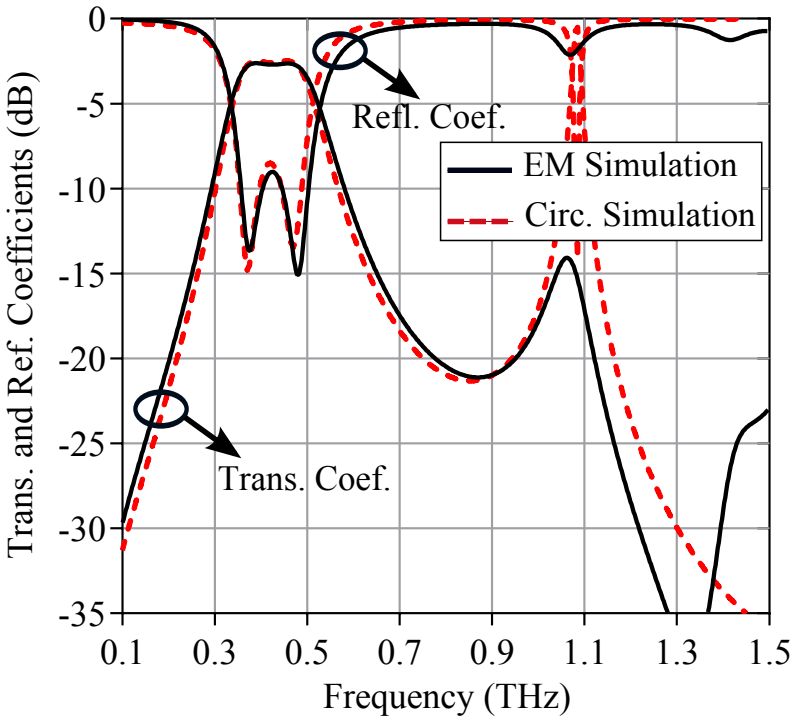

Figure 7.10. Comparison between circuit model and EM simulations before adding the CCSR. Simulation results of the proposed FSS for the normal incidence angle. The parameters used in simulations are: $C_{L1} = C_{L2} = 4.2$ fF, $L_1 = L_2 = 45$ pH, $R_1 = R_2 = 6.5\ \Omega$, $D_x = D_y = 130\ \mu$m, $h = 100\ \mu$m, $t = 10\ \mu$m, $w = 10\ \mu$m and $s = 5\ \mu$m.

applied to the front and back metal layers. The relative permeability of the PDMS is $\mu_r = 1$. By assuming a Butterworth filter response, the values of the circuit elements in Fig. 7.8(a) are calculated using the synthesis method described in Section 7.3.2. The calculated values are $C_1 = C_2 = 4.23$ fF, $L_1 = L_2 = 45$ pH and $L_{1,2} = 130$ pH. The unit cell size is considered as $D_x = D_y = D = 130$ µm, which is slightly smaller than the $\lambda_0/5$, where λ_0 is the free space wavelength at 0.42 THz. The circuit parameters can be mapped into the geometrical dimensions of the FSS: $w = 14.8$ µm, $s = 4.5$ µm and $h = 103$ µm. Now, w and s can be optimised in simulation for obtaining more accurate values. Equation (7.10) is reasonably accurate since the capacitance between the patches in Fig. 7.9(b) corresponds directly to the capacitance between the patches and grid in Fig. 7.7. On the other hand, the presence of those square metallic patches in the vicinity of the wire grid affects the magnetic field and hence reduces the inductance. So, the final optimised value of w is expected to be smaller than the value obtained from (7.9). For optimisation, we firstly consider the calculated value of w from (7.9) based on the synthesised value of L_1 and L_2. Now, by having D and w, the value of

s will be determined from (7.10) to satisfy the synthesised value of C_1 and C_2. The unit cell is then simulated to obtain the L and C values. If the inductance of the wire grid obtained from the simulation is smaller than the synthesised value, the previous steps are then repeated with a smaller value for w, until desired consistency between the simulation results and the synthesised values is achieved. The optimised equivalent circuit and geometrical parameters of the designed FSS are listed in the caption of Fig. 7.10. As seen, the optimised value for s is very close to the value obtained from (7.10) but, the optimised value of w is smaller than the value predicted by (7.9).

After mapping the synthesised values of the L and C parameters to the geometrical parameters of the FSS, the values of the resistances in Fig. 7.8 can be determined by curve fitting of the EM and circuit simulation results. Fig. 7.10 shows a comparison between the results obtained from the circuit simulation with ADS and from the full-wave electromagnetic simulation with CST Microwave Studio. Both of the transmission and reflection coefficients are shown. As can be observed in Fig. 7.10, there is a good agreement between the circuit model and the full-wave electromagnetic simulation of the FSS. The good agreement confirms that the circuit based synthesis procedure offers an efficient analytical method for designing the proposed FSS configuration.

The results in Fig. 7.10 are obtained without considering the effect of the CCSR. As explained before, the combination of CCSR (L_3, C_3) and C_{L2} adds a transmission zero that can be used to improve the out-of-band response of the FSS. The frequency of this zero can be calculated from (7.2) and can be tuned by varying w_c and d_c. Fig. 7.11 shows the transmission response of the FSS by considering $w_c = 20$ μm and $d_c = 65$ μm. As seen, the out-of-band response in Fig. 7.11 is improved with respect to Fig. 7.10 since the transmission coefficient stays below -27 dB up to 1.45 THz.

The values of L_3 and C_3 elements that represent the effect of the CCSR can be determined by a semi-analytical procedure described as follows: the zero frequency provided by L_3, C_3 and C_{L2} can be calculated from (7.2). The value of C_{L2} as listed in caption of Fig. 7.11 is already designed by the synthesis procedure. On the other hand, the zero frequency is obtained from EM simulation in CST Microwave Studio (f_{Z1} in Fig. 7.11). By putting arbitrary capacitors of C_{ar} between the capacitive square patches and the wire grid in the back layer of the FSS in CST Microwave Studio, the capacitance

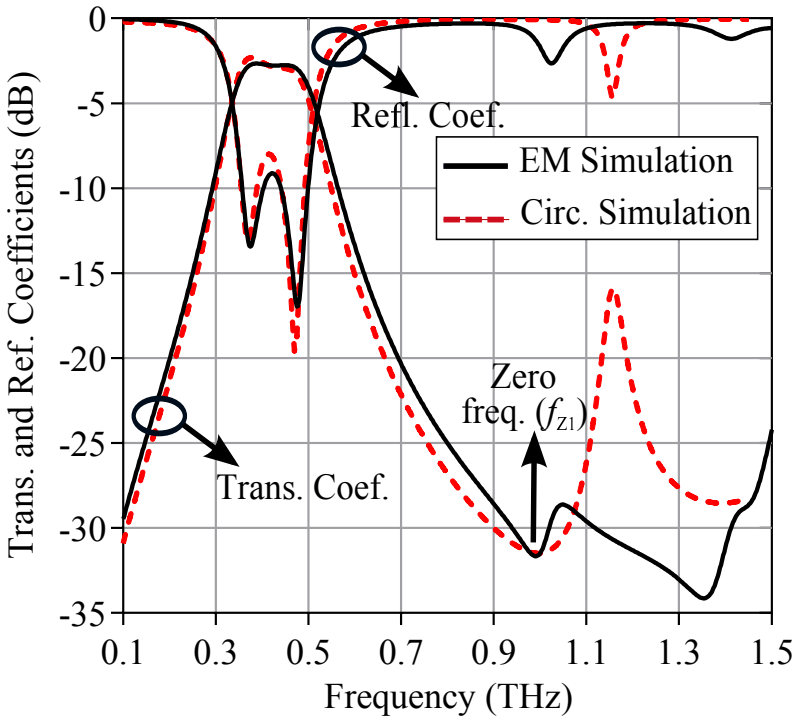

Figure 7.11. Comparison between circuit model and EM simulations after adding the CCSR. Simulation results of the proposed FSS for the normal incidence angle by considering the effect of the complementary cross-shaped resonator. The complementary cross shaped resonator dimensions are: $w_c = 20$ μm, $d_c = 65$ μm and $L_3 = 3$ pH, $C_3 = 2.9$ fF, $R_2 = 1.2\ \Omega$ and $R_3 = 4.25\ \Omega$ are considered in circuit model simulations. The other parameters are the same as the Fig.7.10.

between the wire grid and square patches will be increased to $C_{L2} + C_{\text{ar}}$. This will shift down the zero frequency to

$$f_{Z2} = \frac{1}{2\pi\sqrt{L_3(C_3 + C_{L2} + C_{\text{ar}})}}. \tag{7.12}$$

So, by solving (7.2) and (7.12), the unknown values of L_3 and C_3 are determined. The calculated L_3 and C_3 for the designed FSS are given in Fig. 7.11.

It should be noted that the circuit model in Fig. 7.8(a) and the results in Fig. 7.11 are only valid for normal incidence. For oblique incidence, both of the free-space equivalent impedance Z_0 and the dielectric spacer impedance Z_T need to be changed to

$$Z_{0,\text{TE}} = Z_0 / \cos\theta \tag{7.13}$$

$$Z_{0,\mathrm{TM}} = Z_0 \cos\theta, \tag{7.14}$$

$$Z_{T,\mathrm{TE}} = Z_{0,\mathrm{TE}} / \sqrt{\epsilon_r}, \tag{7.15}$$

$$Z_{T,\mathrm{TM}} = Z_{0,\mathrm{TM}} / \sqrt{\epsilon_r}, \tag{7.16}$$

where $Z_0 = 377\ \Omega$ is the free-space characteristic impedance. In addition, the equivalent impedance in the front and back layers need to be modified for the oblique incidence (Cavallo *et al.* 2014a). A model describing the effect of oblique incidence on the impedance of the layers and the couplings in higher order Floquet modes is available for the square patch array (Cavallo *et al.* 2014a, Cavallo *et al.* 2014b). This model gives an insightful understanding of the FSS response under oblique incidence and in higher order Floquet modes.

7.3.4 Fabrication process

The FSS structure is fabricated to experimentally validate the simulation results by utilising standard microfabrication techniques. The FSS is composed of alternating three layers of PDMS and two layers of patterned metal. In the first step, as a supporting substrate, a 3 inch silicon wafer is coated with 20 nm aluminium (Al), which enables final release of the multi-layer structure from silicon in a freestanding form. A 10 μm PDMS layer acting as encapsulation is spin-coated on the Al-coated silicon wafer. First metallisation step is performed with 200 nm gold (Au) with a 20 nm adhesion layer of chromium (Cr) deposited by electron beam evaporation (PVD75, Kurt J. Lesker Co.) at a rate of 0.1 nm/s. Metal layers are pattered by photolithography followed by wet chemical etching. Photoresist is then stripped off with acetone, rinsed with isopropanol and dried with high purity nitrogen.

Then, a second PDMS layer of 100 μm thickness, acting as dielectric spacer, is spun-on and cured on a leveled surface at room temperature to ensure thickness uniformity. Subsequently, the second layer of metallisation followed by photolithography with alignment and etching is performed. To encapsulate the second level of metallisation, a third PDMS layer of 10 μm is spun-on to complete the fabrication. The resulting structure is then peeled off from the supporting silicon and transferred onto a 3 inch

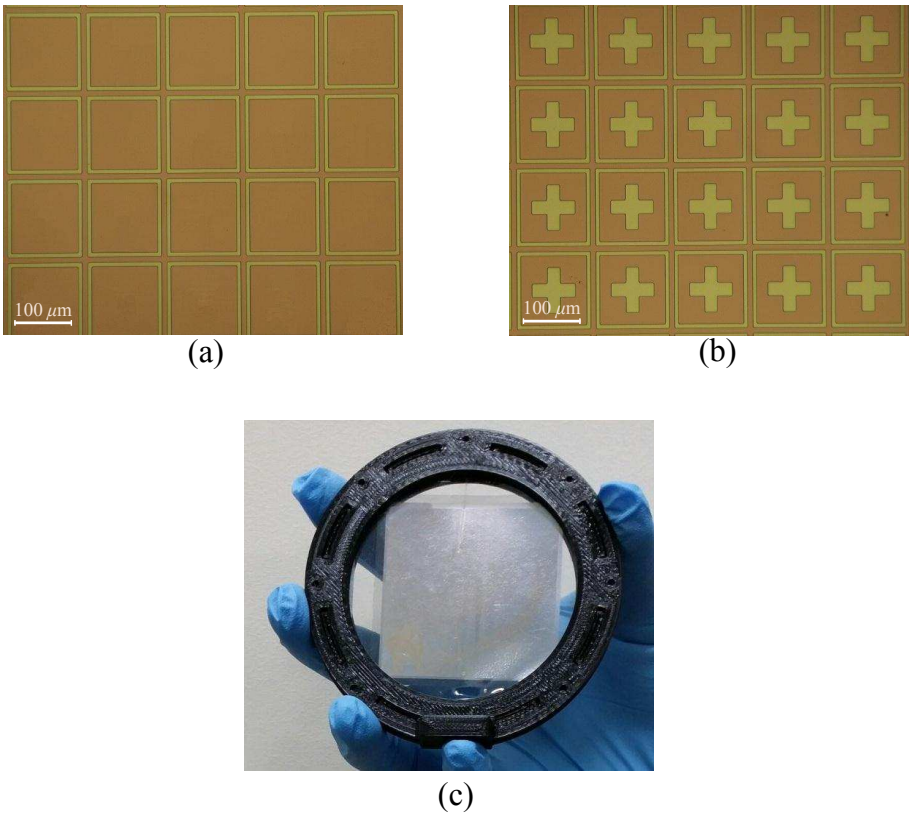

Figure 7.12. Fabricated second-order terahertz FSS. Optical micrographs of the (a) front and (b) back layers. (c) Frame supported MEFSS after release.

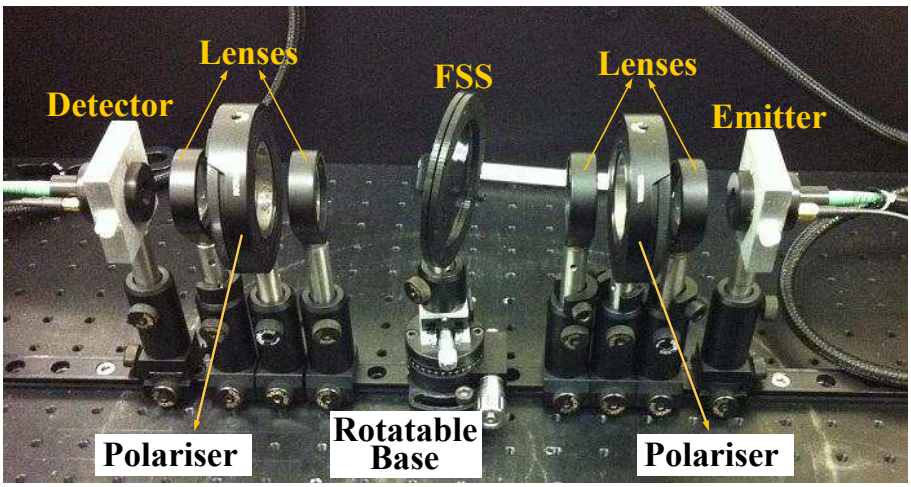

Figure 7.13. Measurement setup. Free-space measurement setup. A rotatable base is considered for measuring the FSS performance at oblique angles of incidence.

clamp for testing. Figure 7.12 shows micrographs of the front and back metal layers and the fabricated structure supported in a clamp for testing.

7.3.5 Results and discussion

This section presents the simulation and experimental measurement results to evaluate the performance of the designed FSS under different conditions. The free-space measurement is performed using the Menlo Systems GmbH Tera K15. The measurement setup is shown in Fig. 7.13. The setup is composed of Tera 15-SL25-FC and Tera 15-DP25-FC antenna modules acting as emitter and detector respectively that provide 2-port S-parameter measurement. The four identical lenses are made of polymer with a diameter of 50 mm, an effective focal length of 54 mm, and a working distance of 46 mm. A rotatable base is used for the FSS to evaluate its response for different oblique angles of incidence. The emitter and detector can be rotated around the propagation axis to obtain TE and TM polarisations. Two polarisers are placed between the lenses to have better polarisation purity in TE and TM mode measurements. A broadband terahertz pulse is radiated from the emitter through the FSS to the detector. The four lenses collimate and focus the beam onto the FSS. The transmission response is then normalised with a response obtained from free-space measurement.

In Fig. 7.14, the measured transmission response of the fabricated FSS is plotted to-

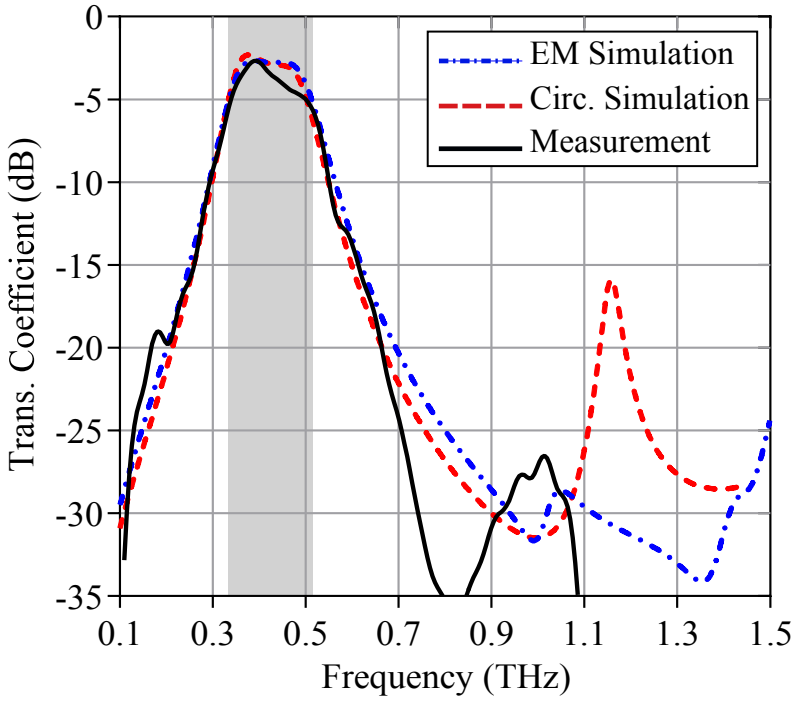

Figure 7.14. Measured and simulated transmission responses. Comparison between the simulation and measurement results of the FSS transmission coefficient under normal angle of incidence. The -3 dB bandwidth is shaded in grey.

gether with the electromagnetic and equivalent circuit simulation results at normal angle of incidence. As seen in this figure, a good agreement between the simulation and measurement results is achieved within the measurement bandwidth. The center frequency is 0.42 THz and the -3 dB bandwidth of the passband is around 45%. This is wider than the designed 35% bandwidth because the dissipation losses in PDMS decrease the quality factor (Q) of the front and back layers and hence increase the bandwidth. A wide out-of-band rejection is obtained up to 1.5 THz below -25 dB. The maximum loss in the passband is less than 5 dB. This loss is mainly attributed to the dielectric loss in the PDMS layers. Additional simulations (not shown) reveal that by replacing PDMS layers with a lower loss material such as cyclo-olefin copolymer (COC), the insertion loss in passband is reduced to 1 dB. The discrepancies between the measured and EM simulation results in the out-of-band response is attributed to the limited dynamic range of the measurement system.

The performance of the proposed FSS for the oblique angles of incidence is also investigated through simulation and measurement. The simulated and measured transmission coefficients of the FSS for the TE polarisation are shown in Fig. 7.15. In addition, Fig. 7.16 presents the simulated and measured transmission coefficients for the TM polarisation. In both cases, the results are presented for $0^\circ - 60^\circ$ incidence angles. As observed, the FSS can reasonably sustain its original response at very large incidence angles. However, the fractional bandwidth (FBW) is decreased for the TE polarisation response as the angle of incidence increases. On the contrary, for the TM polarisation, the FBW is increased as the incidence angle increases. This is mainly due to a change in the wave impedance for the two modes as described through (7.13)-(7.16) (Behdad 2008). So, as the angle of incidence increases, $Z_{0,\mathrm{TE}}$ will be increased resulting in a larger loaded quality factor in the input/output resonators that causes a smaller fractional bandwidth. On the other hand, in the TM mode, $Z_{0,\mathrm{TM}}$ will be decreased by increasing θ, and thus leads to a smaller loaded quality factor in the input/output resonators and a larger fractional bandwidth. A small discrepancy between the measured TE and TM transmission responses under normal incidence is possibly caused by a small difference in the system alignment and by a small anisotropy in the sample.

7.4 Conclusion

In summary, this chapter has presented the application of metamaterial-inspired miniaturised elements in designing terahertz frequency selective surfaces.

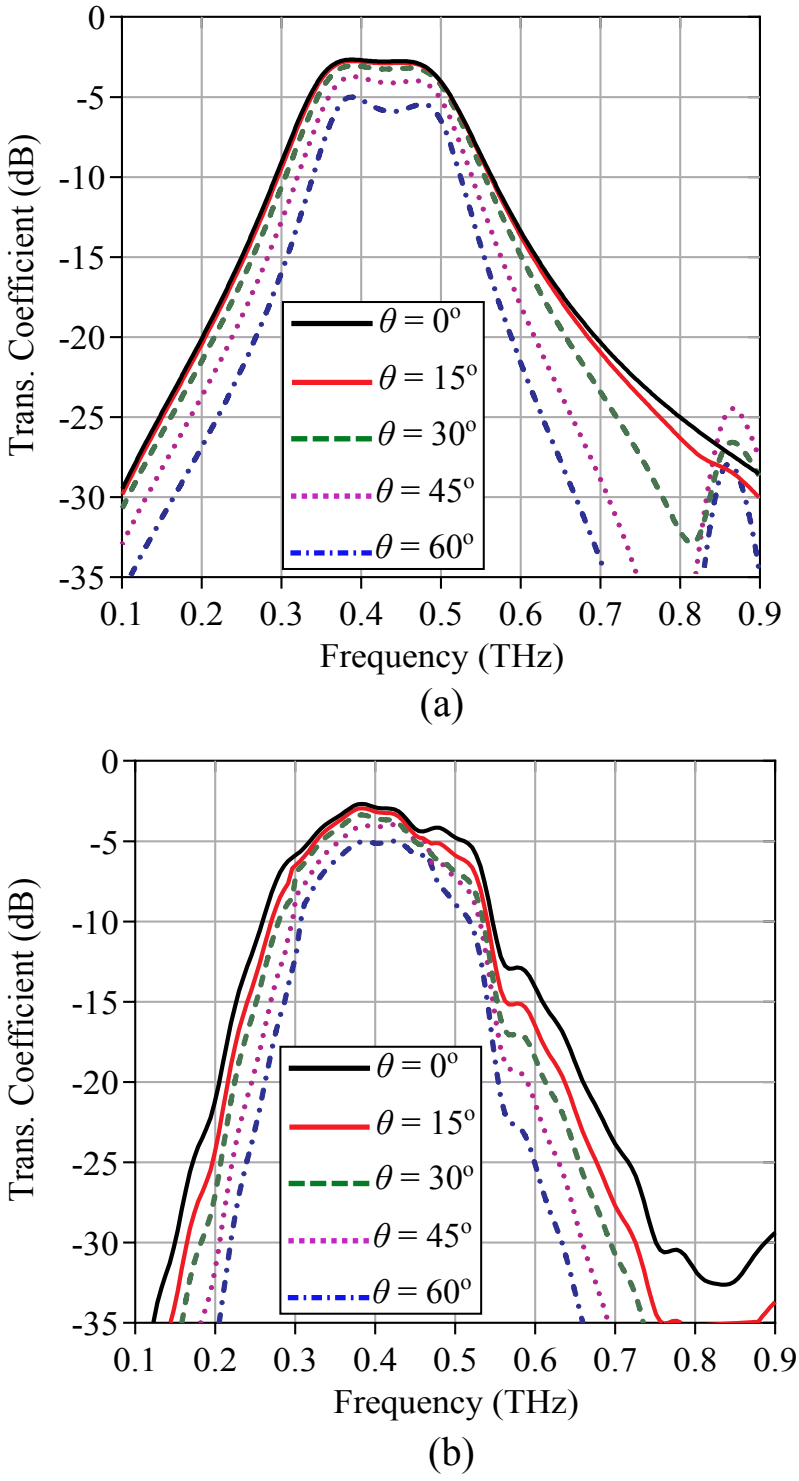

Figure 7.15. Scanning angle performance under TE polarisation. Transmission responses of the proposed FSS for oblique angles of incidence with TE polarisation. (a) Simulated transmission responses in CST Microwave Studio. (b) Measured transmission responses.

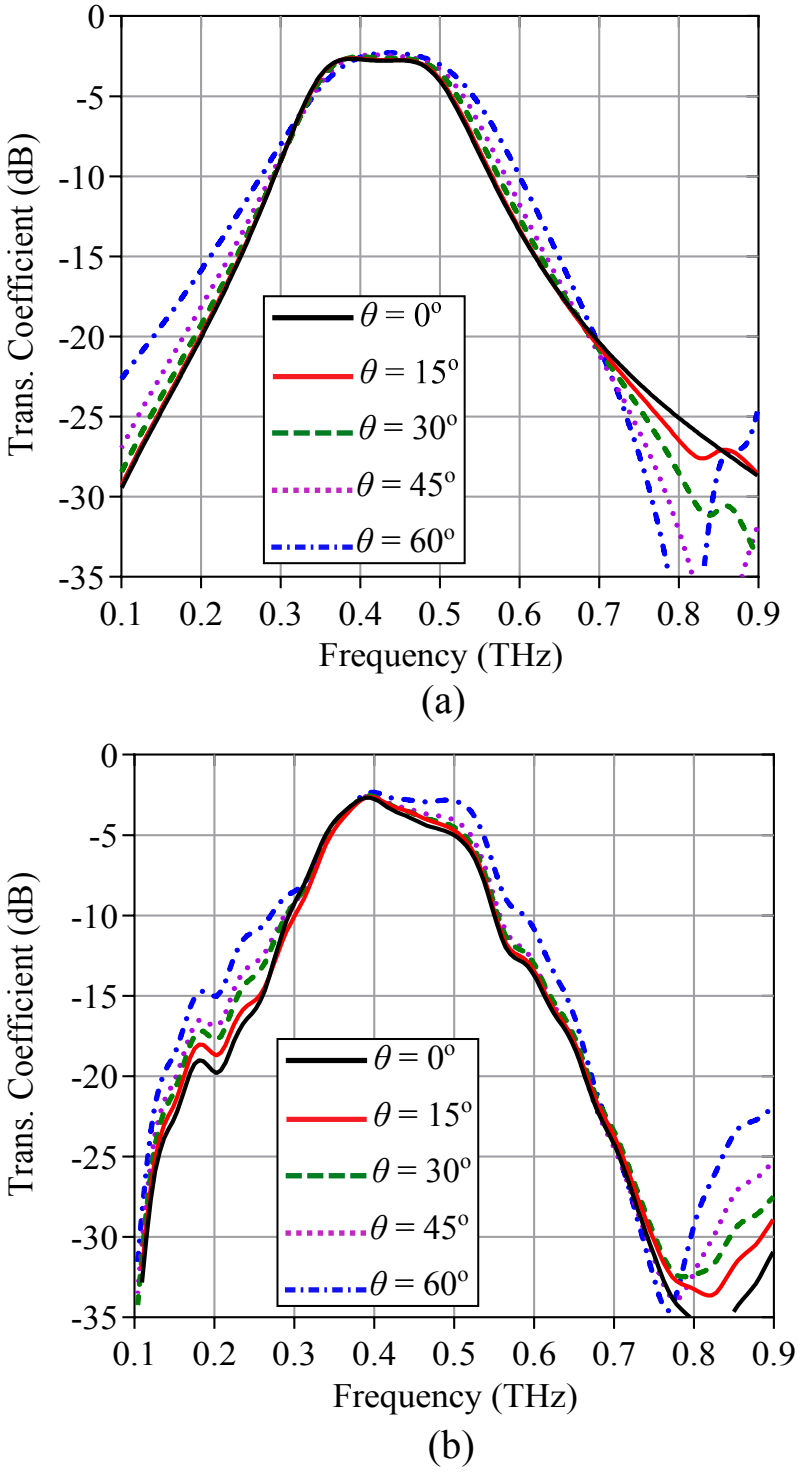

Figure 7.16. Scanning angle performance under TM polarisation. Transmission responses of the proposed FSS for oblique angles of incidence with TM polarisation. (a) Simulated transmission responses in CST Microwave Studio. (b) Measured transmission responses.

Two new second-order bandpass FSS prototypes have been proposed. The first FSS prototype has been designed on a quartz substrate. An equivalent circuit model has been developed for better insight into the FSS frequency response. The simulation results of filter show a good selectivity in the passband. Further, a harmonic-free out-of-band response up to 0.8 THz is achieved. The FSS shows a good immunity with respect to oblique angles of the incident wave.

The second bandpass THz-FSS has been designed and implemented on a PDMS dielectric substrate. An equivalent circuit is considered for modelling the FSS response. A simple synthesis procedure has been developed based on the equivalent circuit and the standard filter theory for designing the proposed FSS. The presented synthesis procedure has been verified through both simulation and experimental results. The results show a wide out-of-band rejection below -25 dB up to 1.5 THz. In addition, the spectral responses of the FSS are consistent over a wide range of incidence angles for both the TE and TM polarisations. The transmission level of the FSS in the passband can be improved significantly by a low loss polymer such as COC for dielectric layers.

Chapter 8

Conclusion and future work

DEVELOPED around the concept of metamaterials, the original contributions in this thesis are presented in three major parts. The first part relates to the compact microwave planar filters based on the metamaterial-inspired dual-mode resonators. The second part is on the metamaterials-based microwave sensors. The last part presents the frequency selective surfaces for microwave and terahertz applications based on the metamaterial-inspired miniaturised element unit cells. This chapter provides the conclusions of this dissertation and suggests future research on each of the three self-contained parts discussed in this thesis.

8.1 Part I: Metamaterial-inspired filters

8.1.1 Metamaterial-inspired dual-mode filters: Chapter 3

Background: Highly compact filters and circuit components are essential in developing many lightweight and portable electronics and communication systems. Conventional microwave filters suffer integrability limitations. In order to achieve more compact filters and circuit components, it is crucial for the resonators as a building blocks to be much smaller than the operational wavelength.

Methodology: Metamaterial-inspired resonators such SRRs and CSRRs showed promising potential in miniaturising the size of conventional RF subsystems such as filters, couplers and other circuits. This is because of the distributed capacitance and inductance embedded in their geometry that result in high quality factor resonators with compact sizes. Here, metamaterial-based dual-mode resonators are introduced as an alternative building block for designing compact microwave filters. A dual-mode complementary split-ring resonator (DMCSRR) has been developed by introducing a defect to a conventional CSRR. Furthermore, the dual-mode behaviour of the complementary electric-LC (ELC) resonators is incorporated in designing compact filters.

Results: The dual-mode metamaterial resonators has been applied to the design of compact bandpass and bandstop filters. Bandpass and bandstop filters designed based on dual-mode CSRR show compact sizes of $0.0625\lambda_g \times 0.18\lambda_g$ and $0.1\lambda \times 0.18\lambda_g$, where λ_g is the guided wavelength. Moreover, the dual-mode bandpass filter based on complementary electeic-LC resonator has a compact size of $0.11\lambda_g \times 0.08\lambda_g$.

Original contribution: For the first time, dual-mode metamaterial-inspired resonators have been developed and their electromagnetic behaviour has been modelled accurately based on lumped element circuits. These resonators have effectively been used in designing miniaturised microwave planar filters (Ebrahimi *et al.* 2014a, Ebrahimi *et al.* 2014f).

Future work: The dual-mode resonators introduced in this thesis have been utilised for designing second-order compact bandpass and bandstop filters. The applications of these resonators are not restricted to the second-order filters. Future potential applications can be in the design of miniaturised dual-band filters or higher-order dual-mode filters. They can also be applied in designing differential transmission lines or differential filters with improved differential-to-common-mode ratios.

8.2 Part II: Metamaterial-inspired sensors

8.2.1 Metamaterial-inspired microfluidic sensors: Chapter 4

Background: Microwave sensors for dielectric materials including liquids are of interest in biosensing and chemical detection since they provide a label free, non-invasive and real-time characterisation of biological or chemical samples. Despite that, a main drawback associated with these designs is that a large volume of liquid solution is required to interact with the sensing field. Microwave microfluidic sensors considerably decrease the amount of the required liquid for testing by integrating a tiny channel to deliver the liquid sample to the most sensitive part of the sensor. However, the existing microwave planar sensors exhibit lower quality factor and moderate fringing field that are crucial for high sensitivity.

Methodology: In order to enhance the fringing fields, complementary metamaterial resonators have been incorporated in the design of microwave microfluidic sensors. A complementary split-ring resonator (CSRR) coupled with a microstrip transmission line has been used for designing a microfluidic sensor with improved sensitivity. In addition, a complementary electric-LC (ELC) resonator loaded on a microstrip line is used for implementing a compact microfluidic sensor for characterisation of aqueous solutions.

Results: The designed CSRR-based microfluidic sensor has been fabricated and tested with ethanol-water solutions with different concentrations. The measurements showed an enhancement in the sensitivity of CSRR-based sensor by fourfold with respect to the conventional SRR-based microfluidic sensors. Additionally, the complementary electric-LC based microfluidic sensor has been used to determine the glucose concentrations in water. The measurement showed an accurate linear sensitivity of the device in determination of glucose concentration in aqueous solutions.

Original contribution: A high sensitivity microfluidic sensor has been developed with CSRR that provides strong fringing electric field around the channel suited for accurate dielectric characterisation. The designed sensor shows four times more sensitivity with respect to the conventional microwave microfluidic sensors (Ebrahimi *et al.* 2014c).

Future work: The designed CSRR-based sensor is suitable for biological applications. For applications in harsh industrial environment conditions or sensing the liquids with more viscosity an optimised design without the microfluidic channel would be of interest for more robust measurements. Furthermore, for implantable or on-body health

monitoring applications the improved design on flexible and biocompatible substrates is desirable.

8.2.2 Metamaterial rotation and displacement sensors: Chapter 5

Background: Metamaterial resonators such as split-ring resonators (SRRs), complementary split-ring resonators (CSRRs), and electric-LC resonators provide a high quality factor resonance, which is very sensitive to the environmental and geometrical parameters of the device. This makes them ideal for implementing displacement, symmetry, and rotation sensors. Despite their high sensitivity, existing metamaterial-inspired displacement and rotation sensors suffer low dynamic ranges and non-linearity of the response.

Methodology: The U-shaped coupled resonators have been used for designing a wide-dynamic-range rotation sensor. The resonators are meandered in a way that rotation results in a larger coupling between the resonators. The large coupling shifts the resonance frequency down that can be used for detection of the rotation angle. For implementing a displacement sensor with a wide dynamic range, a complementary electric-LC resonator loaded with a microstrip line is considered. Here, the displacement of the microstrip line with respect to the symmetry line of the resonator shifts the odd-mode resonance frequency down. The frequency shift is used to measure the displacement of the transmission line with respect to the resonator.

Original contribution: A wide dynamic-range rotation sensor has been designed extending the sensitivity range up to 180°. Besides that, a linear rotation sensing characteristic has been obtained by asymmetrically tapering the shapes of U-shaped resonators. The designed rotation sensor is compatible with MEMS technology integration (Ebrahimi *et al.* 2014d). A displacement sensor with a wide dynamic range of 1.6 mm is designed based on a microstrip-line loaded complementary-ELC resonator. The sensor dynamic range can be extended by optimising the microstrip line width or the resonator shape. Since the operation principle of the proposed sensor is based on the variation of the resonance frequency, rather than the notch level, it has a better immunity to the noise (Ebrahimi *et al.* 2014f).

Future work: Although, the dynamic range of the rotation sensor is extended up to 180°, in some applications a wider dynamic range up to 360° is required. So, an improved design with 360° dynamic range could be investigated for these applications.

Moreover, some modification on the rotation sensor might be of interest to use it for angular rotation speed or acceleration sensing. Furthermore, the designed displacement sensor has been validated with a series of static designs. A sensor with movable parts fabricated by using MEMS technology should be considered in real-world applications.

8.3 Part III: Metamaterial-inspired FSSs

8.3.1 Tunable and dual-band FSSs: Chapter 6

Background: The advent of new multi-band and multi-standard electronic communication systems urges the design of components with tunable, reconfigurable, and multiband functionalities. A major challenge in tunable and reconfigurable FSSs is the bias network that adds undesirable spurious band to the spectral response of the FSSs. In addition, in multiband FSS designs it is challenging to have a stable frequency response under oblique angles especially at higher passbands.

Methodology: In this dissertation, miniaturised elements are used instead of the conventional resonant unit cells for designing frequency selective surfaces. Thus, the unit cell size of the designed FSSs is much smaller than the operation wavelength. This results in a stable frequency response with respect to the oblique incidence angles. Also, the bias networks are designed in a way that they have minimal effect on the original FSS response. It has been performed by embedding the bias network in the FSS unit cell geometry.

Original contribution: For the first time, a low-profile second-order tunable bandpass FSSs has been designed based on varactor diodes. Tunability is obtained by integrating varactors in capacitive parts of the unit cells. A bias network has been embedded in the FSS structure by using an inductive wire grid in each layer of the FSS. This tunable FSS concept has been verified by fabricating a FSS prototype and measuring it in a parallel plate waveguide setup (Ebrahimi *et al.* 2015b). Furthermore, a dual-band FSS has been proposed with a unit cell size of $\lambda_0/10$. The designed FSS shows a stable frequency response under oblique incidence for both of the TE and TM polarisations of the incident wave. The passband frequencies of the FSS can be independently designed by properly optimising the unit cell dimensions (Ebrahimi *et al.* 2014a).

Future work: We have designed and validated a second-order bandpass FSS for low microwave frequencies. However, the varactor diodes are not applicable at higher microwave and millimetre-wave frequencies. Further research is required for designing higher-order tunable FSSs at higher frequencies based on alternative approaches such as liquid crystals or other tuning mechanisms.

8.3.2 Miniaturised elements terahertz FSSs: Chapter 7

Background: Frequency selective surfaces (FSSs) are fundamental components of terahertz imaging and spectrometry systems. A drawback associated with the conventional THz-FSS structures is their low selectivity, out-of-band harmonics, and sensitivity to the oblique angles of the EM radiation.

Methodology: Miniaturised elements are considered as alternatives in designing terahertz FSSs with higher-order responses. A double layer FSS has been designed. Since the FSS is made of miniaturised elements, a circuit model has been utilised for modelling its frequency response, and a synthesis procedure based on the equivalent circuit is developed for an analytical design procedure.

Original contribution: For the first time, a second-order terahertz bandpass FSS has been designed and verified based on miniaturised elements. The FSS shows a harmonic-free out-of-band response upto $3f_0$ where f_0 is the center frequency of the passband. The FSS response shows a very good stability for oblique angles of the incidence wave for both TE and TM polarisations (Ebrahimi *et al.* 2015a).

Future work: The miniaturised elements have shown a good performance in designing terahertz FSS with improved out-of-band response and high stability in the scan angle response. Further research is needed to apply them in designing new beamforming elements such as reflectarrays, transmitarrays, polarisation rotators, polarisation convertors at the terahertz frequency range.

Bibliography

ABDULJABAR-A., ROWE-D. J., PORCH-A., AND BARROW-D. (2014). Novel microwave microfluidic sensor using a microstrip split-ring resonator, *IEEE Transactions on Microwave Theory and Techniques*, **62**(3), pp. 679–688.

ALBISHI-A. M., BOYBAY-M. S., AND RAMAHI-O. M. (2012). Complementary split-ring resonator for crack detection in metallic surfaces, *IEEE Microwave and Wireless Components Letters*, **22**(6), pp. 330–332.

ALICI-K. B., AND OZBAY-E. (2007). Electrically small split ring resonator antennas, *Journal of Applied Physics*. art. no. 083104.

AL-JOUMAYLY-M., AND BEHDAD-N. (2009). A new technique for design of low-profile, second-order, bandpass frequency selective surfaces, *IEEE Transactions on Antennas and Propagation*, **57**(2), pp. 452–459.

AL-JOUMAYLY-M., AND BEHDAD-N. (2010). Low-profile, highly-selective, dual-band frequency selective surfaces with closely spaced bands of operation, *IEEE Transactions on Antennas and Propagation*, **58**(12), pp. 4042–4050.

ANGELOVSKI-A., PENIRSCHKE-A., AND JAKOBY-R. (2011). CRLH-mass flow detector array for cross-sectional detection of inhomogeneous distributed flow regimes in pipelines, *IEEE 41st European Microwave Conference (EuMC)*, pp. 611–614.

ATHUKORALA-L., AND BUDIMIR-D. (2009). Compact dual-mode open loop microstrip resonators and filters, *IEEE Microwave and Wireless Components Letters*, **19**(11), pp. 698–700.

ATHUKORALA-L., AND BUDIMIR-D. (2011). Compact second-order highly linear varactor-tuned dual-mode filters with constant bandwidth, *IEEE Transactions on Microwave Theory and Techniques*, **59**(9), pp. 2214–2220.

AZEMI-S. N., GHORBANI-K., AND ROWE-W. S. (2013). A reconfigurable FSS using a spring resonator element, *IEEE Antennas and Wireless Propagation Letters*, **12**, pp. 781–784.

AZNAR-F., GIL-M., BONACHE-J., AND MARTIN-F. (2008a). Modelling metamaterial transmission lines: a review and recent developments, *Opto-Electronics Review*, **16**(3), pp. 226–236.

AZNAR-F., GIL-M., BONACHE-J., JELINEK-L., BAENA-J., MARQUÉS-R., AND MARTÍN-F. (2008b). Characterization of miniaturized metamaterial resonators coupled to planar transmission lines through parameter extraction, *Journal of Applied Physics*. art. no. 114501.

AZNAR-F., VÉLEZ-A., DURÁN-SINDREU-M., BONACHE-J., AND MARTÍN-F. (2009). Elliptic-function CPW low-pass filters implemented by means of open complementary split ring resonators (OC-SRRs), *IEEE Microwave and Wireless Components Letters*, **19**(11), pp. 689–691.

BAENA-J. D., BONACHE-J., MARTÍN-F., SILLERO-R. M., FALCONE-F., LOPETEGI-F. F. T., LASO-M. A., GARCÍA-J. G., GIL-I., AND PORTILLO-M. F. (2005). Equivalent-circuit models for split-ring resonators and complementary split-ring resonators coupled to planar transmission lines, *IEEE Transactions on Microwave Theory and Techniques*, **53**(4), pp. 1451–1461.

BAENA-J. D., MARQUES-R., MEDINA-F., AND MARTEL-J. (2004). Artificial magnetic metamaterial design by using spiral resonators, *Physical Review B*. art. no. 014402.

BAO-J.-Z., SWICORD-M. L., AND DAVIS-C. C. (1996). Microwave dielectric characterization of binary mixtures of water, methanol, and ethanol, *The Journal of Chemical Physics*. art. no. 4441.

BASARAN-S. C., AND ERDEMLI-Y. E. (2009). A dual-band split-ring monopole antenna for wlan applications, *Microwave and Optical Technology Letters*, **51**, pp. 2685–2688.

BAYATPUR-F. (2009). *Metamaterial-Inspired Frequency-Selective Surfaces*, PhD thesis, The University of Michigan.

BAYATPUR-F., AND SARABANDI-K. (2008a). Multipole spatial filters using metamaterial-based miniaturized-element frequency-selective surfaces, *IEEE Transactions on Microwave Theory and Techniques*, **56**(12), pp. 2742–2747.

BAYATPUR-F., AND SARABANDI-K. (2008b). Single-layer high-order miniaturized-element frequency-selective surfaces, *IEEE Transactions on Microwave Theory and Techniques*, **56**(4), pp. 774–781.

BAYATPUR-F., AND SARABANDI-K. (2009a). A tunable metamaterial frequency-selective surface with variable modes of operation, *IEEE Transactions on Microwave Theory and Techniques*, **57**(6), pp. 1433–1438.

BAYATPUR-F., AND SARABANDI-K. (2009b). Tuning performance of metamaterial-based frequency selective surfaces, *IEEE Transactions on Antennas and Propagation*, **57**(2), pp. 590–592.

BAYATPUR-F., AND SARABANDI-K. (2010). Design and analysis of a tunable miniaturized-element frequency-selective surface without bias network, *IEEE Transactions on Antennas and Propagation*, **58**(4), pp. 1214–1219.

BEHDAD-N. (2008). A second-order band-pass frequency selective surface using nonresonant subwavelength periodic structures, *Microwave and Optical Technology Letters*, **50**(6), pp. 1639–1643.

BEHDAD-N., AL-JOUMAYLY-M., AND SALEHI-M. (2009). A low-profile third-order bandpass frequency selective surface, *IEEE Transactions on Antennas and Propagation*, **57**(2), pp. 460–466.

BILOTTI-F., TOSCANO-A., AND VEGNI-L. (2007). Design of spiral and multiple split-ring resonators for the realization of miniaturized metamaterial samples, *IEEE Transactions on Antennas and Propagation*, **55**(8), pp. 2258–2267.

BONACHE-J., GIL-I., GARCÍA-GARCÍA-J., AND MARTÍN-F. (2006a). Novel microstrip bandpass filters based on complementary split-ring resonators, *IEEE Transactions on Microwave Theory and Techniques*, **54**(1), pp. 265–271.

BONACHE-J., GIL-I., GARCÍA-GARCÍA-J., AND MARTÍN-F. (2007). Compact microstrip band-pass filters based on semi-lumped resonators, *IET Microwaves, Antennas Propagation*, **1**(4), pp. 932–936.

BONACHE-J., GIL-M., GIL-I., GARCÍA-GARCÍA-J., AND MARTÍN-F. (2006b). On the electrical characteristics of complementary metamaterial resonators, *IEEE Microwave and Wireless Components Letters*, **16**(10), pp. 543–545.

BONACHE-J., SISO-G., GIL-M., INIESTA-A., GARCIA-RINCON-J., AND MARTIN-F. (2008). Application of composite right/left handed (CRLH) transmission lines based on complementary split ring resonators (CSRRs) to the design of dual-band microwave components, *IEEE Microwave and Wireless Components Letters*, **18**(8), pp. 524–526.

BOSSARD-J. A., WERNER-D. H., MAYER-T. S., AND DRUPP-R. P. (2005). A novel design methodology for reconfigurable frequency selective surfaces using genetic algorithms, *IEEE Transactions on Antennas and Propagation*, **53**(4), pp. 1390–1400.

BOUYGE-D., MARDIVIRIN-D., BONACHE-J., CRUNTEANU-A., POTHIER-A., DURÁN-SINDREU-M., BLONDY-P., AND MARTÍN-F. (2011). Split ring resonators (SRRs) based on micro-electromechanical deflectable cantilever-type rings: application to tunable stopband filters, *IEEE Microwave and Wireless Components Letters*, **21**(5), pp. 243–245.

BOYBAY-M. S., AND RAMAHI-O. M. (2012). Material characterization using complementary split-ring resonators, *IEEE Transactions on Instrumentation and Measurement*, **61**(11), pp. 3039–3046.

BOYBAY-M. S., JIAO-A., GLAWDEL-T., AND REN-C. L. (2013). Microwave sensing and heating of individual droplets in microfluidic devices, *Lab on a Chip*, **13**(19), pp. 3840–3846.

CALOZ-C., AND ITOH-T. (2004). Transmission line approach of left-handed (LH) materials and microstrip implementation of an artificial LH transmission line, *IEEE Transactions on Antennas and Propagation*, **52**(5), pp. 1159–1166.

CALOZ-C., AND ITOH-T. (2005). *Electromagnetic Metamaterials: Transmission Line Theory and Microwave Applications*, John Wiley & Sons.

CASSE-B., LU-W., HUANG-Y., GULTEPE-E., MENON-L., AND SRIDHAR-S. (2010). Super-resolution imaging using a three-dimensional metamaterials nanolens, *Applied Physics Letters*. art. no. 023114.

CATALÁ-CIVERA-J. M., CANÓS-A. J., PEÑARANDA-FOIX-F. L., AND DE LOS REYES DAVÓ-E. (2003). Accurate determination of the complex permittivity of materials with transmission reflection measurements in partially filled rectangular waveguides, *IEEE Transactions on Microwave Theory and Techniques*, **51**(1), pp. 16–24.

CAVALLO-D., SYED-W., AND NETO-A. (2014a). Closed-form analysis of artificial dielectric layers-part I: Properties of a single layer under plane-wave incidence, *IEEE Transactions on Antennas and Propagation*, **62**(12), pp. 6256–6264.

CAVALLO-D., SYED-W., AND NETO-A. (2014b). Closed-form analysis of artificial dielectric layers-part II: Extension to multiple layers and arbitrary illumination, *IEEE Transactions on Antennas and Propagation*, **62**(12), pp. 6265–6273.

CHAHADIH-A., CRESSON-P. Y., HAMOUDA-Z., GU-S., MISMER-C., AND LASRI-T. (2015). Microwave/microfluidic sensor fabricated on a flexible Kapton substrate for complex permittivity characterization of liquids, *Sensors and Actuators A: Physical*, **229**, pp. 128–135.

CHANG-T., LANGLEY-R. J., AND PARKER-E. A. (1994). Frequency selective surfaces on biased ferrite substrates, *Electronics Letters*, **30**(15), pp. 1193–1194.

CHEN-H., RAN-L., HUANGFU-J., ZHANG-X., CHEN-K., GRZEGORCZYK-T. M., AND KONG-J. A. (2004). Left-handed materials composed of only S-shaped resonators, *Physical Review E*. art. no. 057605.

CHEN-H., RAN-L.-X., HUANG-FU-J. T., ZHANG-X.-M., CHEN-K. S., GRZEGORCZYK-T. M., AND KONG-J. A. (2005). Magnetic properties of S-shaped split-ring resonators, *Progress In Electromagnetics Research*, **51**, pp. 231–247.

CHEN-T., LI-S., AND SUN-H. (2012). Metamaterials application in sensing, *Sensors*, **12**(3), pp. 2742–2765.

CHIANG-Y.-J., YANG-C.-S., YANG-Y.-H., PAN-C.-L., AND YEN-T.-J. (2011). An ultrabroad terahertz bandpass filter based on multiple-resonance excitation of a composite metamaterial, *Applied Physics Letters*. art. no. 191909.

CHIU-C.-N., AND CHANG-K.-P. (2009). A novel miniaturized-element frequency selective surface having a stable resonance, *IEEE Antennas and Wireless Propagation Letters*, **8**, pp. 1175–1177.

CHRETIENNOT-T., DUBUC-D., AND GRENIER-K. (2013). A microwave and microfluidic planar resonator for efficient and accurate complex permittivity characterization of aqueous solutions, *IEEE Transactions on Microwave Theory and Techniques*, **61**(2), pp. 972–978.

COSTA-F., MONORCHIO-A., AND VASTANTE-G. P. (2011). Tunable high-impedance surface with a reduced number of varactors, *IEEE Antennas and Wireless Propagation Letters*, **10**, pp. 11–13.

COUTTS-G. M., MANSOUR-R. R., AND CHAUDHURI-S. K. (2008). Microelectromechanical systems tunable frequency-selective surfaces and electromagnetic-bandgap structures on rigid-flex substrates, *IEEE Transactions on Microwave Theory and Techniques*, **56**(7), pp. 1737–1746.

CUI-Y., SUN-J., HE-Y., WANG-Z., AND WANG-P. (2013). A simple, tunable, and highly sensitive radio-frequency sensor, *Applied Physics Letters*. art. no. 062906.

DONG-Y. (2012). *Substrate Integrated Waveguide Based Metamaterial Components and Novel Miniaturized Planar Antennas*, PhD thesis, University of California, Los Angeles.

DONG-Y., TOYAO-H., AND ITOH-T. (2012). Design and characterization of miniaturized patch antennas loaded with complementary split-ring resonators, *IEEE Transactions on Antennas and Propagation*, **60**(2), pp. 772–785.

EBRAHIMI-A., NIRANTAR-S., WITHAYACHUMNANKUL-W., BHASKARAN-M., SRIRAM-S., AL-SARAWI-S., AND ABBOTT-D. (2015a). Second-order terahertz bandpass frequency selective surface with miniaturized elements, *IEEE Transactions on Terahertz Science and Technology*, **5**(5), pp. 761–769.

EBRAHIMI-A., SHEN-Z., WITHAYACHUMNANKUL-W., AL-SARAWI-S., AND ABBOTT-D. (2015b). Varactor-tunable second-order bandpass frequency selective surface with embedded bias network, *IEEE Transactions on Antennas and Propagation*. Submitted.

EBRAHIMI-A., WITHAYACHUMNANKUL-W., AL-SARAWI-S., AND ABBOTT-D. (2014a). Compact dual-mode wideband filter based on complementary split-ring resonator, *IEEE Microwave and Wireless Components Letters*, **24**(3), pp. 152–154.

EBRAHIMI-A., WITHAYACHUMNANKUL-W., AL-SARAWI-S., AND ABBOTT-D. (2014b). Design of dual-band frequency selective surface with miniaturized elements, *International Workshop on Antenna Technology: "Small Antennas, Novel EM Structures and Materials, and Applications" (iWAT)*, pp. 201–204.

EBRAHIMI-A., WITHAYACHUMNANKUL-W., AL-SARAWI-S., AND ABBOTT-D. (2014c). High-sensitivity metamaterial-inspired sensor for microfluidic dielectric characterization, *IEEE Sensors Journal*, **14**(5), pp. 1345–1351.

EBRAHIMI-A., WITHAYACHUMNANKUL-W., AL-SARAWI-S., AND ABBOTT-D. (2014d). Metamaterial-inspired rotation sensor with wide dynamic range, *IEEE Sensors Journal*, **14**(8), pp. 2609–2614.

EBRAHIMI-A., WITHAYACHUMNANKUL-W., AL-SARAWI-S., AND ABBOTT-D. (2014e). Second-order bandpass frequency selective surface for terahertz applications, *IEEE 39th International Conference on Infrared, Millimeter, and Terahertz waves (IRMMW-THz)*. DOI:10.1109/IRMMW-THz.2014.6956237.

EBRAHIMI-A., WITHAYACHUMNANKUL-W., AL-SARAWI-S. F., AND ABBOTT-D. (2014f). Dual-mode behavior of the complementary electric-LC resonators loaded on transmission line: Analysis and applications, *Journal of Applied Physics*. art. no. 083705.

EBRAHIMI-A., YAGHMAEE-P., WITHAYACHUMNANKUL-W., FUMEAUX-C., AL-SARAWI-S., AND ABBOTT-D. (2013). Interlayer tuning of X-band frequency-selective surface using liquid crystal, *Proceedings of Asia Pacific Microwave Conference (APMC2013)*, pp. 1118–1120.

ELEFTHERIADES-G. V., IYER-A. K., AND KREMER-P. C. (2002). Planar negative refractive index media using periodically LC loaded transmission lines, *IEEE Transactions on Microwave Theory and Techniques*, **50**(12), pp. 2702–2712.

ELEFTHERIADES-G. V., SIDDIQUI-O., AND IYER-A. K. (2003). Transmission line models for negative refractive index media and associated implementations without excess resonators, *IEEE Microwave and Wireless Components Letters*, **13**(2), pp. 51–53.

ENGHETA-N., AND ZIOLKOWSKI-R. W. (2006). *Metamaterials: Physics and Engineering Explorations*, John Wiley & Sons.

FALCONE-F., LOPETEGI-T., BAENA-J. D., MARQUÉS-R., MARTÍN-F., AND SOROLLA-M. (2004a). Effective negative-ϵ; stopband microstrip lines based on complementary split ring resonators, *IEEE Microwave and Wireless Components Letters*, **14**(6), pp. 280–282.

FALCONE-F., MARTÍN-F., BONACHE-J., MARQUÉS-R., LOPETEGI-T., AND SOROLLA-M. (2004b). Left handed coplanar waveguide band pass filters based on bi-layer split ring resonators, *IEEE Microwave and Wireless Components Letters*, **14**(1), pp. 10–12.

FAN-J.-W., LIANG-C.-H., AND LI-D. (2007). Design of cross-coupled dual-band filter with equal-length split-ring resonators, *Progress in Electromagnetics Research*, **75**, pp. 285–293.

FATHELBAB-W. (2011). Two novel classes of band-reject filters realizing broad upper pass bandwidth-synthesis and design, *IEEE Transactions on Microwave Theory and Techniques*, **59**(2), pp. 250–259.

FOK-S.-W., CHEONG-P., TAM-K.-W., AND MARTINS-R. P. (2006). A novel microstrip square-loop dual-mode bandpass filter with simultaneous size reduction and spurious response suppression, *IEEE Transactions on Microwave Theory and Techniques*, **54**(5), pp. 2033–2041.

FUCHI-K., TANG-J., CROWGEY-B., DIAZ-A. R., ROTHWELL-E. J., AND OUEDRAOGO-R. O. (2012). Origami tunable frequency selective surfaces, *IEEE Antennas and Wireless Propagation Letters*, **11**, pp. 473–475.

GARBOVSKIY-Y., REISMAN-L., CELINSKI-Z., CAMLEY-R., AND GLUSHCHENKO-A. (2011). Metallic surfaces as alignment layers for nondisplay applications of liquid crystals, *Applied Physics Letters*. art. no. 073301.

GARCÍA-GARCÍA-J., MARTÍN-F., FALCONE-F., BONACHE-J., BAENA-J. D., GIL-I., AMAT-E., LOPETEGI-T., LASO-M. A., AND ITURMENDI-J. A. M. (2005). Microwave filters with improved stopband based on sub-wavelength resonators, *IEEE Transactions on Microwave Theory and Techniques*, **53**(6), pp. 1997–2006.

GARCIA-LAMPEREZ-A., AND SALAZAR-PALMA-M. (2006). Dual band filter with split-ring resonators, *IEEE MTT-S International Microwave Symposium Digest*, pp. 519–522.

GIANVITTORIO-J., RAHMAT-SAMII-Y., AND ROMEU-J. (2001). Fractal FSS: various self-similar geometries used for dual-band and dual-polarized FSS, *Proceedings of IEEE Antennas and Propagation Society International Symposium, 2001*, Vol. 3, pp. 640–643.

GIL-I., BONACHE-J., GARCÍA-GARCÍA-J., AND MARTÍN-F. (2006a). Tunable metamaterial transmission lines based on varactor-loaded split-ring resonators, *IEEE Transactions on Microwave Theory and Techniques*, **54**(6), pp. 2665–2674.

GIL-I., BONACHE-J., GIL-M., GARCÍA-GARCÍA-J., MARTÍN-F., AND MARQUÉS-R. (2006b). Accurate circuit analysis of resonant-type left handed transmission lines with inter-resonator coupling, *Journal of Applied Physics*. art. no. 074908.

GIL-M., BONACHE-J., AND MARTÍN-F. (2007a). Metamaterial filters with attenuation poles in the pass band for ultra wide band applications, *Microwave and Optical Technology Letters*, **49**(12), pp. 2909–2913.

GIL-M., BONACHE-J., GARCIA-GARCIA-J., MARTEL-J., AND MARTÍN-F. (2007b). Composite right/left-handed metamaterial transmission lines based on complementary split-rings resonators and their applications to very wideband and compact filter design, *IEEE Transactions on Microwave Theory and Techniques*, **55**(6), pp. 1296–1304.

GOELDEN-F., GAEBLER-A., GOEBEL-M., MANABE-A., MUELLER-S., AND JAKOBY-R. (2009). Tunable liquid crystal phase shifter for microwave frequencies, *Electronics letters*, **45**(13), pp. 686–687.

GÖRÜR-A., KARPUZ-C., AND AKPINAR-M. (2003). A reduced-size dual-mode bandpass filter with capacitively loaded open-loop arms, *IEEE Microwave and Wireless Components Letters*, **13**(9), pp. 385–387.

GRBIC-A., AND ELEFTHERIADES-G. V. (2002a). A backward-wave antenna based on negative refractive index LC networks, *IEEE Antennas and Propagation Society International Symposium*, Vol. 4, pp. 340–343.

GRBIC-A., AND ELEFTHERIADES-G. V. (2002b). Experimental verification of backward-wave radiation from a negative refractive index metamaterial, *Journal of Applied Physics*, **92**(10), pp. 5930–5935.

GREGORY-A. P., AND CLARKE-R. N. (2006). A review of RF and microwave techniques for dielectric measurements on polar liquids, *IEEE Transactions on Dielectrics and Electrical Insulation*, **13**(4), pp. 727–743.

GRENIER-K., DUBUC-D., POLENI-P.-E., KUMEMURA-M., TOSHIYOSHI-H., FUJII-T., AND FUJITA-H. (2009). Integrated broadband microwave and microfluidic sensor dedicated to bioengineering, *IEEE Transactions on Microwave Theory and Techniques*, **57**(12), pp. 3246–3253.

HILL-R., AND MUNK-B. (1996). The effect of perturbating a frequency-selective surface and its relation to the design of a dual-band surface, *IEEE Transactions on Antennas and Propagation*, **44**(3), pp. 368–374.

HOFMANN-M., FISCHER-G., WEIGEL-R., AND KISSINGER-D. (2013). Microwave-based noninvasive concentration measurements for biomedical applications, *IEEE Transactions on Microwave Theory and Techniques*, **61**(5), pp. 2195–2204.

HONG-J.-S. G., AND LANCASTER-M. J. (2004). *Microstrip Filters for RF/Microwave Applications*, Vol. 167, John Wiley & Sons.

HONG-J.-S., SHAMAN-H., AND CHUN-Y.-H. (2007). Dual-mode microstrip open-loop resonators and filters, *IEEE Transactions on Microwave Theory and Techniques*, **55**(8), pp. 1764–1770.

HORESTANI-A., ABBOTT-D., AND FUMEAUX-C. (2013a). Rotation sensor based on horn-shaped split ring resonator, *IEEE Sensors Journal*, **13**(8), pp. 3014–3015.

HORESTANI-A. K., DURÀN-SINDREU-M., NAQUI-J., FUMEAUX-C., AND MARTÌN-F. (2014a). Coplanar waveguides loaded with S-shaped split-ring resonators: Modeling and application to compact microwave filters, *IEEE Antennas and Wireless Propagation Letters*, **13**, pp. 1349–1352.

HORESTANI-A. K., DURÀN-SINDREU-M., NAQUI-J., FUMEAUX-C., AND MARTÌN-F. (2014b). S-shaped complementary split ring resonators and their application to compact differential bandpass filters with common-mode suppression, *IEEE Microwave and Wireless Components Letters*, **24**(3), pp. 149–151.

HORESTANI-A. K., FUMEAUX-C., AL-SARAWI-S. F., AND ABBOTT-D. (2012). Split ring resonators with tapered strip width for wider bandwidth and enhanced resonance, *IEEE Microwave and Wireless Components Letters*, **22**(9), pp. 450–452.

HORESTANI-A. K., FUMEAUX-C., AL-SARAWI-S. F., AND ABBOTT-D. (2013b). Displacement sensor based on diamond-shaped tapered split ring resonator, *IEEE Sensors Journal*, **13**(4), pp. 1153–1160.

HORESTANI-A. K., NAQUI-J., ABBOTT-D., FUMEAUX-C., AND MARTÍN-F. (2014c). Two-dimensional displacement and alignment sensor based on reflection coefficients of open microstrip lines loaded with split ring resonators, *Electronics Letters*, **50**(8), pp. 620–622.

HUANG-X., SHEN-Z., FENG-Q., AND LI-B. (2015). Tunable 3-D bandpass frequency-selective structure with wide tuning range, *IEEE Transactions on Antennas and Propagation*, **63**(7), pp. 3297–3301.

HU-W., ISMAIL-M., CAHILL-R., GAMBLE-H., DICKIE-R., FUSCO-V., LINTON-D., REA-S., AND GRANT-N. (2006). Tunable liquid crystal reflectarray patch element, *Electronics Letters*, **42**(9), pp. 509–511.

ISLAM-R., ELEK-F., AND ELEFTHERIADES-G. (2004). Coupled-line metamaterial coupler having co-directional phase but contra-directional power flow, *Electronics Letters*, **40**(5), pp. 315–317.

IYER-A. K., AND ELEFTHERIADES-G. V. (2002). Negative refractive index metamaterials supporting 2-D waves, *IEEE MTT-S International Microwave Symposium Digest*, Vol. 2, pp. 1067–1070.

JARAUTA-E., LASO-M., LOPETEGI-T., FALCONE-F., BERUETE-M., BAENA-J., BONACHE-J., GIL-I., GARCIA-GARCIA-J., AND MARCOTEGUI-A. (2004). Metamaterial microstrip backward couplers for fully planar fabrication techniques, *12th International Conference on Terahertz Electronics, Infrared and Millimeter Waves*, pp. 185–186.

JENKINS-S., HODGETTS-T., CLARKE-R., AND PREECE-A. (1990). Dielectric measurements on reference liquids using automatic network analysers and calculable geometries, *Measurement Science and Technology*, **1**(8), pp. 691–702.

KAPILEVICH-B., AND LITVAK-B. (2011). Optimized microwave sensor for online concentration measurements of binary liquid mixtures, *IEEE Sensors Journal*, **11**(10), pp. 2611–2616.

KÄRKKÄINEN-M., AND IKONEN-P. (2005). Patch antenna with stacked split-ring resonators as an artificial magneto-dielectric substrate, *Microwave and Optical Technology Letters*, **46**(6), pp. 554–556.

KASHANIANFARD-M., AND SARABANDI-K. (2013). Metamaterial inspired optically transparent band-selective ground planes for antenna applications, *IEEE Transactions on Antennas and Propagation*, **61**(9), pp. 4624–4631.

KIANI-G., FORD-K. L., OLSSON-L. G., ESSELLE-K. P., AND PANAGAMUWA-C. J. (2010). Switchable frequency selective surface for reconfigurable electromagnetic architecture of buildings, *IEEE Transactions on Antennas and Propagation*, **58**(2), pp. 581–584.

KIANI-G. I., FORD-K. L., ESSELLE-K. P., WEILY-A. R., PANAGAMUWA-C., AND BATCHELOR-J. C. (2008). Single-layer bandpass active frequency selective surface, *Microwave and Optical Technology Letters*, **50**(8), pp. 2149–2151.

KIM-B.-H., LEE-Y.-J., LEE-H.-J., HONG-Y., YOOK-J.-G., CHUNG-M. H., CHO-W., AND CHOI-H. H. (2014). A gas sensor using double split-ring resonator coated with conducting polymer at microwave frequncies, *IEEE Sensors Symposium*, pp. 1815–1818.

KIM-J., BABAJANYAN-A., HOVSEPYAN-A., LEE-K., AND FRIEDMAN-B. (2008). Microwave dielectric resonator biosensor for aqueous glucose solution, *Review of Scientific Instruments*. art. no. 86107.

KIM-O. S., AND BREINBJERG-O. (2009). Miniaturised self-resonant split-ring resonator antenna, *Electronics Letters*, **45**(4), pp. 196–197.

KUKI-T., FUJIKAKE-H., AND NOMOTO-T. (2002). Microwave variable delay line using dual-frequency switching-mode liquid crystal, *IEEE Transactions on Microwave Theory and Techniques*, **50**(11), pp. 2604–2609.

LAI-A., ITOH-T., AND CALOZ-C. (2004). Composite right/left-handed transmission line metamaterials, *IEEE Microwave Magazine*, **5**(3), pp. 34–50.

LAN-F., YANG-Z., QI-L., GAO-X., AND SHI-Z. (2014). Terahertz dual-resonance bandpass filter using bilayer reformative complementary metamaterial structures, *Optics Letters*, **39**(7), pp. 1709–1712.

LEE-H.-J., LEE-H.-S., YOO-K.-H., AND YOOK-J.-G. (2008). On the possibility of biosensors based on split ring resonators, *IEEE 38th European Microwave Conference*, pp. 1222–1225.

LEE-H.-J., LEE-J.-H., MOON-H.-S., JANG-I.-S., CHOI-J.-S., YOOK-J.-G., AND JUNG-H.-I. (2012). A planar split-ring resonator-based microwave biosensor for label-free detection of biomolecules, *Sensors and Actuators B: Chemical*, **169**, pp. 26–31.

LEVY-R., SNYDER-R., AND SHIN-S. (2006). Bandstop filters with extended upper passbands, *IEEE Transactions on Microwave Theory and Techniques*, **54**(6), pp. 2503–2515.

LI-B., AND SHEN-Z. (2013). Synthesis of quasi-elliptic bandpass frequency-selective surface using cascaded loop arrays, *IEEE Transactions on Antennas and Propagation*, **61**(6), pp. 3053–3059.

LI-B., AND SHEN-Z. (2014). Wideband 3D frequency selective rasorber, *IEEE Transactions on Antennas and Propagation*, **62**(12), pp. 6536–6541.

LI-G., CHAN-Y., MOK-T., AND VARDAXOGLOU-J. (1995). Analysis of frequency-selective surfaces on a biased ferrite substrate, *International Journal of Electronics*, **78**(6), pp. 1159–1175.

LI-J., WITHAYACHUMNANKUL-W., CHANG-S., AND ABBOTT-D. (2011). Metamaterial-based strain sensors, *Proceedings of the 7th International Conference on Intelligent Sensors, Sensor Networks and Information Processing (ISSNIP)*, pp. 30–32.

LIMA-A., PARKER-E. A., AND LANGLEY-R. J. (1994). Tunable frequency selective surface using liquid substrates, *Electronics Letters*, **30**(4), pp. 281–282.

LI-M., AND BEHDAD-N. (2012). Fluidically tunable frequency selective/phase shifting surfaces for high-power microwave applications, *IEEE Transactions on Antennas and Propagation*, **60**(6), pp. 2748–2759.

LI-M., AND BEHDAD-N. (2013). Frequency selective surfaces for pulsed high-power microwave applications, *IEEE Transactions on Antennas and Propagation*, **61**(2), pp. 677–687.

LI-M., YU-B., AND BEHDAD-N. (2010). Liquid-tunable frequency selective surfaces, *IEEE Microwave and Wireless Components Letters*, **20**(8), pp. 423–425.

LIN-X. Q., AND CUI-T. J. (2008). Controlling the bandwidth of split ring resonators, *IEEE Microwave and Wireless Components Letters*, **18**(4), pp. 245–247.

LIU-J.-C., SHU-D.-S., ZENG-B.-H., AND CHANG-D.-C. (2008). Improved equivalent circuits for complementary split-ring resonator-based high-pass filter with C-shaped couplings, *IET Microwaves, Antennas & Propagation*, **2**(6), pp. 622–626.

LU-M., LI-W., AND BROWN-E. R. (2011). Second-order bandpass terahertz filter achieved by multilayer complementary metamaterial structures, *Optics Letters*, **36**(7), pp. 1071–1073.

MANARA-G., MONORCHIO-A., AND MITTRA-R. (1999). Frequency selective surface design based on genetic algorithm, *Electronics Letters*, **35**(17), pp. 1400–1401.

MANDAL-M. K., DIVYABRAMHAM-K., AND SANYAL-S. (2008). Compact, wideband bandstop filters with sharp rejection characteristic, *IEEE Microwave and Wireless Components Letters*, **18**(10), pp. 665–667.

MARQUÉS-R., MARTEL-J., MESA-F., AND MEDINA-F. (2002). Left-handed-media simulation and transmission of EM waves in subwavelength split-ring-resonator-loaded metallic waveguides, *Physical Review Letters*. art. no. 183901.

MARQUÉS-R., MARTÍN-F., AND SOROLLA-M. (2011). *Metamaterials with Negative Parameters: Theory, Design and Microwave Applications*, Vol. 183, John Wiley & Sons.

MARQUÉS-R., MESA-F., MARTEL-J., AND MEDINA-F. (2003). Comparative analysis of edge-and broadside-coupled split ring resonators for metamaterial design-theory and experiments, *IEEE Transactions on Antennas and Propagation*, **51**(10), pp. 2572–2581.

MARTÍN-F., BONACHE-J., FALCONE-F., SOROLLA-M., AND MARQUÉS-R. (2003a). Split ring resonator-based left-handed coplanar waveguide, *Applied Physics Letters*, **83**(22), pp. 4652–4654.

MARTÍN-F., FALCONE-F., BONACHE-J., MARQUÉS-R., AND SOROLLA-M. (2003b). Miniaturized coplanar waveguide stop band filters based on multiple tuned split ring resonators, *IEEE Microwave and Wireless Components Letters*, **13**(12), pp. 511–513.

MELIK-R., UNAL-E., PERKGOZ-N. K., PUTTLITZ-C., AND DEMIR-H. V. (2009a). Flexible metamaterials for wireless strain sensing, *Applied Physics Letters*. art. no. 181105.

MELIK-R., UNAL-E., PERKGOZ-N. K., PUTTLITZ-C., AND DEMIR-H. V. (2009b). Metamaterial-based wireless strain sensors, *Applied Physics Letters*. art. no. 011106.

MIAS-C. (2005). Varactor-tunable frequency selective surface with resistive-lumped-element biasing grids, *IEEE Microwave and Wireless Components Letters*, **15**(9), pp. 570–572.

MOALLEM-M., AND SARABANDI-K. (2012). Miniaturized-element frequency selective surfaces for millimeter-wave to terahertz applications, *IEEE Transactions on Terahertz Science and Technology*, **2**(3), pp. 333–339.

MOMENI HASAN ABADI-S., LI-M., AND BEHDAD-N. (2014). Harmonic-suppressed miniaturized-element frequency selective surfaces with higher order bandpass responses, *IEEE Transactions on Antennas and Propagation*, **62**(5), pp. 2562–2571.

MUELLER-S., KOEBERLE-M., GOELDEN-F., PENIRSCHKE-A., GAEBLER-A., LAPANIK-A., HAASE-W., AND JAKOBY-R. (2008). W-band characterization of anisotropic liquid crystals at room temperature, *IEEE 38th European Microwave Conference*, pp. 119–122.

MUELLER-S., PENIRSCHKE-A., DAMM-C., SCHEELE-P., WITTEK-M., WEIL-C., AND JAKOBY-R. (2005). Broad-band microwave characterization of liquid crystals using a temperature-controlled coaxial transmission line, *IEEE Transactions on Microwave Theory and Techniques*, **53**(6), pp. 1937–1945.

MUNK-B. A. (2005). *Frequency Selective Surfaces: Theory and Design*, John Wiley & Sons.

NAGLICH-E. J., LEE-J., PEROULIS-D., AND CHAPPELL-W. (2012). Extended passband bandstop filter cascade with continuous 0.85-6.6-GHz coverage, *IEEE Transactions on Microwave Theory and Techniques*, **60**(1), pp. 21–30.

NAQUI-J., AND MARTÍN-F. (2013). Transmission lines loaded with bisymmetric resonators and their application to angular displacement and velocity sensors, *IEEE Transactions on Microwave Theory and Techniques*, **61**(12), pp. 4700–4713.

NAQUI-J., DURÁN-SINDREU-M., AND MARTÍN-F. (2011). Novel sensors based on the symmetry properties of split ring resonators (SRRs), *Sensors*, **11**(8), pp. 7545–7553.

NAQUI-J., DURÁN-SINDREU-M., AND MARTÍN-F. (2012). Alignment and position sensors based on split ring resonators, *Sensors*, **12**(9), pp. 11790–11797.

NAQUI-J., DURÁN-SINDREU-M., AND MARTÍN-F. (2013a). Differential and single-ended microstrip lines loaded with slotted magnetic-LC resonators, *International Journal of Antennas and Propagation*. DOI: 10.1155/2013/640514.

NAQUI-J., DURÁN-SINDREU-M., AND MARTÍN-F. (2013b). Selective mode suppression in microstrip differential lines by means of electric-LC (ELC) and magnetic-LC (MLC) resonators, *Applied Physics A*. vol. 115, no. 2, pp. 637–643.

NAQUI-J., FERNÁNDEZ-PRIETO-A., MESA-F., MEDINA-F., AND MARTÍN-F. (2014). Effects of interresonator coupling in split ring resonator loaded metamaterial transmission lines, *Journal of Applied Physics*. art. no. 194903.

NESHAT-M., GIGOYAN-S., SAEEDKIA-D., AND SAFAVI-NAEINI-S. (2008). Travelling-wave whispering gallery resonance sensor in millimetre-wave range, *Electronics Letters*, **44**(17), pp. 1020–1022.

NGUYEN-H. V., AND CALOZ-C. (2007). Generalized coupled-mode approach of metamaterial coupled-line couplers: Coupling theory, phenomenological explanation, and experimental demonstration, *IEEE Transactions on Microwave Theory and Techniques*, **55**(5), pp. 1029–1039.

NGUYEN-TRONG-N., KAUFMANN-T., AND HALL-L. (2015). Analysis and design of a reconfigurable antenna based on half-mode substrate-integrated cavity, *IEEE Transactions on Antennas and Propagation*, **63**(8), pp. 3345–3353.

NIU-W., HUANG-M., XIAO-Z., AND YANG-J. (2010). Sensitivity enhancement in optical waveguide sensors based on tm wave and metamaterials, *Proc. IEEE 9th International Symposium on Antennas Propagation and EM Theory (ISAPE)*, pp. 697–700.

O´HARA-J. F., WITHAYACHUMNANKUL-W., AND AL-NAIB-I. (2012). A review on thin-film sensing with terahertz waves, *Journal of Infrared, Millimeter, and Terahertz Waves*, **33**(3), pp. 245–291.

OU-Y.-C., AND REBEIZ-G. M. (2011). Lumped-element fully tunable bandstop filters for cognitive radio applications, *IEEE Transactions on Microwave Theory and Techniques*, **59**(10), pp. 2461–2468.

PAN-W., HUANG-C., CHEN-P., PU-M., MA-X., AND LUO-X. (2013). A beam steering horn antenna using active frequency selective surface, *IEEE Transactions on Antennas and Propagation*, **61**(12), pp. 6218–6223.

PAUL-O., BEIGANG-R., AND RAHM-M. (2009). Highly selective terahertz bandpass filters based on trapped mode excitation, *Optics Express*, **17**(21), pp. 18590–18595.

PENDRY-J. B. (2000). Negative refraction makes a perfect lens, *Physical Review Letters*. art. no. 3966.

PENIRSCHKE-A., SCHUSSLER-M., AND JAKOBY-R. (2007). New microwave flow sensor based on a left-handed transmission line resonator, *IEEE/MTT-S International Microwave Symposium*, pp. 393–396.

POZAR-D. M. (2009). *Microwave Engineering*, John Wiley & Sons.

PUCCI-E., RAJO-IGLESIAS-E., KEHN-M. N. M., AND QUEVEDO-TERUEL-O. (2012). Enhancing the efficiency of compact patch antennas composed of split-ring resonators by using lumped capacitors, *IEEE Antennas and Wireless Propagation Letters*, **11**, pp. 1362–1365.

PUENTES-M., MAASCH-M., SCHUSSLER-M., AND JAKOBY-R. (2012). Frequency multiplexed 2-dimensional sensor array based on split-ring resonators for organic tissue analysis, *IEEE Transactions on Microwave Theory and Techniques*, **60**(6), pp. 1720–1727.

ROMEU-J., AND RAHMAT-SAMII-Y. (2000). Fractal FSS: a novel dual-band frequency selective surface, *IEEE Transactions on Antennas and Propagation*, **48**(7), pp. 1097–1105.

ROWE-D. J., AL-MALKI-S., ABDULJABAR-A., PORCH-A., BARROW-D., AND ALLENDER-C. J. (2014). Improved split-ring resonator for microfluidic sensing, *IEEE Transactions on Microwave Theory and Techniques*, **62**(3), pp. 689–699.

ROWE-D. J., PORCH-A., BARROW-D. A., AND ALLENDER-C. J. (2012). Microfluidic device for compositional analysis of solvent systems at microwave frequencies, *Sensors and Actuators B: Chemical*, **169**, pp. 213–221.

ROWE-D. J., PORCH-A., BARROW-D., AND ALLENDER-C. J. (2013). Microfluidic microwave sensor for simultaneous dielectric and magnetic characterization, *IEEE Transactions on Microwave Theory and Techniques*, **61**(1), pp. 234–243.

SAFWAT-A. M., TRETYAKOV-S., AND RÄISÄNEN-A. (2007). Dual bandstop resonator using combined split ring resonator and defected ground structure, *Microwave and Optical Technology Letters*, **49**(6), pp. 1249–1253.

SALEHI-M., AND BEHDAD-N. (2008). A second-order dual X-/Ka-band frequency selective surface, *IEEE Microwave and Wireless Components Letters*, **18**(12), pp. 785–787.

SANS-M., SELGA-J., RODRÍGUEZ-A., BONACHE-J., BORIA-V. E., AND MARTÍN-F. (2014). Design of planar wideband bandpass filters from specifications using a two-step aggressive space mapping (ASM) optimization algorithm, *IEEE Transactions on Microwave Theory and Techniques*, **62**(12), pp. 3341–3350.

SARABANDI-K., AND BEHDAD-N. (2007). A frequency selective surface with miniaturized elements, *IEEE Transactions on Antennas and Propagation*, **55**(5), pp. 1239–1245.

SAZEGAR-M., ZHENG-Y., KOHLER-C., MAUNE-H., NIKFALAZAR-M., BINDER-J., AND JAKOBY-R. (2012). Beam steering transmitarray using tunable frequency selective surface with integrated ferroelectric varactors, *IEEE Transactions on Antennas and Propagation*, **60**(12), pp. 5690–5699.

SAZEGAR-M., ZHENG-Y., MAUNE-H., DAMM-C., ZHOU-X., AND JAKOBY-R. (2011). Compact tunable phase shifters on screen-printed bst for balanced phased arrays, *IEEE Transactions on Microwave Theory and Techniques*, **59**(12), pp. 3331–3337.

SCHOENLINNER-B., ABBASPOUR-TAMIJANI-A., KEMPEL-L. C., AND REBEIZ-G. M. (2004). Switchable low-loss RF MEMS Ka-band frequency-selective surface, *IEEE Transactions on Microwave Theory and Techniques*, **52**(11), pp. 2474–2481.

SCHURIG-D., MOCK-J., JUSTICE-B., CUMMER-S. A., PENDRY-J. B., STARR-A., AND SMITH-D. (2006). Metamaterial electromagnetic cloak at microwave frequencies, *Science*, **314**(5801), pp. 977–980.

SHAMAN-H., AND HONG-J.-S. (2007). Wideband bandstop filter with cross-coupling, *IEEE Transactions on Microwave Theory and Techniques*, **55**(8), pp. 1780–1785.

SHANG-Y., SHEN-Z., AND XIAO-S. (2013). On the design of single-layer circuit analog absorber using double-square-loop array, *IEEE Transactions on Antennas and Propagation*, **61**(12), pp. 6022–6029.

SHANG-Y., SHEN-Z., AND XIAO-S. (2014). Frequency-selective rasorber based on square-loop and cross-dipole arrays, *IEEE Transactions on Antennas and Propagation*, **62**(11), pp. 5581–5589.

SHELBY-R. A., SMITH-D. R., AND SCHULTZ-S. (2001). Experimental verification of a negative index of refraction, *Science*, **292**(5514), pp. 77–79.

SIEVENPIPER-D., ZHANG-L., BROAS-R. F. J., ALEXOPOLOUS-N. G., AND YABLONOVITCH-E. (1999). High-impedance electromagnetic surfaces with a forbidden frequency band, *IEEE Transactions on Microwave Theory and Techniques*, **47**(11), pp. 2059–2074.

SMITH-D. R., PADILLA-W. J., VIER-D., NEMAT-NASSER-S. C., AND SCHULTZ-S. (2000). Composite medium with simultaneously negative permeability and permittivity, *Physical Review Letters*. art. no. 4184.

SMITH-D. R., PENDRY-J. B., AND WILTSHIRE-M. C. (2004). Metamaterials and negative refractive index, *Science*, **305**(5685), pp. 788–792.

SU-L., NAQUI-J., MATA-CONTRERAS-J., AND MARTÌN-F. (2015). Modeling and applications of metamaterial transmission lines loaded with pairs of coupled complementary split ring resonators (CSRRs), *IEEE Antennas and Wireless Propagation Letters*. DOI: 10.1109/LAWP.2015.2435656.

TAKEMURA-N. (2013). Tunable inverted-L antenna with split-ring resonator structure for mobile phones, *IEEE Transactions on Antennas and Propagation*, **61**(4), pp. 1891–1897.

TAYA-S. A., AND SHABAT-M. M. (2011). Sensitivity enhancement in optical waveguide sensors using metamaterials, *Applied Physics A*, **103**(3), pp. 611–614.

TRETYAKOV-S., SIHVOLA-A., AND JYLHÄ-L. (2005). Backward-wave regime and negative refraction in chiral composites, *Photonics and Nanostructures-Fundamentals and Applications*, **3**(2), pp. 107–115.

VÉLEZ-A., AZNAR-F., DURAN-SINDREU-M., BONACHE-J., AND MARTÍN-F. (2010). Stop-band and band-pass filters in coplanar waveguide technology implemented by means of electrically small metamaterial-inspired open resonators, *IET Microwaves, Antennas & Propagation*, **4**(6), pp. 712–716.

VÉLEZ-P., DURÁN-SINDREU-M., NAQUI-J., BONACHE-J., AND MARTÍN-F. (2014). Common-mode suppressed differential bandpass filter based on open complementary split ring resonators fabricated in microstrip technology without ground plane etching, *Microwave and Optical Technology Letters*, **56**(4), pp. 910–916.

VÉLEZ-P., NAQUI-J., FERNANDEZ-PRIETO-A., DURAN-SINDREU-M., BONACHE-J., MARTEL-J., MEDINA-F., AND MARTÍN-F. (2013). Differential bandpass filter with common-mode suppression based on open split ring resonators and open complementary split ring resonators, *IEEE Microwave and Wireless Components Letters*, **23**(1), pp. 22–24.

VENDIK-I., VENDIK-O., KOLMAKOV-I., AND ODIT-M. (2006). Modelling of isotropic double negative media for microwave applications, *Opto-Electronics Review*, **14**(3), pp. 179–186.

VENDIK-O. G., AND GASHINOVA-M. (2004). Artificial double negative (DNG) media composed by two different dielectric sphere lattices embedded in a dielectric matrix, *Proc. IEEE 34th European Microwave Conference*, Vol. 3, pp. 1209–1212.

VESELAGO-V. G. (1968). The electrodynamics of substances with simultaneously negative values of ϵ and μ, *Physics-Uspekhi*, **10**(4), pp. 509–514.

WITHAYACHUMNANKUL-W., AND ABBOTT-D. (2009). Metamaterials in the terahertz regime, *IEEE Photonics Journal*, **1**(2), pp. 99–118.

WITHAYACHUMNANKUL-W., FUMEAUX-C., AND ABBOTT-D. (2010). Compact electric-LC resonators for metamaterials, *Optics Express*, **18**(25), pp. 25912–25921.

WITHAYACHUMNANKUL-W., FUMEAUX-C., AND ABBOTT-D. (2011). Planar array of electric-LC resonators with broadband tunability, *IEEE Antennas and Wireless Propagation Letters*, **10**, pp. 577–580.

WITHAYACHUMNANKUL-W., JARUWONGRUNGSEE-K., FUMEAUX-C., AND ABBOTT-D. (2012). Metamaterial-inspired multichannel thin-film sensor, *IEEE Sensors Journal*, **12**(5), pp. 1455–1458.

WITHAYACHUMNANKUL-W., JARUWONGRUNGSEE-K., TUANTRANONT-A., FUMEAUX-C., AND ABBOTT-D. (2013). Metamaterial-based microfluidic sensor for dielectric characterization, *Sensors and Actuators A: Physical*, **189**, pp. 233–237.

WITHAYACHUMNANKUL-W., PNG-G., YIN-X., ATAKARAMIANS-S., JONES-I., LIN-H., UNG-B., BALAKRISHNAN-J., NG-B.-H., FERGUSON-B., MICKAN-S., FISCHER-B. M., AND ABBOTT-D. (2007). T-ray sensing and imaging, *Proceedings of the IEEE*, **95**(8), pp. 1528–1558.

WU-B., FAN-J., ZHAO-L., AND LIANG-C. (2007). Design of dual-band filter using defected split-ring resonator combined with interdigital capacitor, *Microwave and Optical Technology Letters*, **49**(9), pp. 2104–2106.

YAGHMAEE-P., FUMEAUX-C., BATES-B., MANABE-A., KARABEY-O. H., AND JAKOBY-R. (2012a). Frequency tunable S-band resonator using nematic liquid crystal, *Electronics Letters*, **48**(13), pp. 798–800.

YAGHMAEE-P., HORESTANI-A. K., BATES-B., AND FUMEAUX-C. (2012b). A multi-layered tunable stepped-impedance resonator for liquid crystal characterization, *IEEE Asia-Pacific Microwave Conference (APMC)*, pp. 776–778.

YAGHMAEE-P., KARABEY-O. H., BATES-B., FUMEAUX-C., AND JAKOBY-R. (2013a). Electrically tuned microwave devices using liquid crystal technology, *International Journal of Antennas and Propagation*. Article ID 824214.

YAGHMAEE-P., WITHAYACHUMNANKUL-W., HORESTANI-A. K., EBRAHIMI-A., BATES-B., AND FUMEAUX-C. (2013b). Tunable electric-LC resonators using liquid crystal, *IEEE Antennas and Propagation Society International Symposium (APSURSI)*, IEEE, pp. 382–383.

YANG-J., HUANG-M., XIAO-Z., AND PENG-J. (2010). Simulation and analysis of asymmetric metamaterial resonator-assisted microwave sensor, *Modern Physics Letters B*, **24**(12), pp. 1207–1215.

YARDIMCI-N. T., YANG-S.-H., BERRY-C. W., AND JARRAHI-M. (2015). High-power terahertz generation using large-area plasmonic photoconductive emitters, *IEEE Transactions on Terahertz Science and Technology*, **5**(2), pp. 223–229.

YU-K. B., OGOURTSOV-S., BELENKY-V., MASLENIKOV-A., AND OMAR-A. S. (2000). Accurate microwave resonant method for complex permittivity measurements of liquids [biological], *IEEE Transactions on Microwave Theory and Techniques*, **48**(11), pp. 2159–2164.

ZARIFI-M. H., THUNDAT-T., AND DANESHMAND-M. (2015). High resolution microwave microstrip resonator for sensing applications, *Sensors and Actuators A: Physical*, **233**, pp. 224–230.

ZENDEJAS-J. M., GIANVITTORIO-J. P., RAHMAT-SAMII-Y., AND JUDY-J. W. (2006). Magnetic MEMS reconfigurable frequency-selective surfaces, *Journal of Microelectromechanical Systems*, **15**(3), pp. 613–623.

ZHANG-Y., HONG-W., YU-C., KUAI-Z.-Q., DON-Y.-D., AND ZHOU-J.-Y. (2008). Planar ultrawideband antennas with multiple notched bands based on etched slots on the patch and/or split ring resonators on the feed line, *IEEE Transactions on Antennas and Propagation*, **56**(9), pp. 3063–3068.

ZHELUDEV-N. I. (2010). The road ahead for metamaterials, *Science*, **328**(5978), pp. 582–583.

ZHOU-M., TONG-C.-M., FU-S.-H., WU-L.-N., AND LI-X.-M. (2010). A novel spiral defected ground structure and its application to the design of dual bandstop filter, *2010 International Symposium on Signals Systems and Electronics (ISSSE)*, Vol. 2. DOI: 10.1109/ISSSE.2010.5607006.

ZHU-J., AND ELEFTHERIADES-G. V. (2009). A compact transmission-line metamaterial antenna with extended bandwidth, *IEEE Antennas and Wireless Propagation Letters*, **8**, pp. 295–298.

ZHU-Y., VEGESNA-S., KURYATKOV-V., HOLTZ-M., SAED-M., AND BERNUSSI-A. A. (2012). Terahertz bandpass filters using double-stacked metamaterial layers, *Optics Letters*, **37**(3), pp. 296–298.

ZIOLKOWSKI-R. W., AND ENGHETA-N. (2003). Metamaterial special issue introduction, *IEEE Transactions on Antennas and Propagation*, **51**(10), pp. 2546–2549.

ZVEREV-A. I. (1967). *Handbook of Filter Synthesis*, Vol. 47, Wiley New York.

List of Acronyms

BW Bandwidth

CELC Complementary electric-LC

COC Cyclic olefin copolymer

CPW Coplanar waveguide

CRLH TL Composite right/left hand transmission line

CSRR Complementary split-ring resonator

DMCSRR Dual-mode complementary split-ring resonator

DPS Double positive

DNG Double negative

ELC Electric-LC

EM Electromagnetic

ENG Epsilon-negative

FBW Fractional bandwidth

FSS Frequency selective surface

LHM Left-handed media

MEMS Microelectromechanical systems

MMW Millimeter wave

MNG Mu-negative

PDMS Polydimethylsiloxane

RF Radio frequency

RHM Right-handed media

SRR Split-ring resonator

TE Transverse electric

TL Transmission line

TM Transverse magnetic

Index

Biography

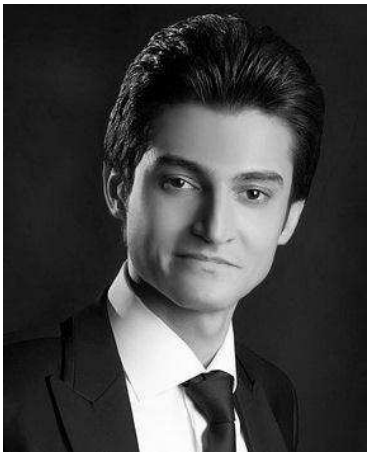

Amir Ebrahimi was born in Babol, Iran, in 1986. He received the B.Sc. degree in electrical and computer engineering from the University of Mazandaran, Iran, in 2008, and the M.Sc. degree in electronic engineering with first class honours from Babol University of Technology, Babol, Iran, 2011 under supervision of Prof. Hossein MiarNaimi. From 2009 to 2012, he was a research assistant in Integrated Circuits Research Laboratory (ICRL), Babol University of Technology.

In 2012, he started his PhD degree under Dr Said Al-Sarawi, Dr Withawat Withayachumnankul, and Prof. Derek Abbott, in the School of Electrical & Electronic Engineering, The University of Adelaide. During 2014–2015, he was a visiting scholar in the School of Electrical & Electronic Engineering, Nanyang Technological University (NTU), Singapore, hosted by Prof. Zhongxiang Shen. During his candidature, Mr Ebrahimi received a number of awards and scholarships including, the International Postgraduate Research Scholarship (IPRS) by the Australian Government (2012), Australian Postgraduate Award (APA) (2012), Australian National Fabrication Facility (ANFF) award for fabricating high performance microwave microfluidic sensors in collaboration with the Ian Wark Research Institute, University of South Australia (2013), the University of Adelaide D. R. Stranks Traveling Fellowship (2014), the Simon Rockliff Scholarship for outstanding postgraduate mentorship from DSTO (2015), and the Yarman-Carlin best student paper award at the Mediterranean Microwave Symposium, Lecce, Italy (2015). Mr Ebrahimi has served as a reviewer for a number of recognised journals including *IEEE Microwave and Wireless Components Letter*, *IEEE Sensors Journal*, *Applied Physics Letters*, and *Journal of Applied Physics*. He is a member of Institution of Engineers Australia (IEAust) and a graduate student member of the IEEE, IEEE Microwave Theory and Techniques Society, and the Australian Nanotechnology Network.

Amir Ebrahimi
amir.ebrahimi@adelaide.edu.au

Scientifc Genealogy of
Amir Ebrahimi

Formalised supervisor relationship
Mentoring relationship
Nobel prize

"If I have seen further it is by standing on the shoulders of Giants."
Isaac Newton